



UNITED NATIONS  
UNIVERSITY

**UNU-GTP**

 **ORKUSTOFNUN**



**Snorralaug, Reykholt, W-Iceland**

Getenesh Hailegiorgis Abebe

**MULTI-DIMENSIONAL INVERSION OF ELECTROMAGNETIC DATA  
FROM ALALOBEDA, TENDAHO GEOTHERMAL FIELD IN  
NE-ETHIOPIA AND ITS GEOTHERMAL SIGNIFICANCE**

Report 5  
December 2019



UNITED NATIONS  
UNIVERSITY

**UNU-GTP**

Geothermal Training Programme

Orkustofnun, Grensasvegur 9,  
IS-108 Reykjavik, Iceland

Reports 2019  
Number 5

# **MULTI-DIMENSIONAL INVERSION OF ELECTROMAGNETIC DATA FROM ALALOBEDA, TENDAHO GEOTHERMAL FIELD IN NE-ETHIOPIA AND ITS GEOTHERMAL SIGNIFICANCE**

**MSc thesis**

School of Engineering and Natural Sciences  
Faculty of Earth Sciences  
University of Iceland

by

**Getenesh Hailegiorgis Abebe**  
Geological Survey of Ethiopia  
P.O. Box 2302  
Addis Ababa,  
ETHIOPIA  
*getenesh19@gmail.com*

United Nations University  
Geothermal Training Programme  
Reykjavík, Iceland  
Published in December 2019

ISBN 978-9979-68-554-8 (PRINT)  
ISBN 978-9979-68-555-5 (PDF)  
ISSN 1670-7427

This MSc thesis has also been published in October 2019 by the  
School of Engineering and Natural Sciences, Faculty of Earth Sciences  
University of Iceland

## INTRODUCTION

The Geothermal Training Programme of the United Nations University (UNU) has operated in Iceland since 1979 with six-month annual courses for professionals from developing countries. The aim is to assist developing countries with significant geothermal potential to build up groups of specialists that cover most aspects of geothermal exploration and development. During 1979-2019, 718 scientists and engineers from 63 developing countries have completed the six-month courses, or similar. They have come from Africa (39%), Asia (35%), Latin America (14%), Europe (11%), and Oceania (1%). There is a steady flow of requests from all over the world for the six-month training and we can only meet a portion of the requests. Most of the trainees are awarded UNU Fellowships financed by the Government of Iceland.

Candidates for the six-month specialized training must have at least a BSc degree and a minimum of one-year practical experience in geothermal work in their home countries prior to the training. Many of our trainees have already completed their MSc or PhD degrees when they come to Iceland, but many excellent students with only BSc degrees have made requests to come again to Iceland for a higher academic degree. From 1999, UNU Fellows have also been given the chance to continue their studies and study for MSc degrees in geothermal science or engineering in co-operation with the University of Iceland. An agreement to this effect was signed with the University of Iceland. A similar agreement was also signed with Reykjavik University in 2013. The six-month studies at the UNU Geothermal Training Programme form a part of the graduate programme.

It is a pleasure to introduce the 67<sup>th</sup> UNU Fellow to complete MSc studies under a UNU-GTP Fellowship. Getenesh Hailegiorgis Abebe, *Physicist* by education, from Geological Survey of Ethiopia (GSE), completed the six-month specialized training in *Geophysical Exploration* at UNU Geothermal Training Programme in October 2015. Her research report was entitled: *Processing and joint 1D inversion of MT and TEM data from Alalobeda geothermal field in Tendaho, NE-Ethiopia*. After two years of geothermal work for GSE in Ethiopia, she came back to Iceland for MSc studies at the School of Engineering and Natural Sciences, Faculty of Earth Sciences at University of Iceland in August 2017. In October 2019, she defended her *MSc thesis* in *Geophysical Exploration*, presented here, entitled: *Multi-dimensional inversion of electromagnetic data from Alalobeda, Tendaho geothermal field in NE-Ethiopia and its geothermal significance*. Her studies in Iceland were financed by the Government of Iceland through a UNU-GTP Fellowship from the UNU Geothermal Training Programme. We congratulate Getenesh on the achievements and wish her all the best for the future. We thank the School of Engineering and Natural Sciences, Faculty of Earth Sciences at University of Iceland for the co-operation, and her supervisors for the dedication.

Finally, I would like to mention that Getenesh' MSc thesis with the figures in colour is available for downloading on our website [www.unugtp.is](http://www.unugtp.is) (to change to [www.groctp.org](http://www.groctp.org) by January 2020), under publications.

With warmest greetings from Iceland,

Lúdvík S. Georgsson, Director  
United Nations University  
Geothermal Training Programme

## ACKNOWLEDGEMENTS

This thesis is written during the hard time of my life, I lost my lovely Father, Uncle and Aunt; therefore, above all, I would like to thank the almighty God who gave me the strength to complete it.

I sincerely thank the United Nations University Geothermal Training Programme (UNU-GTP) and the Government of Iceland for sponsoring me to pursue the master's study. I would like to express my special gratitude towards the entire UNU-GTP staff, Director of UNU-GTP Mr. Lúdvík S. Georgsson, Deputy Director Mr. Ingimar G. Haraldsson, Ms. Málfríður Ómarsdóttir, Ms. Thórhildur Ísberg, Ms. Vigdís Harðardóttir and Mr. Markús A.G. Wilde for their great care and help throughout the study period.

I would like to express my sincere gratitude to my supervisors Gylfi Páll Hersir, Ásdís Benediktsdóttir and Halldór Geirsson for their continued guidance and support, constructive feedback, for their patient, motivation and immense knowledge. I have been extremely lucky to have supervisors who care so much, and who responded to my questions and queries so promptly. You have set an example of excellence as supervisor, instructor and role model. I would also like to thank my fellow Diego and Charles Muturia for their guidance and assistance for being there whenever I needed their help. Thanks to all UNU-GTP fellows and friends at the University of Iceland for the good time we spend together and sharing experience. I wish to thank the University of Iceland and ISOR-Iceland GeoSurvey for providing access to facilities and training required for successful completion of this master study.

I am very thankful to my employer company Geological Survey of Ethiopia (GSE) for the study leave, allowing use of data and continued support. Special thanks to Ato Solomon Kebede, Geothermal Resource Exploration and Evaluation Assessment directorate, and Ato Hundie Melka, chief geologist of Geological Survey of Ethiopia. I express my deep sense of gratitude to all my colleagues in the geothermal department back home giving me all the necessary information for my thesis work and people who have willingly helped me out with their abilities. You will forever remain in my heart. I would like to express my special gratitude and thanks to ICEIDA people (Icelandic International Development Agency, presently carried out by the Directorate for International Development Cooperation within the Ministry for Foreign Affairs (MFA)) for giving me the opportunity to participate in the field work. I am highly indebted to ELC-Consult Company people for providing me with all the information and data regarding my thesis and for their support in completing my thesis.

My deepest appreciation goes to my beloved family for their unconditional support and everlasting love throughout my entire life and my studies. I have no words thank all the people who were in our side during our difficult time in our life.

## DEDICATION

*I would like to dedicate this thesis to my beloved father, uncle and aunt who passed away during my study, who taught me to preserve and prepared me to face the challenges with faith and humility. You were giving me constant inspiration to my life. Although you are not here to give me strength and support, I always feel your presence that used to urge me to strive to achieve my goals in life. You always had confidence in me and offered me encouragement and support in all my endeavours.*

*I would like also to dedicate this thesis to my lovely mother, sisters and brothers, who helped me to finish this work during this difficult time in my life.*

## ABSTRACT

Measuring the electrical resistivity of rocks is one of the main geothermal prospecting techniques commonly used today. A resistivity survey was carried out in Alalobeda geothermal prospect, Ethiopia through the combined use of MT and TEM soundings. The study area is around 250 km<sup>2</sup>. In this study, 1D joint inversion of 108 MT and TEM sounding pairs and a 3D inversion of the off-diagonal static shift corrected impedance tensor elements of 107 MT soundings were done. The static shift correction of the MT data was made by jointly inverting the MT and TEM data from the same site. Shift correction was done for the two polarizations before the 3D inversion was performed. The WSINV3DMT code was used to carry out 3D inversion of the MT data. The robustness of the final 3D inversion model was tested by using two different initial models. The first initial model was compiled from the 1D joint inversion of MT and TEM soundings which gave a Root Mean Square (RMS) of 1.7; the second model was a homogeneous Earth of resistivity 10  $\Omega$ m, which gave an RMS of 1.2. The final models show similar resistivity structures at shallow depths (the uppermost few hundred m) but the 10  $\Omega$ m initial model could not resolve the deep structures.

The main objective of the survey was to come up with a detailed resistivity model and image the deep resistivity structure, detect and characterize a possible geothermal reservoir of the Alalobeda geothermal prospect compare different interpretational techniques and propose drilling sites. The results of the 1D joint inversion of MT/TEM data and 3D inversion of MT data gave comparable results at shallow depths. However, at deeper levels 3D inversion reveals much more consistent details confirming that the resistivity structure in the area is highly three dimensional.

The resistivity models resulting from the 1D and 3D inversions are presented in the form of depth-slice maps and cross-sections. The results of the inversion show three main resistivity structures. The first one is a layer of very low resistivity (<10  $\Omega$ m) at shallow depth down to 300 m b.s.l., which is correlated with conductive sedimentary formation and/or smectite alteration. The second layer has high resistivity between the depths of 1000 m to around 4000 m b.s.l., which correlates with the resistive Afar Stratoid basalt Series and/or chloride-epidote alteration. The high resistivity layer is cut by vertical low resistivity columns that follow the main faults in the area and most likely reflect the up flow of geothermal fluid from depth into the sediments/surface. Beneath the high resistivity at a depth of 5000 m b.s.l. a deep conductor has been imaged that could be associated with a heat source.

From the 1D and 3D inversions lithological contacts and lineaments were identified. Sharp resistivity contacts or fault lines with an orientation of NE-SW transverse faults and NW-SE fault were observed. These identified faults and lineaments are in good agreement with gravimetric and micro-seismic results. From this study, the up flow zone of the survey area are mapped and locations of exploratory well sites are proposed based on the resistivity results. Here, three well sites are proposed in the study area, (1) to the southwest of the survey area into one of the up flow zones along the Tendaho graben shoulder; (2) to the east of the survey area into the up flow zone; (3) to the northeast of the surface manifestations of the survey area into the up flow zone.

## TABLE OF CONTENTS

	Page
1. INTRODUCTION.....	1
2. TENDAHO GEOTHERMAL FIELD.....	3
2.1 Introduction .....	3
2.2 Location of the study area .....	3
2.3 Geological and tectonic setting of Tendaho .....	4
2.4 Structures controlling the geothermal system in Tendaho .....	5
2.5 Geothermal manifestation .....	5
2.6 Review of previous geo-scientific studies .....	6
2.6.1 Previous geological studies .....	6
2.6.2 Previous geophysical studies.....	7
2.6.3 Previous geochemical studies.....	8
3. APPLICATION OF RESISTIVITY METHODS IN GEOTHERMAL EXPLORATION.....	11
3.1 Various resistivity measurement methods.....	11
3.2 Resistivity of rocks .....	11
3.2.1 Porosity and pore structure of the rocks.....	11
3.2.2 Salinity of fluids.....	12
3.2.3 Temperature .....	13
3.2.4 Fluid saturation.....	13
3.3 Resistivity structure of high temperature geothermal systems .....	13
4. MT METHOD.....	16
4.1 Overview of MT .....	16
4.1.1 Source of MT soundings .....	16
4.1.2 The basic theory of EM and Maxwell's equations.....	17
4.1.3 EM wave in conductive media .....	17
4.1.4 Non-vertical incidence in conductive half-space .....	21
4.1.5 Depth of penetration.....	21
4.2 Homogenous earth.....	22
4.3 Horizontally layered earth .....	23
4.4 MT transfer functions .....	24
4.4.1 Impedance tensor .....	25
4.4.2 Geomagnetic transfer functions .....	25
4.5 Dimensionality of MT transfer functions .....	26
4.5.1 1D Earth .....	26
4.5.2 2D Earth .....	26
4.5.3 3D Earth .....	27
4.6 Rotation of impedance tensor.....	28
4.7 Dimensionality indicators.....	28
4.7.1 Impedance polar diagram .....	29
4.7.2 Skew.....	29
4.7.3 Ellipticity.....	30
4.7.4 Tipper magnitude .....	30
5. MT STATIC SHIFT PROBLEM.....	31
5.1 MT data distortion due to anomalous body .....	31
5.1.1 Voltage distortion.....	31
5.1.2 Current distortion .....	32
5.2 Topographic effect.....	32

	Page
6. DATA ACQUISITION, INSTRUMENTATION AND DATA PROCESSING .....	33
6.1 Instrumentation and field survey .....	33
6.2 Processing MT data .....	36
6.3 Estimation of MT transfer function .....	38
6.4 Remote reference estimate .....	38
7. TEM METHOD .....	41
7.1 General concepts .....	41
7.2 TEM instrumentation and field measurements .....	42
7.3 TEM data processing .....	42
8. MULTI-DIMENSIONAL INVERSION OF EM DATA FROM THE ALALOBEDA GEOHERMAL PROSPECT .....	43
8.1 1D inversion .....	43
8.2 Joint 1D inversion of MT and TEM soundings .....	43
8.3 Static shift correction .....	43
8.4 Results and interpretations of the joint 1D inversion .....	44
8.4.1 Resistivity cross-sections .....	44
8.4.2 Resistivity depth-slices .....	48
8.5 Geo-electrical strike analysis .....	50
8.5.1 Tipper Strike .....	51
8.5.2 Induction arrows .....	52
8.6 Conclusion from the 1D joint inversion .....	53
9. 3D INVERSION OF MT DATA .....	54
9.1 3D MT code .....	54
9.1.1 Overview of the WSINV3DMT code .....	54
9.1.2 Static shift correction .....	54
9.1.3 Preparation of data .....	56
9.1.4 3D model mesh grid design .....	56
9.1.5 3D modelling parameters and initial models .....	58
9.2 Results of the 3D inversion .....	58
9.2.1 Comparison of different initial models .....	58
9.2.2 Resistivity depth-slice maps based on the 3D inversion .....	60
9.2.3 Vertical cross-section through the 3D model .....	63
9.3 Comparisons of 1D and 3D results .....	67
10. UP FLOW ZONES .....	73
11. CONCLUSIONS AND RECOMMENDATIONS .....	75
REFERENCES .....	76
APPENDIX I: 1D joint inversion of MT and TEM data .....	81
APPENDIX II: Resistivity cross-sections based on 1D joint inversion .....	88
APPENDIX III: Resistivity depth slices / maps based on 1D joint inversion .....	101
APPENDIX IV: 3D inversion data fit .....	103
APPENDIX V: 3D Resistivity depth slices .....	115
APPENDIX VI: Resistivity cross-sections based on the 3D inversion .....	118

## LIST OF FIGURES

	Page
1. Map showing the East African Rift; the Main Ethiopian Rift, Kenya Rift and Western Branch ..1	
2. Location map of the Ethiopian Rift and geothermal prospect areas .....2	
3. An aerial photograph of Tendaho and the three geothermal fields .....3	
4. Picture showing the ridge of the Alalobeda prospect.....6	
5. Simplified geological map of the Afar triple junction .....6	
6. Geological stratigraphy of well TD2, TD4 and TD1 .....7	
7. Residual Bouguer gravity map.....8	
8. Horst graben structure .....8	
9. Structural map derived from gravimetric interpretation superimposed on topographic DEM .....9	
10. Gignenbach diagram for geothermal well fluids in Dubti and Alaalobeda .....9	
11. Triangular diagram with main anions for water samples collected in Alalobeda .....10	
12. Electrical resistivity of a NaCl solution as a function of concentration and temperature .....12	
13. Electrical resistivity of a NaCl solution as a function of temperature for different pressures .....13	
14. General resistivity structure of a high-temperature geothermal system in basaltic rocks.....14	
15. Typical resistivity structure of a high temperature geothermal area .....14	
16. Sources of EM field .....16	
17. An EM wave incident on the surface of the Earth. ....21	
18. 2D model and the concept of polarizations in magnetotellurics .....27	
19. Rotation of reference frame .....28	
20. Polar diagrams of the impedance tensor showing 1D, 2D and 3D form of plots.....29	
21. Static shift due to electric field distortion .....31	
22. Current channelling leading to current distortion .....32	
23. Effect of a ridge and valley on current density and correction for the topographic effects .....32	
24. Standard setup of an MT sounding .....33	
25. Hole filled with a mixture of salty water, bentonite and soil and installation of an electrode ....34	
26. Digging of a shallow trench and leveling the magnetic sensor.....35	
27. Buring the vertical magnetic sensor.....35	
28. Connected data logger, and checking the online status of data acquisition .....36	
29. Wooden box used for protecting the data logger from the sun and wind .....36	
30. Time series plot of electric and magnetic field components .....37	
31. SSMT2000 processing package .....37	
32. MTeditor, showing the apparent resistivity and phase curves .....40	
33. An example of processed MT data from Alalobeda prospect area for two soundings .....40	
34. The central loop TEM sounding configuration.....41	
35. Basic principles of the TEM method .....41	
36. Location map of MT and TEM soundings from the Alalobeda prospect .....44	
37. Result of joint 1D inversion of an MT and TEM sounding, station A011 .....45	
38. A histogram of the static shift parameters, and static shift multipliers in Alalobeda prospect ....45	
39. An example of static shift correction of MT data from Alalobeda prospect.....46	
40. Location of resistivity cross-sections based on the 1D model .....46	
41. Resistivity cross-section PL-03 based on joint 1D Occam inversion of TEM and MT data .....47	
42. Resistivity cross-section PT-04 based on joint 1D Occam inversion of TEM and MT data .....48	
43. Resistivity depth-slice at 300 m a.s.l. based on 1D Occam inversion.....49	
44. Resistivity depth-slice at 200 m b.s.l. based on 1D Occam inversion .....49	
45. Resistivity depth-slice at 600 m b.s.l. based on 1D Occam inversion .....50	
46. Resistivity depth-slice at 5000 m b.s.l. based on 1D Occam inversion .....51	
47. Tipper strike for 0.1-10 s.....51	
48. Tipper strike for 10-100 s.....52	
49. Induction arrows for 0.03 s, corresponding to a depth of a few hundred m.....52	
50. Induction arrows for 30 s, corresponding to a depth of a few km.....53	
51. Joint 1D inversion of TEM and MT.....55	
52. Histogram, and a spatial distribution map of static shift multipliers of the xy-mode .....55	
53. Histogram and a spatial distribution map of static shift multipliers for the yx-mode.....55	

	Page
54. The centre of the 3D model grid with dimension of central grid squares 400 m × 400 m.....	57
55. The 3D model grid.....	57
56. Data fit between the measured data and model response for station A001.....	58
57. Resistivity depth-slice at 300 m a.s.l. showing a comparison of models from 3D inversion.....	59
58. Resistivity depth-slice at 5000 m b.s.l. showing a comparison of models from 3D inversion ....	59
59. Resistivity cross-section NS_E-3800 - comparison based on different initial models .....	60
60. Depth-slice through the J1D model at 200 m a.s.l .....	61
61. Depth-slice through the J1D model at 600 m b.s.l.....	61
62. Depth-slice through the J1D model at 2000 m b.s.l.....	62
63. Depth-slice through the J1D model at 5000 m b.s.l.....	62
64. Resistivity cross-sections NS_E-3800 .....	63
65. Resistivity cross-sections NS_E-2600 .....	64
66. Resistivity cross-sections NS_E1400.....	64
67. Resistivity cross-sections NS_E4600.....	65
68. Resistivity cross-sections EW_N-600.....	65
69. Resistivity cross-sections EW_N-4200.....	66
70. Resistivity cross-sections EW_N600.....	66
71. Resistivity cross-sections EW_N3800 .....	67
72. Comparison of 1D and 3D resistivity cross-sections NS-3800.....	68
73. Comparison of 1D and 3D resistivity cross-sections NS5000 .....	69
74. Comparison of 1D and 3D resistivity cross-sections EW-1000.....	70
75. Comparison between resistivity depth-slices for 1D and 3D inversion at 100 m a.s.l.....	70
76. Comparison between resistivity depth-slices for 1D and 3D inversion at 1000 m b.s.l .....	71
77. Comparison between resistivity depth-slices for 1D and 3D inversion at 5000 m b.s.l .....	72
78. Map showing the up flow zones in Alalobeda geothermal prospect.....	73
79. Maps showing the most prominent heat source .....	74

## ACRONYMS AND ABBREVIATIONS

MT	Magnetotelluric
AMT	Audio-magnetotelluric
TEM	Transient electromagnetic
EM	Electromagnetic
TE	Transverse electric
TM	Transverse magnetic
EDI	Electrical data interchange
USF	Universal Sounding Format
TemxZ	Program for processing Zonge TEM data
TemxV	Program for processing V8 TEM data
TEMTD	1D MT/TEM inversion program
V8	Phoenix TEM equipment
m a.s.l.	Metres above sea level
m b.s.l.	Metres below sea level
WSINV3DMT	3D inversion program
EARS	East African Rift System
MER	Main Ethiopian Rif

## EXPLANATION OF SYMBOLS

### Notation

$E$ ( $V\ m^{-1}$ )	Electric field intensity
$B$ (T)	Magnetic induction
$H$ ( $A\ m^{-1}$ )	Magnetic field intensity
$D$ ( $C\ m^{-2}$ )	Electric displacement
$\eta$ ( $C\ m^{-3}$ )	Electric charge density of free charges
$J$ ( $A\ m^{-2}$ )	Electric current density
$\sigma$ ( $Sm^{-1}$ )	Electric conductivity
$\mu$ (H/m)	Magnetic permeability
$\epsilon$ (F/m)	Electric permittivity
$\delta$ (m)	Electromagnetic skin depth
$T$ (s)	Period
$f$ (Hz)	Frequency
$t$ (s)	Time
$\omega$ (rad/s)	Angular frequency
$\rho$ ( $\Omega m$ )	Resistivity (specific resistance)
$\hat{Z}$ ( $\Omega$ )	Impedance tensor (2x2 matrices)
$\rho_a$ ( $\Omega m$ )	Apparent resistivity
$\phi$ ( $^\circ$ )	Impedance phase
$i$ ( $\sqrt{-1}$ )	Imaginary number
$k$ ( $m^{-1}$ )	Propagation constant (wave number)
$\mathcal{T}$	Tipper
$\Re$	Real part of the Tipper
$\Im$	Imaginary part of the Tipper
$M_r$	Length of the real part of the induction arrow
$M_q$	Length of imaginary part of the induction arrow
$x, y$ and $x', y'$	Reference frame and reference frame rotated through an angle $\theta$

## 1. INTRODUCTION

The East African Rift system (EARS) is one of the areas in the world where numerous sites for harnessing potential geothermal energy are found, see Figure 1. Exploration of geothermal energy began in the Main Ethiopian Rift (MER) in 1969 with a collaboration between the Ethiopian Government and United Nations Development Program (UNDP) (Bekele, 2012). The most significant geothermal resources of Ethiopia, identified by surface exploration studies, are located along the MER and in the Afar Depression, both belonging to the great EARS (Endeshaw, 1988; UNDP, 1973). Among them is Tendaho, one of the geothermal fields in the MER System see Figure 1. Since then about 23 geothermal prospects have been identified for direct use and electricity generation, see Figure 2 (JICA, 2015). However, most of the resources have not been explored and evaluated in detail. All the prospects are at different stages of exploration.

Energy plays an important role in the strategic development of Ethiopia, because it is a source of foreign exchange and it is a catalyst for industrial progress. Even though Ethiopia has a diversity of modern energy sources (hydro, solar, wind, geothermal and natural gas etc.), it does not fully use its resources, and it still relies on imported petroleum and petroleum products. Considering the shortage of modern energy supplies in the country and environmental degradation of fossil fuel and then hydro relies highly on seasonal rainfall, geothermal energy needs to be developed in Ethiopia to serve as a source of reliable energy base (Kebede, 2010; Teklemariam and Beyene, 2005). Presently the government tries to invite the private sector to develop sustainable energy by giving priority to geothermal energy.

Most geophysical methods have been applied in exploration of geothermal resources. However, various electrical and thermal methods have been the most useful ones. Especially electromagnetic methods that include magnetotelluric (MT) and transient electromagnetic (TEM) are currently the most widely used resistivity methods, due to their ability to recover complex resistivity structures of the subsurface of the Earth (Flóvenz et al., 2012).

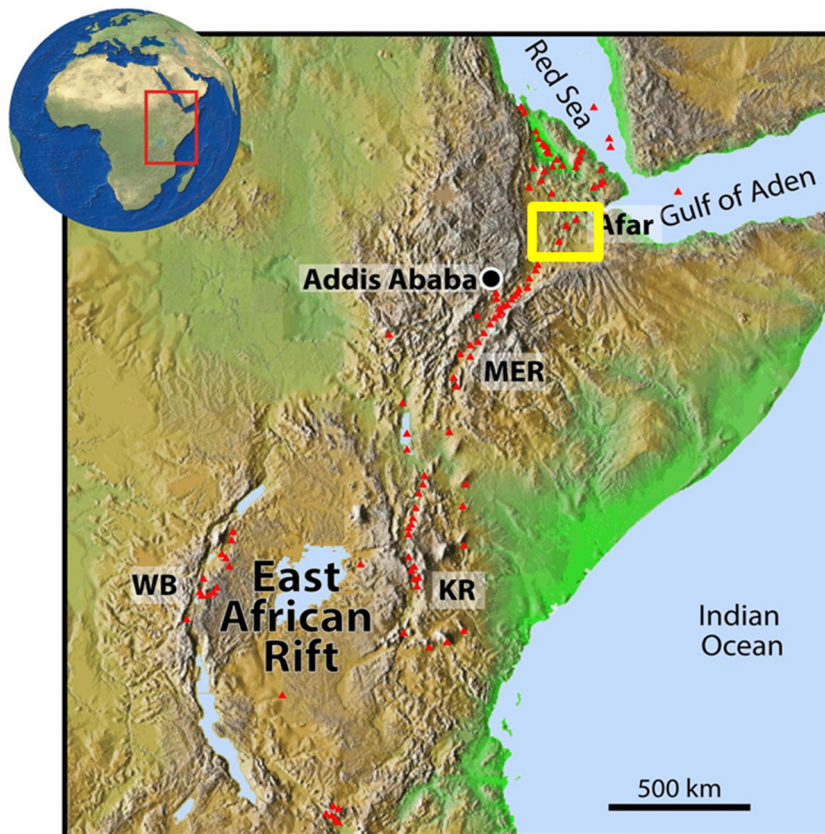


FIGURE 1: Map showing the East African Rift. Main Ethiopian Rift (MER), Kenya Rift (KR) and, Western Branch (WB); the yellow rectangle shows the Tendaho geothermal field

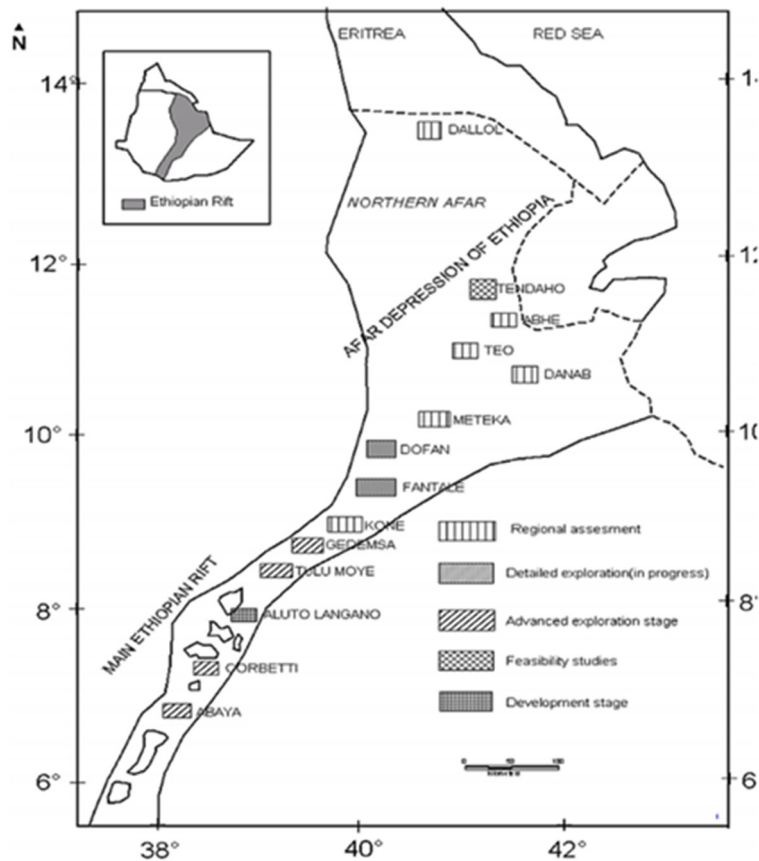


FIGURE 2: Location map of the Ethiopian Rift and geothermal prospect areas (Kebede, 2013)

Geothermal exploration in Tendaho had been intermittently going on from 1969 up to date. From 2014 to 2015 a detailed geo-scientific exploration was conducted in Alalobeda geothermal prospect by Geological Survey of Ethiopia (GSE) and an Italian consulting company (ELC - Electroconsult) financed by Icelandic International Development Agency (ICEIDA) and Nordic Development Fund (NDF) (ELC 2015a, 2015b, 2015c). A resistivity survey consisting of MT and TEM soundings was a part of the project. A total of 132 co-located MT/TEM sounding data were collected and from the 132 stations 27 MT stations were collected in 2013 by GSE. The TEM data are used for static shift correction of the MT data.

Three-dimensional (3D) inversion of MT data has become a common practice in geothermal exploration. 3D inversion of MT data can give much more reliable and detailed results than inversion in terms of 1D inversion (Árnason et al., 2010; Lichoro, 2013). The 3D inversions are computing intensive. Advances in computer technologies and software development have made 3D inversion of MT data practical.

In this project, 3D inversion of the static shift corrected MT data are discussed. In order to study the robustness of the results, the 3-D inversion was done using two different initial models and the results were compared with the results of the joint 1D inversion of the MT and TEM data. Initially, the plan was to use three or more initial models, but unfortunately the inversion did not converge. Therefore, we were forced to present what we have. A total of 108 MT/TEM soundings from Alalobeda prospect in Tendaho were 1D jointly inverted and 107 static shift corrected MT soundings 3D inverted. One of the MT stations (A011) was removed from the 3D inversion because the data fit was not good enough.

Here, the objective is to get a detailed subsurface resistivity model and image the deep resistivity structure, delineate and characterize a possible geothermal reservoir of the Alalobeda geothermal prospect and at the same time to compare the resistivity models derived from 1D and 3D inversion. Finally, to suggest the drilling are

## 2. TENDAHO GEOTHERMAL FIELD

### 2.1 Introduction

The rift zone of Ethiopia has already been intensively studied by UNDP, GSE, CNR-CNRS and others (Aquater, 1979). A reconnaissance survey by these organizations led to the identification of several geothermal prospects along the rift see Figure 2. Tendaho was one of the prospects selected for future studies, as one of the most promising geothermal area of the country because of its size and location. The geophysical work discussed here (MT and TEM) is a part of a cooperative study of the Alalobeda geothermal prospect involving GSE, ICEIDA and NDF through the consulting company ELC. Other studies included surface geology, geochemistry, passive seismic monitoring, and gravity.

### 2.2 Location of the study area

The Tendaho prospect is located in the central Afar depression about 600 km from the capital city Addis Ababa in northeast of Ethiopia. Alalobeda geothermal prospect is one of the three geothermal areas in Tendaho graben, the other two are Dubti and Ayrobera (Figure 3). In Dubti a detailed geoscientific research has been done and wells have been drilled. Alalobeda prospect is located on the western margin of Tendaho graben; 15 km southwest of Dubti plantation, south-southeast of Logiya town. It is characterized by a flat plain and a stratified mountainous range. The elevation of the area varies from 300 to 800 m.

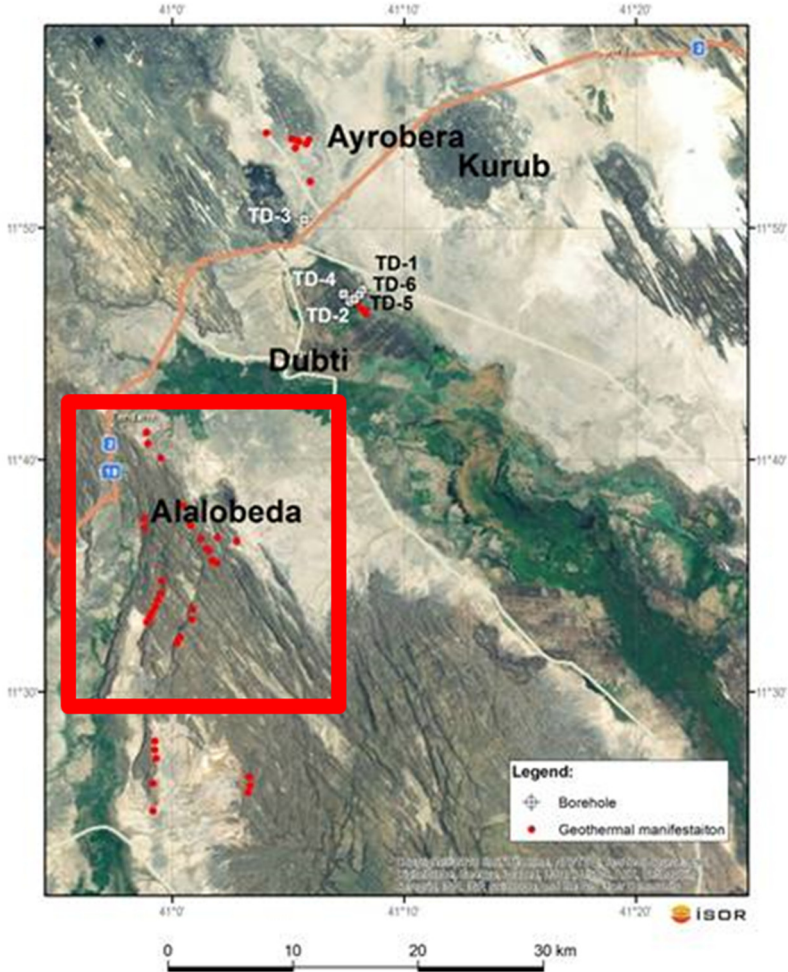


FIGURE 3: An aerial photograph of Tendaho and the three geothermal fields – geothermal surface manifestations are denoted by red dots and boreholes by white squares. The red rectangle shows study area

The region is settled by Afar people. Most of the Afar people are pastoralists who graze camels, cattle's, goats, sheep and donkeys as well. Crop cultivation is not common like the rest of the country's rural areas. Owing to the fertile alluvial soil and water supply of Awash River, the most important economic activity for the past 4 to 5 decades has been cultivation of cotton at Dubti, Det Bahri, Tangaye Koma and Asayita plantation (Bekele, 2012). Currently, the main agricultural product of the area is sugar cane and maize cultivation along the Awash River, utilizing the Awash Dam which is directed through canals to Dubti, Det Bahri, Tangaye Koma and Asayita.

Dubti, the wereda seat of the government and Det Bahri started as satellite towns for the farms that bear their names. Semera town has become the capital city of the Afar region in 2004 and is growing fast. An asphalt road from Addis Ababa branches at Semera to continue to Djibouti and Assab. The road that branches off from the main road a few kilometres before reaching Logiya town passes over the bridge of the dam, which is formed by the Awash River dam lake (Tendaho lake). It gives access to the Alalobeda prospect.

Currently, the only sea-route out of Ethiopia is through Djibouti. A temporary storage facility area has been built in Semera to minimize the cost for port services. The traffic on the highway and the services needed in association with this have benefited to the growth of Logiya town. Semera, which started out as a road maintenance camp, has also served as the campsite for the geothermal exploration project since the 1990s.

The energy consumed by the rural population is mainly obtained from biomass fuel: wood from acacia trees, camel and goat droppings. However, all four towns have electricity supply, used primarily for household lighting and in the commercial sector. Dubti and Logiya are now connected to the EEPCo diesel generator in Semera. Dubti farm generates its own electricity for use at its ginnery and workshop and for air conditioning and lighting. Diesel fuel is used to generate power for irrigation and drainage pumping.

In general, in the Afar region, the climate is of arid type and it is one of the hottest places in the country. The mean day time minimum and maximum temperature are 36-45°C at the Alalobeda prospect, respectively. The rainy season of the area is July-September.

### **2.3 Geological and tectonic setting of Tendaho**

The Afar depression is located at a triple junction characterised by thinned continental crust, where three important tectonic structures converge; the Red Sea (NW-SE), the Gulf of Aden (ENE-WSW) and the Main Ethiopian Rift (NNE-SSW) see Figure 1, deforming a broad area and developing Danakil microplates (Stein et al., 1991; Eagles et al., 2002; Redfield et al., 2003). The mean spreading rates of the Aden propagator is ~1.1 cm/yr (Cattin et al., 2005), the northern portion of the Red Sea propagator ~2 cm/yr (Jestin et al., 1994) significantly higher than the MER which is ~2.5 mm/yr (Wolfenden et al., 2004).

The Afar region corresponds to an area of active extensional tectonics and of volcanism, related to the presence of a broad mantle plume, from where the Red Sea and the Ethiopian Rift system radiate. The tectonic style of the region is characterized by the presence of normal faults and open fissures, often associated with strike-slip faults, striking parallel to or at a small angle with the rifting axes. Normal faulting is responsible for the formation of the Tendaho graben, a 50 km wide structure trending NW-SE and joining the Ethiopian Rift close to Dama Ale volcano around 70 km northeast of Alalobeda prospect.

The new Oceanic crust along the axes with NNW-SSE and WNW-ESE direction is the result of the separation between the Arabian, Nubian and Somalian plates (Aquater, 1979). The rifting in Afar began an early Miocene age (25 m.y.) on continental arch, where important basaltic activities were in progress since Pleistocene (see more details in Aquater, 1979). Therefore, the Afar rift is believed to be reached at its present geological setting during the Pleistocene period, with the emergence of the axial zones of

crustal separation (Aquater, 1979; Aquater, 1996). The Afar depression is one of the two places on Earth where a spreading oceanic ridge can be studied on land, the other being Iceland (Abbate et al., 1995). The beginning of the rift formation was by a change in the magmatic products: transitional basalts and peralkaline granites or rhyolites in place of a more alkali. Results of K-Ar age and radiometric data showed that the initiation of Afar rift started in early Miocene age (25 m.y.). For further details see Section 2.6.1.

## **2.4 Structures controlling the geothermal system in Tendaho**

The main faults and fractures in Tendaho graben form a prominent NW-SE trending rift zone, where the circulation of thermal water is probably taking place. Satellite imagery and field observations show that the main lineament is NW-SE, indicating the prevalence of the trend of the Red Sea (Aquater, 1979; Aquater, 1980; and UNDP, 1973). At the western margin of the Tendaho graben where the Alalobeda prospect is located, NW-SE and NE-SW trending lineaments crisscrossed each other forming grid faults. Within the graben E-W and N-S trending structures are observed, though they are not prominent (Mamo and Bekele, 2014). In the vicinity of the geothermal areas, the most identifiable point of intersection is near Alalobeda prospect, where NNE-SSW trending faults of the MER terminate and deflect into the main NW-SE trend that bounds the graben at its southwest edge (Stimac et al., 2014).

Therefore, those structures probably represent the important conduits for the circulation of the thermal water. From geological and geophysical studies, we may conclude that, Tendaho geothermal field is a fault controlled geothermal system.

## **2.5 Geothermal manifestation**

In general, where the region is fractured by faults, the geothermal fluid may rise directly to the surface producing various hydrothermal surface manifestations that are in the form of hot springs, fumaroles, altered ground, mud pools and steaming ground. The presence of such manifestations is an indication of the possible existence of a geothermal field. However, such indications are not absolutely essential; because geothermal fields may exist without surface manifestations. There are hot springs that are unrelated to high-enthalpy fluids such as those related to water that rapidly rises along deep faults in areas with a normal geothermal gradient. Study of hydrothermal surface manifestations must be made within the general hydrogeological framework. On one hand it requires a knowledge of the hydrology of the area (rain fall pattern, underground circulation) of the main structures controlling the hydrothermal systems and the structural characteristics of each spring. On the other hand, it requires detailed geochemical exploration, providing data for the hydro-geological model and detecting leakage manifestations from the geothermal reservoir.

The geothermal prospects in Ethiopia are within the MER which is a part of the great EARS. The main hydrothermal surface manifestations are also found along the MER system. In some of the prospect areas the measured temperature of the hot springs reaches 100°C.

Hydrothermal manifestations are either active or fossil. The hydrothermal manifestations in Tendaho are concentrated along the main faults bordering the Tendaho graben particularly in the western part and along the active tectonic directions at the graben centre see Figure 3. The impressive fumarole manifestations in Alalobeda are present on the acid rocks of Magenti Ale near the Dit Bahari plantation. They are aligned along the eastern bordering fault of the Saha spring. Some fossil fumarole deposits occur at the southern base of Kurub volcano. The Ayrodera fumaroles are aligned on the extension of the fault wall bordering the Ayrobera horst to the west, which is south of Gabelayitu to Assaita. Numerous manifestations are found in Dubti prospect. All these hydrothermal manifestations are aligned in the NNW-SSE direction and probably connected to active faults of the Manda Hararo (UNDP, 1973; Aquater, 1979).

## 2.6 Review of previous geo-scientific studies

### 2.6.1 Previous geological studies

Here, some of the previous geological studies in Afar depression are described. The northern part of the Tendaho rift is tectonically characterized by open fissures and active faults which define a pattern of a NW-SE elongated block with typical wavelength of some hundreds of meters. The northeast-trending Tendaho graben where the Alalobeda manifestations are located has a width of about 50 km and joins the Ethiopian Rift close to Dama Ale volcano west of Lake Abe. From a stratigraphic point of view the youngest rocks of the regions are Quaternary axial fissural basalts and subordinate rhyolites and associated products and central volcanoes.

A geological survey was conducted in Alalobeda prospect in 2015 through a collaboration between GSE and ELC. It led to a conclusion that Alalobeda has two group of rocks (see Figure 4 and Figure 9):

- (1) A ridge of Plio-Pleistocene age forming volcanic rocks and their minor intercalated sediments;
- (2) (2) a rift floor dated from Pleistocene to present filling continental sediments intercalated with some lava flows (for more details see ELC's geological report (2015a)).



FIGURE 4: Picture showing the ridge of the Alalobeda prospect

As mentioned earlier Alalobeda prospect is located in the central Afar depression, along the western margin of the Tendaho graben. Figure 5 shows the volcanic products recognized in the study area which can broadly be subdivided into three distinct groups:

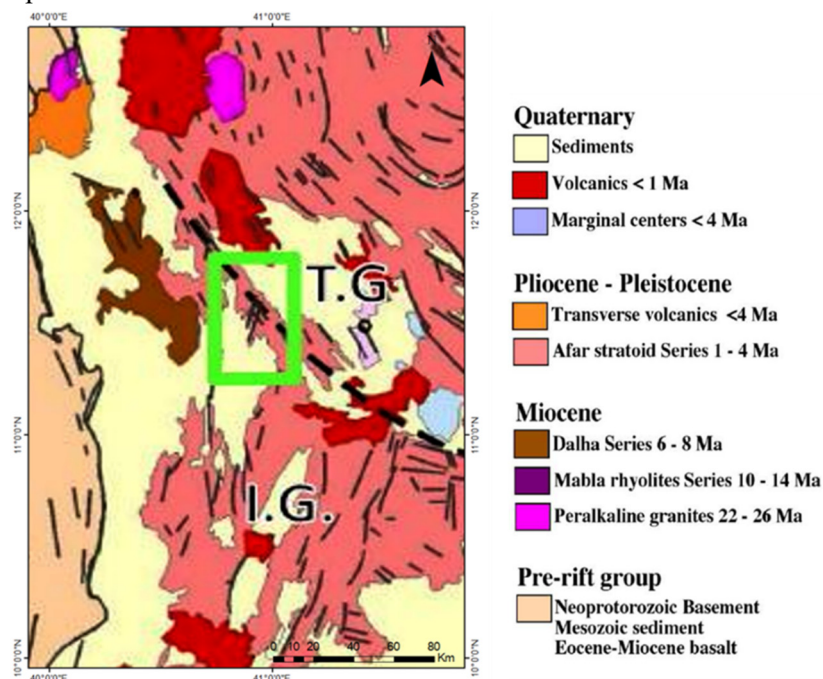


FIGURE 5: Simplified geological map of the Afar triple junction, modified from Beyene and Abdesalam (2005) – green rectangle shows the location of the study area; T.G.=Tendaho Graben; A.G.=Goba Graben; I.G.=Issa Graben (ELC, 2015a)

- *Upper extrusive complex (< 1 Ma)*: basalts of fissural or central origin and of subordinate rhyolites;
- *Middle extrusive complex (1-4 Ma), referred to as Afar Stratoid series (ASS)*, consisting of a sequence of basaltic flows of fissural origin with associated rhyolitic centres and sedimentary/pyroclastic intercalations; and
- *Lower Extrusive Complex (4-15 Ma), including the Dalha basalts and the Mabila rhyolites*. The borders of the graben are underlain byproducts of the Stratoid basalt Series, whereas the graben itself is filled up by clastic sediments locally intercalated with basalts of the Middle Extrusive complex (~ 1,400 m thick).

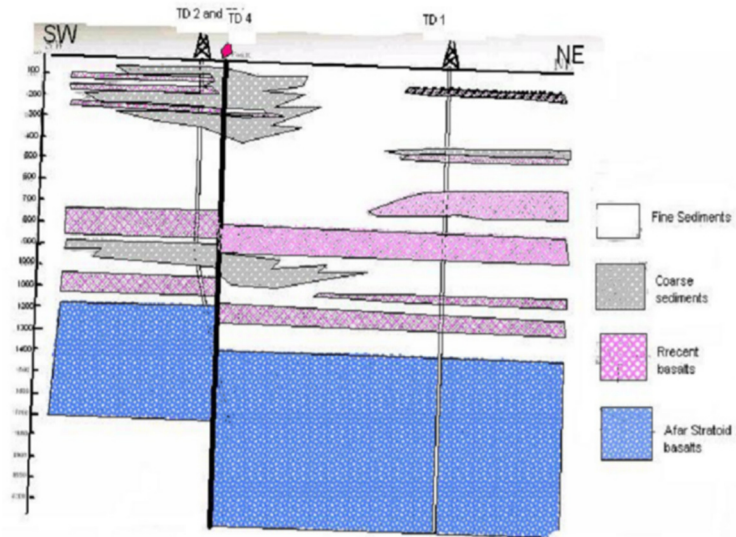


FIGURE 6: Geological stratigraphy of well TD2, TD4 and TD1 (Battistelli et al., 2002), in Dubti, for location see Figure 3

Figure 6 shows the geological stratigraphy of wells in the Dubti geothermal prospect. It shows that the depth to the Afar Stratoid Basalt Series varies from 1200 m to 1400 m from the surface. These results will be compared with resistivity cross-sections from Alalobeda prospect in Sections 8.4.1 and 9.2.3.

## 2.6.2 Previous geophysical studies

In Tendaho, the first reconnaissance survey was done by UNDP and EIGS in 1973 (Megersa and Getaneh, 2006), to investigate deep structures and to delineate possible geothermal reservoirs. Regional and semi-detailed geophysical studies include: vertical electrical sounding (VES), magnetics and gravity from the Afar depression.

In 1972 seismic measurement was done in the Afar lowland and Ethiopian highlands. The interpretation shows a crustal thinning and upwelling of the hot upper-mantel material underneath Afar (Berckhemer and Baier, 1975).

An MT survey was carried out in Afar in 1971, to investigate the electrical resistivity distribution (Berkthold, 1975), which identified a layer with resistivity varying from 200-500  $\Omega\text{m}$  in the uppermost km. A gravity survey was performed by Aquater (1980) which revealed a -57 mGal gravity anomaly in Dubti plantation which was attributed to thick sediments. A gravity survey carried out by ELC (2015c) in Alalobeda inferred different lineaments, geological structures and strike slip faults beneath the thick sediments.

Figure 7 shows a Bouguer gravity map of Alalobeda prospect. (ELC, 2015c). It indicates positive anomaly on the graben shoulder with maximum value of +4.3 mGal which correlates with the dense volcanic basalt and negative anomaly in the plain area with a minimum value of -5.1 mGal correlating with the sediments which have lower density than the basalts (ELC, 2015c).

Figure 8 shows the horst-graben structures (white lines) hidden by the sediments imaged by the elevation of the ASS bedrock resulting from the 3D inversion of gravity data. It shows the resultant fault system (white lines) traced along the maxima of the bedrocks horizontal gradient. The main fault system that originates in the main graben depression is marked by MF1 (heavy grey line). The dash black lines indicate the steep drop off of the bedrock topography that divides the main depression into two sub-regions D1 and D2, separated by the second main fault system MF2 (dashed grey line) (ELC, 2015c).

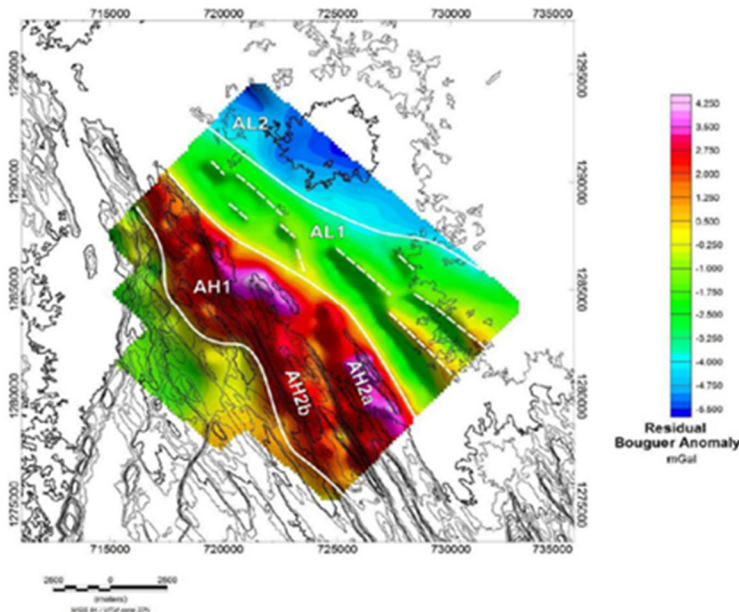


FIGURE 7: Residual Bouguer gravity map. AH: positive anomaly divided into three subsectors AH1, AH2a and AH2b. AL: negative anomaly over the plain, divided into two sub-sectors AL1 and AL2; taken from ELC, 2015c

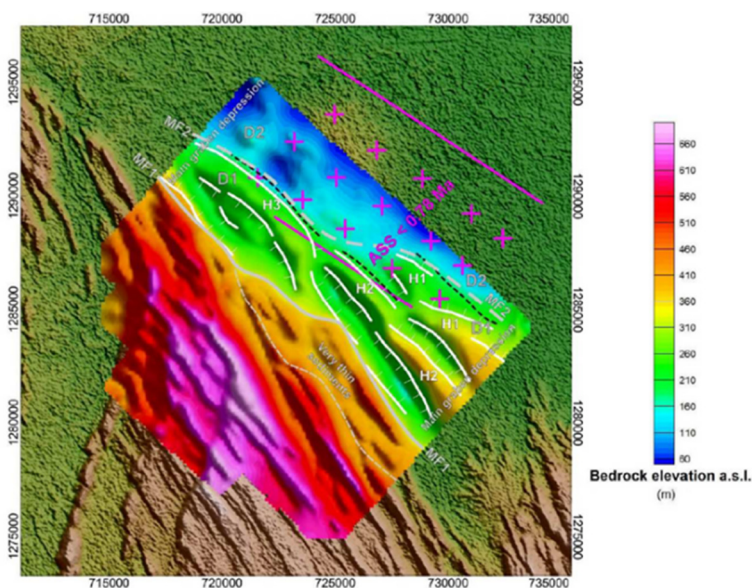


FIGURE 8: Horst graben structure - the dashed black lines indicate the steep drop off of the bedrock topography that sub-divides the bedrock topography into two sub regions D1 and D2; taken from ELC, 2015c

### 2.6.3 Previous geochemical studies

Here, some of the previous geochemical studies in Afar depression are described. In the Northern Afar region water samples were collected for chemical and isotopic analyses (Gonfiantini et al., 1973). Later, gas samples were collected in fumaroles along the MER (Craig, 1977). The results of the exploration activities confirmed the existence of circulating high-temperature geothermal fluid at great depth that could be used for power generation.

In 2012, Teclu and Mekonen (2013) carried out a radon gas survey in the Ayrobera prospect and identified NNE-SSW and NNW-SSW trending anomalous structures. These structures also cross each other.

The D2 region corresponds approximately with the negative magnetic anomaly that has been interpreted as a region of dominantly normal-polarity intrusions and dikes originated in the past ~0.8 Ma of extension (Armadillo et al., 2014). The positive magnetic anomaly in D1 region indicates reversed magnetic polarity due to ASS basalts formed during the reverse Matuyama Chron (> 0.78 Ma). The inversion of magnetic data results indicate that the 0.78 Ma (Yellow line) isochrones correspond to the structural lineament (MF1, dashed black line) (Armadillo et al, 2014).

Figure 9 shows the structural map derived from the interpretation of the gravimetric data (ELC (2015c)). From the 3D inversion of gravity data, the main faults and lineaments were mapped. The resistivity results will be compared with the faults inferred by gravity in Section 9.2.3. In Figure 9 white contours indicate the top of the modelled enhanced high-density region in the Afar Stratoid basalt Series. The body is divided into two sectors B1 and B2a/B2b. Dashed yellow lines are inferred MER trending faults (MERF). MF0, MF1 and MF2: main fault system controlling the main depression of the graben composed by the D0, D1 and D2 sectors. H1-H3: mapped horsts (white lines) in the ASS bedrock. Magenta crosses and lines: region of dominantly normal-polarity intrusions and/or dikes originated in the past 0.78 Ma. Red dashed line: strike slip fault (ELC (2015c)).

Alalobeda's gases differ from those of Dubti because of their low H<sub>2</sub> and CO content (Aquater, 1996). The hot spring water from Alalobeda and Bagalodoma are sodium chloride type with high sulphate contents (Aquater, 1996). The Na, K, Mg diagram (Figure 10) shows that the Alalobeda water has a trend towards full equilibrium (Aquater, 1996).

A radon survey which was done by Teclu and Mekonen (2013) revealed the distribution of buried faults, joints and fractures. The investigation confirmed that the anomalous values are concentrated in the NNE-SSE and N-S direction of the Alalobeda prospect. A geochemical report done by Aquater (1996) using Fournier's quartz geothermometer concluded 229°C. A recent geochemical report done by ELC (2015b) concluded that from the Na-K and K-Mg geothermometers of Giggenbach (1988) based on the samples from Alalobeda thermal spring indicate a reservoir temperature of 220°C. The Na-K and silica (quartz) geothermometers by Giggenbach et al. (1994) and Fournier (1973) indicate deep geothermal reservoir temperature close to 200°C. From the ternary diagram the Alalobeda water is chloride rich.

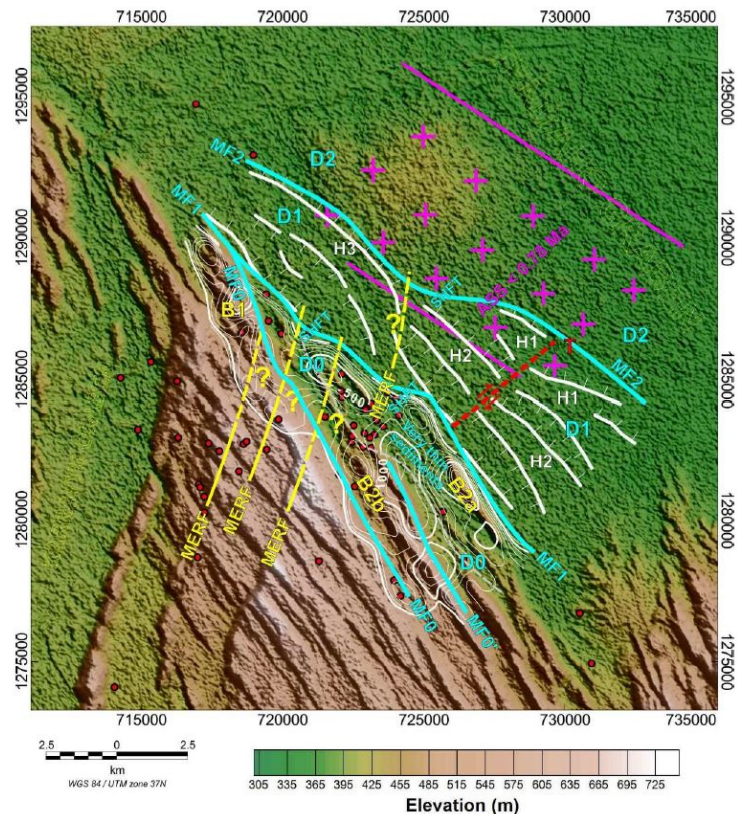


FIGURE 9: Structural map derived from the gravimetric interpretation superimposed on the topographic DEM; red circles: epicentres of recent seismic activity from Belachew et al. (2013); taken from ELC, 2015c

Figure 11 shows that the samples from thermal manifestations of Alalobeda, are chloride rich waters with significant relative concentrations of sulphate (20-23 eq%) and low relative concentration of HCO<sub>3</sub>+CO<sub>3</sub>. The reservoir liquids of the geothermal wells in Dubti TD-1, TD-2, TD-4, TD-5 and TD-6 are mature, chloride rich waters, as expected. Sample ALB-W-10, coming from the fumarolic area situated to the NW of the thermal manifestations of Alalobeda, is bicarbonate-rich water. Sample from the Awash River Dam Lake ALB-W-17, is bicarbonate-(sulphate) water.

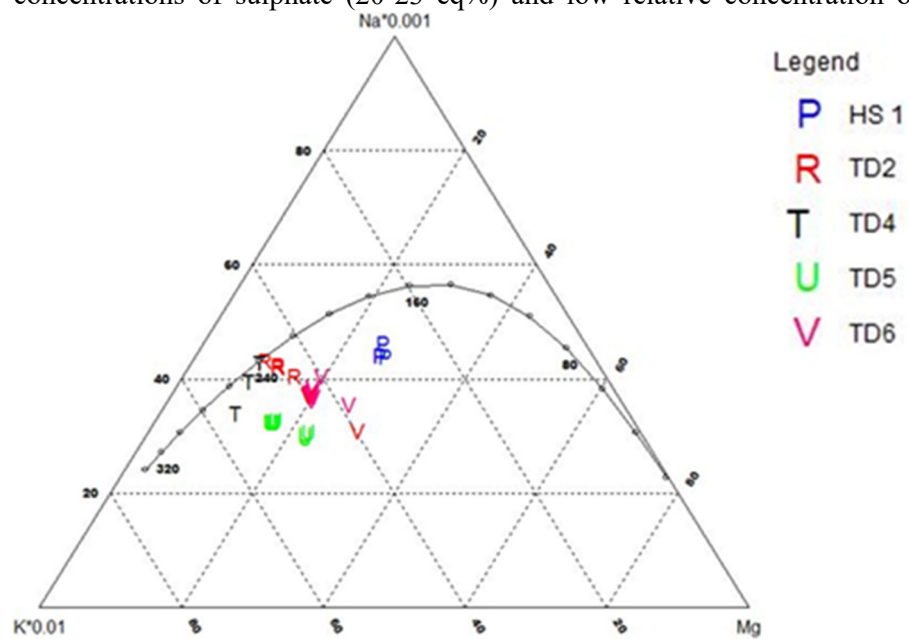


FIGURE 10: Giggenbach diagram (TD2, TD4, TD5 and TD6 are geothermal wells in Dubti and HS1 from Alalobeda)

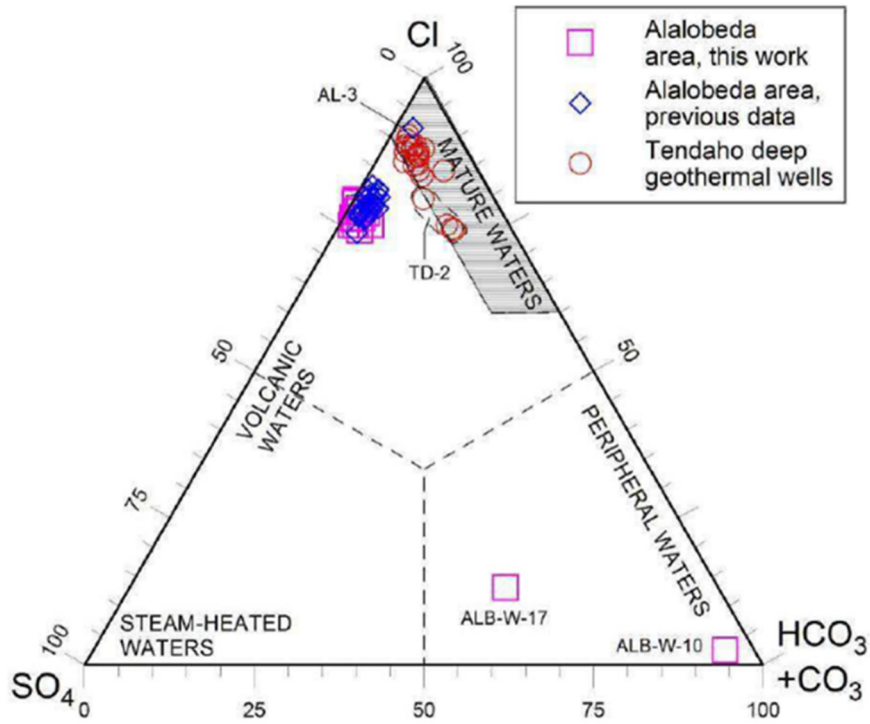


FIGURE 11: Triangular diagram with the main anions (modified from Giggenbach, 1988) for the water samples collected in the Alalobeda in 2015 and also from previous studies and the water samples from Tendaho deep geothermal wells (ELC, 2015b)

### 3. APPLICATION OF RESISTIVITY METHODS IN GEOTHERMAL EXPLORATION

Electrical resistivity methods are the most crucial geophysical methods used in the exploration of geothermal resources. This is because resistivity is highly sensitive to temperature, hydrothermal alteration of rocks, salinity, permeability and porosity. All are directly related to the physical properties of the geothermal reservoir (Hersir and Björnsson, 1991). Resistivity methods are based on injecting a current into the Earth and measuring the signal generated by the current at the surface. Different resistivity methods have been used in geothermal resource exploration during the past decades. The resistivity methods used in geothermal exploration are direct current (DC) and EM methods. In present time EM methods are widely used because they are more sensitive to low resistivity structures than DC methods.

#### 3.1 Various resistivity measurement methods

Resistivity measurements are not only used in geothermal exploration, but also in mineral industry, as well as in groundwater, oil and gas exploration. Resistivity methods are divided into two main methods. DC methods are used to infer the subsurface resistivity based on injecting a constant current into the Earth through a pair of electrodes and monitoring the potential signal it creates. There are several DC methods that has been used in the past for geothermal exploration. Some of the DC resistivity are Schlumberger soundings, Head-on profiling, Dipole-dipole soundings and profiling (see more details in Hersir and Björnsson, 1991 and Flóvenz et al., 2012).

EM methods: in this method a current varying with time in an active/controlled or passive/natural way is used instead of DC currents. MT and audio-magnetotellurics (AMT) are passive methods. The fluctuations in the natural magnetic field of the Earth and the corresponding induced electric field are measured. AMT is used to measure in the high frequency range 10-1000 Hz to investigate shallow depths. On the other hand, TEM is an active method; a magnetic field is built up by transmitting a current into a loop and monitor the transient decay of the magnetic field as the current is turned off, see further details on the MT and TEM methods in Sections 1 and 7.

#### 3.2 Resistivity of rocks

Resistivity of a material is defined as the product of the electrical resistance in Ohm ( $\Omega$ ) between opposite faces of a cube of length  $L$  (m) and its cross-sectional area  $A$  ( $m^2$ ) divided by  $L$  (Kearey and Brooks, 1994). It is given by:

$$\rho = \frac{RA}{L} \quad (3.1)$$

where,  $\rho$  is resistivity of the material ( $\Omega m$ );  $R$  resistance ( $\Omega$ );  $L$  length (m) and  $A$  cross-sectional area. The specific resistivity  $\rho$  depends on the material and is defined through Ohm's law.

The electrical field strength,  $E$  (V/m) at a point in a material is proportional to the current density  $j$  ( $A/m^2$ ):

$$E = \rho j \quad (3.2)$$

Factors affecting the resistivity of the geothermal reservoir and the surrounding area are discussed briefly in the next subsections. The most common factors that affect the resistivity of rocks include: Porosity (pore structure) of the rocks, salinity, temperature, fluid saturation, conductivity of the rock matrix and hydrothermal alteration.

##### 3.2.1 Porosity and pore structure of the rocks

Porosity is defined as the ratio between the pore volume and the total volume of the material:

$$\phi_t = \frac{V_V}{V_T} \quad (3.3)$$

where,  $\phi_t$  is porosity;  $V_V$  is volume of void space (openings) and  $V_T$  is the total or bulk volume of the material (rock or soil).

There are three main types of porosity (Hersir and Björnsson, 1991): Intergranular, the pores are the space between grains or particles in a compact material like sediments and volcanic ash; joints-fissures or fractures is a net of fine fissures caused by tension and cooling of the rock which is common in igneous rocks and lava; and vugular, as the material is dissolved, big and irregular pores are formed and the material is washed away, or formed by gas in volcanic rocks and limestone.

Rocks can conduct electricity when the pore space is interconnected and filled with water. There are large voids, called storage pores, and finer connected pores in all types of porosity. Most of the electrical current flow is within the connecting pores (Hersir and Árnason, 2009). In many cases, studies show that the resistivity of water-saturated rocks varies approximately with the inverse square of the porosity. The empirical law that describes how-resistivity depends on porosity if ionic conduction in the fluid dominates other conduction mechanisms in the rock is called Archie's law (Archie, 1942).

$$\rho = \rho_w a \phi_t^{-n} \quad (3.4)$$

where,  $\rho$  is the bulk (measured) resistivity ( $\Omega\text{m}$ );  $\rho_w$  is resistivity of the pore fluid ( $\Omega\text{m}$ );  $a$  is an empirical parameter, which varies from  $< 1$  for intergranular porosity to  $> 1$  for joint porosity, usually around 1 and  $n$  is cementing factor, an empirical parameter, which varies from 1.2 for unconsolidated sediments to 3.5 for crystalline rocks, usually around 2.

Equation 3.4 is valid if the resistivity of the pore fluid is of the order of 2  $\Omega\text{m}$  or less, but it becomes less reliable if the resistivity is much higher (Flóvenz et al., 1985). However, if the conductivity is dominated by the saturating fluid, Archie's law seems to be a fair approximation.

### 3.2.2 Salinity of fluids

Salinity is a measure of the total amount of salts in water or soil. Groundwater may contain a variety of salts in the solution. Therefore, equivalent salinity is defined as the salinity of NaCl-solution with the same resistivity as the particular solution. Mobility of the ions does not vary widely, and equivalent salinity is, therefore, close to true salinity.

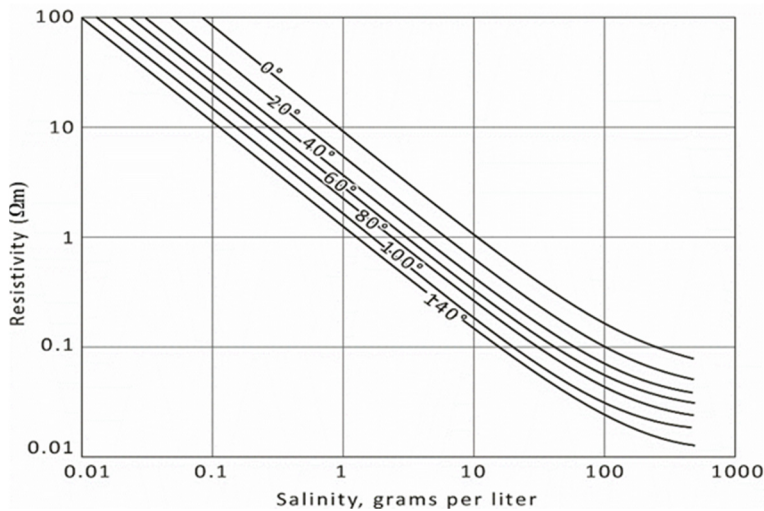


FIGURE 12: Electrical resistivity of a NaCl solution as a function of concentration and temperature (Flóvenz et al., 2012; based on Keller and Frischknecht, 1966)

expressed by the following Equation Hersir and Björnsson, 1991):

$$\sigma = F(c_1 q_1 m_1 + c_2 q_2 m_2 + \dots) \quad (3.5)$$

where,  $\sigma$  is conductivity (S/m);  $F$  Faraday's number ( $9.65 \cdot 10^4$  C/mole);  $c_i$  concentration of ions;  $q_i$  valance of ions and  $m_i$  mobility of different ions.

### 3.2.3 Temperature

At temperatures 0-200°C, resistivity of aqueous solutions decreases with increasing temperature as shown on Figure 13. This is due to increasing mobility of ions at increasing temperature caused by a decrease in the viscosity of the water. This relationship is described by Dakhnov (1962):

$$\rho_w = \frac{\rho_{wo}}{1 + \alpha(T - T_o)} \quad (3.6)$$

where,  $\rho_{wo}$  is resistivity of the fluid at temperature  $T_o$  ( $\Omega\text{m}$ ), and  $\alpha$  is a temperature coefficient of resistivity ( $^{\circ}\text{C}^{-1}$ ) ( $\approx 0.0023^{\circ}\text{C}^{-1}$  for  $T_o=25^{\circ}\text{C}$ ).

At high temperatures, a decrease in the dielectric permittivity of the water results in a decrease in numbers of dissociated ions in the solution. The resistivity of the fluids starts to increase when the temperature is above 300°C (Quist and Marshall, 1968).

### 3.2.4 Fluid saturation

In geothermal areas the rocks below groundwater table are water or steam saturated. Water saturation causes a significant decrease in resistivity. That is why resistivity methods are frequently used to find the depth to the groundwater table. The rocks above the groundwater table are partially saturated and the resistivity depends on the degree of saturation (rocks are mostly resistive themselves). Water rock interaction and alteration mineralogy is discussed below.

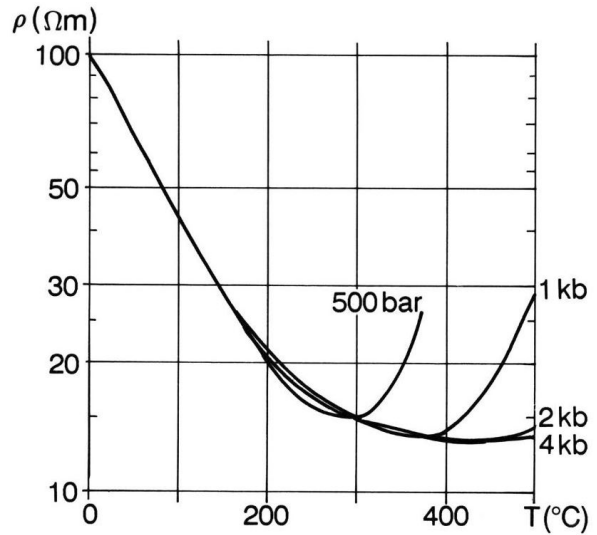


FIGURE 13: Electrical resistivity of a NaCl solution as a function of temperature for different pressures (Hersir and Björnsson, 1991; based on Quist and Marshall, 1968)

### 3.3 Resistivity structure of high-temperature geothermal systems

High-temperature geothermal systems are found in regions, where there is elevated heat flow and structural settings that support vigorous fluid circulation through fractures. These regions are generally located along the main tectonic regimes and over mantle hot spots (Stimac, 2015).

Water-rock interaction is the interaction of water with rocks and causes changes in the chemistry of both the water and the rock. Alteration minerals are formed where the hydrothermal water reacts with the host rock. Formation of alteration minerals depends on the type of primary minerals, the chemical composition of the geothermal fluid and temperature. Moreover, the intensity of the alteration is further dependent on the contact time and texture of the host rock (Hersir and Björnsson, 1991; Árnason et al., 2000). Porosity and permeability also control the intensity of the alteration.

The relationship between subsurface resistivity, hydrothermal alteration, temperature and conduction mechanism is summarized in Figure 14. Generally, below temperature of 50°C the alteration intensity is low, resistivity relatively high and the main conduction mechanism is pore fluid conduction. Low-temperature alteration minerals, zeolites and clay minerals like smectite are formed at temperature above around 50-100°C and we have surface conduction mechanism. Smectite has hydrated and loosely bound cations and high cation exchange capacity (CEC) which makes the minerals conductive (Lévy et al., 2018). At temperature between 200°C and 250°C there is a transition called mixed layer clay zone, where smectite and chlorite coexist in a mixture (Hersir and Björnsson, 1991; Árnason et al., 2000; Flóvenz et al., 2012) whereas, the change in illite seems to occur at somewhat lower temperature or 180°C. At a temperature of about 250°C chlorite becomes the dominant alteration mineral. Hence resistivity increases again, since chlorite has low cation exchange capacity which makes them resistive.

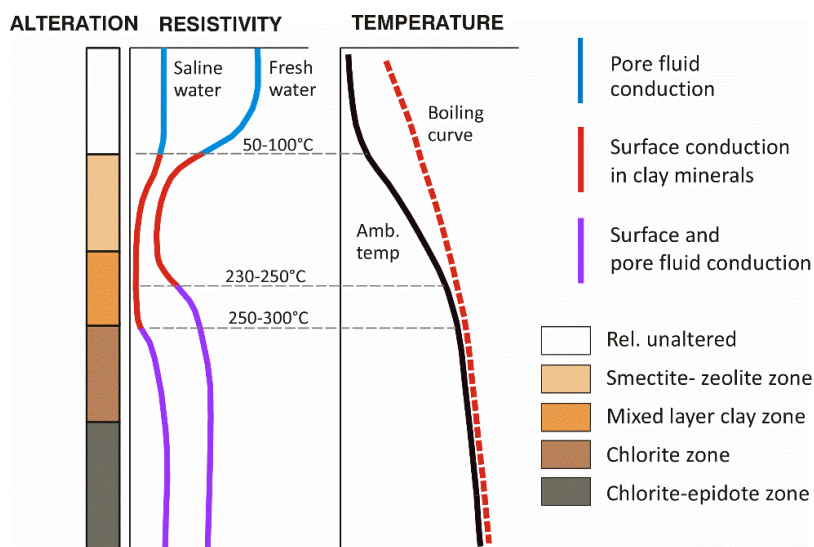


FIGURE 14: The general resistivity structure of a high-temperature geothermal system in basaltic environment showing conduction mechanism and surface resistivity variations as a function of alteration and temperature (Flóvenz et al., 2012).

As the temperature increases to 250-270°C, epidote becomes abundant. There, resistivity starts to increase again, because epidote has low cation exchange capacity (Árnason et al., 2000; Lévy et al., 2018). Here, surface and pore fluid conduction are dominant.

The resistivity structure of high-temperature geothermal fields in volcanic environment has been studied by several authors (Árnason et al., 1987; Árnason et al., 2000; Ussher et al., 2000; Flóvenz et al., 2012; Lévy et al., 2018). Generally speaking, a typical resistivity structure shows, high resistivity in the uppermost part of the subsurface indicating cold or unaltered

rocks (Figure 15). Below the high resistivity, a conductive cap is found consisting of conductive alteration minerals like smectite. Below the conductive cap the resistivity increases as a core of high resistivity appears. The transition from the conductive cap to the resistive core coincides with a change in mineral alteration from smectite to mixed-layered clay zone at a temperature of 230-250°C. As the temperature increases further to 250-270°C, more resistive alteration minerals like epidote become abundant and the resistivity starts to increase again.

To generalize what was discussed before a typical resistivity cross-section is shown in Figure 15 from Nesjavellir high-temperature geothermal system in SW Iceland. The rocks in the area are almost entirely composed of basalts in various forms as lavas, scoria layers, hyaloclastite or intrusions. No correlation

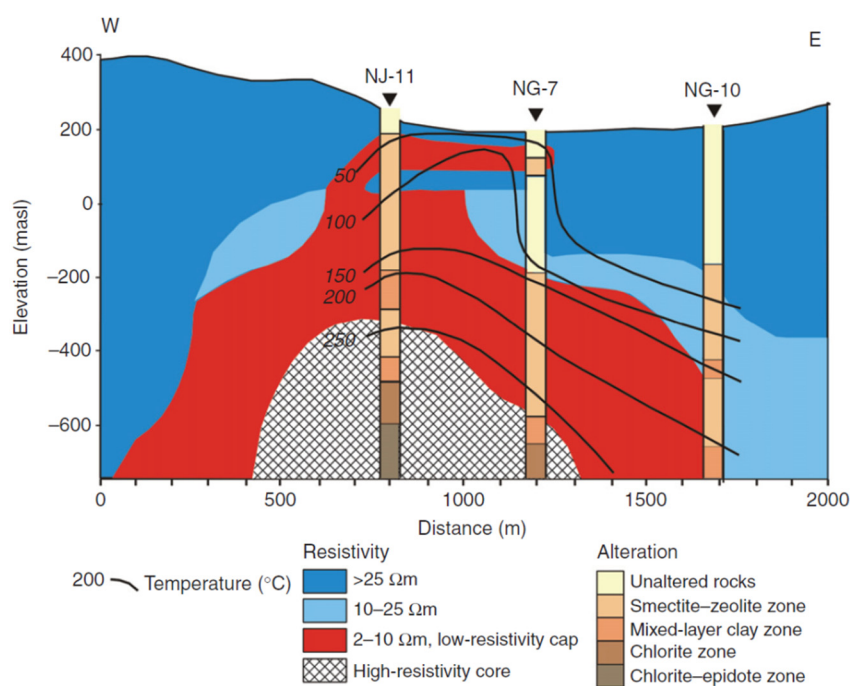


FIGURE 15: Typical resistivity structure of a high-temperature geothermal area (Nesjavellir geothermal field, SW-Iceland); it clearly shows the correlation between the subsurface resistivity structure, alteration mineralogy and the formation temperature (Árnason et al., 1987)

was found between resistivity and lithology in the boreholes in Nesjavellir. The cross-section shows a broad shallow lying high-resistivity anomaly caused by unaltered rock. Below, an up-doming conductive cap consisting of smectite and zeolite appears. Then a resistive core is seen as the temperature increases consisting of high-temperature alteration minerals.

Resistivity is directly related to the alteration minerals but not necessarily related to present rock temperature. If the alteration and the temperature are in equilibrium, the subsurface resistivity structure reflects not only the alteration, but it also shows the expected temperature. However, the geothermal system might not be active - could be fossil - resistivity reflects alteration that was formed in the past, but the temperature is not there anymore. On the other hand, when the geothermal system is young being heated up the alteration is lagging behind, still not in equilibrium with the temperature. The alteration minerals show lower temperature than measured in the wells. Therefore, care must be taken when interpreting resistivity structure and temperature.

## 4. MT METHOD

### 4.1 Overview of MT

MT is a passive EM method which is used to determine the electrical properties of the Earth's subsurface through measuring the fluctuation of the natural electric and magnetic fields in orthogonal directions on Earth's surface, in the frequency range of  $10^{-4}$  Hz to  $10^4$  Hz.

MT theory was first proposed in the fifties by Tikhonov (1950), Cagniard (1953) and Kato and Kikuchi (1950). Cagniard developed formulas that show the relationship between  $E_x$  and  $H_y$  on the surface of a layered medium. The fluctuations of the EM fields are mainly due to ionospheric currents, thunderstorms and also because of artificial sources for example, power lines.

The electric field  $E_x$  and  $E_y$  is measured using an electric cable through the potential difference between two pairs of electrodes whereas the magnetic field is measured using induction coils in orthogonal directions (i.e.  $H_x$ ,  $H_y$  and  $H_z$ ). From the measured orthogonal electric and magnetic fields variations of the so-called impedance are derived which contain information about the resistivity structure of the subsurface. The MT method is used for probing deep structures of the Earth from tens of meters to several tens of kilometres depending on the recording period and the resistivity structure under the site. There are two ranges of frequency in MT data acquisition: high frequency (short periods) which is used to detect shallow structures due to their short depth of penetration whereas low frequency (long periods) is used to detect deep structures of the Earth.

#### 4.1.1 Source of MT soundings

The Earth's EM field contains a wide frequency spectrum generated by two different sources. The source of the high frequency ( $> 1$  Hz) signal comes from thunderstorms mainly in the tropics (Figure 16). The signal caused by the thunderstorms is known as *sferics* and consists of a broad range of EM frequencies. These EM signals propagate around the world in the form of guided waves between the Earth and ionosphere (Volland, 1982). Whereas the source of low frequency ( $< 1$  Hz) comes mainly from the interaction between the solar wind and the Earth's magnetic field. Solar wind is a continual stream of plasma radiating mainly proton and electron from the sun. The largest geomagnetic field variations occur during magnetic storms, due to a sporadic increase at which plasma is ejected from the sun. Magnetic storms last for several days, and they become visible at high latitudes in the forms of Aurora Borealis and Aurora Australis, or northern and southern lights, respectively. The natural EM fluctuations have low magnitudes for frequencies between 0.5 and 5 Hz (Figure 16). This is called the dead band, because in this range the MT soundings usually have a reduced data quality.

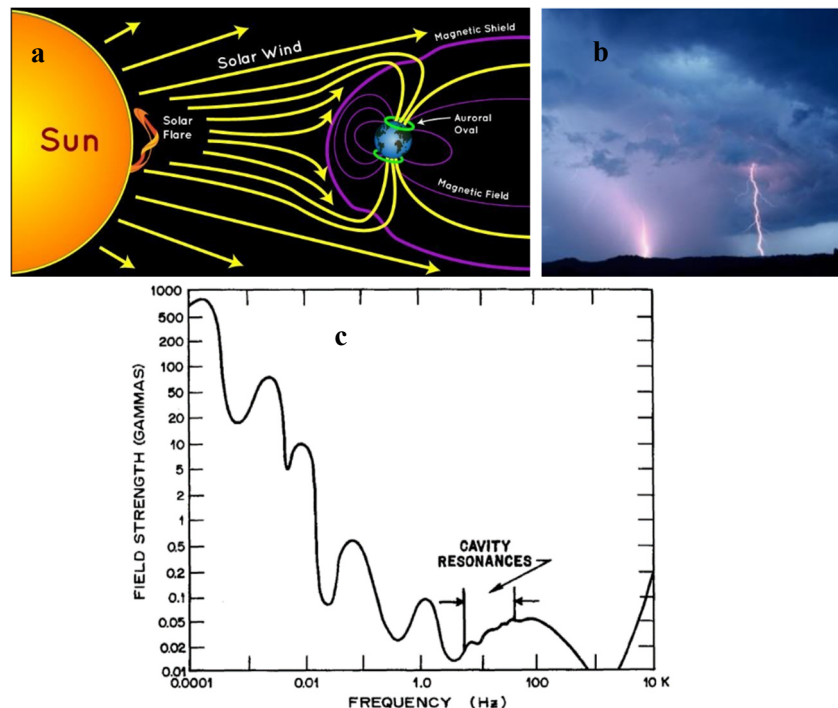


FIGURE 16: Sources of EM field; (a) Interaction of solar wind with magnetosphere; (b) lighting discharge; and (c) Earth's magnetic field spectrum.

### 4.1.2 The basic theory of EM and Maxwell's equations

Nowadays, EM methods are used extensively in surface exploration studies of geothermal areas, because resistivity, the physical parameters derived from those methods is the formation of the subsurface to be investigated. EM methods can either be passive or active depending on the source of the field. MT is a passive EM method which utilizes the natural geomagnetic signal. Whereas TEM is one of the active EM methods which is using an artificial signal source.

The EM fields at a given frequency can be described by Maxwell's equations in a conductive media:

$$\nabla \times \mathbf{E} = - \frac{\partial \mathbf{B}}{\partial t} \quad (4.1)$$

$$\nabla \times \mathbf{H} = \mathbf{j} + \frac{\partial \mathbf{D}}{\partial t} \quad (4.2)$$

$$\nabla \cdot \mathbf{B} = 0 \quad (4.3)$$

$$\nabla \cdot \mathbf{D} = \eta \quad (4.4)$$

where  $\mathbf{E}$  is the electric field (V/m),  $\mathbf{B}$  is magnetic induction (T),  $\mathbf{H}$  is the magnetic intensity (A/m),  $\mathbf{D}$  is the electric displacement current (C/m<sup>2</sup>),  $\mathbf{j}$  is the electric current density (A/m<sup>2</sup>),  $\eta$  is the electric charge density owing to free charges (C/m<sup>3</sup>), Curl ( $\nabla \times$ ) and div ( $\nabla \cdot$ ) are conventional vector calculus expressions.

Faraday's law described in Equation 4.1 states that time variations of the magnetic field induce corresponding fluctuations in the electric field flowing in a closed loop with its axis oriented in the direction of the induced field. Ampere's law Equation 4.2 states that any closed loop of electrical current will have an associated magnetic field proportional to the magnitude of the total current flow.

For linear and isotropic media, the vector fields in the Maxwell's equations (4.1 – 4.4) can be related through the constitutive relationships as follows:

$$\mathbf{j} = \sigma \mathbf{E} \quad (4.5)$$

$$\mathbf{B} = \mu \mathbf{H} \quad (4.6)$$

$$\mathbf{D} = \varepsilon \mathbf{E} \quad (4.7)$$

where  $\sigma$  is the electrical conductivity (S/m),  $\varepsilon = \varepsilon_r \varepsilon_0$  dielectric permittivity (F/m), and  $\mu = \mu_r \mu_0$  magnetic permeability (H/m).

### 4.1.3 EM wave in conductive media

For a homogeneous and isotropic conductive medium, substituting Equations 4.5-4.7 into Faraday's law and Ampere's law, Maxwell's equations (4.1 and 4.2)) can be rewritten as follows:

$$\nabla \times \mathbf{E} = -\mu \frac{\partial \mathbf{H}}{\partial t} \quad (4.8)$$

$$\nabla \times \mathbf{H} = \sigma \mathbf{E} + \varepsilon \frac{\partial \mathbf{E}}{\partial t} \quad (4.9)$$

assuming harmonic dependence of the oscillating electromagnetic fields;  $\mathbf{H}, \mathbf{E} \sim e^{i\omega t}$ , where  $\omega = 2\pi\nu$  (angular frequency),  $\nu$  (frequency),  $\nu = 1/T$ ,  $T$  (period) and  $i = \sqrt{-1}$

By taking the time derivative of  $\mathbf{H}$  and  $\mathbf{E}$  we get the following:

$$\frac{\partial}{\partial t} \mathbf{H} = i\omega \mathbf{H} \quad (4.10)$$

$$\frac{\partial^2}{\partial t^2} \mathbf{H} = -\omega^2 \mathbf{H} \quad (4.11)$$

Similarly, for the electric field we get the following:

$$\frac{\partial}{\partial t} \mathbf{E} = i\omega \mathbf{E} \quad (4.12)$$

$$\frac{\partial^2}{\partial t^2} \mathbf{E} = -\omega^2 \mathbf{E} \quad (4.13)$$

By substituting Equations 4.10 and 4.12 into Equations 4.8 and 4.9, respectively, gives the following:

$$\nabla \times \mathbf{E} = -i\mu \omega \mathbf{H} \quad (4.14)$$

$$\nabla \times \mathbf{H} = \sigma \mathbf{E} + i\varepsilon \omega \mathbf{E} = (\sigma + i\varepsilon \omega) \mathbf{E} \quad (4.15)$$

By taking the curl of Equation 4.8 and substituting in Equation 4.9, the diffusion equation can be derived in terms of the time varying electric field, from which information concerning the conductivity structure of the Earth can be extracted:

$$\nabla \times (\nabla \times \mathbf{E}) = -\mu \frac{\partial}{\partial t} (\nabla \times \mathbf{H}) = -\mu \frac{\partial}{\partial t} \left[ \sigma \mathbf{E} + \varepsilon \frac{\partial}{\partial t} \mathbf{E} \right] \quad (4.16)$$

$$\nabla \times (\nabla \times \mathbf{E}) = -\mu \sigma \frac{\partial}{\partial t} \mathbf{E} - \mu \varepsilon \frac{\partial^2}{\partial t^2} \mathbf{E} \quad (4.17)$$

Using the vector identity:

$$\nabla \times (\nabla \times \mathbf{A}) = (\nabla \cdot \nabla \cdot \mathbf{A}) - \nabla^2 \mathbf{A} \quad (4.18)$$

where,  $\mathbf{A}$  is any vector.

In a homogeneous conductive medium no charges are accumulated (i.e.  $\nabla \cdot \mathbf{E} = \mathbf{0}$ ) then Equation 4.17 becomes using Equation 4.18:

$$\nabla^2 \mathbf{E} = \mu \sigma \frac{\partial}{\partial t} \mathbf{E} + \mu \varepsilon \frac{\partial^2}{\partial t^2} \mathbf{E} \quad (4.19)$$

By following a similar procedure, taking the curl of Equation 4.9) and substitute Equation 4.8, we get a similar equation for the magnetic field,  $\mathbf{H}$ :

$$\nabla^2 \mathbf{H} = \mu \sigma \frac{\partial}{\partial t} \mathbf{H} + \mu \varepsilon \frac{\partial^2}{\partial t^2} \mathbf{H} \quad (4.20)$$

In a non-conductive medium, where,  $\sigma = 0$  Equations 4.19 and 4.20 can be reduced to non-diffusive wave equation:

$$\nabla^2 \mathbf{E} = \mu \varepsilon \frac{\partial^2}{\partial t^2} \mathbf{E} \quad (4.21)$$

$$\nabla^2 \mathbf{H} = \mu \varepsilon \frac{\partial^2}{\partial t^2} \mathbf{H} \quad (4.22)$$

Equations 4.21 and 4.22 describe the nature of the EM wave propagation in a non-conductive medium with the velocity  $v = \frac{1}{\sqrt{\varepsilon\mu}}$ . Assuming the time dependence of the EM fields as  $\sim e^{i\omega t}$ , and substituting Equations 4.12 and 4.13 into Equation 4.19 and substituting Equations 4.10 and 4.11 into Equation 4.20, respectively we get:

$$\nabla^2 \mathbf{E} = (i\omega\mu\sigma - \omega^2\mu\varepsilon)\mathbf{E} \quad (4.23)$$

$$\nabla^2 \mathbf{H} = (i\omega\mu\sigma - \omega^2\mu\varepsilon)\mathbf{H} \quad (4.24)$$

Defining the wave number  $k$ :

$$k^2 = i\omega\mu\sigma - \omega^2\mu\varepsilon = i\omega\mu(\sigma + i\omega\varepsilon) \quad (4.25)$$

Equations 4.23 and 4.24 become the Helmholtz vector differential equations:

$$\nabla^2 \mathbf{E} = k^2 \mathbf{E} \quad (4.26)$$

$$\nabla^2 \mathbf{H} = k^2 \mathbf{H} \quad (4.27)$$

The resistivity of the subsurface is usually in the range of  $\rho \approx 1 - 10^4 \Omega\text{m}$  (or  $\sigma \approx 1 - 10^{-4} \text{ S/m}$ ). The periods used in MT are usually  $T \approx 10^{-4} - 10^4$ ,  $\epsilon = \epsilon_0 \epsilon_r$ ,  $\epsilon_0 = 8.85 \cdot 10^{-12} \text{ F/m}$ ,  $\epsilon_r \approx 1-100$ . The angular velocity is  $\omega = 2\pi/T$ . Then:

$$(\omega\epsilon)_{\max} = 2\pi \cdot 10^{-4} \cdot 8.85 \cdot 10^{-12} \cdot 100 \approx 5 \cdot 10^{-5}.$$

This implies that  $\sigma \gg \omega\epsilon$  (quasi-static approximation). Thus, the wave propagation constant  $k$  is reduced to:

$$k^2 = i\omega\mu\sigma \quad (4.28)$$

The Helmholtz vector Equations 4.26 and 4.27 can now be reduced to the diffusion equation:

$$\nabla^2 \mathbf{E} = i\omega\mu\sigma \mathbf{E} \quad (4.29)$$

$$\nabla^2 \mathbf{H} = i\omega\mu\sigma \mathbf{H} \quad (4.30)$$

Let us consider the Cartesian coordinate system,  $i, j$  and  $k$  being unit vectors in x (north), y (east) and z (vertically downward) direction, and a vector field  $A = (A_x, A_y, A_z)$ . From the assumption of a plane wave, propagating vertically downward, there is no variation of the electric and magnetic vector with respect to x and y (i.e.  $\partial/\partial x = \partial/\partial y = 0$ ) as explained in section 4.1.4.

Let  $i, j$  and  $k$  being unit vectors in x, y and z directions, then curl of a vector field  $\mathbf{A} = (A_x, A_y, A_z)$  is:

$$\nabla \times \mathbf{A} = \det \begin{vmatrix} i & j & k \\ \partial & \partial & \partial \\ \partial x & \partial y & \partial z \\ A_x & A_y & A_z \end{vmatrix} \quad (4.31)$$

$$\nabla \times \mathbf{A} = \left( \frac{\partial A_z}{\partial y} - \frac{\partial A_y}{\partial z} \right) i - \left( \frac{\partial A_z}{\partial x} - \frac{\partial A_x}{\partial z} \right) j + \left( \frac{\partial A_y}{\partial x} - \frac{\partial A_x}{\partial y} \right) k \quad (4.32)$$

where,  $\mathbf{A}$  is any vector.

Using the curl of the vector, Equation 4.8 gives:

$$\frac{\partial E_z}{\partial y} - \frac{\partial E_y}{\partial z} = -\mu \frac{\partial H_x}{\partial t} \Rightarrow \frac{\partial E_y}{\partial z} = i\mu\omega H_x \quad (4.33)$$

$$\frac{\partial E_x}{\partial z} - \frac{\partial E_z}{\partial x} = -\mu \frac{\partial H_y}{\partial t} \Rightarrow \frac{\partial E_x}{\partial z} = -i\mu\omega H_y \quad (4.34)$$

$$\frac{\partial E_y}{\partial x} - \frac{\partial E_x}{\partial y} = 0 \quad (4.35)$$

Similarly, Equation 4.9 gives:

$$\frac{\partial H_z}{\partial y} - \frac{\partial H_y}{\partial z} = -\sigma E_x + \epsilon \frac{\partial E_x}{\partial t} \Rightarrow -\frac{\partial H_y}{\partial z} = \sigma E_x + i\epsilon\omega E_x \quad (4.36)$$

$$\frac{\partial H_y}{\partial z} = -(\sigma + i\epsilon\omega) E_x \quad (4.37)$$

$$\frac{\partial H_x}{\partial z} - \frac{\partial H_z}{\partial x} = \sigma E_y + \epsilon \frac{\partial E_y}{\partial t} \Rightarrow \frac{\partial H_x}{\partial z} = \sigma E_y + i\epsilon\omega E_y \quad (4.38)$$

$$\frac{\partial H_x}{\partial z} = (\sigma + i\epsilon\omega) E_y \quad (4.39)$$

$$\frac{\partial H_y}{\partial x} - \frac{\partial H_x}{\partial y} = \sigma E_z + \epsilon \frac{\partial E_z}{\partial t} = 0 \quad (4.40)$$

Taking the derivative of Equations 4.33 and 4.34 with respect to z and substituting into Equations 4.39 and 4.37, respectively we get:

$$\frac{\partial^2 E_y}{\partial^2 z} = i\mu\omega \frac{\partial H_x}{\partial z} = i\mu\omega(\sigma + i\varepsilon\omega)E_y \quad (4.41)$$

$$\frac{\partial^2 E_x}{\partial^2 z} = i\mu\omega \frac{\partial H_y}{\partial z} = i\mu\omega(\sigma + i\varepsilon\omega)E_x \quad (4.42)$$

$$\frac{\partial^2 E_y}{\partial^2 z} = k^2 E_y \quad (4.43)$$

$$\frac{\partial^2 E_x}{\partial^2 z} = k^2 E_x \quad (4.44)$$

where,  $k^2 = i\mu\omega(\sigma + i\varepsilon\omega) \sim i\mu\omega\sigma$ .

Equations 4.43 and 4.44 are ordinary differential equation. They have the general solution:

$$E_{x,y} = (A_{x,y}e^{kz} + B_{x,y}e^{-kz})e^{i\omega t} \quad (4.45)$$

where,  $A_{x,y}$  and  $B_{x,y}$  are constants to be determined.

Differentiating Equation 4.45 with respect to  $z$  and substituting into Equations 4.33 and 4.34 we get the following:

$$H_x = -\frac{1}{i\mu\omega} \frac{\partial E_y}{\partial z} = -\frac{k}{i\mu\omega} (A_y e^{kz} - B_y e^{-kz})e^{i\omega t} \quad (4.46)$$

$$H_y = \frac{1}{i\mu\omega} \frac{\partial E_x}{\partial z} = \frac{k}{i\mu\omega} (A_x e^{kz} - B_x e^{-kz})e^{i\omega t} \quad (4.47)$$

Considering a homogeneous Earth, as  $z \rightarrow \infty$ , we find  $\mathbf{H} \rightarrow 0$  and  $\mathbf{E} \rightarrow 0$ . This condition leads to  $A_{x,y} = 0$  and Equation 4.45 can be reduced to the following:

$$E_{x,y} = B_{x,y}e^{-kz}e^{i\omega t} \quad (4.48)$$

Then Equations 4.46 and 4.47 can be written as follows:

$$H_x = -\frac{k}{i\mu\omega} B_y e^{-kz} e^{i\omega t} \quad (4.49)$$

$$H_y = \frac{k}{i\mu\omega} B_x e^{-kz} e^{i\omega t} \quad (4.50)$$

For a homogenous Earth Equation 4.48 can be rewritten as follows:

$$E_x = B_x e^{-kz} e^{i\omega t}; E_y = B_y e^{-kz} e^{i\omega t} \quad (4.51)$$

Using Equation 4.51, the magnetic field in  $x$  and  $y$  direction in Equations 4.49 and 4.50 can be rewritten in more general form, as follows:

$$H_x = -\frac{k}{i\mu\omega} E_y \quad (4.52)$$

$$H_y = \frac{k}{i\mu\omega} E_x \quad (4.53)$$

Rearranging Equation 4.52 and 4.53, we get the following equation for the electric field:

$$E_y = -\frac{i\mu\omega}{k} H_x \quad (4.54)$$

$$E_x = \frac{i\mu\omega}{k} H_y \quad (4.55)$$

The above equations show that the  $\mathbf{E}$  and  $\mathbf{H}$  fields are perpendicular to each other.

#### 4.1.4 Non-vertical incidence in conductive half-space

In the MT method, EM waves are considered to be plane waves. The magnetic and electric fields are perpendicular to each other. Consider a plane EM wave of angular frequency  $\omega$  and wave vector  $\mathbf{k}_o$  arriving at the surface of a homogeneous Earth with conductivity  $\sigma$  and making an incidence angle,  $\theta_i$  with the z-axis (Figure 17). When the wave arrives at the surface it will be reflected back and refracted. The refracted wave propagates into the half space with an angle, of refraction  $\theta_t$ .

According to Snell's law we get the following:

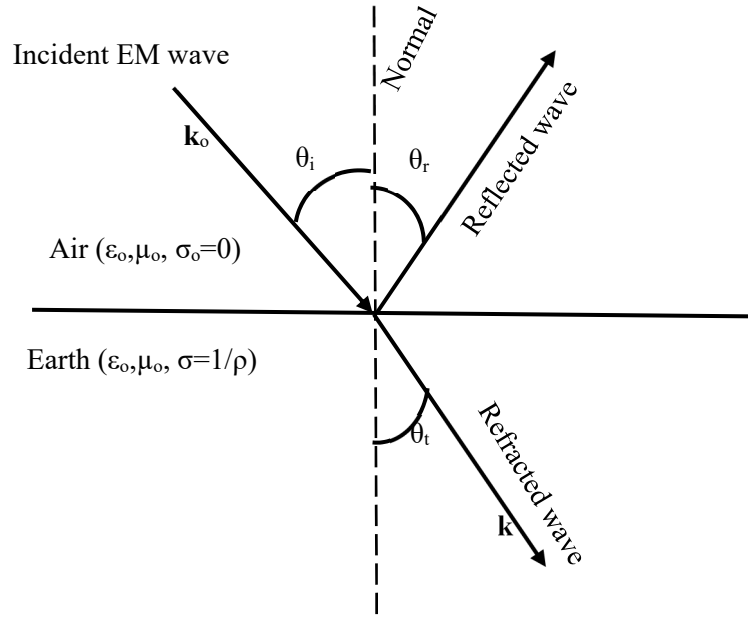


FIGURE 17: An EM wave incident on the surface of the Earth

$$\frac{1}{v_o} \sin \theta_i = \frac{1}{v} \sin \theta_t \quad (4.56)$$

where,  $v_o$  and  $v$  is the velocity of the wave in air and in the half-space, respectively.

The velocities are given as:

$$v_o = \frac{1}{\sqrt{\epsilon_o \mu_o}}; \quad v = \sqrt{\frac{2\omega}{\mu_o \sigma}} \quad (4.57)$$

Hence, we calculate the refracted angle as follows:

$$\sin \theta_t = \sin \theta_i \sqrt{\frac{2\epsilon_o \omega}{\sigma}} \quad (4.58)$$

Assuming the  $\rho$ , resistivity of the subsurface rock is  $< 10^4 \Omega\text{m}$ , and  $\omega < 10^3 \text{ Hz}$ ,  $\epsilon_o = 8.85 \text{ F/m}$ , then  $2\epsilon_o \omega / \sigma < 10^{-3}$ . The refracted angle,  $\theta_t$ , is, therefore, close to zero. The refracted wave which has a wave vector  $\mathbf{k}$  travels vertically downwards for all angles of incidence,  $\theta_i$ .

#### 4.1.5 Depth of penetration

The skin depth is where the EM wave has decayed to  $e^{-1}$  of its amplitude at the surface. Skin depth is used to estimate the depth of penetration of EM waves. When the depth is increasing the EM wave becomes insensitive to the conductivity structure of the subsurface which is deeper than the skin depth. The depth of penetration of an EM wave within the Earth depends on the frequency of the wave and the subsurface resistivity structure of the Earth it penetrated. The wave number,  $k$ , in Equation 4.28 can be rewritten as follows:

$$\begin{aligned} k &= \sqrt{i} \sqrt{\omega \mu \sigma} = \sqrt{2i/2} \sqrt{\omega \mu \sigma} = \sqrt{(1+2i-1)/2} \sqrt{\omega \mu \sigma} = \sqrt{(1+i)^2/2} \sqrt{\omega \mu \sigma} \\ &= \left( \frac{1+i}{\sqrt{2}} \right) \sqrt{\omega \mu \sigma} = \sqrt{\omega \mu \sigma / 2} + i \sqrt{\omega \mu \sigma / 2} \end{aligned} \quad (4.59)$$

Equation 4.59 shows that the wave number,  $k$ , has a real and imaginary part. The real part is associated with the attenuation of the EM wave. Taking the inverse of the real part of  $k$ , we find the skin depth formula. Whereas the imaginary part is associated with the phase:

$$\delta = 1/\text{Re}(k) = \sqrt{2/\omega\mu\sigma} \quad (4.60)$$

or:

$$\delta = \sqrt{\frac{2}{2\pi/T \cdot 4\pi \cdot 10^{-7}\sigma}} \quad (4.61)$$

$$\delta = \sqrt{\frac{2T\rho}{2\pi \cdot 4\pi \cdot 10^{-7}}} \quad (4.62)$$

$$\delta = \frac{10^3}{\pi} \sqrt{\frac{20T\rho}{8}} \quad (4.63)$$

$$\delta = 500\sqrt{\rho T} \text{ m} \quad (4.64)$$

where,  $\rho$  is the resistivity and  $T$  is the period.

Skin depth is used to estimate the depth of penetration. Shorter periods yield shallow depth of penetration whereas long periods have a greater depth of penetration. The MT method gives a wide range of penetration depths compared to active EM methods like TEM, which is limited by the period and the size of the receiver loop.

## 4.2 Homogenous earth

Cagniard (1953); Keller and Frischknecht (1966) came up with an excellent introduction to the theory of EM field over a plane layered Earth, where the theory of the propagation of EM plane wave is linear, homogeneous and isotropic. A plane wave of frequency  $f$  (Hz) propagates vertically downwards into a homogeneous and isotropic medium. The wave is composed of the time varying magnetic field ( $\mathbf{H}$ ) and electric field ( $\mathbf{E}$ ), which are orthogonal to each other on the horizontal plane. The ratio of the electric to the magnetic field intensity is a characteristic measure of the EM properties of the medium called the characteristic impedance tensor denoted by  $\mathbf{Z}$ , see Section 4.4.1. Impedance is the most important MT parameter which includes information of the electrical property of the interior of the Earth subsurface. From Equations 4.54 and 4.55 the impedance can be given as:

$$Z_{xy} = \frac{E_x}{H_y} = -\frac{E_y}{H_x} = \frac{i\mu\omega}{k} \quad (4.65)$$

where,  $Z_{xy}$  is the characteristic impedance,  $E_x$  the electric field intensity (north) and  $H_y$  the magnetic field intensity (east).

Substituting the wave propagation number  $k$  from Equation 4.28), the impedance in Equation 4.65) can be rewritten as:

$$Z_{xy} = \frac{i\mu\omega}{\sqrt{i\omega\mu\sigma}} = \sqrt{\frac{i^2\mu^2\omega^2}{i\omega\mu\sigma}} = \sqrt{\frac{i\mu\omega}{\sigma}} = \sqrt{i}\sqrt{\mu\omega\rho} \quad (4.66)$$

$$Z_{xy} = \sqrt{\mu\omega\rho} e^{i\pi/4} \quad (4.67)$$

The angle  $\pi/4$  is the phase difference between  $E_x$  and  $H_y$ , i.e. the magnetic field lags behind the electric field by  $\pi/4$  rad or  $45^\circ$ .

If the Earth is a homogeneous and isotropic half space the true resistivity of the Earth can be calculated. It is related to the characteristic impedance through the following relation:

$$\rho = \frac{1}{\omega\mu} |Z_{xy}|^2 \quad (4.68)$$

Using the practical units of the electric and magnetic fields we can derive a more generalized formula for the resistivity from Equation 4.68. The unit for the electric field  $\mathbf{E}$  is V/m, the practical unit is in mV/km ( $\mathbf{E}'$ ) or  $\mathbf{E}=\mathbf{E}' \cdot 10^{-6}$ . Using Equation 4.6,  $\mathbf{B}=\mu\mathbf{H}$ ,  $\mathbf{B}$  is the magnetic field in Tesla (T), practical unit for  $\mathbf{B}$  is gamma ( $\mathbf{B}'$ ) ( $\gamma = 10^{-9}$  Tesla = nT), magnetic field intensity is  $\mathbf{H}=\mathbf{B}/\mu=(1/\mu) \mathbf{B}' \cdot 10^{-9}$  T and  $\mu = 4\pi \cdot 10^{-7}$  (H/m). Then the resistivity is given as follows:

$$\begin{aligned} \rho &= \frac{1}{\omega\mu} \left| \frac{E_x}{H_y} \right|^2 = \frac{T}{2\pi\mu} \left| \frac{E_x' \cdot 10^{-6}\mu}{B_y' \cdot 10^{-9}} \right|^2 = \frac{T4\pi}{2\pi} \left| \frac{E_x'}{B_y'} \right|^2 10^{-7} \cdot 10^6 \\ &= 2T \cdot 10^{-1} \left| \frac{E_x'}{B_y'} \right|^2 \end{aligned} \quad (4.69)$$

$$\rho = 0.2T \left| \frac{E_x'}{B_y'} \right|^2 \quad (4.70)$$

$$\rho = 0.2T \left| \frac{E_x'}{H_y} \right|^2 \quad (4.71)$$

where,  $\rho$  is resistivity in  $\Omega\text{m}$  and  $T$  is period in s.

For a horizontally layered Earth, Equation 4.71 gives the apparent resistivity, which is dependent on the period:

$$\rho_a = \frac{1}{\omega\mu} |Z_o|^2 = 0.2T \left| \frac{E_x'}{H_y} \right|^2 \quad (4.72)$$

where,  $Z_o$  is the impedance at the surface.

The phase is also given as:

$$\theta = \arg(Z_o) \quad (4.73)$$

where,  $Z_o$  is the impedance at the surface.

### 4.3 Horizontally layered earth

Consider an EM wave is travelling into the Earth within a set of layers, each layer has a uniform conductivity  $\sigma_i$  and a thickness of  $d_i$ . The current flow is excited while travelling downward into the Earth by the plane EM wave. The plane EM wave impedance  $\hat{Z}$  is determined by a recursive formula. The impedance is continuous across the surface. Therefore, the surface impedance at  $Z=d_{i-1}$  is the characteristic impedance.

By substituting Equations 4.45 and 4.46 or 4.47 into Equation 4.65, we can derive the transfer function at the top and bottom of the  $i^{\text{th}}$  layer. For the impedance at the top of the  $i^{\text{th}}$  layer we get the following:

$$\hat{Z}_{i-1} = \frac{i\mu\omega (A_i e^{kz_{i-1}} + B_i e^{-kz_{i-1}}) e^{i\omega t}}{k (A_i e^{kz_{i-1}} - B_i e^{-kz_{i-1}}) e^{i\omega t}} \quad (4.74)$$

where,  $\hat{Z}_{i-1}$  is the depth to the top of the  $i^{\text{th}}$  layer.

And the impedance of the bottom of the  $i^{\text{th}}$  layer is given as:

$$\hat{Z}_i = \frac{i\mu\omega (A_i e^{kz_i} + B_i e^{-kz_i}) e^{i\omega t}}{k (A_i e^{kz_i} - B_i e^{-kz_i}) e^{i\omega t}} \quad (4.75)$$

where,  $\hat{Z}_i$  is the depth to the bottom of the  $i^{\text{th}}$  layer.

Let  $Z_s = \frac{i\mu\omega}{k}$  be the characteristic impedance. Dividing the denominator and the numerator of Equation 4.74 by  $(A_i B_i)^{1/2}$  and rearranging gives the following:

$$\hat{Z}_{i-1} = Z_s \frac{\left(\frac{A_i}{B_i}\right)^{1/2} e^{kz_{i-1}} + \left(\frac{B_i}{A_i}\right)^{1/2} e^{-kz_{i-1}}}{\left(\frac{A_i}{B_i}\right)^{1/2} e^{kz_{i-1}} - \left(\frac{B_i}{A_i}\right)^{1/2} e^{-kz_{i-1}}} \quad (4.76)$$

$$\left(\frac{A_i}{B_i}\right)^{1/2} = Z_s \frac{\left(\frac{A_i}{B_i}\right)^{1/2} e^{kz_{i-1}} + \left(\frac{B_i}{A_i}\right)^{1/2} e^{-kz_{i-1}}}{\left(\frac{A_i}{B_i}\right)^{1/2} e^{kz_{i-1}} - \left(\frac{B_i}{A_i}\right)^{1/2} e^{-kz_{i-1}}} \quad (4.77)$$

$$\left(\frac{A_i}{B_i}\right)^{1/2} = Z_s \frac{\left(\frac{B_i}{A_i}\right)^{1/2} [Z_s e^{kz_{i-1}} + Z_{i-1} e^{-kz_{i-1}}]}{[Z_s e^{kz_{i-1}} + Z_{i-1} e^{-kz_{i-1}}]} \quad (4.78)$$

Similarly, for Equation 4.75 we get the following:

$$\hat{Z}_i = Z_s \frac{\left(\frac{A_i}{B_i}\right)^{1/2} e^{kz_i} + \left(\frac{B_i}{A_i}\right)^{1/2} e^{-kz_i}}{\left(\frac{A_i}{B_i}\right)^{1/2} e^{kz_i} - \left(\frac{B_i}{A_i}\right)^{1/2} e^{-kz_i}} \quad (4.79)$$

From Equation 4.33 and 4.34 we get the following:

$$H_x = \frac{1}{i\mu\omega} \frac{\partial E_y}{\partial z} ; H_y = \frac{1}{i\mu\omega} \frac{\partial E_x}{\partial z} \quad (4.80)$$

and substituting Equation 4.79 into Equation 4.80, we get the following equation without any constant:

$$\hat{Z}_{i-1} = Z_s \frac{\hat{Z}_i + Z_s \tanh(ik_i d_i)}{Z_s + \hat{Z}_i \tanh(ik_i d_i)} \quad (4.81)$$

where,  $d_i = Z_i - Z_{i-1}$  the thickness of the  $i^{\text{th}}$  layer.

Equation 4.81 is a recursive formula. For a horizontally layered Earth Equation 4.71 gives the apparent resistivity, which is dependent on the period.

$$\rho_a = \frac{1}{\omega\mu} |Z_o|^2 = 0.2T \left| \frac{E_x}{H_y} \right|^2 \quad (4.82)$$

where,  $Z_o$  is the impedance at the surface.

The apparent phase is given as:

$$\theta = \arg(Z_o) \quad (4.83)$$

#### 4.4 MT transfer functions

MT transfer functions are responses that are related to the measured component of the EM field at a given frequency. MT transfer functions contain information about the electrical conductivity in the subsurface, as the MT site is located at the centre of the boundary horizon. Therefore, they characterize the resistivity distribution of the underlying material according to the measured frequency.

#### 4.4.1 Impedance tensor

The impedance tensor describes the relation between the orthogonal electric and magnetic fields at a given frequency. In matrix form the tensor can be written as follows:

$$\begin{bmatrix} E_x \\ E_y \end{bmatrix} = \begin{bmatrix} Z_{xx} & Z_{xy} \\ Z_{yx} & Z_{yy} \end{bmatrix} \begin{bmatrix} H_x \\ H_y \end{bmatrix} \quad (4.84)$$

The linear relationship between the electric and the magnetic field spectra is written:

$$E_x(\omega) = Z_{xx}H_x(\omega) + Z_{xy}H_y(\omega) \quad (4.85)$$

$$E_y(\omega) = Z_{yx}H_x(\omega) + Z_{yy}H_y(\omega) \quad (4.86)$$

#### 4.4.2 Geomagnetic transfer functions

To study the conductivity structure of the Earth, the geomagnetic transfer functions are used. The geomagnetic transfer function can be derived in the same way as the MT impedance tensor from the MT time series data. The geomagnetic transfer function is the ratio of the amplitude of the vertical component to the horizontal component of the magnetic field. The vertical magnetic fields are generated by lateral conductivity gradient or discontinuities. The vertical magnetic field is linearly related to the horizontal magnetic fields by:

$$H_z = \mathcal{J}_{zx}H_x + \mathcal{J}_{zy}H_y, \text{ where } \mathcal{J} \text{ is the so-called Tipper} \quad (4.87)$$

In case of 1D Earth the Tipper components  $\mathcal{J}_{zx}$  and  $\mathcal{J}_{zy}$  are zero, because the induced wave of the EM field is perpendicular to the Earth's surface. Therefore, there is no induced vertical magnetic field. But in contrast, near to vertical resistivity boundaries between low and high conductivity structures, for example at the boundary between the ocean and land, there is an induced vertical magnetic field, as a result the value of the Tipper will be maximum. In 2D Earth, the coordinate system can be rotated so that the x-axis is in the strike direction, which consequently is called the T-strike,  $\mathcal{J}_{zx} = 0$ , but  $\mathcal{J}_{zy} \neq 0$ . This is done by minimizing  $|\mathcal{J}_{zx}|$ . The Tipper vector can be decomposed into two real vectors in the horizontal xy-plane.

There exist two different conventions of the real induction arrows:

- (1) Reversed (Parkinson convention, Parkinson, 1959);
- (2) Non-reversed (Wiese convention).

In Wiese convention, the vector points away from the lateral high electrical conductivity (Wiese, 1962). The arrows have a real (in-phase) and imaginary (out-of-phase) part. The magnitude of the induction arrows depends on both the proximity to the conductor and the conductivity contrast. If the conductivity contrast is bigger and the conductor is closer, the arrows become longer (Lichoro, 2013). The absence of induction arrows at a single site does not show an absence of lateral conductivity boundaries. The length of the real ( $M_r$ ) and imaginary ( $M_q$ ) arrow is given by:

$$M_r = (\Re\mathcal{J}_{zx}^2 + \Re\mathcal{J}_{zy}^2)^{1/2} \quad (4.88)$$

$$M_q = (\Im\mathcal{J}_{zx}^2 + \Im\mathcal{J}_{zy}^2)^{1/2} \quad (4.89)$$

where  $\Re$  and  $\Im$  are the real and imaginary part of Tipper, respectively.

The orientation of the arrows  $\theta_r$  and  $\theta_q$ , clockwise positive from the x-direction (usually geomagnetic north), is similarly determined by:

$$\theta_r = \tan^{-1} \left( \frac{\Re\mathcal{J}_{zy}}{\Re\mathcal{J}_{zx}} \right) \quad (4.90)$$

$$\theta_q = \tan^{-1} \left( \frac{\Im\mathcal{J}_{zy}}{\Im\mathcal{J}_{zx}} \right) \quad (4.91)$$

In the 2D Earth, the direction of the induction arrow is perpendicular to the true orientation of the regional geo-electric strike. In other words, in 2D Earth, the induction arrows are associated only with TE mode, which gives  $H_z$ . The principal angle is perpendicular to the geo-electric strike. As a result, the strike direction is  $90^\circ$  from the principal angle. But for a 3D Earth, the direction varies.

#### 4.5 Dimensionality of MT transfer functions

The impedance tensor contains information about the dimensionality of the measured data. In the following subsections it is discussed how the resistivity structure is 1D or more complex. The dimensionality of the MT data, generally dependent on the scale (both the recording period length and the depth of the anomaly). For instance, if we have a generalized homogeneous 3D conductivity anomaly embedded in a uniform Earth: At short periods, the skin depth of the EM field is smaller compared to the dimension of the anomaly, eventually the impedance tensor shows 1D resistivity structure. As the recording period of the sounding increases the impedance tensor shows a 2D resistivity structure. When the recording period of the sounding increases further, the skin depth becomes bigger and it detects all the edge effects of the anomaly. The impedance tensor shows a 3D resistivity structure (Simpson and Bahr, 2005).

##### 4.5.1 1D Earth

In a 1D Earth, the conductivity varies only with depth. The diagonal elements  $Z_{xx}$  and  $Z_{yy}$  are zero, whereas, the off diagonal elements are equal in magnitude but have opposite signs  $Z_{xy} = -Z_{yx}$ . The impedance tensor can be written as follows:

$$Z_{1D} = \begin{pmatrix} 0 & Z_{xy} \\ -Z_{xy} & 0 \end{pmatrix} \quad (4.92)$$

The apparent resistivity is given as:

$$\rho_a = \frac{1}{\omega\mu_0} |Z|^2 \quad (4.93)$$

And the phase is given as:

$$\theta_a = \tan^{-1} \left( \frac{ImZ}{ReZ} \right) \quad (4.94)$$

##### 4.5.2 2D Earth

For 2D Earth, the conductivity varies in one of the two principal horizontal direction as well as with depth but it is constant along the other principal horizontal direction. The direction along which the conductivity is constant is called the geo-electrical strike or electromagnetic strike direction.

In case of pure 2D Earth, the x-direction is parallel to the geo-electric strike and the y-direction is perpendicular to it. Then the diagonal components of the impedance tensor become zero ( $Z_{xx} = Z_{yy} = 0$ ) and the impedance tensor can be written as follows:

$$Z_{2D} = \begin{pmatrix} 0 & Z_{xy} \\ Z_{yx} & 0 \end{pmatrix} \quad (4.95)$$

where,  $Z_{xy} = Z_{TE} = \frac{E_x}{B_y}$ , and  $Z_{yx} = Z_{TM} = \frac{E_y}{B_x}$ .

The apparent resistivity for the two modes can be written as:

$$\begin{aligned} \rho_{xy} &= 0.2T |Z_{xy}|^2 \\ \rho_{yx} &= 0.2T |Z_{yx}|^2 \end{aligned} \quad (4.96)$$

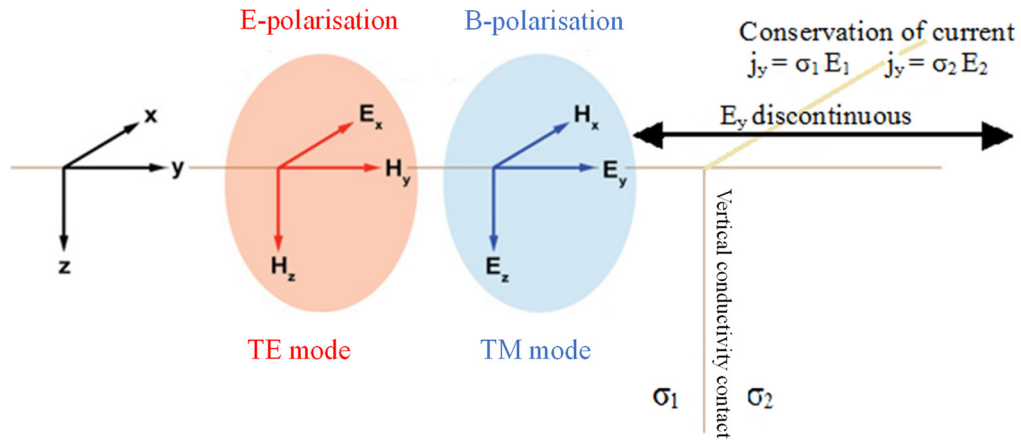


FIGURE 18: 2D model and the concept of polarizations in magnetotellurics and vertical contact between two different zones of conductivity (Teklesenbet, 2012)

where,  $T$  is the period.

Figure 18 shows a simple 2D model, where there are discontinuities in the electrical conductivity ( $\sigma_1$ ,  $\sigma_2$ ) which has an infinite boundary in the strike direction ( $x$ -direction). Then there will be charges generated on those boundaries. This can be confirmed from Ohm's law where,  $\mathbf{J} = \sigma \mathbf{E}$  and at the boundary the normal current density ( $J_n$ ) is continuous, as a result, the electric field in  $y$ -direction ( $E_y$ ) is discontinuous across the boundary and has different amplitudes on either side of the boundary.

In 2D Earth ( $\rho(x,z)$ ), the EM field splits into two independent modes. The transverse magnetic (TM) mode,  $\mathbf{B}$ -polarization, and transverse electric (TE) mode,  $\mathbf{E}$ -polarization. In TM mode the magnetic field is parallel to the electrical strike direction. The current flows perpendicular to the strike direction of the resistivity structure which causes  $E_y$  to be discontinuous and  $\rho_{yx}$  become discontinuous. As a result of these discontinuities TM data are more sensitive to lateral resistivity variations than TE mode. On the other hand, for the TE mode the electric field is parallel to the electrical strike direction (the telluric current flows parallel to the strike of the resistivity structure). In TE mode the apparent resistivity varies smoothly across the discontinuity because the associated electric field ( $E_x$ ) and vertical magnetic field ( $H_z$ ) are continuous across the boundary (Simpson and Bahr (2005); Teklesenbet (2012); Lichoro (2013)).

If the geo-electrical strike is known prior to an MT survey, one of the horizontal axes for the measurement should be aligned along the strike direction. But it's rare that the MT field layout is in the direction of the strike. For this reason, in case of 2D structures the MT data have to be rotated to the respective polarization direction (see Section 4.6).

#### 4.5.3 3D Earth

In 3D Earth the resistivity varies in all directions. The diagonal components of the impedance tensors are non-zero and they are not equal, also the off diagonal components are not equal. The general form of the 3D Earth impedance tensor can be written as follows:

$$Z_{3D} = \begin{pmatrix} Z_{xx} & Z_{xy} \\ Z_{yx} & Z_{yy} \end{pmatrix} \quad (4.97)$$

There are no rotational directions where both the diagonal components of the impedance tensors will vanish. Therefore, all the components of impedance tensors will be used in the interpretation of the data.

## 4.6 Rotation of impedance tensor

In MT field measurements, we usually don't know the geo-electric strike direction beforehand. Therefore, the field measurement layout axes generally don't coincide with the axis parallel or perpendicular to the geo-electric strike direction. As shown in Figure 19,  $x$  and  $y$  are our measurement axes. Then the coordinate axes can be rotated clockwise from north through an angle  $\theta$  by mathematical means to yield a new coordinate system,  $x'$  and  $y'$ .

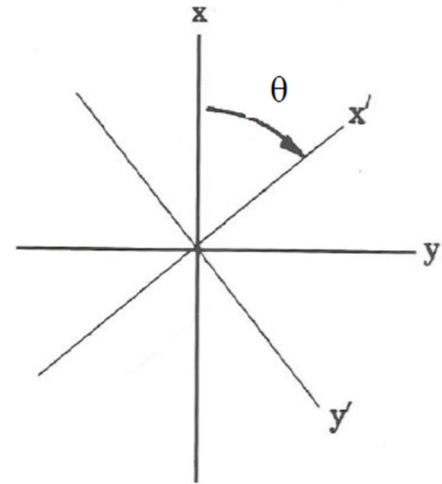


FIGURE 19: Rotation of reference frame

The rotated impedance tensor  $Z'$  can be written as:

$$Z' = R(\theta)ZR^T(\theta) \quad (4.98)$$

where,  $R(\theta) = \begin{bmatrix} \cos \theta & \sin \theta \\ -\sin \theta & \cos \theta \end{bmatrix}$  is the rotation operator,  
and  $R^T(\theta) = \begin{bmatrix} \cos \theta & -\sin \theta \\ \sin \theta & \cos \theta \end{bmatrix}$  is the transpose of  $R$ .

Then Equation 4.98 can be rewritten as:

$$\begin{bmatrix} Z'_{xx} & Z'_{xy} \\ Z'_{yx} & Z'_{yy} \end{bmatrix} = \begin{bmatrix} \cos \theta & \sin \theta \\ -\sin \theta & \cos \theta \end{bmatrix} \begin{bmatrix} Z_{xx} & Z_{xy} \\ Z_{yx} & Z_{yy} \end{bmatrix} \begin{bmatrix} \cos \theta & -\sin \theta \\ \sin \theta & \cos \theta \end{bmatrix} \quad (4.99)$$

Or each rotated impedance tensor components can be written as:

$$Z'_{xx} = Z_{xx}\cos^2\theta + (Z_{xx} + Z_{yy})\sin\theta\cos\theta + Z_{yy}\sin^2\theta \quad (4.100a)$$

$$Z'_{xy} = Z_{xy}\cos^2\theta + (Z_{yy} - Z_{xx})\sin\theta\cos\theta - Z_{yx}\sin^2\theta \quad (4.100b)$$

$$Z'_{yx} = Z_{yx}\cos^2\theta + (Z_{yy} - Z_{xx})\sin\theta\cos\theta - Z_{xy}\sin^2\theta \quad (4.100c)$$

$$Z'_{yy} = Z_{yy}\cos^2\theta - (Z_{xy} + Z_{yx})\sin\theta\cos\theta + Z_{xx}\sin^2\theta \quad (4.100d)$$

In 2D Earth, the geo-electrical strike direction is obtained by minimizing the diagonal component or maximizing the off diagonal components of the impedance tensor:

$$\begin{aligned} |Z'_{xx}|^2 + |Z'_{yy}|^2 &= \text{Minimum} \\ |Z'_{xy}|^2 + |Z'_{yx}|^2 &= \text{Maximum} \end{aligned} \quad (4.101)$$

The angle of the strike  $\theta_0$  is obtained using the following equation:

$$\theta_0 = \frac{1}{4} \tan^{-1} \left| \frac{(Z_{xx} - Z_{yy})(Z_{xy} + Z_{yx})^* + (Z_{xx} - Z_{yy})^*(Z_{xy} + Z_{yx})}{|Z_{xx} - Z_{yy}|^2 - |Z_{xy} - Z_{yx}|^2} \right| \quad (4.102)$$

The \* indicates the complex conjugate. The angle calculated from Equation 4.102 is called Swift angle or Z-strike (Swift, 1967).

For 2D resistivity structures, the geo-electric direction, the rotation of the coordinate system, has always 90° ambiguity as clearly seen by Equation 4.102. In order to overcome this problem, the Tipper strike is used which applies the vertical magnetic field component.

## 4.7 Dimensionality indicators

Analysis of the MT impedance tensor allows to perform geo-electric regionalization, identify structures and to determine their dimensionality and orientation. Understanding of the dimensionality of the MT data is very crucial for the interpretation of the data. The dimensionality parameters could give an indication of the dimensionality of the measured data. The parameters which are used to analyse the dimensionality of the data include, polar diagrams, skew, ellipticity and Tipper magnitude.

### 4.7.1 Impedance polar diagram

Polar diagrams are one of the various parameters which are used to identify the dimensionality of MT data. Polar diagrams are free from structural and frequency limitations. The shape of 1D, 2D and 3D polar diagrams is essentially dependent on the dimensionality and orientation of geo-electrical structures.

For the 1D resistivity structure, the off-diagonal components of impedance have the same magnitude in all directions. Therefore, its amplitude polar diagram plots are circular, whereas polar diagrams for the diagonal components of impedance become minimal or vanishes to a point (Figure 20). For 2D and 3D resistivity structures the principal impedance component polar diagrams elongate in a direction either parallel or perpendicular to the strike (Reddy et al., 1977; Figure 20). For 2D resistivity structure the impedance polar diagrams for  $Z'_{xy}$  has a maximum or minimum amplitude which could be parallel or perpendicular to the strike direction, which form peanut shape, whereas for the  $Z'_{xx}$  (is small) amplitude polar diagrams are symmetric about the strike direction and attain the shape of a clover leaf. For 3D resistivity structure, the amplitude of the polar diagram of  $Z'_{xx}$  and  $Z'_{yy}$  is not symmetric and the amplitude of the polar diagram will not become zero in any direction. Away from the symmetry lines, the polar diagrams are distorted and their magnitude becomes larger, specifically at low frequency indicating 3D structures at depth. Therefore, the polar diagrams for  $Z'_{xx}$  and  $Z'_{xy}$  can be similar and be in the shape of the number eight.

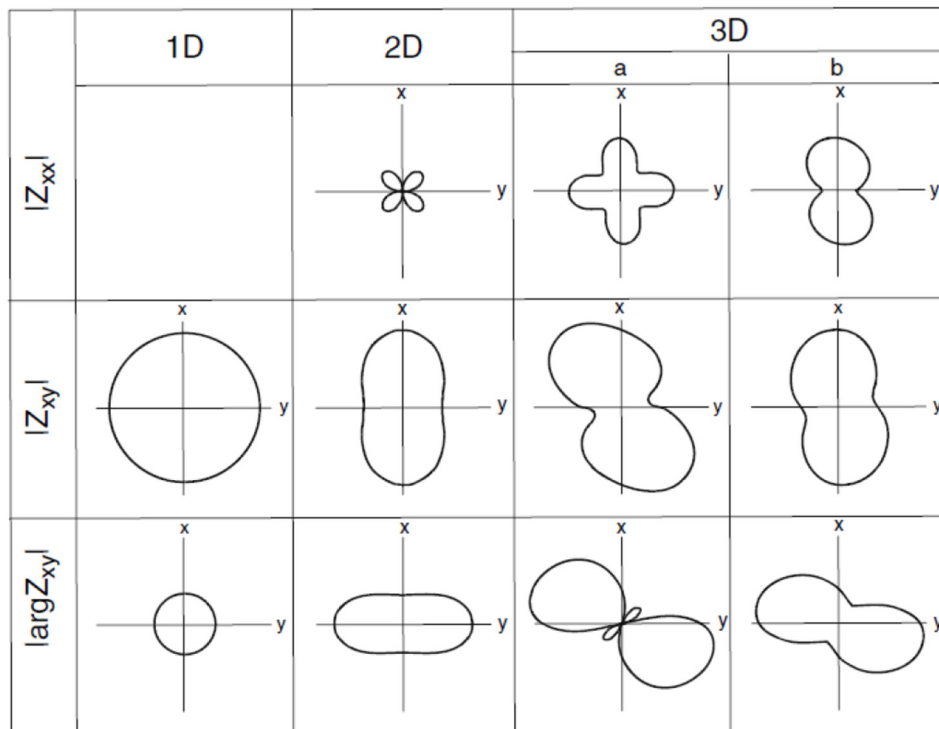


FIGURE 20: Polar diagrams of the impedance tensor showing 1D, 2D and 3D form of plots (Berdichevsky and Dmitriev, 2002)

### 4.7.2 Skew

Skew is the ratio of the sum of the amplitude of the diagonal impedance components to the difference between the off diagonal components. The skew is rotationally invariant. For 1D and 2D Earth, the skew is close to zero. However, the skew may become large if there is local noise sources, local cultural features and in-homogeneities (causing distortion of the data by static shift) (Jones, 2002). Typical value above 0.2 indicates the response of the data could be interpreted as a strong 3D effect in that area. Therefore, skew is an indicator of three dimensionality (Swift, 1967):

$$S = \left| \frac{Z_{xx} + Z_{yy}}{Z_{xy} - Z_{yx}} \right| \quad (4.103)$$

### 4.7.3 Ellipticity

Ellipticity is defined by the diagonal and off diagonal components of the impedance tensor and it varies with rotation. It is written as follows:

$$\text{Ellipticity}(\theta) = \left| \frac{Z_{xx}(\theta) - Z_{yy}(\theta)}{Z_{xy}(\theta) + Z_{yx}(\theta)} \right| \quad (4.104)$$

where  $\theta$  is the angle of rotation.

For noise free data, Ellipticity becomes zero for 1D and 2D resistivity structures (when  $\theta$  is in strike direction), while for 3D resistivity structure it is non-zero.

### 4.7.4 Tipper magnitude

Tipper information comes from the vertical component of the magnetic field. It is a measure of the degree of lateral inhomogeneity in the Earth's subsurface resistivity structure. In general, in multi-dimensional Earth, the vertical magnetic field is linearly related to the horizontal magnetic fields by:  $H_z = \mathcal{T}_x H_x + \mathcal{T}_y H_y$ , where  $\mathcal{T}$  is the Tipper. The Tipper magnitude is written as:

$$|\mathcal{T}| = \left( |\mathcal{T}_x|^2 + |\mathcal{T}_y|^2 \right)^{1/2} \quad (4.105)$$

For 1D Earth, the Tipper is zero (there is no strike direction), whereas for a non 1D Earth the Tipper becomes larger. We have several stations in our survey area that measure the vertical magnetic field, it helps us to resolve the 90° ambiguity of the strike direction as derived from the impedance tensor only.

## 5. MT STATIC SHIFT PROBLEM

MT data suffer from a problem termed static shift because of near surface in-homogeneities that cause distortion of MT data due to an electric field generated from the boundary charges on surficial bodies which persists throughout the entire recording range of an MT sounding. All resistivity methods that measure the electric field on the surface suffer from the static shift problem. Static shift due to subsurface in-homogeneities can have severe influence on the interpretation of MT data by shifting the apparent resistivity curve by a factor on a log scale. MT static shift is a frequency independent galvanic response associated with 3D bodies (Berdichevsky and Dmitriev, 1976). The amount of shift and direction depends on the resistivity structure. Generally static shifts are more common in volcanic/geothermal areas where the subsurface is highly resistive, where small scale conductivity heterogeneities have a more significant effect on electric fields.

The static shift problem cannot be determined directly from MT data recorded at a single site, because apparent resistivity curves from the closest site generally have the same shape but could be shifted parallel to one another. The parallel shift between TE and TM polarization of an MT sounding clearly indicates that static shift is present in the data. However, lack of shift between those polarizations doesn't necessary indicated absence of the shift, since both curves might be shifted by the same amount. The parallel shift in the apparent resistivity curve leads to large errors in the inverted model of the data. The true resistivity curve may lie above, below or between measured levels. Shift as low as 0.1 could lead to 10 times too low resistivity values and 3 times too shallow depths for resistivity boundaries (Árnason, 2008).

Static shift must be removed from the data before final interpretation of the resistivity data is made. One of the best methods to correct the static shift is to measure the magnetic field which is less affected by near surface in-homogeneities by using an active near-surface measurement like central loop TEM method. TEM does not measure electric field and it does not need any electrical contact to the ground, so it is not affected by static shift problem. In this report TEM data were used to correct the MT data from the same location by jointly inverting the MT and TEM data. Moreover, inversion of static shift corrected MT data are closer to the results from well-log resistivity data than the uncorrected MT data (Sternberg et al., 1988). Inverting static shift corrected MT data gives a much more reliable resistivity model of the subsurface.

There are mainly three things that cause static shift problems; 1) Voltage distortion. 2) Current distortion. 3) Topographic distortion. See further details in Sections 5.1.1, 5.1.2 and 5.2, respectively.

### 5.1 MT data distortion due to anomalous body

#### 5.1.1 Voltage distortion

Voltage distortion occurs due to the distortion of the electric field around the electrodes because the electric field is dependent on the resistivity structure of the subsurface, where the voltage difference is measured. If the same amount of current flows through two different resistivity media (Figure 21) and, for example, if  $\rho_2 < \rho_1$ , the electric field over a given length will be low where there is low resistivity medium and vice versa (Árnason, 2015).

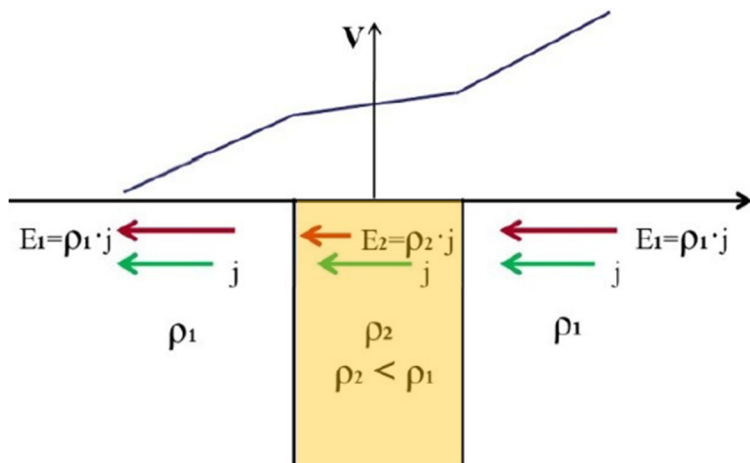


FIGURE 21: Static shift due to electric field distortion (Árnason, 2015)

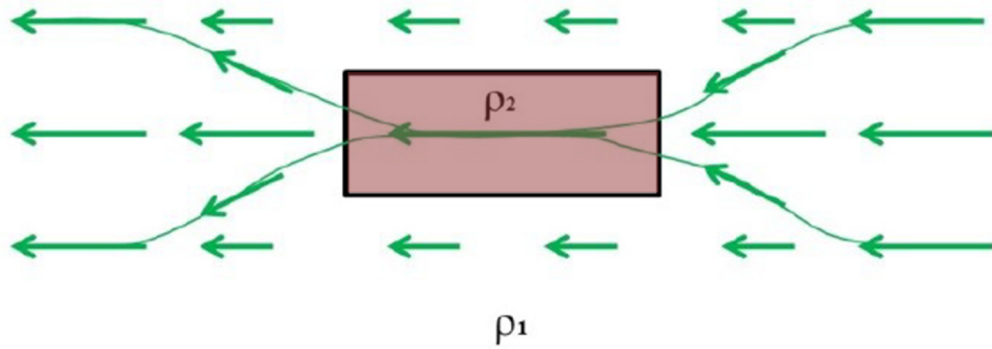


FIGURE 22: Current channelling leading to current distortion (Árnason, 2015)

### 5.1.2 Current distortion

Static shift caused by current distortion is due to an electric field generated from the boundary charges on surficial bodies which persist throughout the entire MT data recording range. The flow of current in the subsurface is controlled by the resistivity structure of the Earth. As shown in Figure 22 the current is more concentrated towards the low resistivity body which is called current channelling. Otherwise the current is repelled or flows away from the resistive body (Árnason, 2015).

### 5.2 Topographic effect

The topographic effect is one of the possible causes for an MT static shift problem. The current flow into the topographic high (ridge) is locally spread out, causing reduction of induced current density, which in turn causes decreasing electrical field strength on the ridge (Figure 23). In contrast, the current flow in the topographic low (valley) is locally concentrated and the current density and the electric field strength is high (Figure 23) (Árnason, 2015; Lichoro, 2013; Jiracek, 1990). Thus, the corresponding apparent resistivity value on the topographic high is low and vice versa.

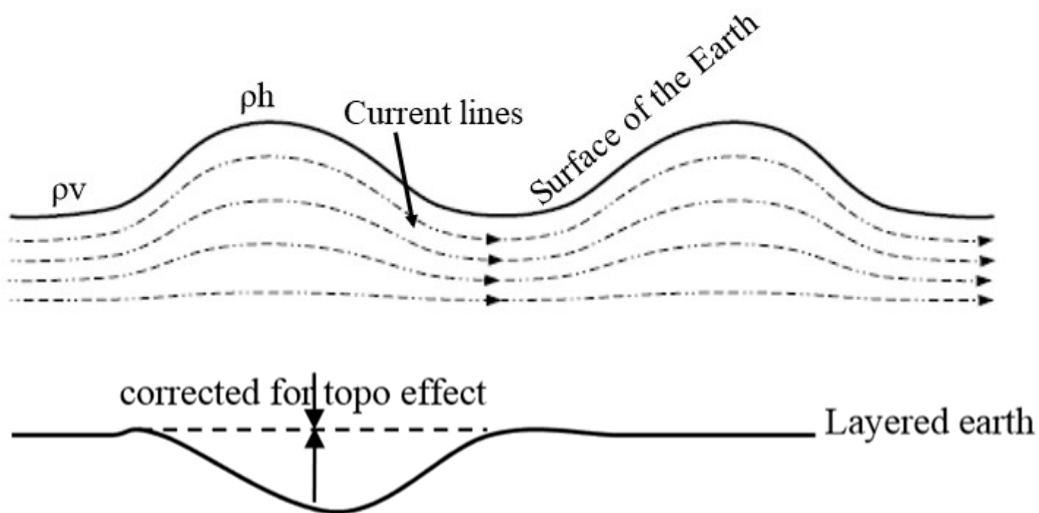


FIGURE 23: Effect of a ridge and valley on current density and correction for the topographic effects (modified from Lichoro, 2013)

## 6. DATA ACQUISITION, INSTRUMENTATION AND DATA PROCESSING

### 6.1 Instrumentation and field survey

An MT field survey was carried out in Alalobeda in two campaigns, in 2013 and 2014-15. MT data acquisition unit from Phoenix Geophysics Ltd Company in Canada (Phoenix Geophysics, 2009) was used in both campaigns. In 2013, due to security problems at the survey site, the data were acquired only during the day-time using two MTU-5A units. The average time length of data acquisition was about 9 hours and a remote reference station was not used in the processing work. In the 2014-15 field campaign, MT data were collected using three MTU-5A units from Phoenix. Two of the MT units are deployed at the survey site and one of the MT unit was kept at the remote reference site.

The instrument used for the MT survey consists of a data logger (MTU), two pairs of electric dipoles for measuring the electric field, three induction coils connected by cables for measuring the time variations of natural magnetic field, battery, compact flash card, GPS and five non-polarizable electrodes, filled with a lead chloride solution in a ceramic container that is designed to ensure good contact with the ground (Figure 24). This Figure shows the standard complete setup of an MT survey.

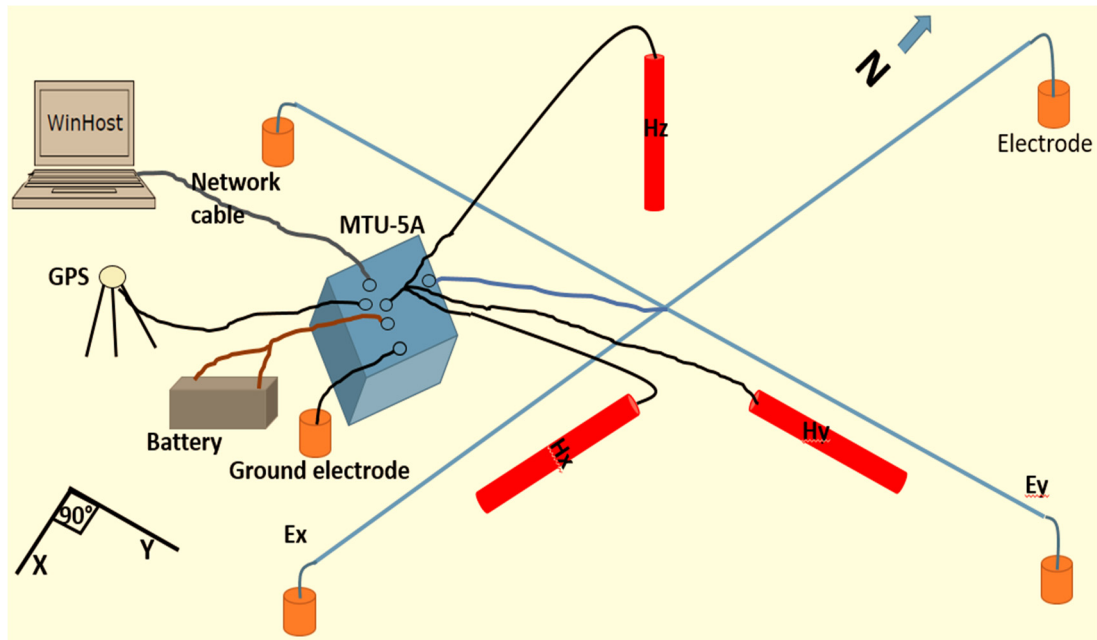


FIGURE 24: Standard setup of an MT sounding

The data logger is the heart of the system. It amplifies, filters and converts the analog signal to digital data format and stores the data in the compact flash card. The data logger has five channels, two channels for the horizontal and orthogonal electric fields ( $E_x$  and  $E_y$ ), three channels for the orthogonal and horizontal magnetic fields ( $H_x$  and  $H_y$ ) and vertical  $H_z$  magnetic field. The electric field components  $E_x$  and  $E_y$  are determined by measuring the potential difference  $\Delta V$ , between two pairs of electrodes, which are connected through a shielded cable to form a dipole at a known distance,  $d$ , which gives  $E = \Delta V/d$ . The electrodes are buried below the surface to mitigate temperature variations.

The survey began when the calibration of the MTU units and the sensors were done. The calibration was carried out at the reference site in Ayrobera about 20 km from the survey site because it has low noise characteristics. The MTU units were calibrated before acquiring data. Calibration of MTU units takes 10-15 minutes after it's powered on in normal temperature. Calibrating magnetic coils takes about one to two hours.

The survey was carried out with three teams, two teams at the survey site and one team at the reference site. Each team needed to record the survey site, conduct an inventory and inspection of the necessary

equipment, verify location and determine the center. Having chosen a suitable position for the data logger the electrodes are located using a tripod and a compass. The electric dipoles are normally aligned in magnetic north-south (N-S) direction and in magnetic east-west (E-W) direction. In this survey, almost for all sites, the dipole length was 100 m. Measuring tape were used to measure the actual dipole length.

In general, the source of low frequency (long periods) signals is low around equator and that is why the dipole length should be long enough in Ethiopia. The longer the dipole the better the signal to noise ratio. The greater the AC voltage induced by the local power grid is the lower is the signal to noise ratio. High AC voltage can result in unusable data when the dynamic range of the system is exceeded. MT stations are placed away from noise sources such as power lines, roads, electric fence, and livestock farming areas etc., although if the ground is very conductive, a distance of about 100 meters away from those noise source is usually enough. And the spot should allow access in all four directions to place the electrodes and sensors. MT data are very sensitive and small disturbances can cause high noise levels. For example, a slight movement of magnetic sensors or wire connecting the electrodes can cause voltage noise. To minimize those disturbances the magnetic sensors and wires are buried in the ground which also helps to minimize thermal effects on the magnetic sensors. We used a notch filter of 50 Hz to eliminate the noise from the electrical power lines.

At all sounding sites the electrodes were buried in a hole about 40 cm deep filled with a mixture of soil with salty water and bentonite, in order to get good ground contact and to reduce the resistance between the ground and the electrodes, (Figure 25). The top of the electrodes is covered with the soil in order to prevent it from the daily temperature variations.



FIGURE 25: Right: Hole filled with a mixture of salty water, bentonite and soil; Left: Electrode installed in a hole 40 cm deep and ready to be covered with soil

If there are difficulties around the sites keeping a standard layout, for example, hills, trees, rocks etc., the electric dipole can be made shorter or longer than normal. It may also have to be oriented otherwise than to the true or magnetic north. Excess telluric cables are laid in elongated S-shapes, not closer than 5 m from the end of the electrode. If the excess cable makes a loop (round shape), it will create an induction that distorts the signal.

Induction coils are used to measure the natural magnetic field in three orthogonal directions i.e. x, y, and z. In Alalobeda all the three components of magnetic field were acquired,  $H_x$  and  $H_y$  are horizontal and orthogonal to each other and  $H_z$  is vertical. It is very crucial to identify, level and orient the direction of the sensors using a spirit level and compass to obtain reliable magnetic data. The  $H_x$  horizontal coil is oriented north-south, placed with its free end towards the north or connector pointing to the south and the other horizontal coil;  $H_y$  is oriented east-west, placed with its free end towards the east or connector pointing to the west. The  $H_x$  and  $H_y$  coils were buried approximately 40-50 cm deep in the ground to prevent any movement by wind and direct expose to sunlight (Figure 26). Before burying the coils, it is necessary to take notes of the serial numbers of each coil and record on the field layout sheet.



FIGURE 26: Digging of a shallow trench and leveling the magnetic sensor

The vertical magnetic coil was buried in an approximately 0.5 m deep hole. In some cases where the site was rocky, the coil was buried deep enough to be stable (Figure 27). The upper part of the vertical coil was covered with plastic and tie using tape to minimize vibrations caused by wind.

Before turning the power on the necessary measurements should be taken and the compact flash card inserted into the MTU unit.

Digital voltmeter was used to measure the dipole voltages AC and DC between the N-S and the E-W pair of E-lines. Measuring these values will help to choose the best gain to set for the survey area when programming the MTU units. Values  $\geq 150$  mV AC may indicate the presence of strong noise source nearby the survey site. Analog Ohmmeter was used for measuring the electrode contact resistance across the dipoles. When preparing the electrodes for field work the voltage



FIGURE 27: Burying the vertical magnetic sensor

and resistance should be measured and they can be paired depending on the measured values, lower values are always preferable. The DC potential between pairs of electrodes (i.e. self-potential) should be  $< 20$  mV. If the resistance between each pair of electrodes is  $\geq 2$  k $\Omega$  the electrode should be replaced. In order to identify the faulty electrode we measure the resistance between the ground terminal to each E-line and between the two E-lines ends of each dipole.

If the measured contact resistance is  $> 2$  k $\Omega$  it may indicate poor ground contact or the electrode is dried up. Contact resistance of the electrodes can be reduced by installing them in salt water before and after field work. This helps the electrochemical environment to stabilize (Vozoff, 1990).

A car battery which is sealed lead acid was used as power supply to the data logger for continuous recording of the data for about 20 hours. The instrument synchronizes to coordinated universal time (UTC) through signal from the Global Positioning System (GPS) satellites.



FIGURE 28: Left: Connected data logger; Right: Checking the online status of data acquisition

Before any connections are made, it is most important that the MTU units are grounded. Then electric and magnetic field sensors, GPS and battery were connected directly to the data logger (Figure 28). Once all the components have been connected, the data logger is powered on and after some time it is synchronized and find satellites. The red led indicator on top of the unit indicates its status. In the Alalobeda field campaigns, a laptop was used for monitoring the data logger during acquisition. Finally, we checked that all mandatory information is entered on the survey layout sheet. The field crew must cross check that all the connections are correct.

Since the survey area is very hot, the MTU-5A unit was protected by putting it into a wooden box to protect it from the sun. The box had holes for air ventilation, (Figure 29). The following day the field crew could check the site and the equipment for disturbances. For example, if the cables were chewed by animals, indicating the site should be repeated. The quality of the data was checked by preliminary processing the data before retrieving the equipment and move to the next station if the current station did not need to be repeated.



FIGURE 29: Wooden box used for protecting the data logger from the sun and wind

## 6.2 Processing MT data

The Earth's natural electric and magnetic field components are measured by the MT geophysical equipment in the subsurface. The data are recorded as time series for the two electric components and three magnetic components. In MT data processing, we take the time series data and calculate apparent resistivity and phase curves. The measured electric and magnetic fields as a function of time (time series) are downloaded from the compact flash card of the MTU units and the quality of the data inspected visually using a program called Synchro Time Series Viewer, which is provided by Phoenix Geophysics in Canada (Phoenix Geophysics, 2009). This program allows imaging and printing of graphical representation of the raw time series data, power spectra which are derived from the time series and coherency between pairs of orthogonal electric and magnetic field components. The magnetic

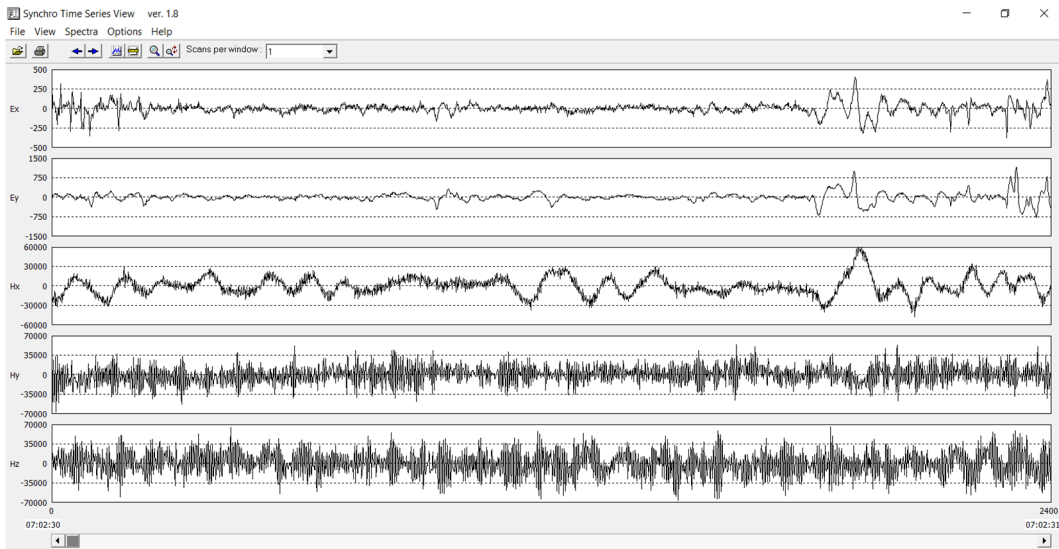


FIGURE 30: Time series plot. The electric field components  $E_x$ ,  $E_y$  and the magnetic field components  $H_x$ ,  $H_y$  and  $H_z$ , respectively

declination of the study area,  $2^\circ$ , should be provided in the STARTUP.TBL file, so that the SSMT2000 program rotates the impedance tensor elements to the geographical north-south direction. A typical example of time series data is shown in Figure 30. The measured data contain both signal and noise. One of the main purposes of data processing is to separate the signal of the measured time series, which relates the response of the earth structures from the noise both random or coherent noise.

The first step in MT data processing involves Fourier transformation from the time domain to frequency domain. The SSMT2000 program shown in Figure 31 uses the downloaded time series files, calibration

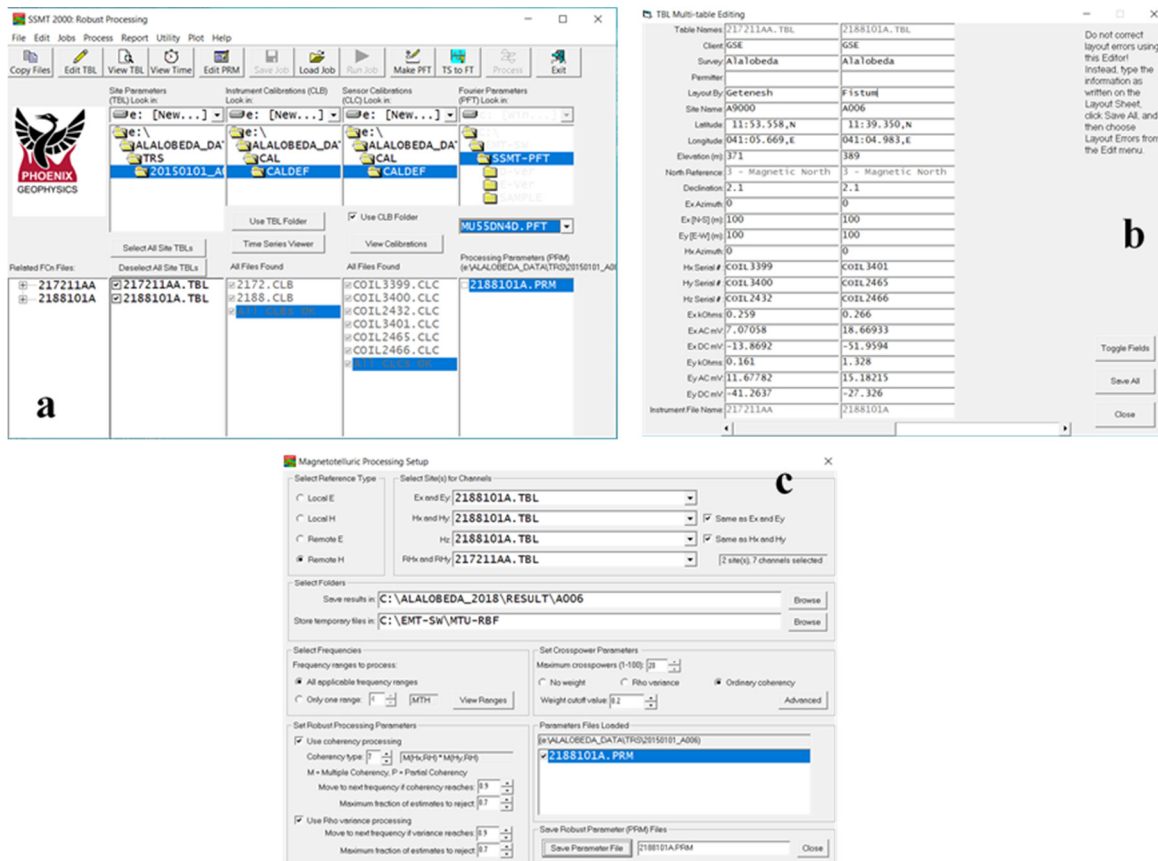


FIGURE 31: SSMT2000 processing package; (a) Main menu; (b) Field parameter file; and (c) processing setup.

Files and site parameter files as input files to produce Fourier coefficient. The processing starts with editing site parameters. Then the data are transformed from TS (time series) to FT (Fourier transform) to generate Fourier coefficients. Here we can edit the time series range, the processing parameters etc. The output files are MT plot files containing multiple cross powers for each frequency that is analysed see further discussion in Section 6.4.

### 6.3 Estimation of MT transfer function

Estimation of the impedance tensor elements has been studied and proposed by the several authors, including Swift (1967). The estimation of the impedance tensor elements is derived from the measured MT data by the use of power spectral density analysis. The impedance tensor is a 2x2 matrix tensor with the diagonal components  $Z_{xx}$  and  $Z_{yy}$  and the off diagonal components  $Z_{xy}$  and  $Z_{yx}$ , which relate the horizontal electric ( $\mathbf{E}$ ) and magnetic ( $\mathbf{H}$ ) fields at a given frequency, as shown in Equation 4.84). The electric and magnetic field spectra is given in Equations 4.85 and. 4.86, respectively.

In MT measurements the data contain noise and it is desirable to make many sets of independent measurements which allow averaging the data to reduce the effect of the noise. Least square and robust data processing methods are used to remove the noise from the data (Simpson and Bahr, 2005). To remove the coherent noise a remote reference method was used see Section 6.4.

The above impedance equations are solved by assuming that  $Z_{ij}$  are constant over an average band (window), which is physically reasonable if the bands are narrow enough. In MT, the electric fields are more affected by noise than the magnetic fields. This indicates that the estimate of impedance which contain the magnetic field is both the least biased one and the best. Therefore, in each band the cross powers are taken with  $H_x$  and  $H_y$  giving the following equations.

$$\langle E_x H_x^* \rangle(\omega) = Z_{xx} \langle H_x H_x^* \rangle(\omega) + Z_{xy} \langle H_y H_x^* \rangle(\omega) \quad (6.1)$$

$$\langle E_y H_x^* \rangle(\omega) = Z_{xy} \langle H_x H_x^* \rangle(\omega) + Z_{yy} \langle H_y H_x^* \rangle(\omega) \quad (6.2)$$

$$\langle E_x H_y^* \rangle(\omega) = Z_{xx} \langle H_x H_y^* \rangle(\omega) + Z_{xy} \langle H_y H_y^* \rangle(\omega) \quad (6.3)$$

$$\langle E_y H_y^* \rangle(\omega) = Z_{yx} \langle H_x H_y^* \rangle(\omega) + Z_{yy} \langle H_y H_y^* \rangle(\omega) \quad (6.4)$$

where,  $H_x^*(\omega)$  and  $H_y^*(\omega)$  are conjugate of the horizontal magnetic field components.

Considering Equations 6.1-6.4 and by solving two equations simultaneously, we get six possible distinct pairs of equations. Therefore, there are six ways of estimating the impedance  $Z_{ij}$  (see more details in Sims et al., 1971; and Simpson and Bahr, 2005). From the above equation we solve  $Z_{ij}$  as follows:

$$Z_{xx} = \frac{\langle E_x H_x^* \rangle \langle H_y H_y^* \rangle - \langle E_x H_y^* \rangle \langle H_y H_x^* \rangle}{\langle H_x H_x^* \rangle \langle H_y H_y^* \rangle - \langle H_x H_y^* \rangle \langle H_y H_x^* \rangle} \quad (6.5)$$

$$Z_{xy} = \frac{\langle E_x H_x^* \rangle \langle H_x H_y^* \rangle - \langle E_x H_y^* \rangle \langle H_x H_x^* \rangle}{\langle H_y H_x^* \rangle \langle H_x H_y^* \rangle - \langle H_y H_y^* \rangle \langle H_x H_x^* \rangle} \quad (6.6)$$

$$Z_{yx} = \frac{\langle E_y H_x^* \rangle \langle H_y H_y^* \rangle - \langle E_y H_y^* \rangle \langle H_y H_x^* \rangle}{\langle H_x H_x^* \rangle \langle H_y H_y^* \rangle - \langle H_x H_y^* \rangle \langle H_y H_x^* \rangle} \quad (6.7)$$

$$Z_{yy} = \frac{\langle E_y H_x^* \rangle \langle H_x H_y^* \rangle - \langle E_y H_y^* \rangle \langle H_x H_x^* \rangle}{\langle H_y H_x^* \rangle \langle H_x H_y^* \rangle - \langle H_y H_y^* \rangle \langle H_x H_x^* \rangle} \quad (6.8)$$

### 6.4 Remote reference estimate

Before using the full potential of MT data, it is necessary to remove the bias effects arising from the noise. In the remote reference method (Goubau et al., 1979; Gamble et al., 1979; Clarke et al., 1983) sensors (usually magnetic sensors) are deployed at a remote site far away from the local measurement site. The distance between the two sites can be several tens of km (10 – 100 km). The uncontaminated

part of the induced field can be coherent over several km, noise is generally random and incoherent. Therefore, by measuring the selected EM field at both local and remote sites, the bias effect arising from the presence of noise that is uncorrelated between the two sites can be removed. Remote reference methods may not be better than single station processing technique, where the noise is coherent (present at both local and remote sites) an example is removing noise generated by DC railways (Pádua et al., 2002).

Multiplying the linear relationship of the electric and magnetic field spectra of the local and remote sites of Equations 6.2 and 6.3 by the remote site component of  $R_x^*(\omega)$  and  $R_y^*(\omega)$  and averaging over frequency intervals we get the following:

$$\langle E_x R_x^* \rangle(\omega) = Z_{xx} \langle H_x R_x^* \rangle(\omega) + Z_{xy} \langle H_y R_x^* \rangle(\omega) \quad (6.9)$$

$$\langle E_y R_y^* \rangle(\omega) = Z_{yx} \langle H_x R_y^* \rangle(\omega) + Z_{yy} \langle H_y R_y^* \rangle(\omega) \quad (6.10)$$

$$\langle E_x R_y^* \rangle(\omega) = Z_{xx} \langle H_x R_y^* \rangle(\omega) + Z_{xy} \langle H_y R_y^* \rangle(\omega) \quad (6.11)$$

$$\langle E_y R_x^* \rangle(\omega) = Z_{yx} \langle H_x R_x^* \rangle(\omega) + Z_{yy} \langle H_y R_x^* \rangle(\omega) \quad (6.12)$$

Equations 6.9-6.10 can be solved for remote reference estimation of the impedance tensor elements  $Z_{ij}$  giving the following:

$$Z_{xx} = \frac{\langle E_x R_x^* \rangle \langle H_y R_y^* \rangle - \langle E_x R_y^* \rangle \langle H_y R_x^* \rangle}{\langle H_x R_x^* \rangle \langle H_y R_y^* \rangle - \langle H_x R_y^* \rangle \langle H_y R_x^* \rangle} \quad (6.13)$$

$$Z_{xy} = \frac{\langle E_x R_x^* \rangle \langle H_x R_y^* \rangle - \langle E_x R_y^* \rangle \langle H_x R_x^* \rangle}{\langle H_y R_x^* \rangle \langle H_x R_y^* \rangle - \langle H_y R_y^* \rangle \langle H_x R_x^* \rangle} \quad (6.14)$$

$$Z_{yx} = \frac{\langle E_y R_x^* \rangle \langle H_y R_y^* \rangle - \langle E_y R_y^* \rangle \langle H_y R_x^* \rangle}{\langle H_x R_x^* \rangle \langle H_y R_y^* \rangle - \langle H_x R_y^* \rangle \langle H_y R_x^* \rangle} \quad (6.15)$$

$$Z_{yy} = \frac{\langle E_y R_x^* \rangle \langle H_x R_y^* \rangle - \langle E_y R_y^* \rangle \langle H_x R_x^* \rangle}{\langle H_y R_x^* \rangle \langle H_x R_y^* \rangle - \langle H_y R_y^* \rangle \langle H_x R_x^* \rangle} \quad (6.16)$$

The remote fields  $R_x$  and  $R_y$  used in the above equations are remote magnetic fields.

In the Alalobeda field survey, one of the MTU units was used as a remote reference sounding located in Ayrobera about 20 km away from the survey area see Figure 3. The remote reference site was used during data processing to get good quality data with higher signal to noise ratio and to remove the local cultural noise from the signal. In the data processing magnetic remote reference was used, because magnetic fields exhibit greater homogeneity, less susceptible to being polarized and is less contaminated by noise than the electric field. Except MT data collected in 2013 (shown as green stars on the location map in Figure 36) almost all data collect in 2015 were processed using remote reference technique.

The Alalobeda data were Fourier transformed to achieve band average cross powers and auto powers which were calculated using a robust processing method in SSMT2000 program. MT-editor is a program which takes the output from SSMT2000 as input (MT plot files). The program displays the resistivity and phase curves and individual cross powers that were used to calculate each point on the curve on Figure 32. The cross powers displayed depend on our choice of 20 or 40 segments that we selected when we ran the SSMT2000 program. Then the cross powers which are mostly affected by noise were masked from the calculations automatically or manually in order to increase the coherency for both apparent phase and resistivity. This program also allows to display different plot files, for example, coherency, Tipper magnitude, impedance and strike direction. After editing and a reasonably smooth curve is achieved of the final cross powers and auto powers, and all relevant MT parameters calculated from them (impedance, resistivity and phase) which are saved as Electrical Data Interchange (EDI) files. Those EDI files are suitable for other geophysical interpretation softwares for example, the Linux based TEMTD, WinGLink and ready for interpretation.

The output files from MTeditor (EDI files) were converted from DOS to Unix format. Then a Linux script called spect2edi developed at ISOR is run which calculates several MT parameters (which are not calculated in MTeditor) and produces the result in standard EDI format which is ready for inversion. An

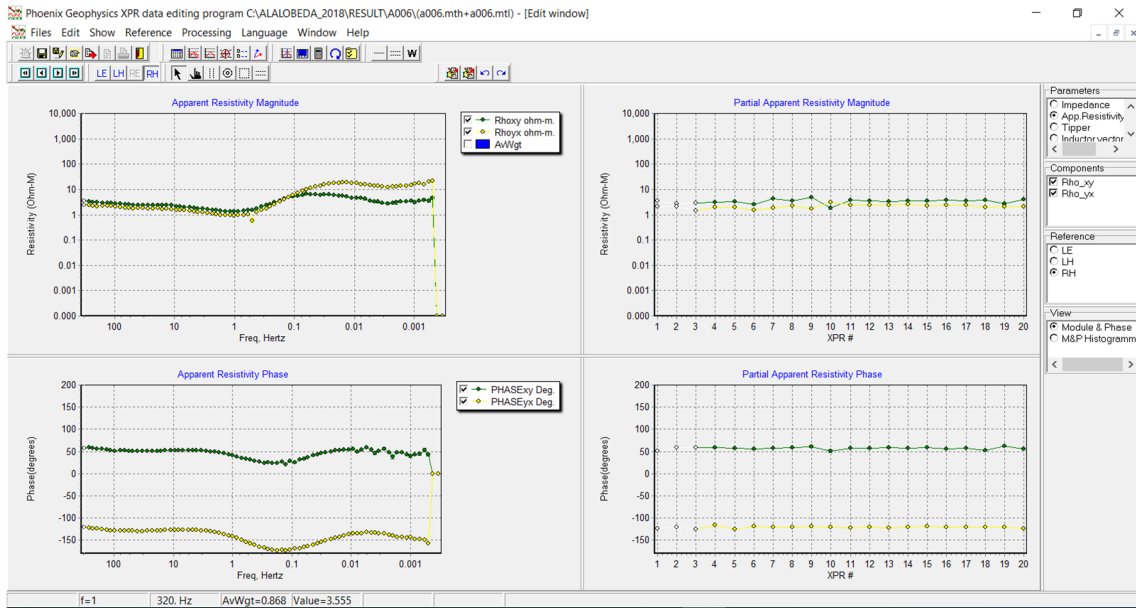


FIGURE 32: MTeditor; Left: Apparent resistivity and phase curves for all frequencies (processed by remote H); and Right: Apparent resistivity and phase for 320 Hz and the 20 segments, white points are masked data points

example of processed MT apparent resistivity and phase curves from Alalobeda geothermal prospect is given in Figure 33, the curves split apart indicating non one-dimensionality of the data.

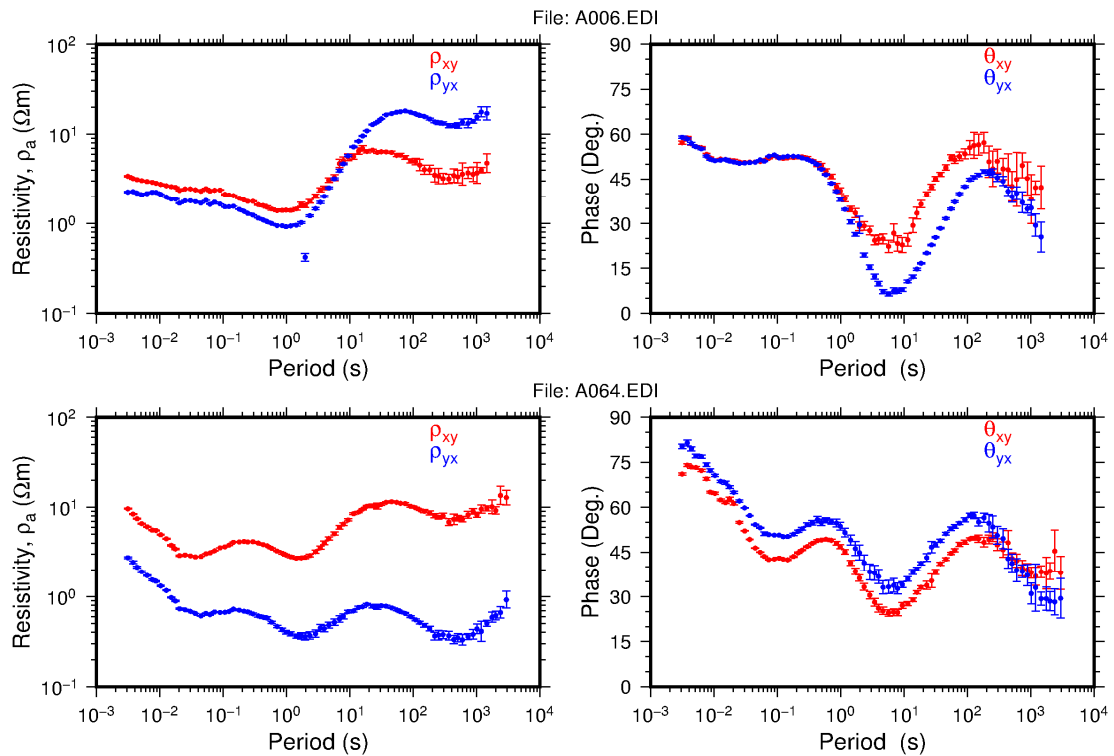


FIGURE 33: An example of processed MT data from Alalobeda prospect area for two soundings, A006 and A064. The apparent resistivity and phase derived from xy (red) and yx (blue) components of the impedance tensor

## 7. TEM METHOD

### 7.1 General concepts

The Transient ElectroMagnetic (TEM) method is an active EM method, where a time varying magnetic field is generated by a controlled artificial source. In recent years the TEM method has become more popular as a complimentary tool to the MT method for investigating the deep structures of the subsurface, especially in volcanic environment.

A loop of wire is laid on the ground and a constant magnetic field of known strength is built up by transmitting a constant current into the loop, see Figure 34. The current in the source loop is abruptly turned off, see Figure 35a. Then the induced current is left without its source and responds by inducing an image of the source loop in the subsurface. This induced current dies out and generates a new secondary magnetic field that varies with time and as a result induces new electrical currents at greater depth in the ground. This new current diffuses downwards and outwards into the ground and generates a secondary magnetic field decaying with time. The decay rate of the secondary magnetic field as a function of time is monitored by measuring the voltage induced in a receiver coil at the centre of the transmitter loop, see Figure 35c. The decay rate of the secondary magnetic field and the current distribution depends on the resistivity structure of the Earth. The decay rate, recorded as a function of time after the current in the transmitter loop is turned off can, therefore, be interpreted in terms of the subsurface resistivity structure (Árnason, 1989; Flóvenz et al., 2012).

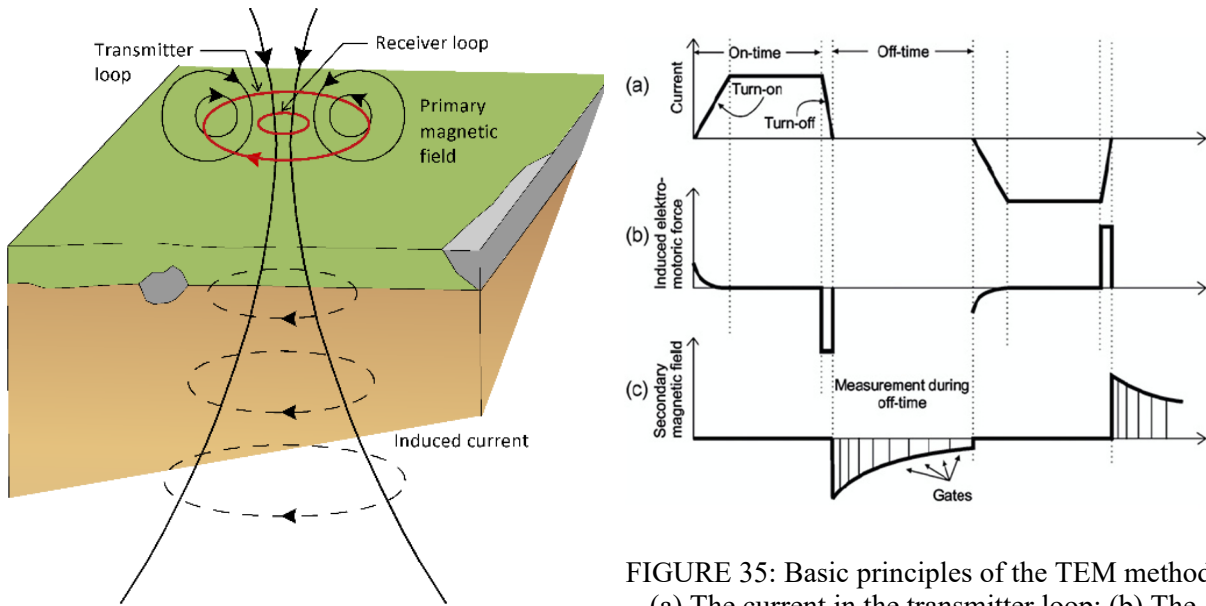


FIGURE 34: The central loop TEM sounding configuration (Flóvenz et al., 2012; based on Hersir and Björnsson, 1991)

FIGURE 35: Basic principles of the TEM method; (a) The current in the transmitter loop; (b) The induced electromotive force in the ground; and (c) Secondary magnetic field measured in the receiver coil (Christensen et al., 2006).

The transmitter and the receiver can be synchronized either by connecting them with a reference cable or synchronized by a high precision crystal clocks, so that the receiver knows when the transmitter will turn off the current (Lichoro, 2013). The depth of penetration of the TEM method depends mainly on the transmitted current, the cross-sectional area of the receiver coil, area of the transmitter loop and the subsurface resistivity.

At late time the induced voltage in the receiver coil in a homogeneous half space of conductivity  $\sigma$  is given by (Árnason, 1989):

$$V(t) = I_o \frac{C(\mu\sigma r^2)^{3/2}}{10\pi^{1/2}t^{5/2}} \quad (7.1)$$

where  $C = A_r n_r A_s n_s \frac{\mu_o}{2\pi r^3}$ ; and

$A_r$	= Cross-sectional area of the receiver coil (m <sup>2</sup> );
$n_r$	= Number of turns in receiver loop;
$A_s$	= Area of transmitter loop (m <sup>2</sup> );
$n_s$	= Number of turns in transmitter loop;
$t$	= Time elapsed after the current in the transmitter is turned off (s);
$\mu$	= Magnetic permeability (H/m);
$V(t)$	= Transient voltage (V);
$r$	= Radius of the transmitter loop (m);
$I_o$	= Current in the transmitter loop (A).

Rearranging Equation 7.1 and substituting  $\sigma = 1/\rho$  gives the late time apparent resistivity  $\rho_a$ , as a function of time after the current in the transmitter is turned off:

$$\rho_a = \frac{\mu}{4\pi} \left[ \frac{2\mu I_o A_r n_r A_s n_s}{5t^2 V(t)} \right]^{2/3} \quad (7.2)$$

## 7.2 TEM instrumentation and field measurements

In the Alalobeda geothermal prospect, the central loop TEM method was used to acquire a total of 124 soundings in the 2015 field campaign. For this study only 106 TEM soundings were used, see the location in Figure 36, in next section. The TEM soundings were acquired using two different instruments from different manufacturing companies, Zonge GDP-32 and Phoenix V8 TEM systems. Both instruments consist of a transmitter, receiver coil with effective area of 10000 m<sup>2</sup> (placed at the centre of the transmitter loop), transmitter loop, connecting cables, transmitter controller and power source. In most cases the measurement was made using a 200 m x 200 m square transmitter loop and in some difficult terrain a 100 m x 100 m square loop. For Zonge TEM, the transmitter controller high precision crystals were on for about an hour or so before data acquisition started to synchronize. This was to ensure that the induced voltage is measured by the receiver at the right time after the current turn-off. Whereas, for the Phoenix V8 TEM, the synchronization was achieved by a radio link between the transmitter and the V8 receiver, the synchronization takes a few minutes. For both instruments the measurement was made at different frequencies allowed by the instruments. Zonge used: 16, 8, 2 and 1 Hz frequency corresponding to last time gate of 12, 25, 98 and 197 ms, respectively. Phoenix used: 25, 5 and 1 Hz frequency corresponding to last time gate of 7, 42 and 212 ms, respectively. The transmitted current was usually in the range of 9-22 Ampere. For both TEM instruments the transmitted signal is recorded by the receiver which is at the centre of the transmitter loop at time intervals logarithmically spaced at sampling time gates after the current is turned-off. Time series stacking was always done in order to improve the signal to noise ratio, thus acquiring good quality data at least up to 70 ms. The recorded data at the receiver memory were later transferred to computer for further data processing.

## 7.3 TEM data processing

The Processing of the raw TEM data was done using the TemX software (developed at Iceland GeoSurvey (ISOR)) which reads and processes central loop TEM sounding data and produce data files ready for interpretation (Árnason, 2006a). Here, two versions of TemX were used. The TEM raw data from Zonge GDP-32 were processed using temZn, whereas the raw data from Phoenix V8 were processed using temxUSF. These two codes only differ by the routine that reads the data but data processing and the interface are the same. This program has a graphical interface which allows the user to edit or reject noisy outliers. It also calculates average of repeated transient voltage measurements and calculates the late time apparent resistivity as a function of time after current turn-off. In this study we used the output file \*.inv from TemX program directly for the joint inversion TEMTD program without calculating separate model for TEM.

## **8. MULTI-DIMENSIONAL INVERSION OF EM DATA FROM THE ALALOBEDA GEOTHERMAL PROSPECT**

### **8.1 1D inversion**

Inversion is used to evaluate the model parameters through the measured data. Here, 1D Occam inversion was done using a program called TEMTD (Árnason, 2006b). This program performs 1D inversion of MT and TEM data separately or jointly. The program can perform both standard layered inversion (inverting resistivity values and layer thicknesses) and Occam (minimum structure) inversion with constant exponentially increasing layer thicknesses with depth. It offers a user specified damping of first order (sharp steps) and second order derivatives (oscillations) of model parameters (logarithm of resistivity and layer thicknesses) (Árnason, 2006b; Árnason et al., 2010).

The TEMTD program solves forward and inverse problems. Forward modelling is a process of predicting data based on some physical or mathematical model with a given set of model parameters. Forward modelling is an important part of the inversion method, because the inversion process uses forward modelling to compute the sensitivity matrix and the response for calculating the misfit. The inversion algorithm used in the TEMTD program is the non-linear least-square inversion of the Levenberg-Marquardt type (Levenberg, 1944; Marquardt, 1963). The misfit function is the mean-square difference between measured and calculated values, chi-square ( $\chi^2$ ), weighted by the standard deviation of the measured values.

### **8.2 Joint 1D inversion of MT and TEM soundings**

In this study, a joint 1D Occam inversion was performed using the apparent resistivity and phase of 108 MT soundings derived from the rotationally invariant determinant of the impedance tensor and the associated TEM sounding data, see Figure 36. The determinant data are preferred to provide a good overview of the subsurface resistivity distribution because it is rotationally invariant regardless of the true dimensionality of the MT data. The TEMTD program determines the best shift parameter of the MT data, see Figure 37. An example of joint 1D inversion of MT and TEM data is given in Figure 37. The best estimate of the shift parameter for this particular example is  $S=0.929$ . The MT apparent resistivity has to be divided by 0.929 (shift multiplier) so that both the TEM and MT data could be fitted with the same 1D model shown to the right on Figure 37. A complete set of all the 1D joint inversion results is given in Appendix I. Figure 36 shows the location of all MT and TEM soundings from the Alalobeda geothermal prospect.

### **8.3 Static shift correction**

To overcome the static shift problem of MT data, the TEM data from the same location or at least within a few tens of meter were used as a remedy for the static shift correction. A histogram of all the static shift parameters is given in Figure 38a. The parameters are mostly in the range of 0.1-2. Figure 38b shows the spatial distribution of the static shift parameter of the prospect. From the map we can see that the apparent resistivity is shifted upwards in most of the area and downwards in some of the area. A small part of the area has not been affected by the static shift as indicated in Figure 38b.

As mentioned before the MT curve is shifted up or down due to near surface in-homogeneities or topographic effect. As an example, results from station A102 is shown in Figure 39. To the left on Figure 39, the MT curve is shifted down and the resistivity model gives wrong resistivity structure; it indicates too shallow depth and too low resistivity, for example that the first conductive layer is at a depth of about 0.04 km and the resistivity is 0.3  $\Omega\text{m}$  and to the right on Figure 39, shows after the static shift correction that the layer is at a depth of 0.08 km and the resistivity is 2  $\Omega\text{m}$ .

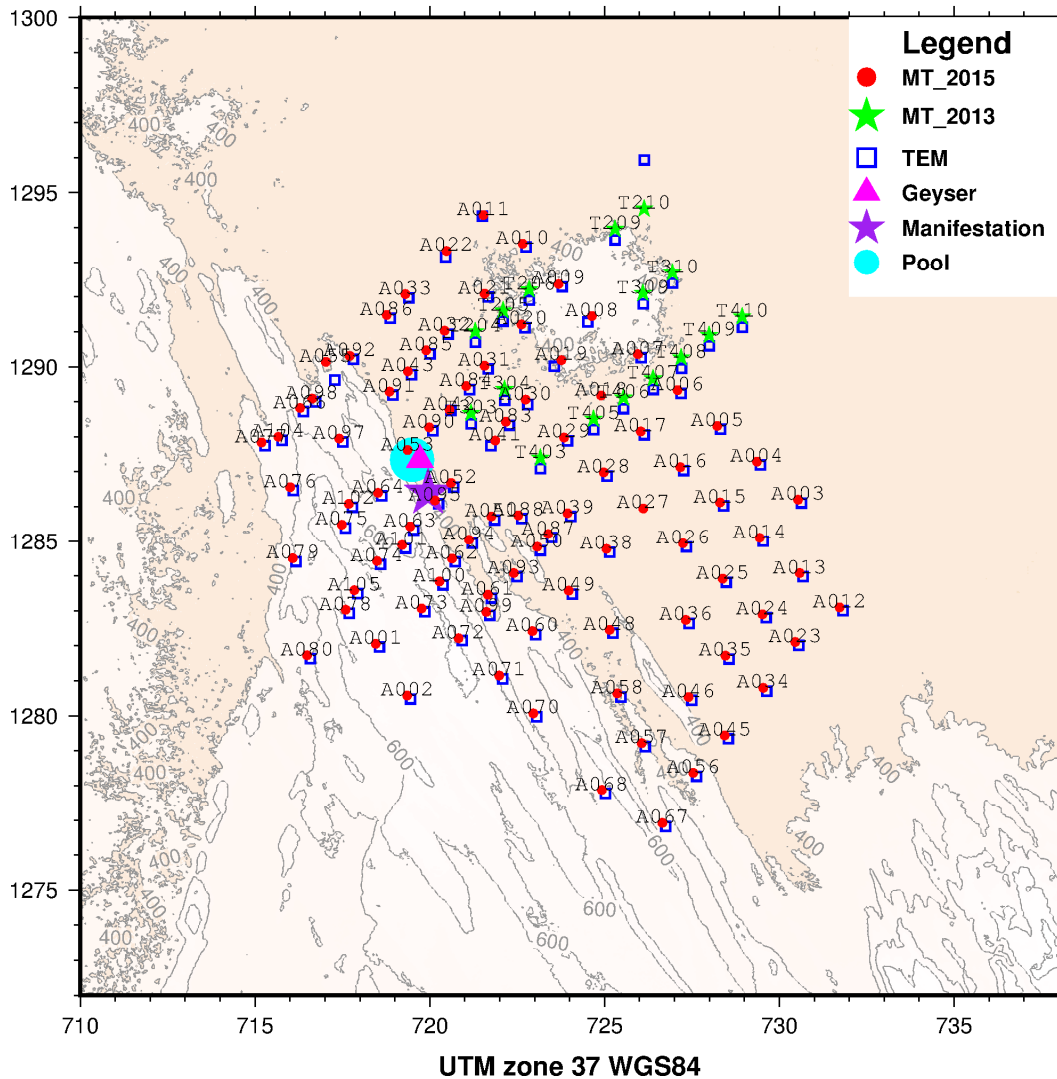


FIGURE 36: Location map of MT and TEM soundings from the Alalobeda prospect

## 8.4 Results and interpretations of the joint 1D inversion

### 8.4.1 Resistivity cross-sections

The TEMCROSS program (Eysteinnsson, 1998) was used to plot resistivity cross-sections based on the results obtained from the joint 1D Occam inversion models of MT and TEM data. Several cross-sections were plotted through the survey area, eleven cross-sections were located perpendicular to the tectonic structure (SW-NE direction) (PT\_01 – PT\_11), while the other seven cross-sections are parallel (SE-NW direction) to it (PL\_01 – PL\_07). The cross-sections are drawn down to a depth of 2000 and 8000 m b.s.l. Their locations are shown in Figure 40. Here below, two cross-sections are discussed, PL\_03 and PT\_04. Additional cross-sections are given in Appendix II. When we relate the observed resistivity structure (i.e. low resistivity related to the sediment whereas high resistivity is related to the Afar stratoid Series), it is based on the stratigraphy and geological formation which is confirmed by the drilled wells in Dubti see Figure 6. We are expecting almost similar geological formation in Alalobeda. The surface geology done by ELC (ELC, 2015a) shows the geological formation.

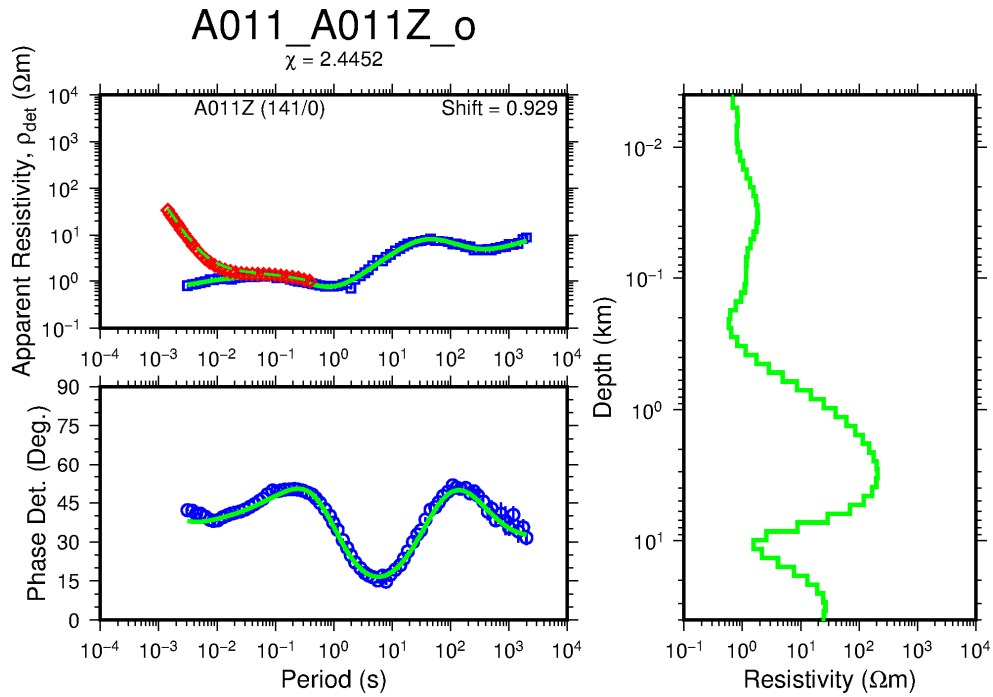


FIGURE 37: Result of joint 1D inversion of an MT and TEM sounding, station A011. TEM apparent resistivity (red diamond) transformed to a pseudo-MT curve, blue square and circle are measured apparent resistivity and phase, respectively, derived from the determinant of the impedance tensor; vertical blue lines are error bars. Green lines show the response of the model calculation; the right panel shows the 1D resistivity model while the left panel its synthetic MT apparent resistivity and phase response in green. Number in parenthesis (141/0) indicates the two stations (MT/TEM) were 141 m apart and the elevation difference zero. A011, on top of figure, shows name of MT station and A011Z name of TEM station. Static shift correction was 0.929

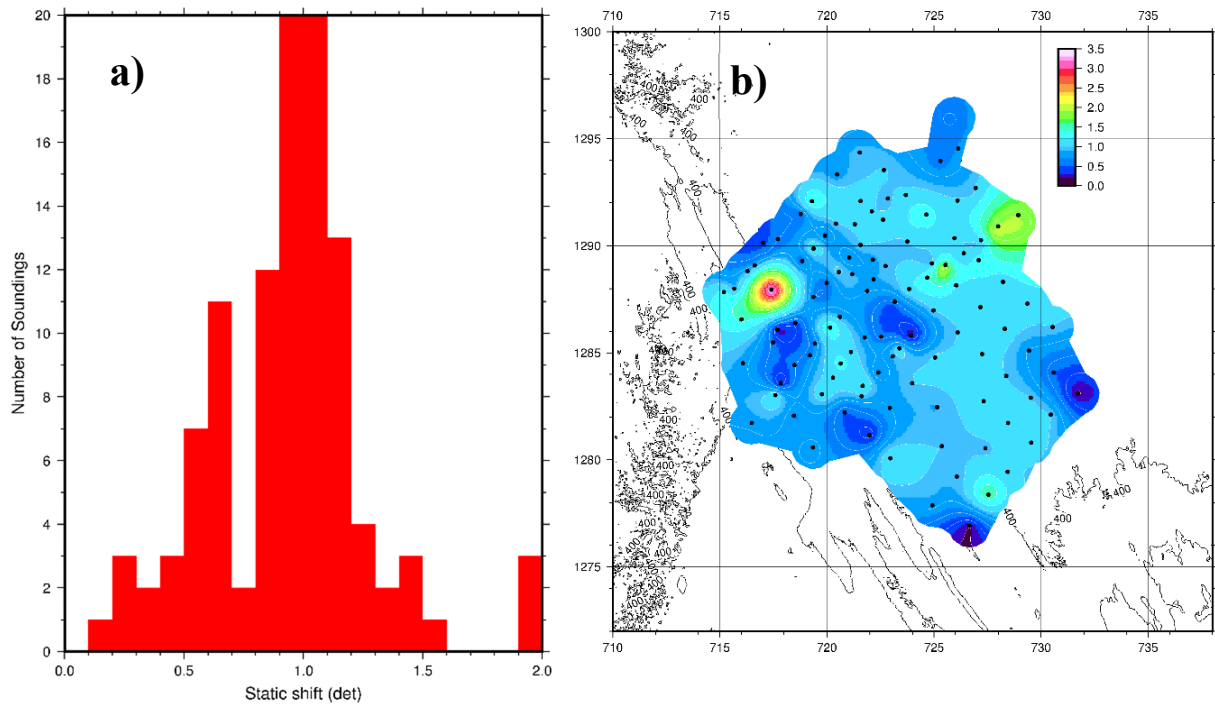


FIGURE 38: a) Histogram of the static shift parameters; and b) Spatial distribution of static shift multipliers in the Alalobeda prospect

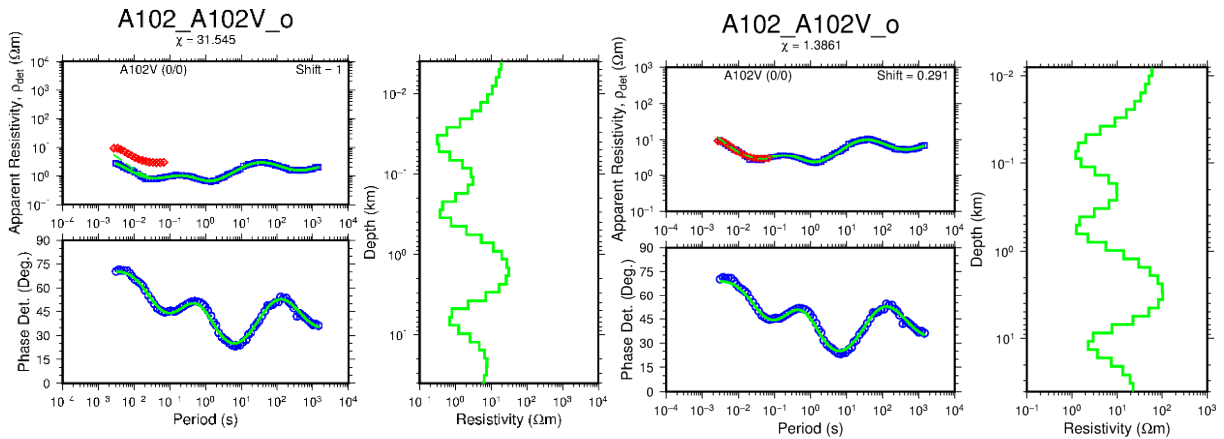


FIGURE 39: An example of static shift correction of MT data from Alalobeda prospect. Left: MT data before static shift correction; Right: Data after static shift correction; for legend see Figure 37

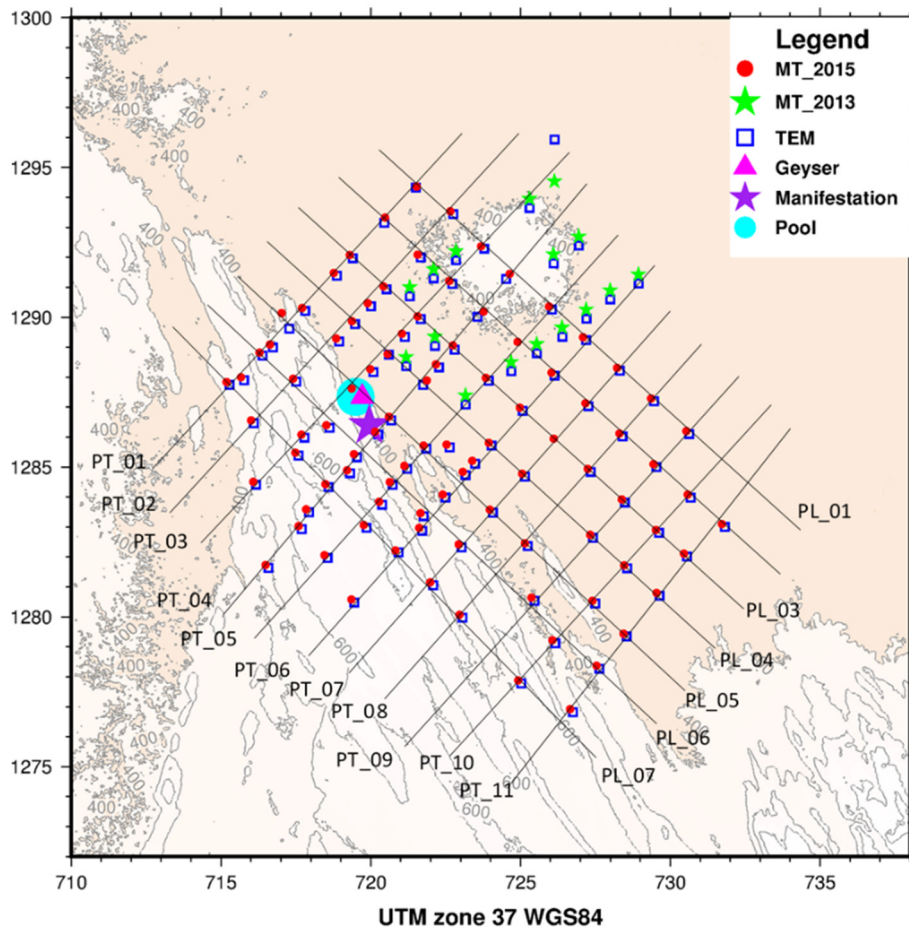


FIGURE 40: Location of resistivity cross-sections based on the 1D model

*Resistivity cross-section PL\_03* is shown in Figure 41. It runs NW-SE parallel to the main geological structure. The resistivity profile is shown for two different depth. This cross-section is characterized by a low resistivity anomaly,  $< 10 \Omega\text{m}$ , down to a depth of approximately 200 m b.s.l., which is associated with shallow sedimentary formation and/or low temperature alteration. Below the low resistivity a high-resistivity layer is found with resistivity values around  $100 \Omega\text{m}$  down to depths varying between 750 and 5500 m from the surface. The high resistivity could be related to the resistive Afar Stratoid basalt Series see Figure 6 the geological stratigraphy of wells from Dubti. At greater depth the resistivity decreases again to  $< 10 \Omega\text{m}$ , indicating the deeper lying conductor that could be related to the geothermal heat source.

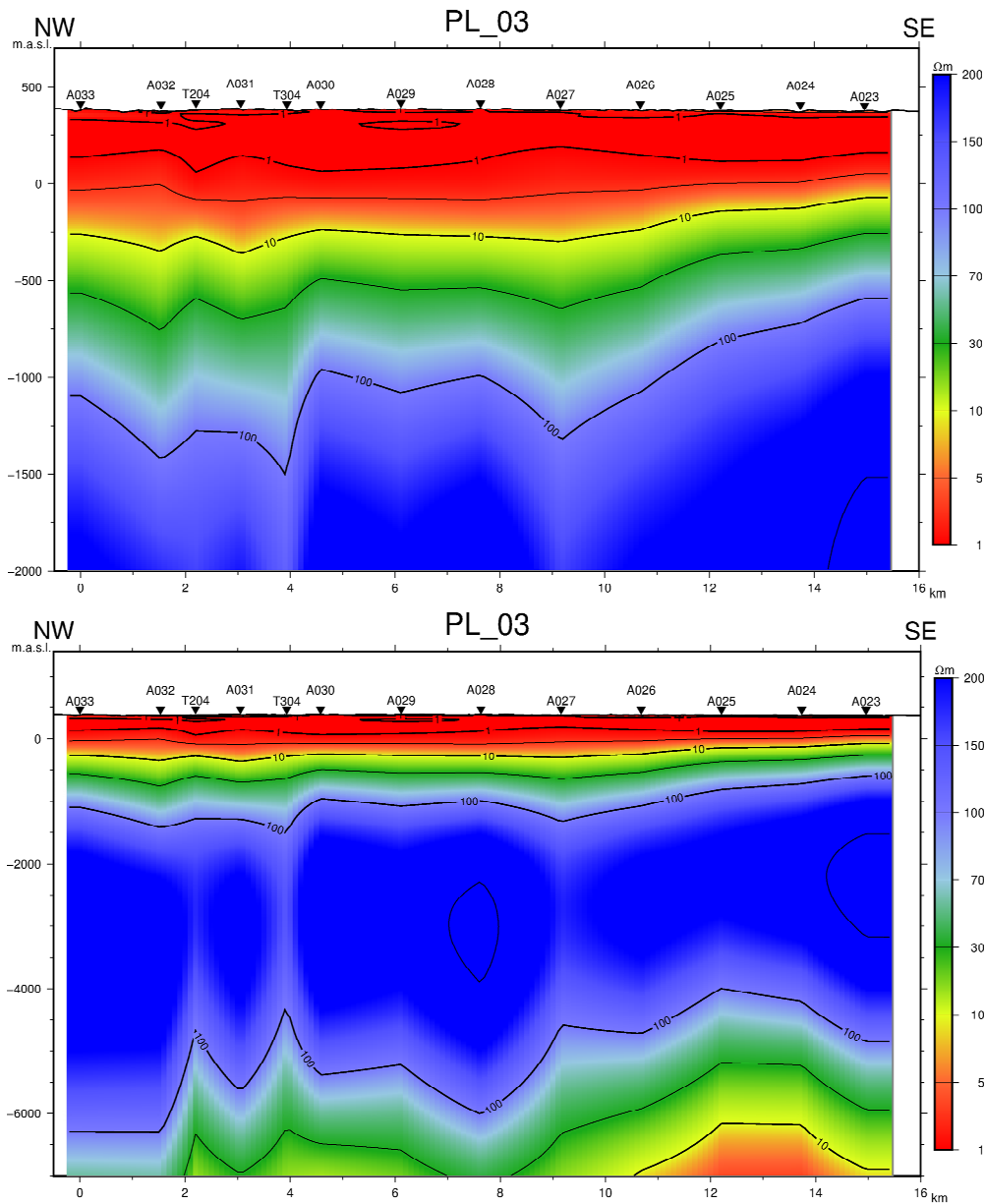


FIGURE 41: Resistivity cross-section PL-03 for two different depth ranges obtained from joint 1D Occam inversion of TEM and MT data, for location see Figure 40

*Resistivity cross-section PT\_04* is shown in Figure 42. It runs NW-SE parallel to the main geological structure. The resistivity profile is shown for two different depths. This cross-section is characterized by a thin layer of a very low resistivity anomaly,  $< 10 \Omega\text{m}$ , down to a depth of approximately 500 m b.s.l. associated with the shallow sedimentary formation and/or low temperature alteration. Below the low resistivity, a high-resistivity layer is found with resistivity values around  $100 \Omega\text{m}$  and even more down to depths varying between 1200 and 5000 m from the surface. The high resistivity could be related to the high-resistive Afar Stratoid basalt Series. The resistivity structure around stations A041, A083 and A105 may indicate the up flow zone in that area. As mentioned before, the high resistivity is believed to correlate to the Afar Stratoid basalt Series as mentioned before from the stratigraphy of the Dubti well the depth to the Afar Stratoid basalt Series is 1000 m to 1200 m, but possibly also influenced by high-temperature alteration minerals like chlorite and epidote. But here the depth to the Afar Stratoid basalt Series is varying 1000 m to 1400 m. At greater depth the resistivity decreases again to  $< 10 \Omega\text{m}$ , indicating the deeper lying conductor that could be related to the geothermal heat source. This low resistivity zone is found below all stations except stations A080 and A095 which show very high resistivity down to great depth. These resistivity discontinuities may indicate some geological structures (fault or lineaments). These structures were also confirmed from the 3D inversion of gravity data (for more details, see ELC's gravimetric report (ELC, 2015c)).

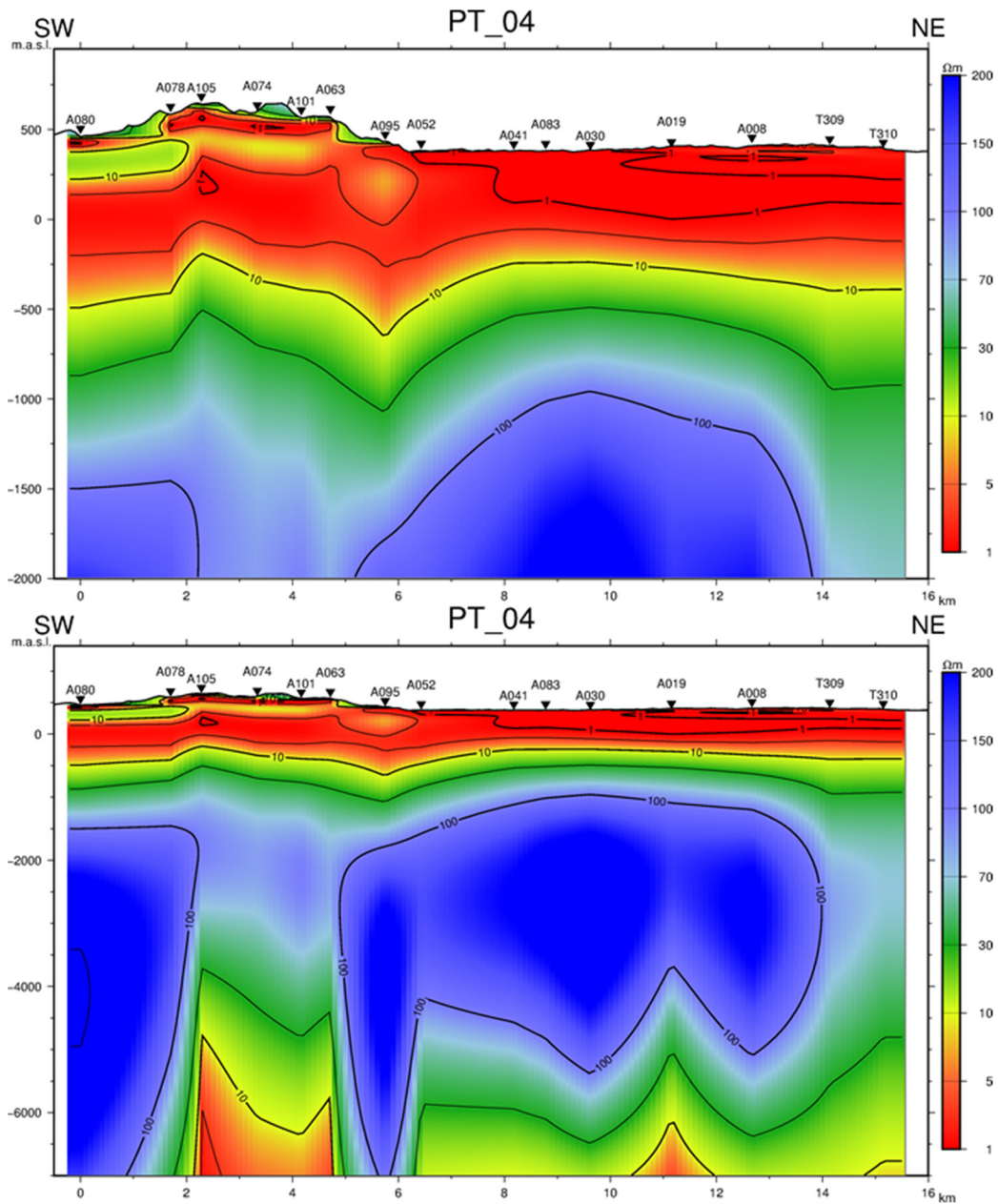


FIGURE 42: Resistivity cross-section PT-04 for two different depth ranges obtained from joint 1D Occam inversion of TEM and MT data, for location see Figure 40

#### 8.4.2 Resistivity depth-slices

The TEMRESD program (Eysteinnsson, 1998) was used to generate resistivity depth-slices based on the results obtained from the joint 1D Occam inversion of MT and TEM data. The depth-slices show the resistivity distribution of the area at different elevations. The elevation of the Alalobeda geothermal field varies from 200 to 800 m a.s.l. Here, four resistivity depth-slices are presented at 300 m a.s.l.; 200, 600 and 8000 m b.s.l. Additional maps are given in Appendix III.

*Resistivity at 300 m a.s.l.* is shown on Figure 43. Predominantly low resistivity covers the entire survey area. The resistivity is very low ( $< 10 \Omega\text{m}$ ) for most of the area and reflects the sedimentary formation found at shallow levels in the area and in some cases eventually low-temperature alteration minerals like smectite; to the south and west of the survey area the resistivity is about  $10 \Omega\text{m}$ .

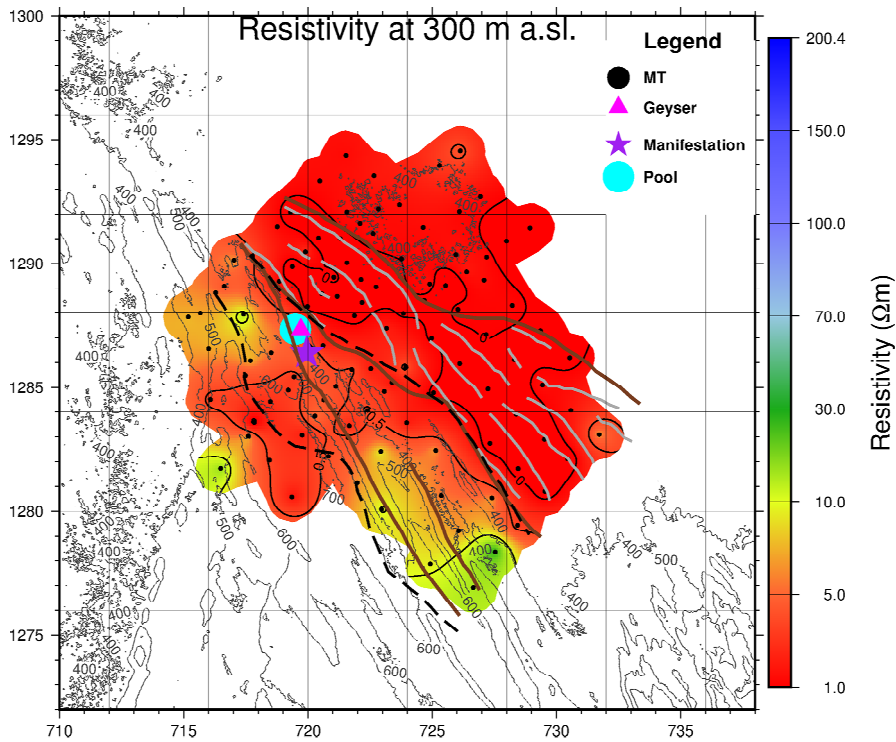


FIGURE 43: Resistivity depth-slice at 300 m a.s.l. based on 1D Occam inversion; gray lines indicate faults, white lines are lineaments inferred from gravity and broken black lines show the gravity low anomaly border (ELC, 2015c)

*Resistivity at 200 m b.s.l.* is shown in Figure 44. The high resistivity associated with the less permeable Afar Stratoid basalt Series covers most of the survey area at this depth with resistivity 10 to 30  $\Omega\text{m}$ . A low resistivity ( $< 10 \Omega\text{m}$ ) is seen along the geological NW-SE structure and farther to the northern part of the survey area. This might be correlated with lateral flow of geothermal fluids, fractures or low-temperature alteration minerals like smectite but the low resistivity which is far to the north might reflect sedimentary formation.

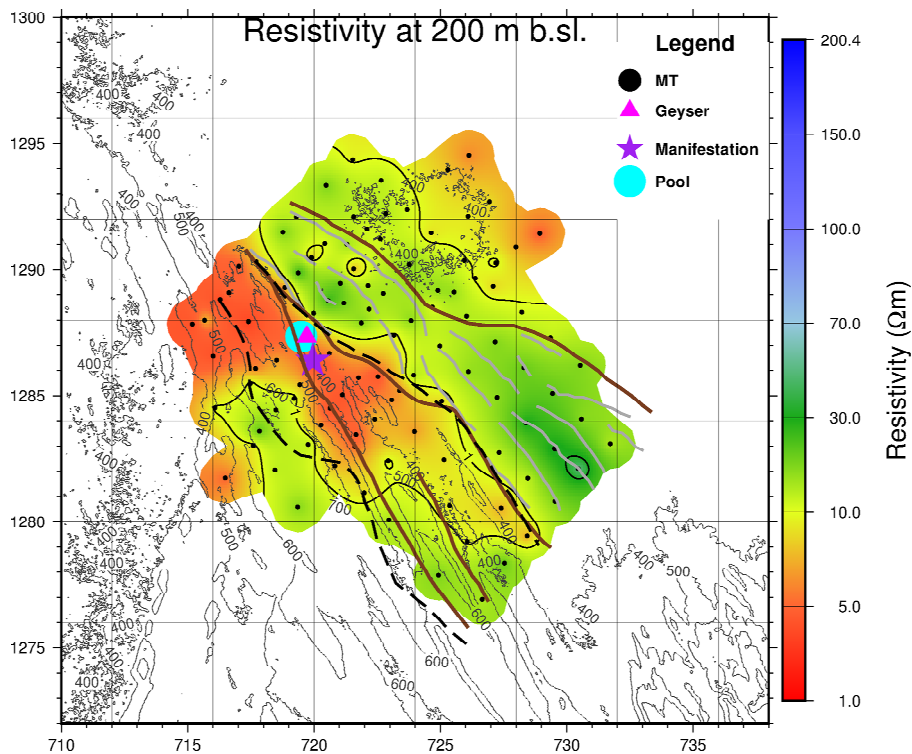


FIGURE 44: Resistivity depth-slice at 200 m b.s.l. based on 1D Occam inversion, for legend, see Figure 43.

*Resistivity at 600 m b.s.l.* is shown in Figure 45. The high resistivity associated with the less permeable Afar Stratoid basalt Series covers most of the survey area at this depth with resistivity about 30  $\Omega\text{m}$ . The resistivity is higher in the northern part of the surface manifestations and southeast of the survey area with the resistivity of around 100  $\Omega\text{m}$ . The low resistivity around 10  $\Omega\text{m}$  is seen along the geological NW-SE structure. This might be correlated with lateral flow of geothermal fluids, fractures or low-temperature alteration minerals like smectite.

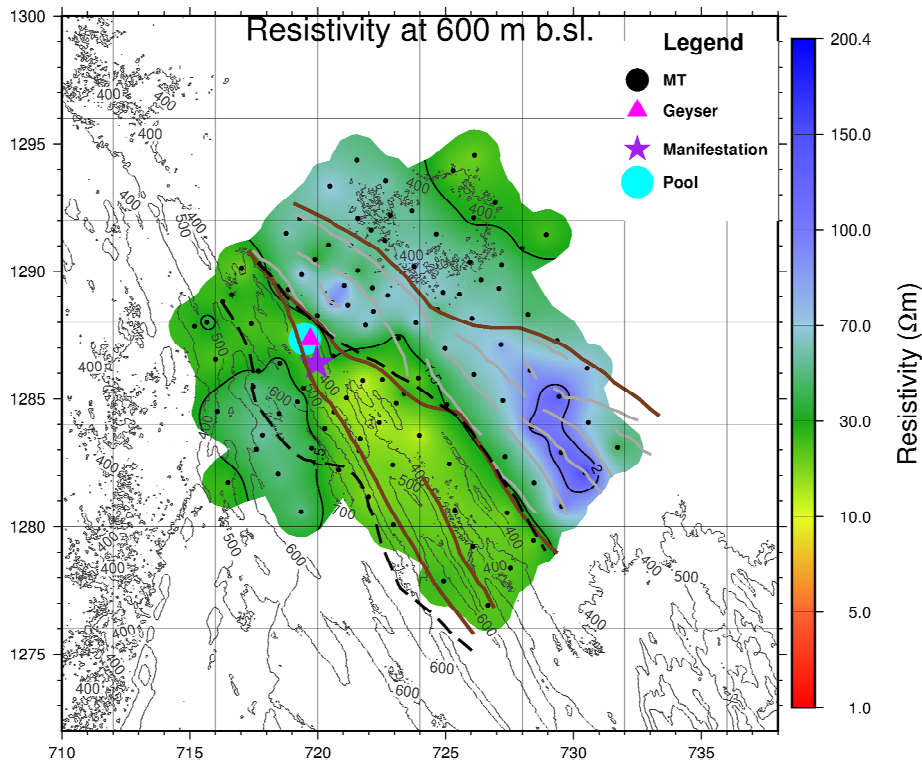


FIGURE 45: Resistivity depth-slice at 600 m b.s.l. based on 1D Occam inversion, for legend see Figure 43

*Resistivity at 5000 m b.s.l.* is shown in Figure 46. Here, the deep lying low-resistivity zone is clearly manifested, with an average resistivity of approximately 5  $\Omega\text{m}$ . It is not clear what the deep lying conductor indicates, but it may be related to the heat source or deep saline sediments. Interestingly, a resistivity anomaly can be seen along the main geological structure trending NW-SE with slightly higher resistivity (100  $\Omega\text{m}$ ), supporting geothermal activities along these structures. To the south and southeast the resistivity is higher than 100  $\Omega\text{m}$ . This will be discussed later with the results of the 3D models.

## 8.5 Geo-electrical strike analysis

The electrical strike direction can be found by strike analysis of the MT data. The electrical strike analysis of MT data gives information on the dimensionality of rock formation and it also indicates the directions of resistivity contrasts; which can be used to infer geological features not seen on the surface. The MT impedance tensor components depend on the orientation of the x- and y-direction of the MT field layout. For 2D Earth the resistivity varies with depth and in one of the two principal horizontal directions. The horizontal angle perpendicular to that direction is called the geo-electrical strike and the angle it makes with the geographic north is called Z-strike. In strike analysis the coordinate system can be rotated in proper direction and the components of the impedance tensor for any desired directions recalculated. The strike analysis is carried out by maximizing the off-diagonal MT impedance tensor components  $|Z_{xy}|^2 + |Z_{yx}|^2$  or by minimizing the diagonal components  $|Z_{xx}|^2 + |Z_{yy}|^2$  with respect to the rotation of the coordinate system.

However, the Z-strike has a 90° ambiguity as determined this way, where the diagonal components of the MT impedance tensor are minimized as if either the x- or y-axis is along the electrical strike. There

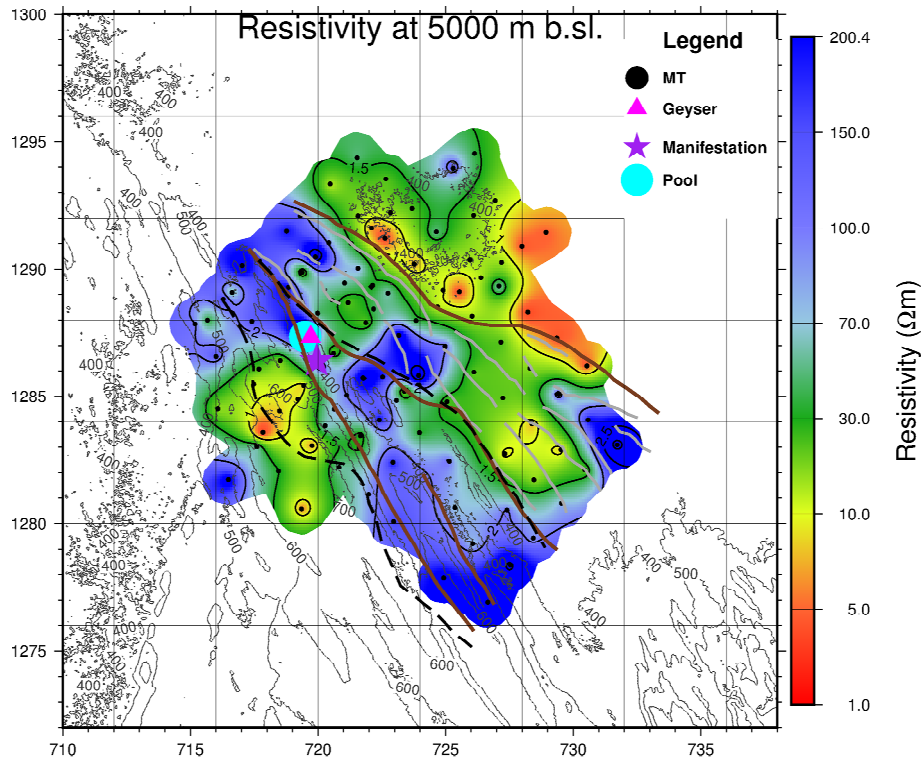


FIGURE 46: Resistivity depth-slice at 5000 m b.s.l. based on 1D Occam inversion, for legend see Figure 43

is no way to distinguishing between  $\theta$  and  $\theta+90^\circ$ , from the tensor alone. In order to overcome this problem, we use the Tipper strike analysis which use the vertical magnetic field component.

### 8.5.1 Tipper Strike

As mentioned before the Z-strike has a  $90^\circ$  ambiguity and the strike direction can't be determined using MT impedance data alone. This  $90^\circ$  ambiguity problem can be overcome by using information from the Tipper vector if the vertical magnetic field ( $H_z$ ) is available. Moreover, geological information might also help to overcome this ambiguity.

The Tipper relates the vertical component of the magnetic field to its horizontal components (see Equation 4.87)). The Tipper strike is shown for two different depth as shown in Figures 47 and 48. Figure 47 show the Tipper strike for 0.1-1 s, corresponding to a depth of several hundred meters: we can see that at high frequencies the strike direction is poorly defined due to local resistivity variations at each site,

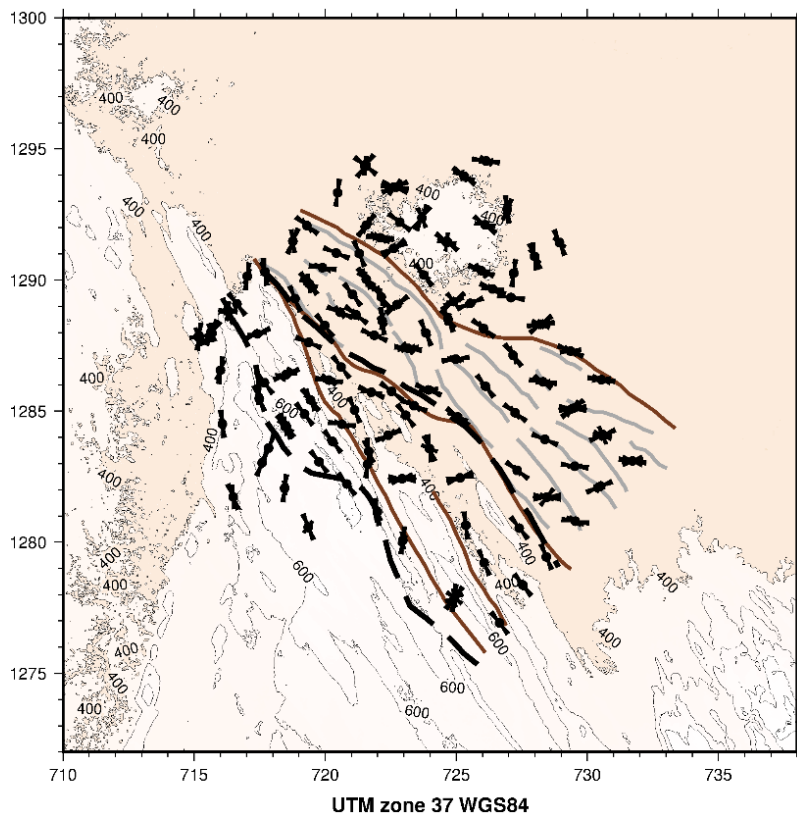


FIGURE 47: Tipper strike for 0.1-10 s, for legend see Figure 43.

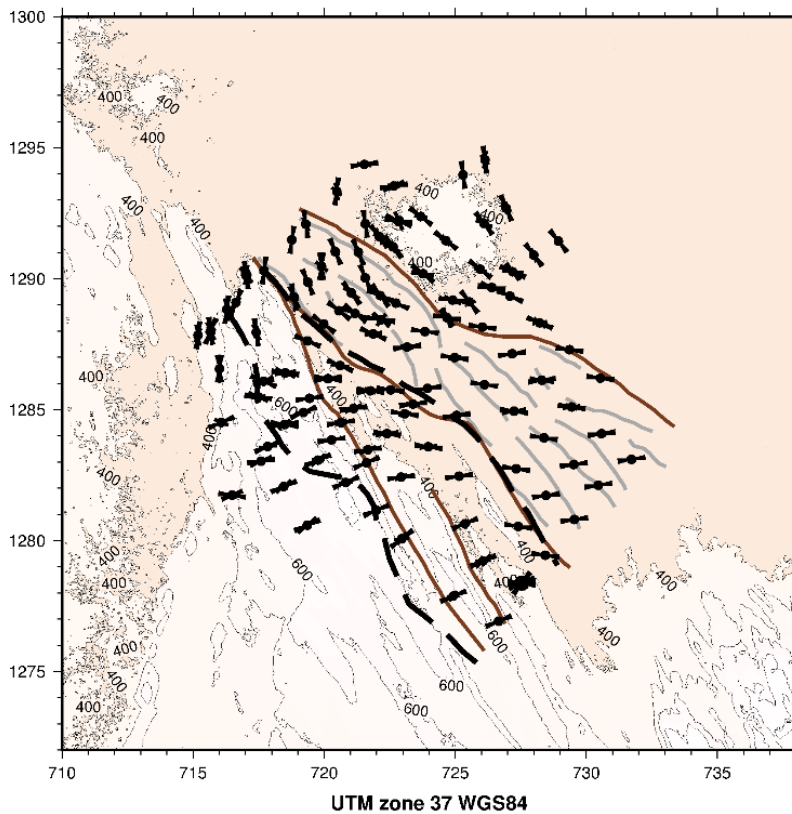


FIGURE 48: Tipper strike for 10-100 s, for legend see Figure 43.

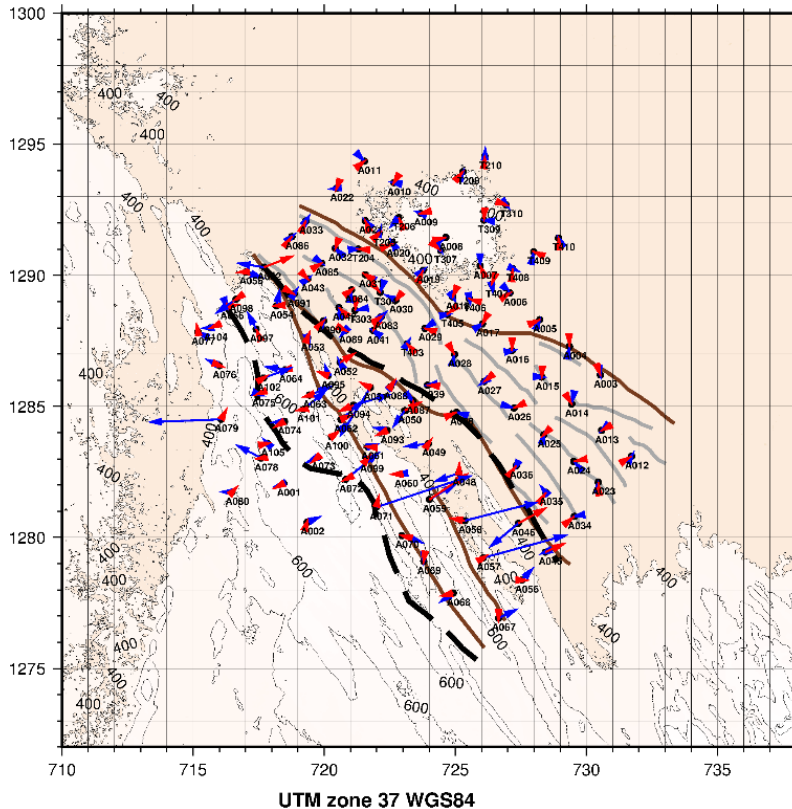


FIGURE 49: Induction arrows for 0.03 s, corresponding to a depth of a few hundred m; blue arrows denote the real part and red arrows the imaginary part, for legend see Figure 43.

but still for these periods the strike direction is in good agreement with the geological strike direction and geological features and lineaments. Figure 48 shows the Tipper strike from 10-100 s, corresponding to a depth of several km: at long periods the Tipper strike direction at each MT station is in good agreement with the geological features and lineaments as inferred by the gravity survey. We can clearly see resistivity discontinuities.

### 8.5.2 Induction arrows

Induction arrows are vector representations derived from complex Tipper (real and imaginary parts). Induction arrows are independent of the MT impedance tensor, so they can provide valuable constraints on the dimensionality and strike analysis of the data. Induction arrows are a convenient way to present the vertical magnetic fields response which is generated by lateral conductivity variation. In other words, induction arrows are used to infer the presence or absence of lateral conductivity variations. There are two conventions for the induction arrows which are: 1) The Parkinson convention, the real part of the vector points towards the low resistivity (Parkinson, 1959). 2) The Wiese convention, in this case the real part points away from the low resistivity (Wiese, 1962). In this work, induction arrows are presented in the Wiese convention, in which the real part points away from the low resistivity. The induction arrows are more affected by local features at shorter periods whereas at longer period it is affected by deep structures. Figure 49 and Figure 50 show induction arrows for two different periods 0.03 s and 30 s, respectively from the Alalobeda

data set. From Figure 49 we can see the real arrows (in blue) point away from the conductive body which is clearly seen from the surface geological structure and also these structures and lineaments are identified by gravity data. At longer periods (Figure 50), we observe large and oblique pointing away from the NE-SW faults or geological lineaments. The largest real arrows with opposite orientation appears along the transition from conductive to resistive body.

### 8.6 Conclusion from the 1D joint inversion

Based on the results of the 1D joint inversion of 108 MT and TEM soundings, the resistivity structure generally reveals three main resistivity layers as seen in the cross-sections:

- At shallow depths down to about 500 m b.s.l. a thin layer of low resistivity values exists ( $< 10 \Omega\text{m}$ ), which can be correlated to the shallow sedimentary formations in the area and/or low temperature alteration, with some influence noted from the lateral flow of geothermal fluid in fractures. Sometimes the depth varies, but 500 m b.s.l. is an approximate and reasonable depth.
- Below the low resistivity layer, the resistivity increases considerably and reaches values of about  $100 \Omega\text{m}$  at a depth of 800 m b.s.l. This layer is associated with the low-permeable Afar stratoid basalt Series. As can be seen from the cross-sections, this layer stretches to deep levels often of the order of 5000-5500 m b.s.l.
- Below the high-resistivity layer, another low resistivity layer is seen ( $< 5 \Omega\text{m}$ ). This deep conductor is either related to the heat source or highly saline sediments at deep levels.
- The effect of the up flow of geothermal fluid is seen in the depth-slices associated with known geothermal structures.
- The strike analysis results are in good agreement with the resistivity models and with geological features and lineaments.

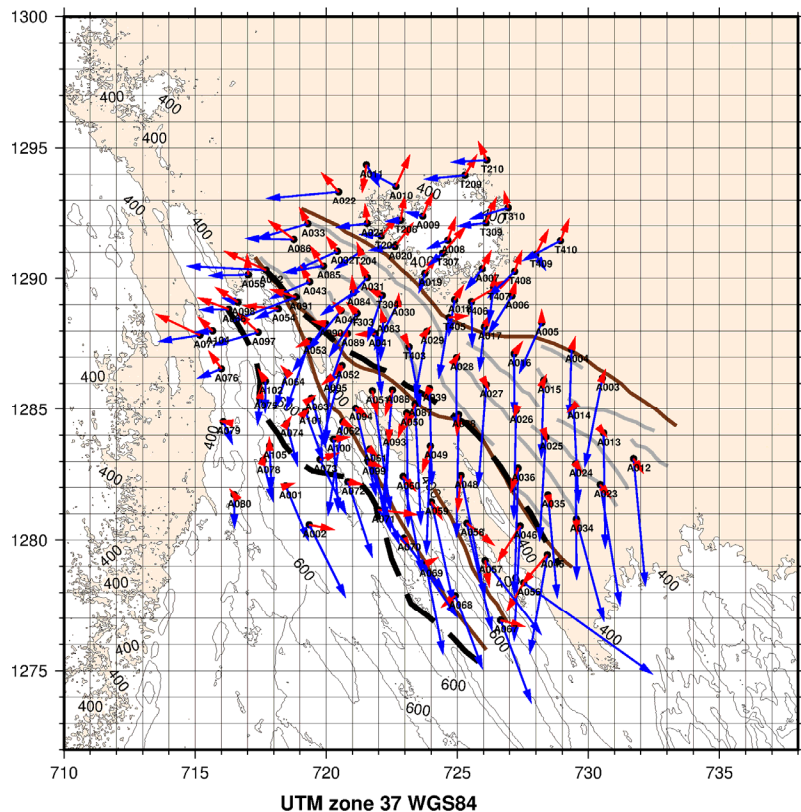


FIGURE 50: Induction arrows for 30 s, corresponding to a depth of a few km; blue arrows denote the real part and red arrows the imaginary part, for legend see Figure 43

## 9. 3D INVERSION OF MT DATA

Nowadays, 3D inversion of MT data has become more reliable. The dimensionality analysis of the MT data from Alalobeda geothermal prospect indicates that the resistivity structure is not 1D especially for the long periods. Therefore, in order to get a better resolution of the resistivity structure of the area, it is necessary to carry out 3D inversion. In this study the 3D inversion was done for the off-diagonal static shift corrected impedance tensor (two real and two imaginary components), for a total of 107 MT soundings and 30 periods. The 3D inversion was done using the inversion program WSINV3DMT (Siripunvaraporn et al., 2005; Siripunvaraporn and Egbert, 2009).

### 9.1 3D MT code

#### 9.1.1 Overview of the WSINV3DMT code

The WSINV3DMT inversion code is a mathematical tool that gives us a model of resistivity which results in an acceptable fit to our data. To get reasonable model one needs to adjust the model and data parameters several times. The code is a full 3D inversion program for MT data. The inversion is extended from 2D data space Occam's inversion (Siripunvaraporn and Egbert, 2000). The inversion seeks the smoothest minimum structure model subjected to an appropriate fit to the data. The Occam inversion was originally introduced by Constable et al. (1987) for 1D inversion of MT data. Then later it was expanded to 2D inversion of MT data by deGroot-Hedlin and Constable (1990). Occam inversion is stable and converges fast to the desired misfit using a small number of iterations compared to most other methods. These inversions are based on model space methods.

The 3D inversion code WSINV3DMT uses finite different forward algorithm and utilizes a formulation of the inverse problem in the data-space rather than in the model space. This approach reduces the dimensionality of the problem dramatically and makes 3D inversion of MT data attainable. Generally, for MT data,  $N \ll M$ . In other words, 3D inversion of MT data is a highly underdetermined problem, (i.e. the number of unknown model parameters are much higher than the number of data values). The data parameter size  $N$  is the total size of the data values (i.e.  $N = N_s \cdot N_r \cdot N_p$ ), where,  $N_s$  is the total number of stations used in the inversion,  $N_r$  the number of responses, in our case it is 4 because we were using only the off-diagonal impedance tensor elements (2 real and 2 imaginary) and  $N_p$ , the total number of periods. On the other hand, the model parameter  $M$  (i.e.  $M = M_x \cdot M_y \cdot M_z$ ), where,  $M_x$  is the number of discretization in  $x$  (north-south),  $M_y$  is the number of discretization in  $y$  and  $M_z$  is the number of discretization in  $z$  (vertical).

#### 9.1.2 Static shift correction

In Section 8.3 we did static shift correction of the determinant but here we did the static shift correction of the  $xy$  and  $yx$  modes, separately. The 3D inversion was performed for the MT impedance tensor elements that may contain static shift. Therefore, static shift correction was needed for the MT impedance tensor elements. The impedance tensor can be static shift corrected through the following Equation Árnason et al., 2010).

$$\begin{bmatrix} Z_{xx}^c & Z_{xy}^c \\ Z_{yx}^c & Z_{yy}^c \end{bmatrix} = \begin{bmatrix} C_x & 0 \\ 0 & C_y \end{bmatrix} \begin{bmatrix} Z_{xx} & Z_{xy} \\ Z_{yx} & Z_{yy} \end{bmatrix}; C_x = \sqrt{\frac{1}{S_{xy}}}; C_y = \sqrt{\frac{1}{S_{yx}}} \quad (9.1)$$

Where,  $Z^c$  is the corrected and  $Z$  the uncorrected impedance tensor,  $S_{xy}$  and  $S_{yx}$  are shift multiplier of  $xy$  (TE) and  $yx$  (TM) apparent resistivity, respectively.

All the 107 un-rotated MT data were jointly inverted with TEM data from the same location, for both the  $xy$  and  $yx$  modes and the shift multipliers,  $S_{xy}$  and  $S_{yx}$  determined. Figure 51 shows an example of joint 1D inversion of TEM and MT data for both modes. Figure 52 and Figure 53 show histograms and the spatial distributions of the static shift multipliers for all MT soundings for  $xy$  and  $yx$  modes, respectively. The shift multipliers for  $S_{xy}$  are in the range of 0.1 – 2.3 whereas, for  $S_{yx}$  they are from

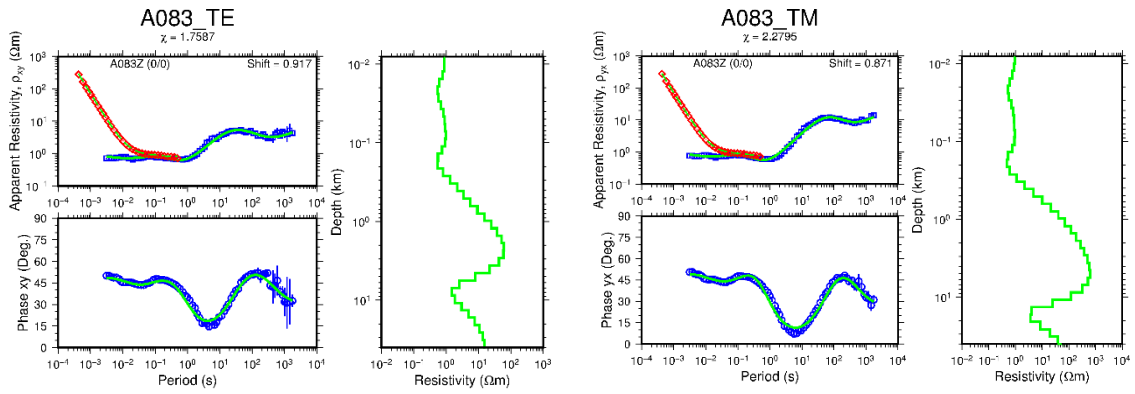


FIGURE 51: Joint 1D inversion of TEM and MT; the xy-mode to left and TEM and the yx-mode of the MT data to the right. Blue squares and circles are the apparent resistivity and phase, respectively. The solid curves in the left panel are the calculated responses from Occam inversion. A083 on top is the name of the station. The number in parenthesis (0/0) indicates the two stations were at the same location and elevation difference was 0 m. On the right corner of the resistivity panel are the shift multipliers, 0.917 for  $\rho_{xy}$  and 0.871 for  $\rho_{yx}$

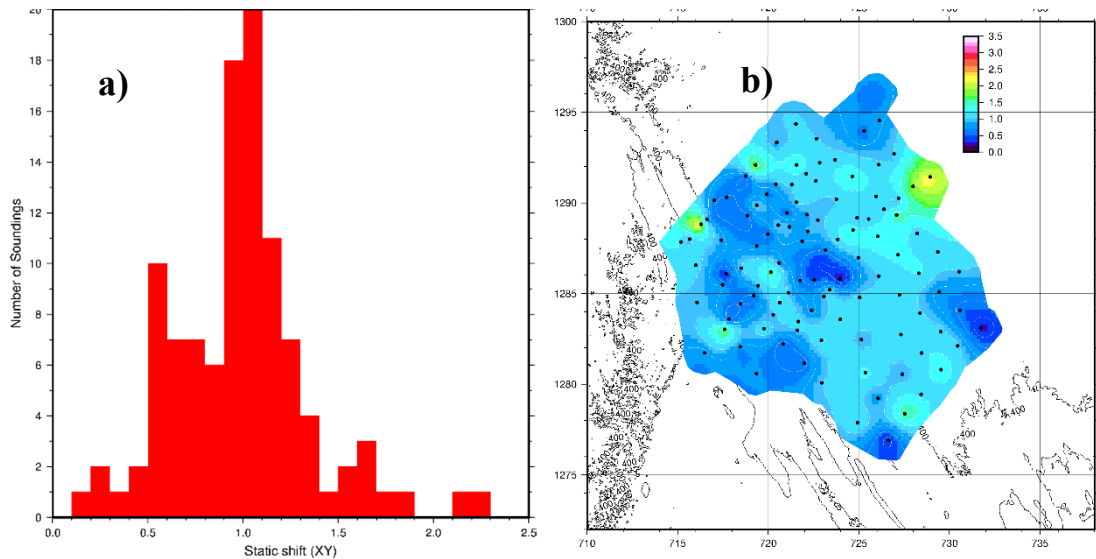


FIGURE 52: a) Histogram; b) Spatial distribution map of the static shift multipliers of the xy-mode

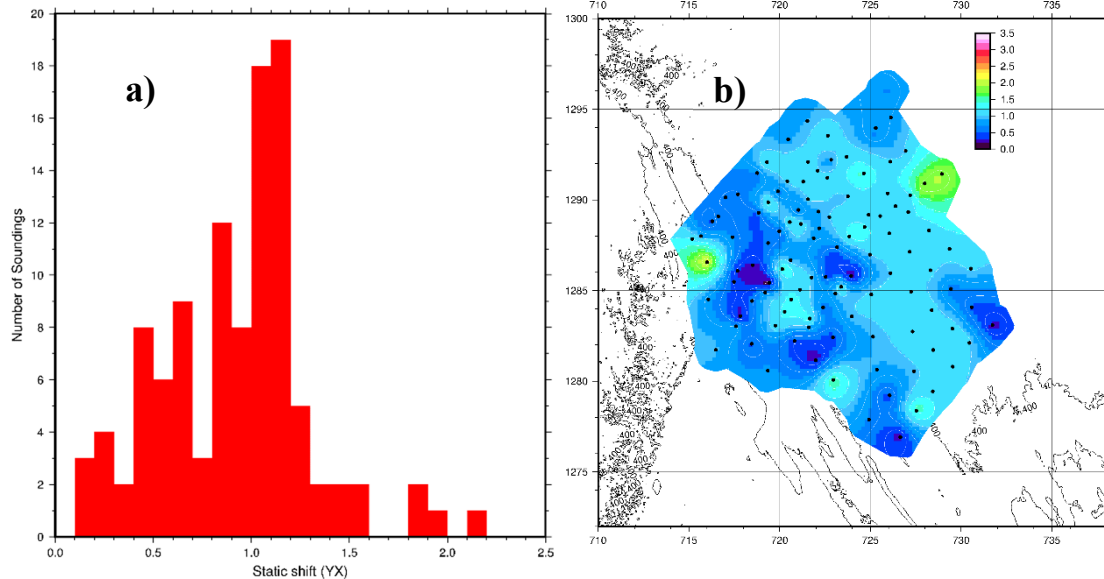


FIGURE 53: a) Histogram; b) Spatial distribution map of the static shift multipliers of the yx-mode

0.1-2.2. To tie the  $\rho_{xy}$  and  $\rho_{yx}$  curves with TEM responses the MT apparent resistivity must be divided by the shift multiplier. The shift map shows that the  $\rho_{xy}$  apparent resistivity curves are shifted downwards on the ridge and around the surface manifestations. This could be due to topographic and near surface in-homogeneities.

### 9.1.3 Preparation of data

In 3D inversion, we used a total of 107 MT soundings, 30 periods and 4 complex static shift corrected impedance tensor elements (2 real and 2 imaginary off-diagonal components). To get a reasonable resistivity model, we exclude the noisy stations and MT stations that do not have a corresponding TEM station. The MT stations we used for 3D inversion are less noisy, with longer period data points and they are evenly distributed over the survey area.

The computational intensity of the inversion is directly proportional to the number of periods that were used for the inversion. Therefore, in order to reduce the computational cost (time and memory) the static shift corrected impedance tensor was resampled at 30 periods, equally spaced on log scale. Here, five data points per decade were selected in the range of 0.0032 s to 700 s. The list of sampled periods was: 0.0032 0.0047 0.0073 0.0111 0.0170 0.0260 0.0397 0.0608 0.0930 0.1422 0.2175 0.3327 0.5090 0.7786 1.1910 1.8219 2.7871 4.2634 6.5218 9.9766 15.2614 23.3456 35.7122 54.6297 83.5680 127.8356 195.5524 299.1402 457.6004 700.0000. This choice of period is a “trade-off” between the computational cost and resolution and depth of investigation. Generally, five periods per decade is considered to give enough resolution to get detailed resistivity structure. Resampling the data is not only to reduce the size but also makes the data smoother. After resampling, we prepared a skip list from the resampled data by skipping the noisy data points (which have large error bars), then those noisy data points will not be included in the inversion. We can skip in xy or yx only or from both if the data point is noisy.

### 9.1.4 3D model mesh grid design

The first step in the 3D inversion was to setup a grid. For the model grid we need to know the grid centre, grid rotation and the extent of the grid. In designing the mesh, a trade-off is required between the size of the grid and the computational time it would require to obtain reasonable solutions to the models. The finer the grid is the larger the time and memory resource required to run the 3D inversion. In 3D inversion, forward modelling solutions depend significantly on the mesh grid discretization used. The 3D model consists of resistivity cubes in a 3D grid mesh defining the internal coordinate system generated from the UTM coordinate system that comes from the data. The centre of the internal coordinate system is in UTM (zone 37) coordinate system 723.5E and 1286.5N in km. This centre is approximately at the centre of the area of interest and data coverage. The rotational angle was 0°. The mesh grid consists of 64 vertical grid cells in x-direction (two edges and 62 internal cells), 64 vertical grid cells in y-direction (two edges and 62 internal cells) and 27 horizontal grid cells in z-direction (one surface, one bottom and 25 horizontal internal cells). The grid design was made by considering the area of interest and the data coverage. The grid is denser in the area of interest and in the area of the data coverage with 400 m grid spacing within the range of  $\pm 12.8$  km from the centre in both x and y-direction. In the area, which the MT soundings cover within the dense grid, there is a uniform model discretization of 40 x 40 squares, 400 m grid spacing in x- and y-directions. Outside the dense area the grid spacing increases exponentially to the edges at  $\pm 138.68$  km in both x- and y-direction. In z-direction the grid planes are denser at shallow depth. The first few layers have a thickness of 20 m, 30 m, 40 m 50 m etc. and then the block sizes start to increase exponentially to a depth of 109.23 km. Figure 54 shows the actual location of the MT soundings in the grid with green dots and the blue triangle shows the centre of the grid. Figure 55 shows the zoom of the grid area. The program requires that the soundings are at the centre of the grid cell. The MT data were slightly adjusted so that they can be at the centre of the grid cells. All resistivity cross-sections are named with reference to their position on the grid and are named by the distance from the centre of the grid. For example, cross-section EW-N2000, refers to the EW cross-section that is 2000 m to the North.

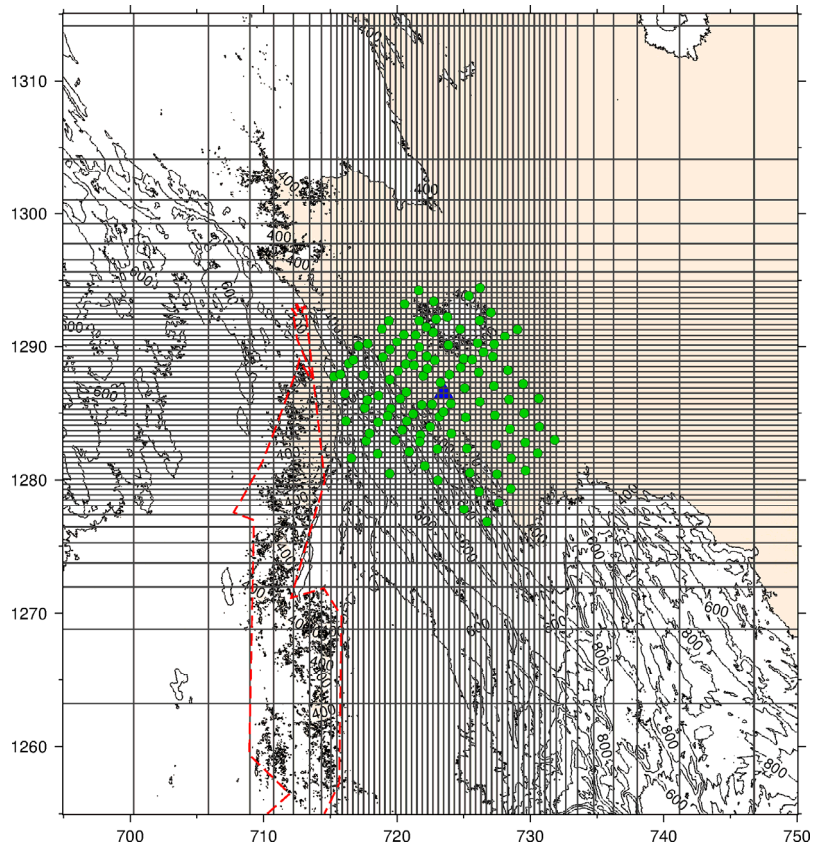


FIGURE 54: A zoom-in to the centre of the 3D model grid with dimension of the central grid squares  $400\text{ m} \times 400\text{ m}$ . MT soundings are shown as in green dots, and the red broken lines the outline of Tendaho dam lake. The blue triangle shows the centre.

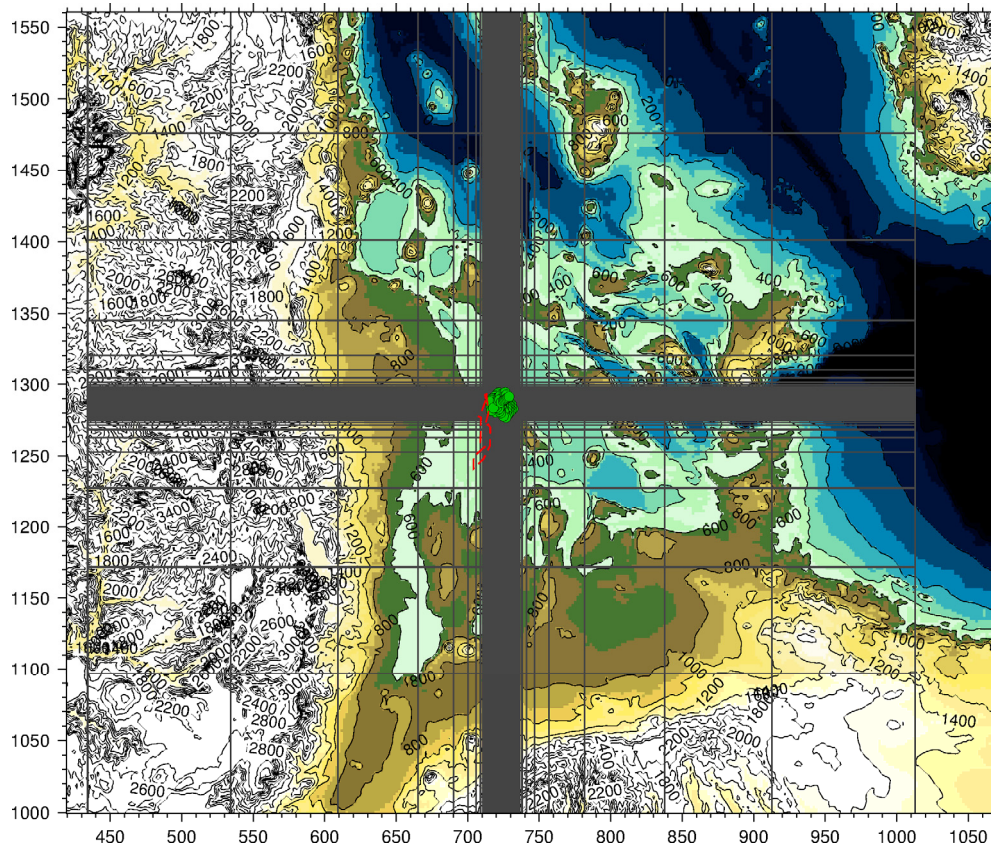


FIGURE 55: The 3D model grid. MT soundings are within the green area at the center of the grey shade, the red broken lines show the outline of Tendaho dam lake and the dark blue is the ocean

### 9.1.5 3D modelling parameters and initial models

Before using the 3D code, we should know our computer RAM size and the sizes of our data and model parameters. In the present case the data set contains 107 sounding, 30 periods and 4 real and imaginary off-diagonal impedance tensor elements, which give us a total of  $N=107 \cdot 30 \cdot 4=12,840$  data points. The model parameter or the model grid size  $M=64 \cdot 64 \cdot 27=110,592$ , the number of grid cells in x, y and z, respectively. To investigate the influence of the initial model on the results, two different initial models were applied:

- 1) Model compiled from joint 1D inversion of MT/TEM sounding pairs, here after referred to as the J1D model;
- 2) A homogeneous half space with resistivity  $10 \Omega\text{m}$ . here after referred to as H010 model.

### 9.2 Results of the 3D inversion

The inversion was executed on a 32 core computer with 132 GB memory. The procedure used in the inversion was to run the inversion for at least 3 iterations (the code finds the best fit of the data and model) at each run which is then restarted with the best model as initial model for the next run. A total of 9 and 12 iterations were performed for the model compiled from the joint 1D inversion (J1D) and the  $10 \Omega\text{m}$  homogeneous half-space (H010) starting model, respectively. Total computer time was 672 and 504 hours of continuous running time for the model compiled from 1D joint inversion and the  $10 \Omega\text{m}$  homogeneous half-space starting model, respectively.

The initial RMS for the model with a starting model compiled from joint 1D inversion model was 26 and reduced to 1.7 and for the  $10 \Omega\text{m}$  homogeneous half-space starting model it went from 90 to 1.2. The inversion was performed until a good RMS was achieved. The RMS value is the difference between the measured and calculated values, weighted by the variance of the measured values. An example of data fit from the model with a starting model compiled from the 1D initial model is shown in Figure 56. Data fit of individual soundings used in the 3D inversion is shown in Appendix IV.

#### 9.2.1 Comparison of different initial models

The 3D program assumes flat surface. The MT data were static shift corrected prior to the inversion which somewhat removes the topographic effects in the data. The resistivity models resulting from the

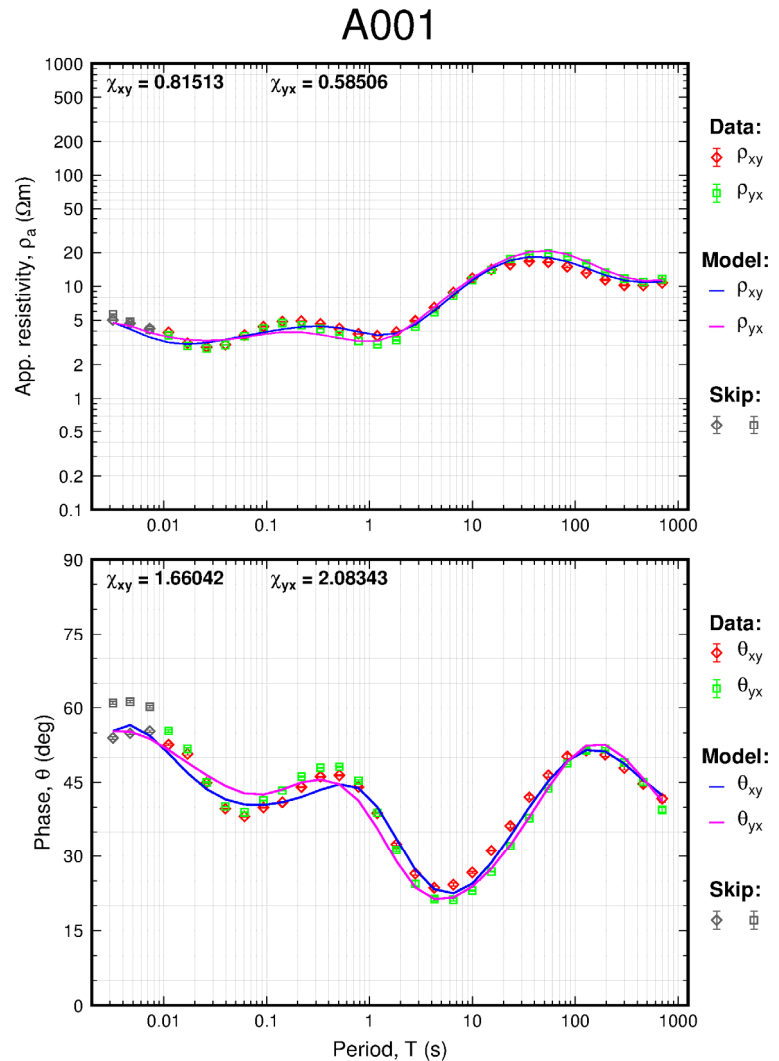


FIGURE 56: Data fit between the measured data and model response for station A001. The red and green symbols are data points whereas the pink and blue lines are model responses, respectively

3D inversion were elevation corrected and the results are presented as smoothed resistivity maps at different elevations and as resistivity cross-sections. Here we also compare the 1D Occam inversion with the results from the 3D inversion.

It is critical to inspect anomalies that are similar in all models to test the robustness of the resistivity models. Figure 57 shows a comparison of the resistivity structures at 300 m a.s.l. As seen in the figure it is evident that results from the J1D and H010 models (see Figure 57a and Figure 57b, respectively) agree quite well at 300 m a.s.l. where there is a low resistivity structure.

Figure 58 shows a comparison of the resistivity structures at 5000 m b.s.l. The J1D model see Figure 58 a and 1D Occam inversion (discussed in Section 8.4) the result give similar resistivity distribution whereas the H010 model see Figure 58b is not comparable to the other two. At this depth the resolution of the MT data is not good which could explain the discrepancies between the models. Also, the 3D model compiled from the 1D model does not stray too far away from the initial model, explaining the resemblance between the two well matching ones.

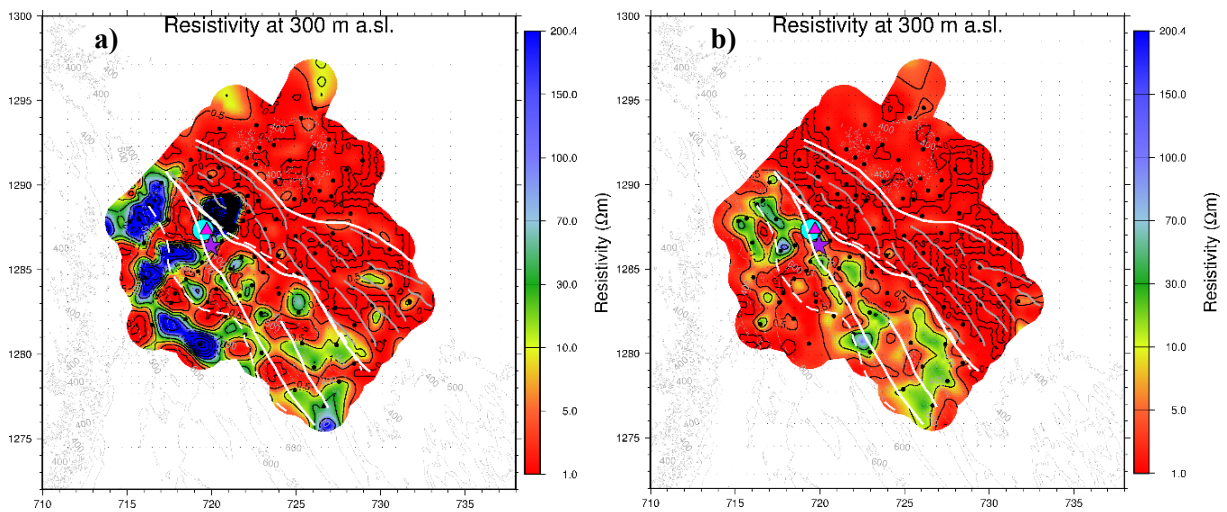


FIGURE 57: Resistivity depth-slice at 300 m a.s.l. showing a comparison of models from the 3D inversion using different initial models; a) J1D model, b) H010 model. White line indicates the fault, white broken lines show the gravity low anomaly border, grey lines indicate lineaments inferred from gravity

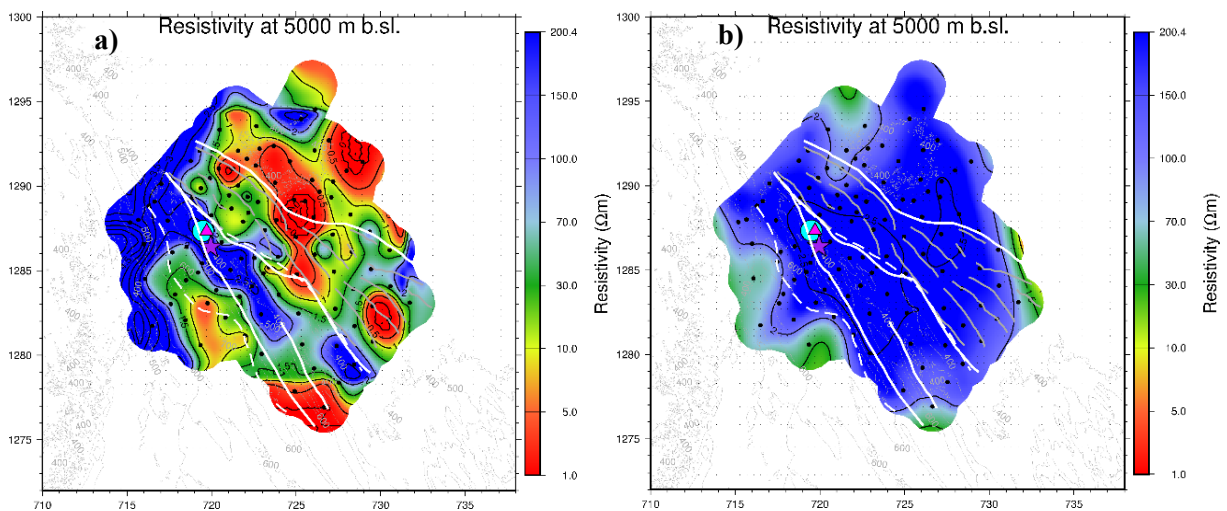


FIGURE 58: Resistivity depth-slice at 5000 m b.s.l. showing a comparison of models from the 3D inversion using different initial models; (a) the J1D model, (b) H010 model; for legend, see Figure 57

Figure 59 shows a comparison of resistivity cross-sections from the J1D and H010 models. Down to a depth of about 2 km they are in agreement but below that depth the H010 model deviates from the other and clearly the 3D model compiled from the 1D inversion has a better resolution of the low resistivity anomalies. The low resistivity column in -4 in the 3D models shows an indication of up flow of geothermal fluid along the NW-SE fault trending graben fault in the southwestern part of the survey area. UP flow along the faults will be discussed later.

The cross-section on Figure 59 from the 1D Occam model, shows low resistivity at depth and an indication of up flow right under the surface manifestations.

The result of the 3D inversion is best explored by looking at resistivity maps at various depths and resistivity cross-sections through the model; using as a starting model, a model compiled from joint 1D inversion of individual TEM/MT sounding pairs (J1D). We also discuss the result from 10  $\Omega\text{m}$  homogeneous half space (H010).

### 9.2.2 Resistivity depth-slice maps based on the 3D inversion

As the data do not cover all the area defined by the fine grid, artefacts are prone to appear in the area outside the data coverage. This is present in the 3D model and must be taken with care or even disregarded. Elevation corrected depth-slice maps through the J1D model are presented from shallow to deeper elevations. A few depth-slice maps are presented here, but more maps are shown in Appendix V in this report.

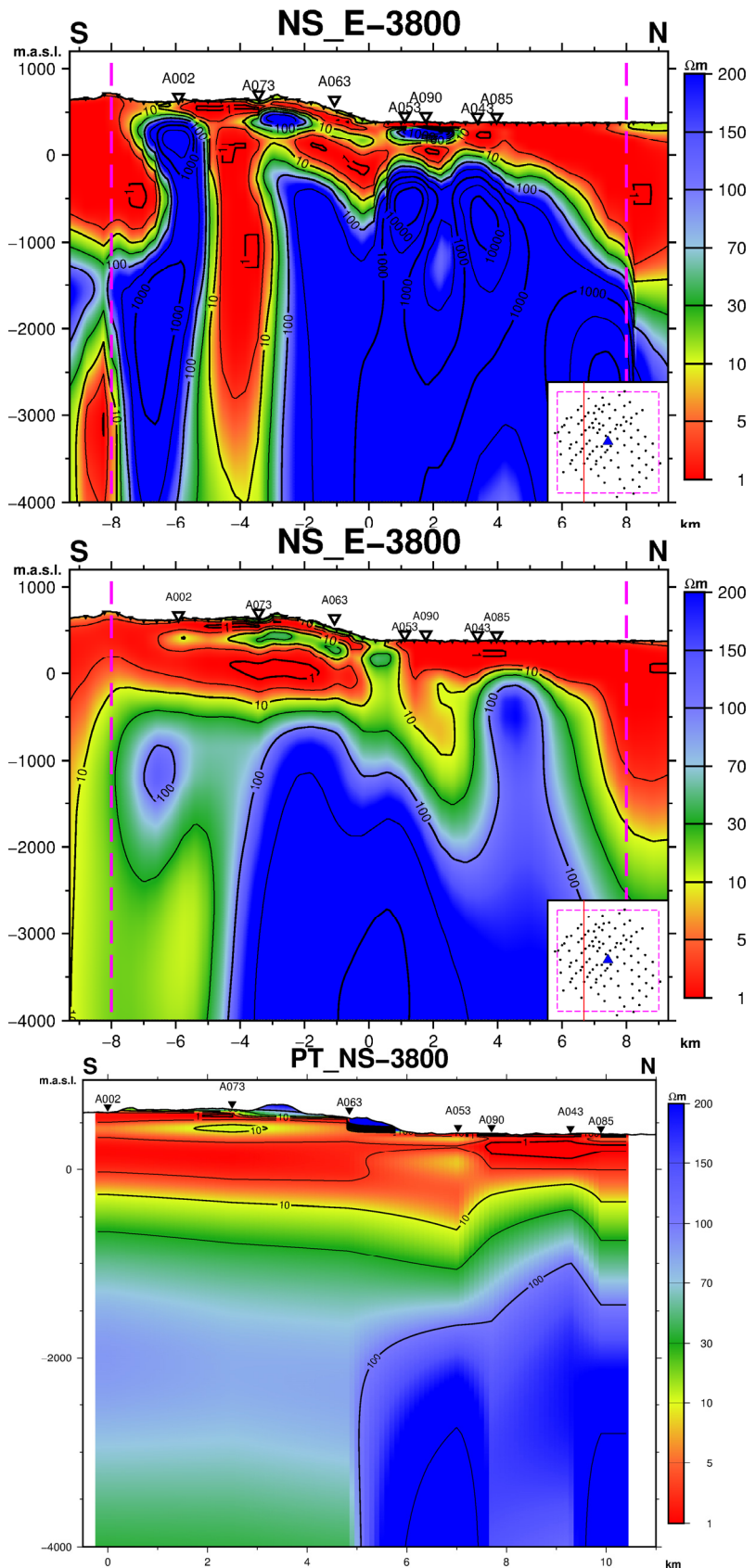


FIGURE 59: Resistivity cross-section showing comparison of different initial models: Top: 1D J1D model; Middle: H010 model; and Bottom: 1D Occam inversion. MT stations' names are given on top, location of the cross-section is in the right corner, pink broken lines show the extent of the fine grid

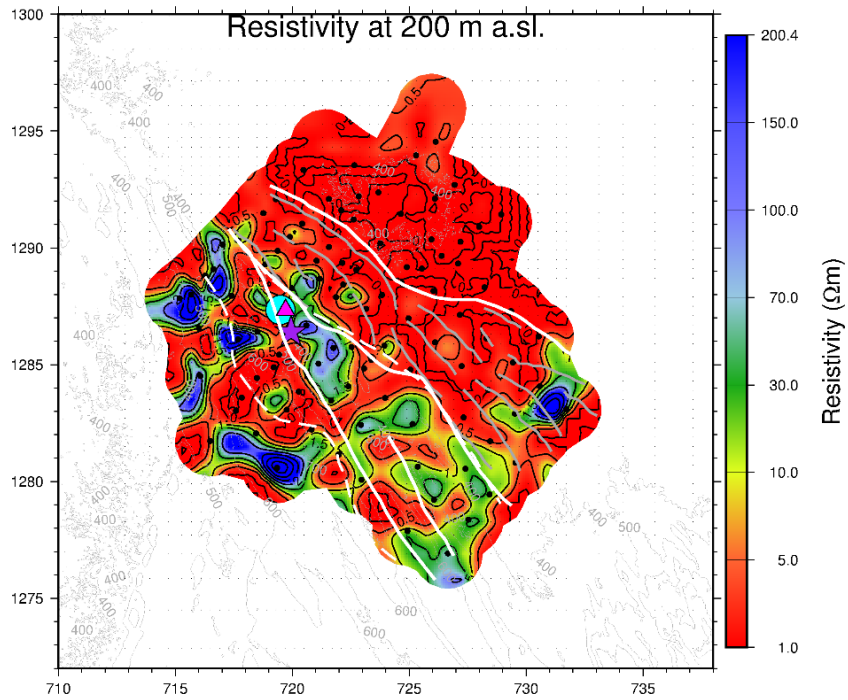


FIGURE 60: Depth-slice through the J1D model at 200 m a.s.l., for legend, see Figure 57

At 200 m a.s.l. (Figure 60) low-resistivity ( $< 10 \Omega\text{m}$ ) is observed in most parts of the survey area, which could relate to saline sediments and/or low temperature alteration. A slightly higher resistivity is noticeable in the western part of the survey area could be unaltered rock or caused by low quality TEM soundings or static shift effects from the topographic.

At 600 m b.s.l. (Figure 61), the resistive core starts to appear more which correlates with the resistive Afar Stratoid basalt. It also shows low-resistivity anomalies trending NW-SE, along the geological structures, specifically to the west and south of the surface manifestations which probably could be up flow zones of the area.

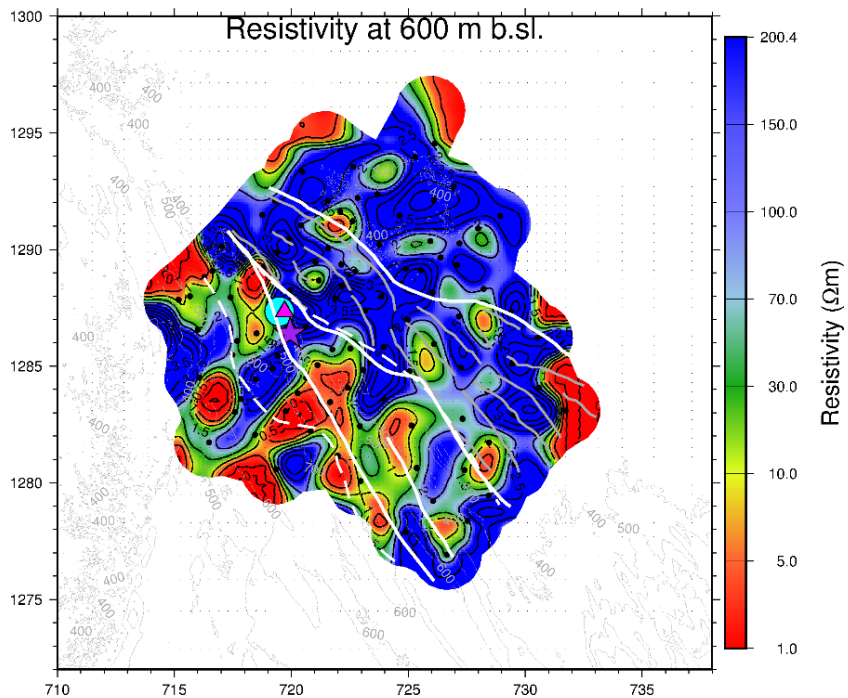


FIGURE 61: Depth-slice through the J1D model at 600 m b.s.l., for legend, see Figure 57

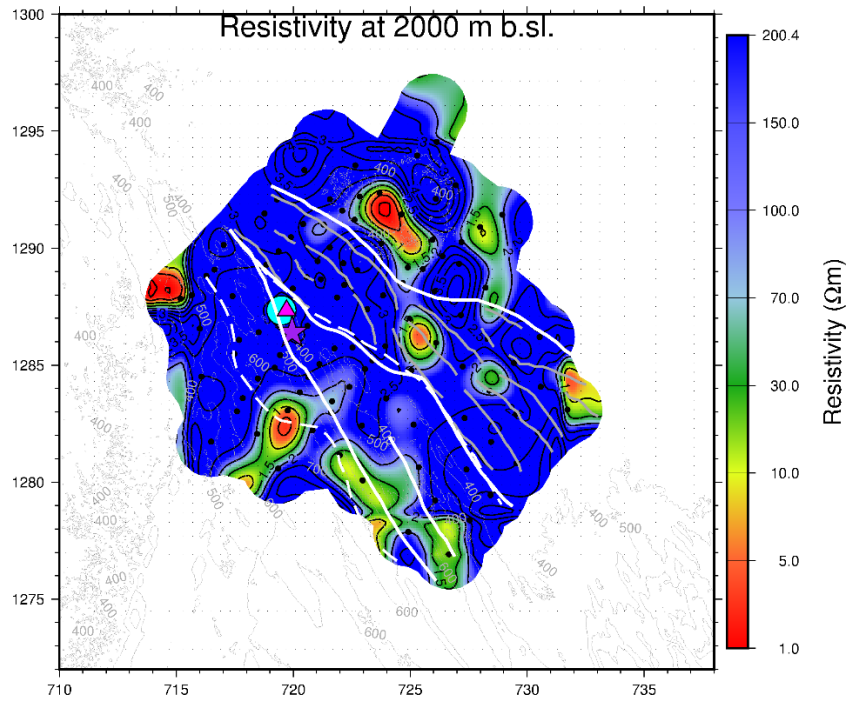


FIGURE 62: Depth-slice through the J1D model at 2000 m b.s.l., for legend, see Figure 57

At 2000 m b.s.l. (Figure 62), in most of the survey area the resistivity is very high or more than 200  $\Omega\text{m}$ ; could be the resistive Afar Stratiod basalt Series. At this depth there are low resistivity to south of the surface manifestations and probably could be related to the up flow zone.

At 5000 m b.s.l. (Figure 63) low-resistivity anomalies are present and the map clearly shows the main up flow zones at depth, hence the heat source.

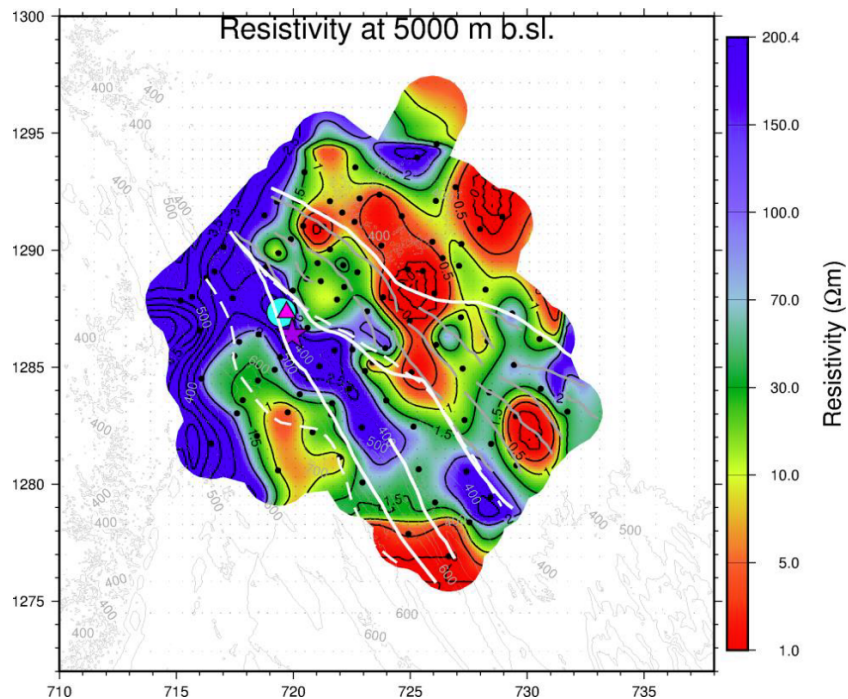


FIGURE 63: Depth-slice through the J1D model at 5000 m b.s.l., for legend, see Figure 57

### 9.2.3 Vertical cross-sections through the 3D model

Several elevation corrected vertical resistivity cross-sections in NS and EW directions through the J1D model are presented below. More cross-sections are shown in Appendix VI.

When the 3D model is thoroughly scrutinized, especially the vertical resistivity cross-sections an interesting picture appears. At first, it has to be noted that artefacts in the corners of the fine grid must be disregarded as they are all outside the data coverage and therefore not supported by data. For clarifications the main faults in the area are marked by Faults 1, 2 and 3 as shown on Figure 78 (see later).

Figure 64 shows a vertical resistivity cross-section, NS\_E-3800. It passes perpendicularly through the three main faults in the survey area. This cross-section is characterized by a thin layer of a very low resistivity,  $< 10 \Omega\text{m}$ , with a varying depth from sea level down to 200 m b.s.l. The layer is most likely associated with the shallow sedimentary formation and/or low temperature alteration. Below the low resistivity, a high-resistivity layer is found with resistivity values around  $100 \Omega\text{m}$  and even more down to depths varying between 1200 and 4000 m from the surface. The high resistivity is most likely related to the high-resistive Afar Stratoid basalt Series. The shallow-lying high-resistivity anomaly observed below stations A053, A073 and A090 could be the high-resistive Afar Stratoid basalt intercalated with the sediment. A low-resistivity column is observed at around  $x=-4$  (A073) and most likely gives an indication of an up flow zone as it lies close to fault 1. There is another indication of a discontinuity or a shallower up flow zone at 0, under the surface manifestations between A053 and A063. These structures were also confirmed by the 3D inversion of gravity data, see Figure 9 (for more details, see ELC's gravimetric report (ELC, 2015c)).

Figure 65 shows a resistivity cross-section, NS\_E-2600. It shows a similar resistivity structure as mentioned before. The plausible up flow zones seen in the cross-sections correspond to the main faults. The first zone is between stations A072 and A062 and corresponds to fault 1 (at around  $x=-4$ ). Two other possible up flow zones are seen along fault 2 and fault 4 at,  $x=+3$  and  $x=+4.5$ .

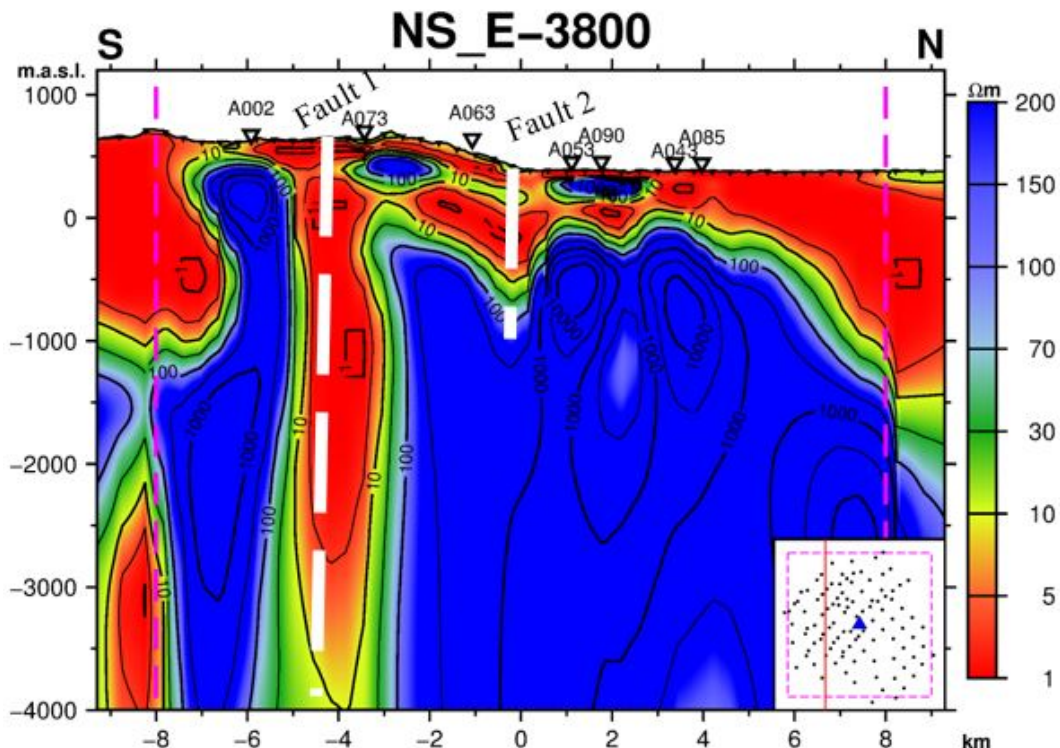


FIGURE 64: Resistivity cross-sections NS\_E-3800. MT stations' names are given on top, the location of the cross-section is in the right corner, pink broken lines show the extent of the fine grid

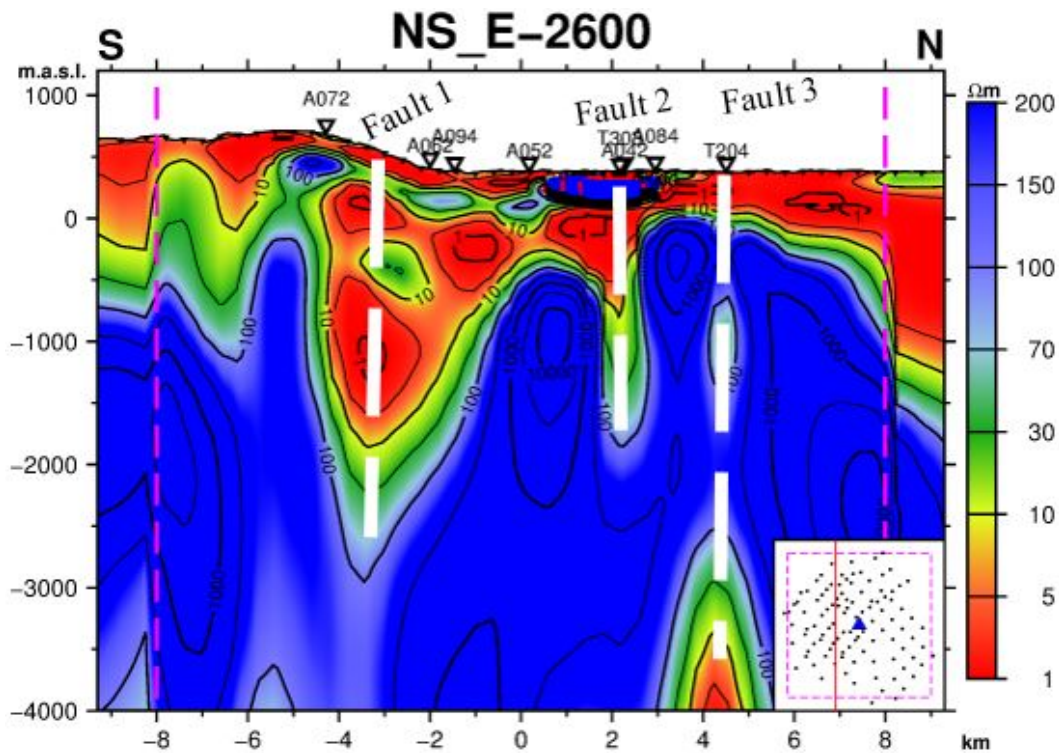


FIGURE 65: Resistivity cross-sections NS\_E-2600. Name of the MT stations are given on top, the location of the cross-section is in the right corner, pink broken lines show the extent of the fine grid

Figure 66 shows a resistivity cross-section, NS\_E1400. It shows a similar resistivity structure as mentioned before. The three plausible up flow zones are at  $x=-5$ ,  $x=-1$  and  $x=+4$  and correspond to faults 1, 2 and 3, respectively. It seems that fault 2 and 3 might have a common up flow from depth in this area, here seen at  $+2$  in x-axis. This may also indicate that their heat source is the same.

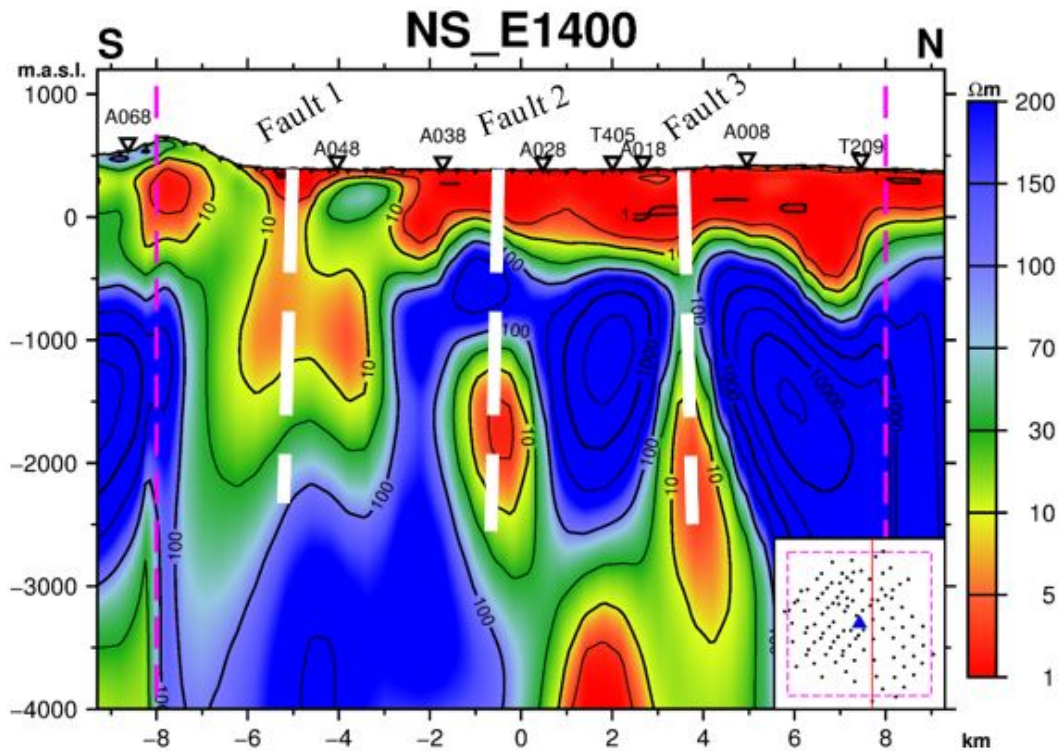


FIGURE 66: Resistivity cross-sections NS\_E1400. MT stations' names are given on top, the location of the cross-section is in the right corner, pink broken lines show the extent of the fine grid

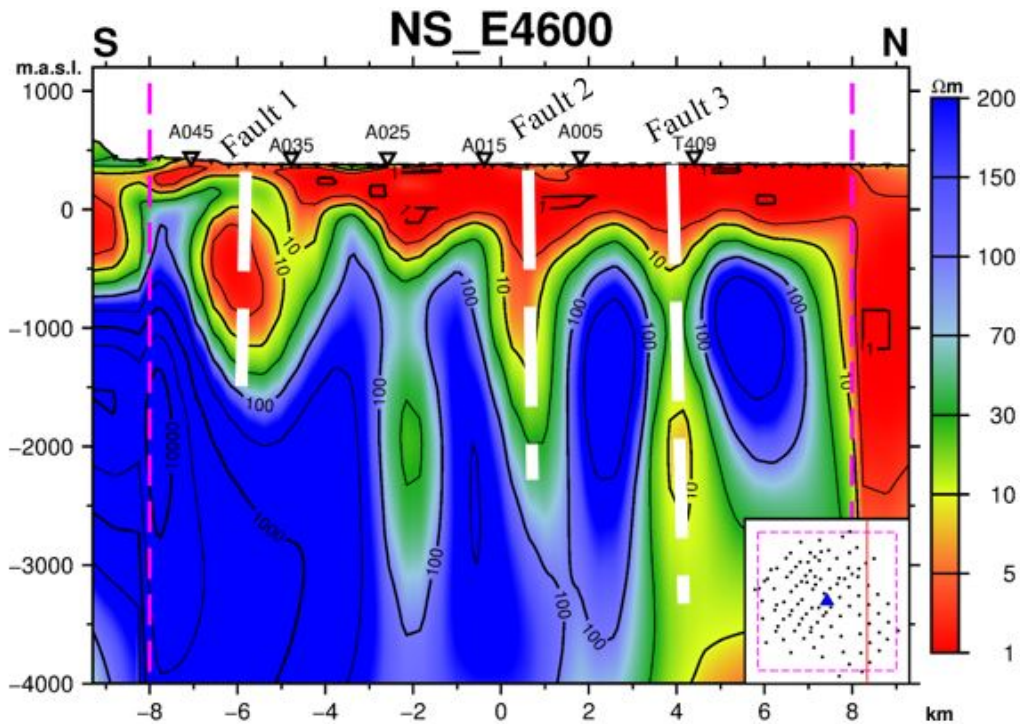


FIGURE 67 Resistivity cross-sections NS\_E4600. MT stations' names are given on top, the location of the cross-section is in the right corner, pink broken lines show the extent of the fine grid

Figure 67 shows a resistivity cross-section, NS\_E4400. This cross-section also shows a similar resistivity structure as mentioned before. Here four up flow zones have been identified. They are located at  $x=-6$ ,  $x=-2$ ,  $x=+1$  and  $x=+4$  for fault 1, MF0 (the small fault between MF0 and MF1 as shown in Figure 2.7), 2 and 3.

The E-W cross-section in Figure 68 to Figure 71 show similar resistivity characteristics and the up flow zones are along the main faults in the area as well.

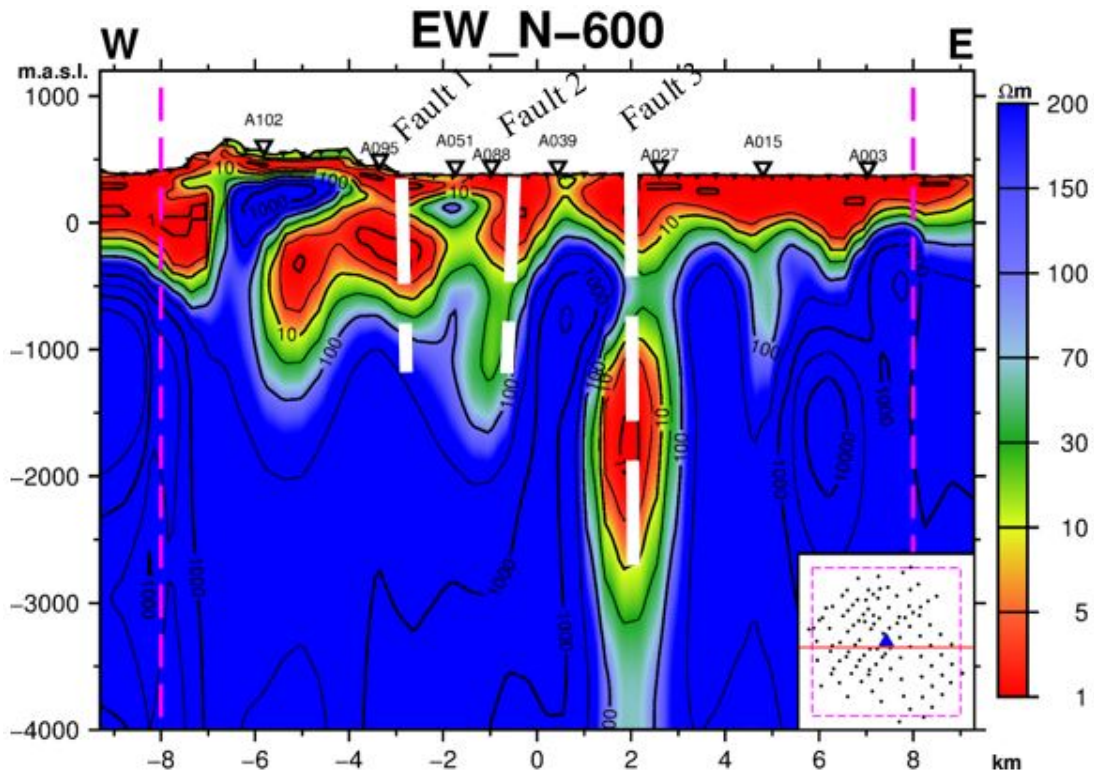


FIGURE 68: Resistivity cross-sections EW\_N-600. Name of the MT stations are given on top, the location of the cross-section is in the right corner, pink broken lines show the extent of the fine grid

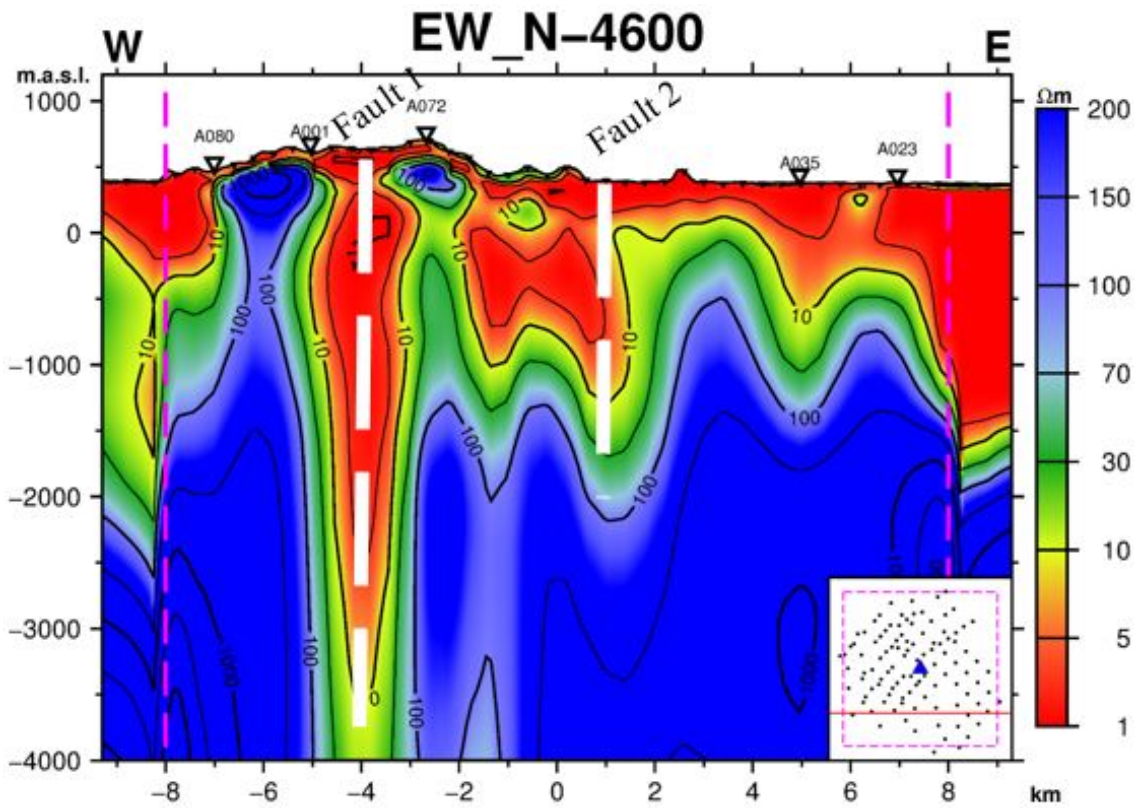


FIGURE 69: Resistivity cross-sections EW\_N-4200. MT stations' names are given on top, the location of the cross-section is in the right corner, pink broken lines show the extent of the fine grid

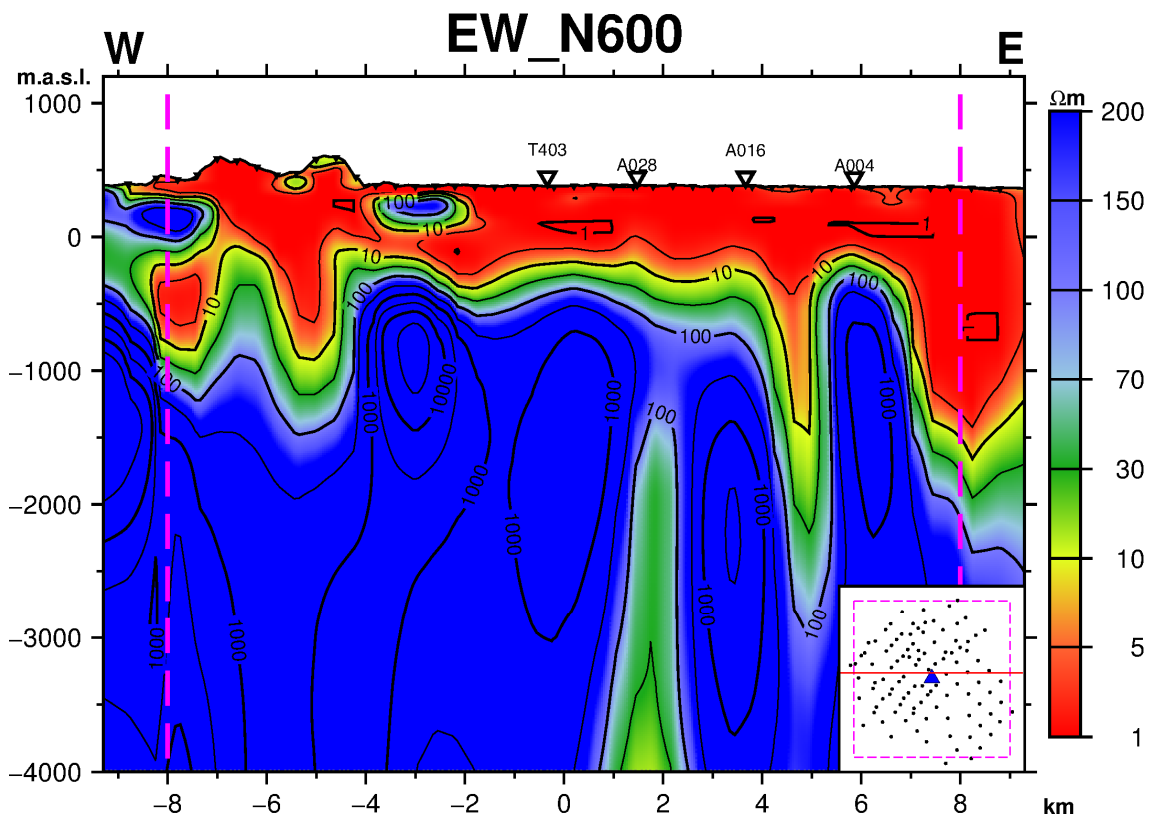


FIGURE 70: Resistivity cross-sections EW\_N600. MT stations' names are given on top, the location of the cross-section is in the right corner, pink broken lines show the extent of the fine grid

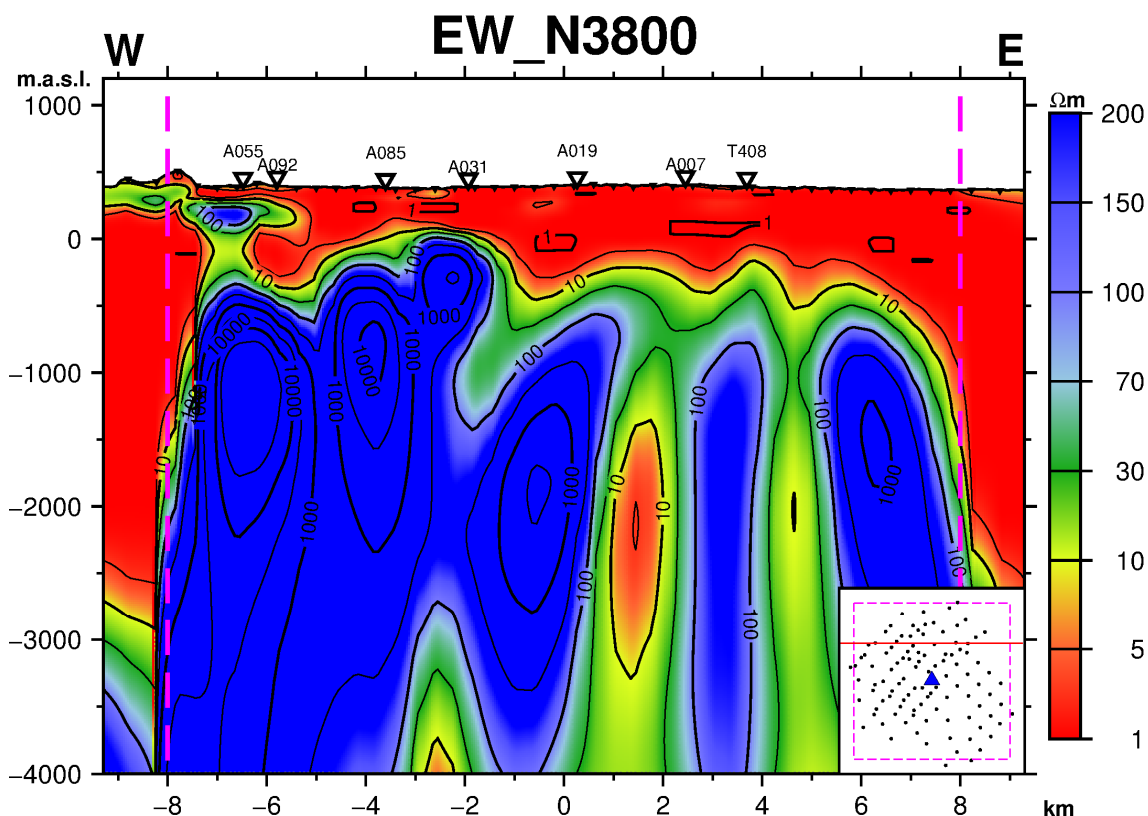


FIGURE 71: Resistivity cross-sections EW\_N3800. MT stations' names are given on top, the location of the cross-section is in the right corner, pink broken lines show the extent of the fine grid

### 9.3 Comparisons of 1D and 3D results

Here the results of the 1D inversion and 3D inversion (J1D model) are compared for three vertical cross-sections and three depth-slices. The resistivity cross-section PT\_NS-3800, based on the 1D and resistivity cross-section NS\_E-3800 based on 3D inversion are shown in Figure 72. Both cross-sections show in general similar resistivity structure down to a depth of 2 km; with a low-resistivity layer ( $< 10 \Omega m$ ) varying in depth from sea-level and down to 300 m b.s.l. The low-resistivity layer is underlain by high-resistivity ( $> 100 \Omega m$ ). The 3D model is somewhat different from the 1D as it shows more structures. A clear resistivity discontinuity is observed between stations A002 and A073. The location of the discontinuity is exactly where the main fault, Fault 1, passes through that area.

Resistivity cross-section PT\_NSE5000 based on the 1D and resistivity cross-section NS\_E5000 based on 3D inversion are shown in Figure 73. Both cross-sections show in general similar resistivity structure down to a depth of 2 km; with a low-resistivity layer ( $< 10 \Omega m$ ) varying in depth from sea level down to 300 m b.s.l. It is underlain by a high-resistivity ( $> 100 \Omega m$ ). Cross-section NS\_E5000 exhibits more structures than the PT\_NSE5000. The four low-resistivity columns seen in the 3D cross-section agree well with the main faults that pass through the area. These are, however, not visible in the 1D cross-section.

Resistivity cross-section PT\_EW-1000 based on 1D inversion and resistivity cross-section EW\_N-1000 based on 3D inversion are shown in Figure 74. Both cross-sections show in general similar resistivity structure down to a depth of 2 km, but they are a bit different. The cross-section from the 1D inversion shows more homogenous resistivity structure; with a low-resistivity layer ( $< 10 \Omega m$ ) down to approximately 450 m b.s.l. and it is underlain by high-resistivity ( $> 100 \Omega m$ ). Cross-section EW\_N-1000 shows more resistivity structure. Below stations A075 and A051 in the 1D cross-section the resistivity is slightly higher around  $10 \Omega m$ . The high resistivity is clearly seen in cross-section based on the 3D inversion. Here we can say that the 1D model cannot see vertical resistivity discontinuities whereas the

3D model clearly sees those discontinuities. Thinning of the low resistivity cap under station A051 indicates up flow zone of the geothermal fluids. This greatly confirmed that the surface manifestation located in that area. As mentioned before the high resistivity could be related to the Afar Stratoid basalts.

Three depth-slices from the 1D and 3D inversions are compared. Figure 75 shows resistivity models at 100 m a.s.l from the J1D and 1D inversion, respectively. Low-resistivity ( $< 10 \Omega\text{m}$ ) is observed in most

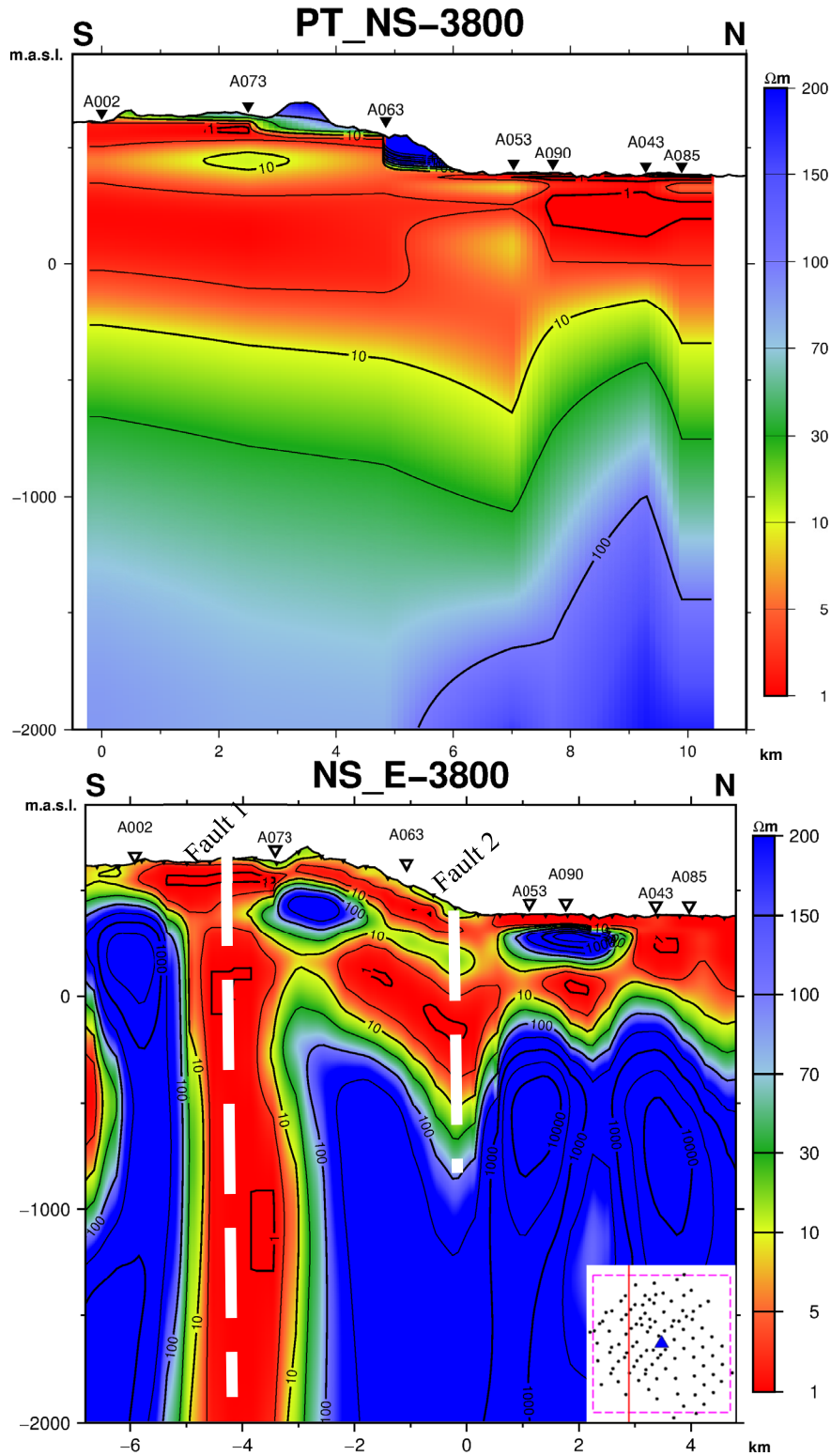


FIGURE 72: Comparison of 1D and 3D resistivity cross-sections; Top: 1D inversion; Bottom: J1D model from the 3D inversion. The location of the cross-section is in the right corner

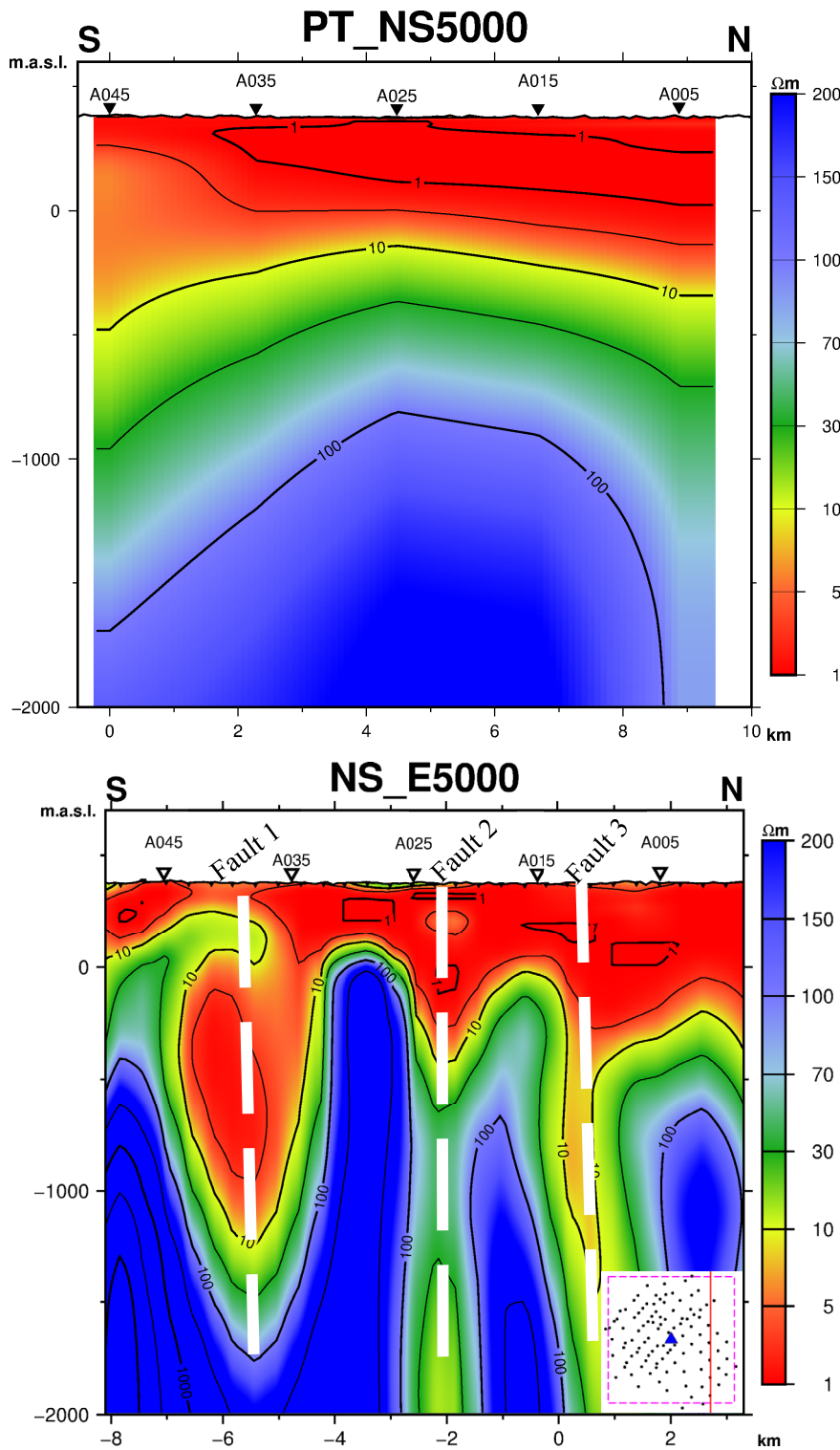


FIGURE 73: Comparison of 1D and 3D resistivity cross-sections;  
 Top: 1D inversion; Bottom: J1D model from the 3D inversion.  
 The location of the cross-section is in the right corner

models at 5000 m b.s.l. from the J1D and 1D inversion, respectively. Most of the area is characterized by low-resistivity. As mentioned before at this depth the resolution of the MT data has diminished greatly. The low-resistivity at depth could be a heat source.

In general, along the main fault and geological lineaments the cross-sections show fairly low resistivity elongated towards the surface through the sediments.

parts of the survey area, which could relate to saline sediments and/or low temperature alteration. But a slight high-resistivity is noticeable along the graben shoulder which may indicate unaltered Afar Stratoid basalt.

Depth-slices from the 1D and 3D inversions are compared in Figure 75 which shows resistivity models at 100 m a.s.l from a) J1D and b) 1D inversion, respectively. Low-resistivity ( $< 10 \Omega\text{m}$ ) is observed in most parts of the survey area, which could relate to saline sediments and/or low temperature alteration. But a slight high resistivity is noticeable along the graben shoulder which may indicate unaltered Afar Stratoid basalt.

Figure 76 shows models at 1000 m b.s.l. from the J1D and 1D inversion, respectively. Most of the survey area exhibits a resistive character of more than  $200 \Omega\text{m}$ . These could be the resistive Afar Stratoid basalt Series or the resistive-core of a geothermal system. The 3D inversion from J1D resolves the resistivity structure better than the 1D inversion. As mentioned before it could be related to the up flow zones on the fault.

Figure 77 shows resistivity

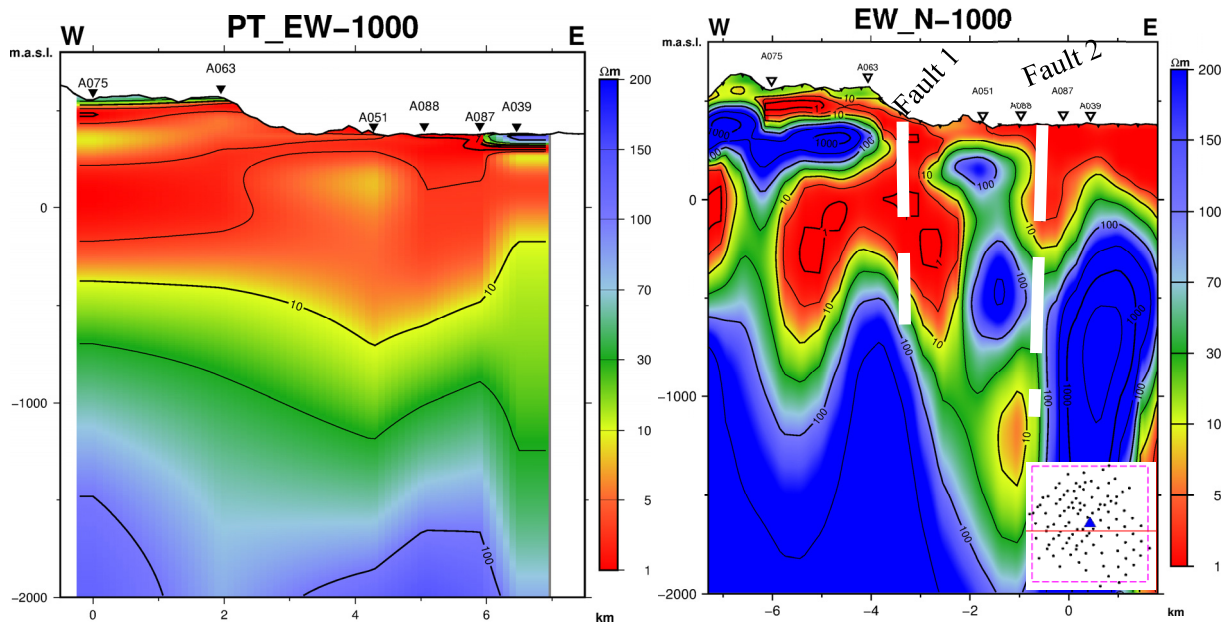


FIGURE 74: Comparison of 1D and 3D resistivity cross-section; Left: A joint 1D Occam inversion of MT and TEM data; Right J1D model from the 3D inversion. Location of the cross-section is in the right corner, pink broken lines show the extent of the fine grid

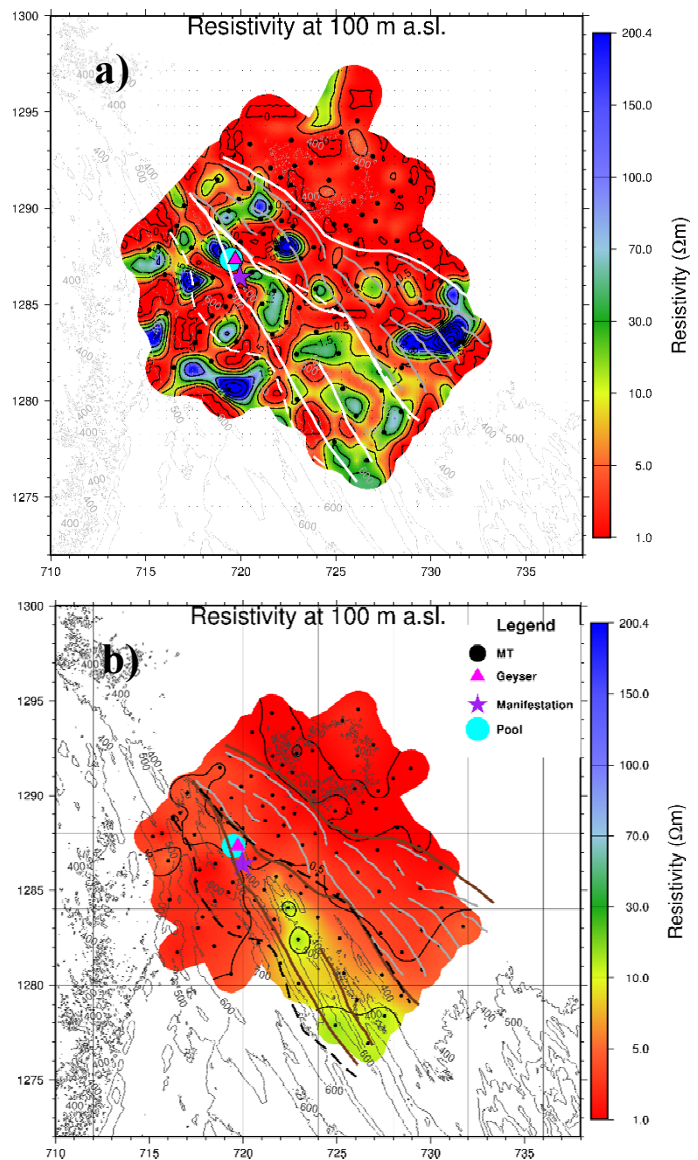


FIGURE 75: Comparison between resistivity depth-slices for 1D and 3D inversion at 100 m a.s.l.; a) J1D model; b) 1D inversion. Legend, see Figure 57

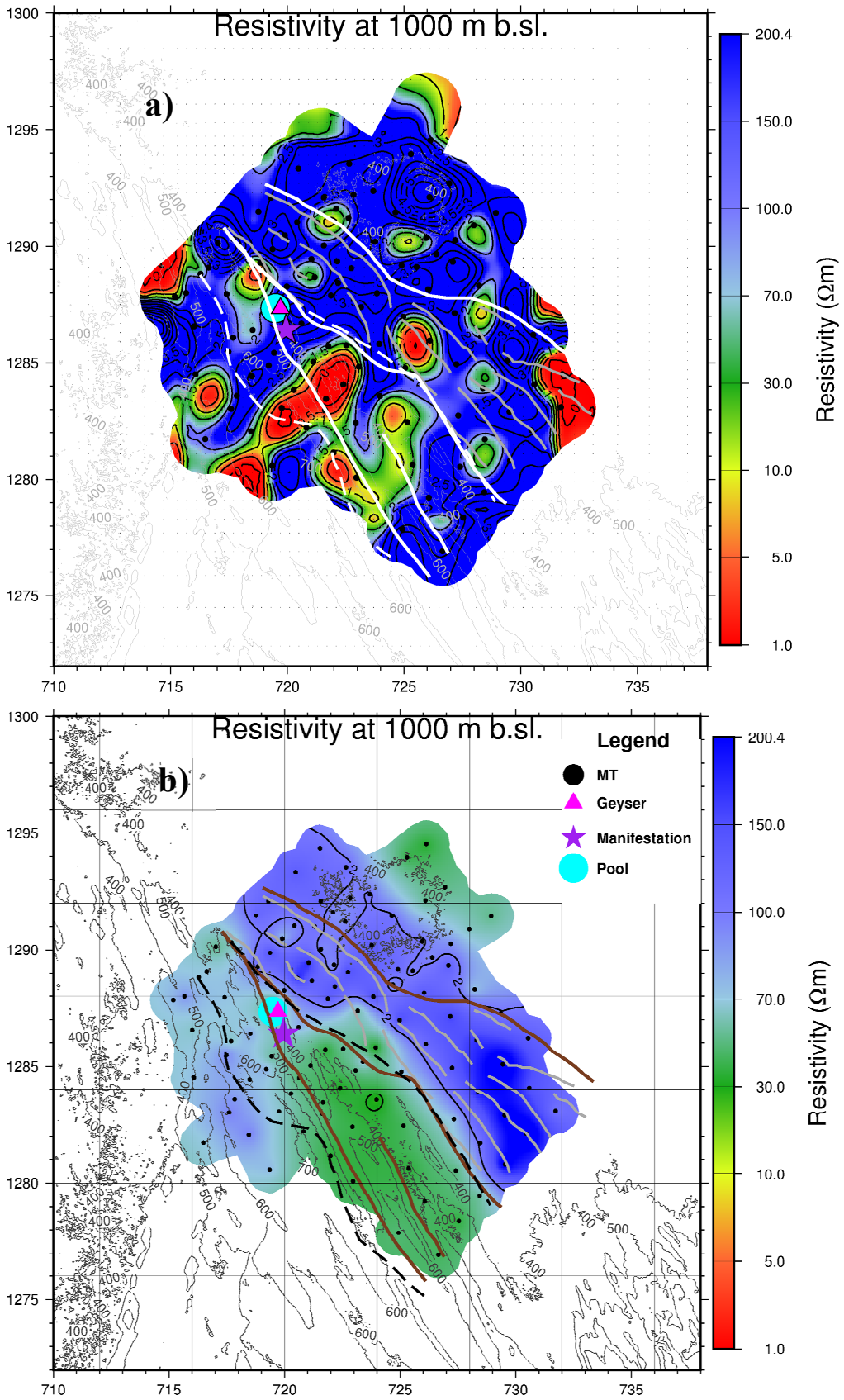


FIGURE 76: Comparison between resistivity depth-slices for 1D and 3D inversion at 1000 m b.s.l.; a) the J1D model; b) 1D inversion. For legend, see Figure 57.

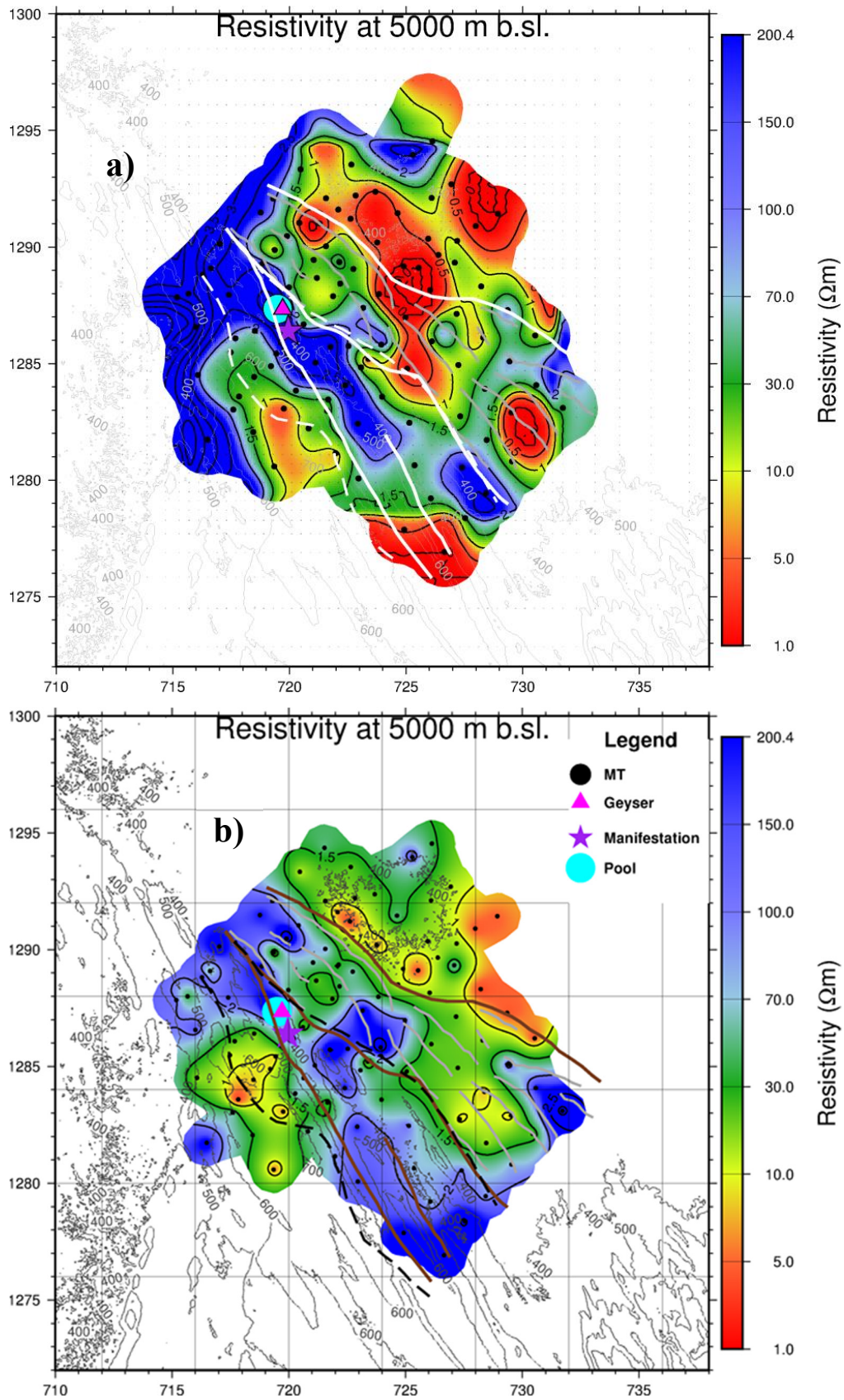


FIGURE 77: Comparison between resistivity depth-slices for 1D and 3D inversion at 5000 m b.s.l.; a) the 1D model; b) 3D inversion. For legend, see Figure 57.

## 10. UP FLOW ZONES

To better describe the findings the main up flow zones detected from the resistivity cross-sections are marked on a map of the area on Figure 78. They clearly follow parts of the main faults in the area which follows a NW-SE trend - the Red Sea fault trend - marked here as Faults 1, 2 and 3.

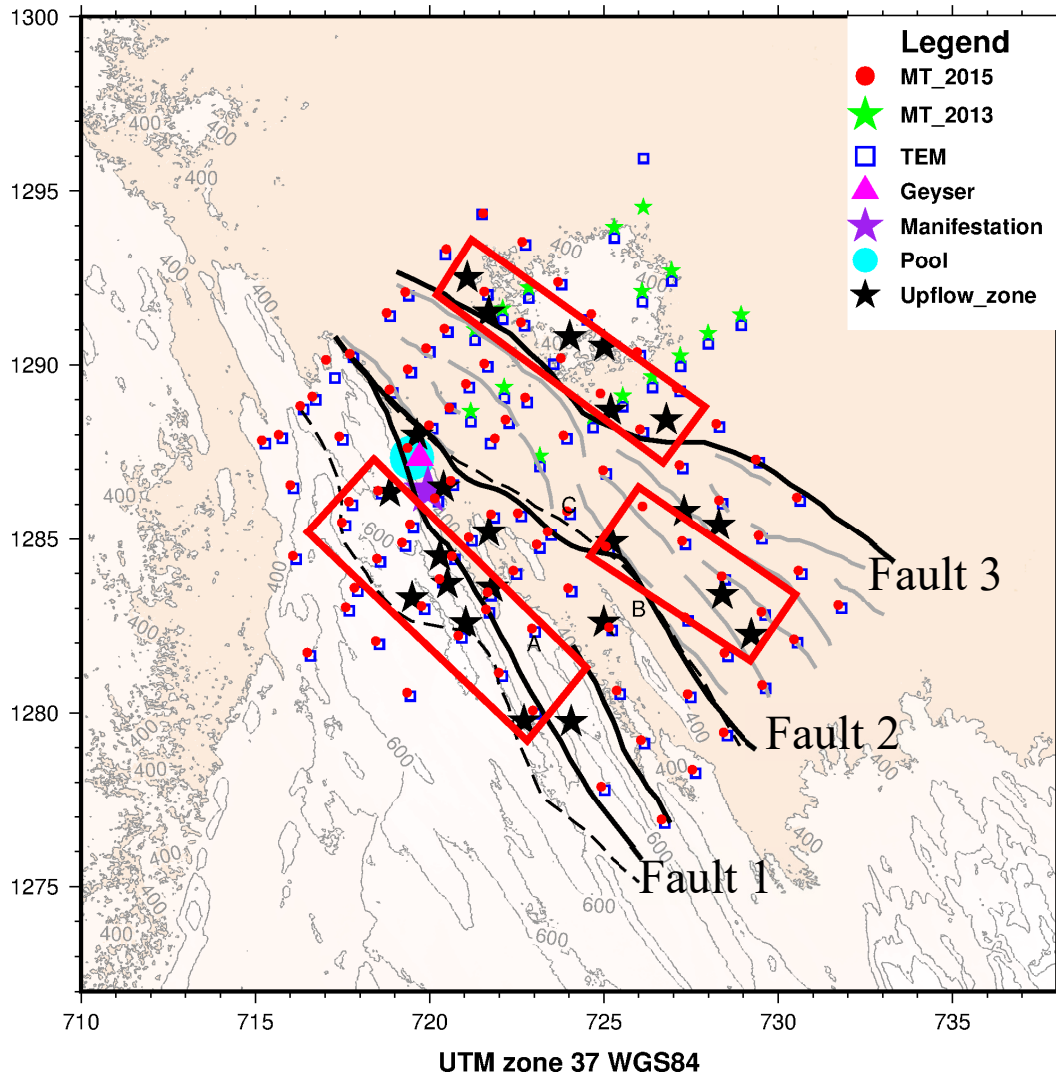


FIGURE 78: Location map of the up flow zones in Alalobeda geothermal prospect.

The main up flow zones can be grouped into three zones A, B and C:

*Zone A:* Follows fault 1 in the area to the south of the surface manifestations. As stated in Section 2, in the vicinity of the geothermal areas, the most identifiable point of intersection is near Alalobeda geothermal prospect, where NNE-SSW trending faults of the MER terminate and deflect into the major NW-SE trend that bounds the graben on its southwest edge (Stimac et al., 2014). This coincides with zone A in the resistivity model. This zone is probably the main up flow zone in the area.

*Zone B:* Follows fault 2 in the area 8 km east-southeast of the surface manifestations.

*Zone C:* Follows fault 3 in the northeast part of the survey area.

Figure 79 shows resistivity maps at 5000 m b.s.l. indicating low resistivity at that depth that coincides with the up flow zones A, B and C.

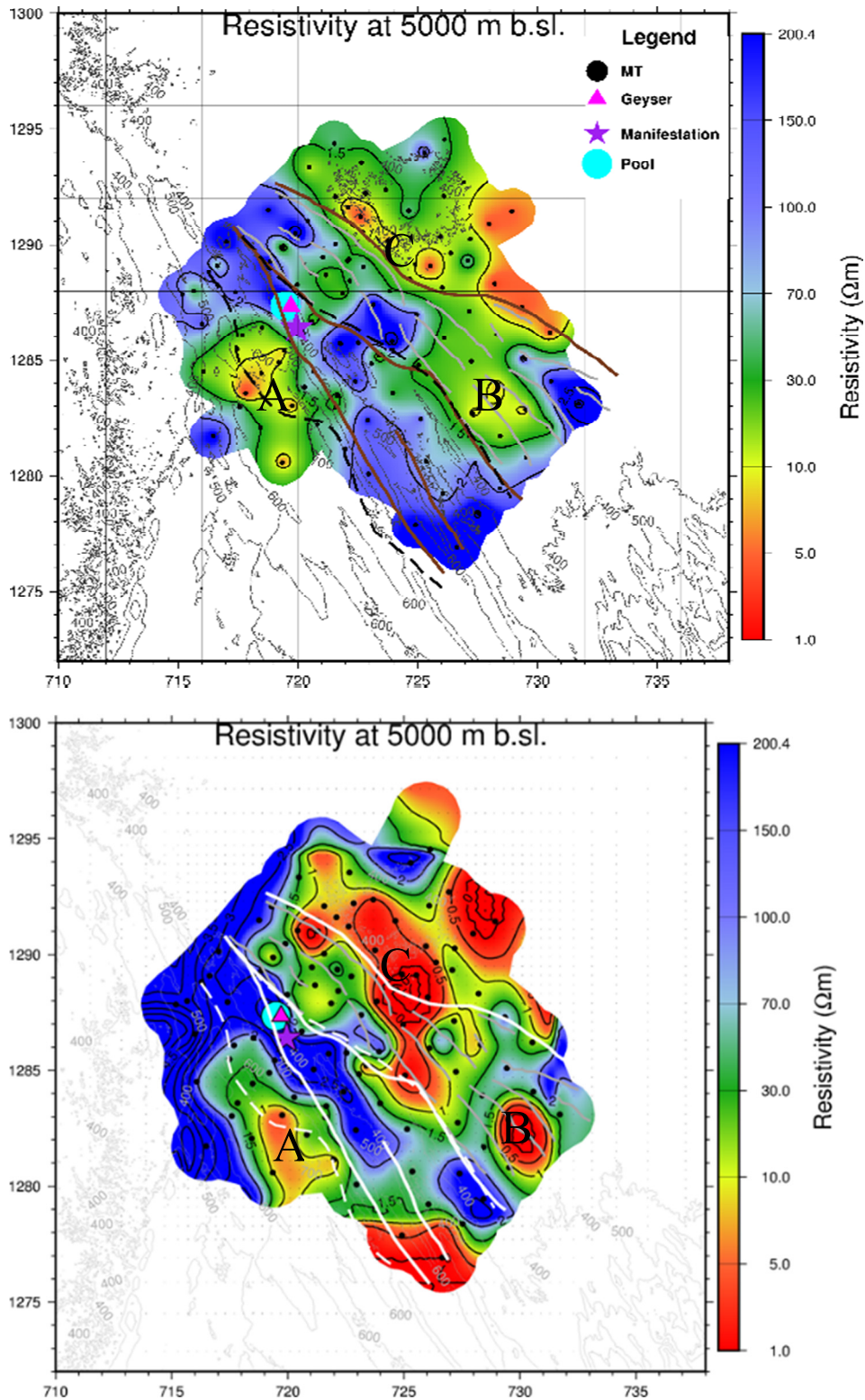


FIGURE 79: Maps showing the most prominent heat source from the up flow zone;  
 Top: 1D inversion; Bottom: 3D inversion(J1D)

From this study, locations of exploratory wells are proposed based on the resistivity results. Here, three wells are proposed in the study area:

- 1) To southwest of the survey area into one of the up flow zones along the Tendaho graben shoulder;
- 2) To the east of the survey area into the up flow zone;
- 3) To northeast of the surface manifestations of the survey area into the up flow zone, see Figure 79.

## 11. CONCLUSIONS AND RECOMMENDATIONS

Multi-dimensional inversion was done for a total of 108 MT and TEM sounding data. The 3D inversion was performed for the static shift corrected off-diagonal impedance tensor elements using 30 periods logarithmically distributed on log scale. Two initial models were run:

- A model compiled from the 1D inversion; and
- A homogenous half space of 10  $\Omega\text{m}$  resistivity.

The results of 1D inversion of MT/TEM data and 3D inversion gave comparable results at shallow depths. However, at deeper level 3D inversion reveals much more consistent details confirming that the resistivity structure in the area is highly three dimensional.

From the resistivity results which indicate the flow of the geothermal fluid and up flow zones and from the faults inferred by gravity, we can say that Alalobeda geothermal prospect is a fault- and fracture-controlled geothermal system.

At shallow depths there is a thin layer with low resistivity associated with sedimentary formation and/or low temperature alteration minerals like smectite. The low resistivity displays a thick layer of sediments as stated above (see conclusions for 1D model) but may well contain alteration minerals in the temperature range less than 230-240°C such as the highly conductive smectite. The low resistivity anomaly is well defined in both the 1D and 3D models. The high resistivity below the sediments is most likely associated with the low-permeable Afar Stratoid basalt Series. The predicted temperature in the system does not exceed 220°C and therefore the basalts most likely do not hold alteration minerals formed in the high-temperature systems at higher temperatures (> 230-240°C). However, if the system was warmer and has cooled down, the chlorite might be present. This will only be confirmed by drilling. Low resistivity at depth in the 1D model as well as the 3D model (J1D), indicates flow of geothermal fluid into the system. The H010 model does not exhibit low resistivity at depth and that might in part be due to lack of resolution at depth.

A few prominent vertical low resistivity anomalies are seen in the vertical cross-sections extending from the resistivity at shallow depth down to even 5 km depth. It turns out that these vertical anomalies follow the main NW-SE fault in the area. The most plausible explanation to this is that these anomalies show the pattern of the geothermal fluid along the faults from depth up to the sedimentary layers. The pathway may contain smectite but the low resistivity may also be caused by the high temperature of the geothermal fluid and or salinity. An example of this is shown Figures 64-71 as resistivity cross-sections through the area.

The 1D and 3D modelling results show resistivity discontinuities that have confirmed faults and lineaments inferred by gravity.

In the vicinity of the geothermal areas, the most identifiable point of tectonic intersection is near Alalobeda prospect, where NNE-SSW trending faults of the MER terminate and deflect into the major NW-SE trend that bounds the graben on its southwest edge (Stimac et al., 2014). This coincides with the potential main up flow zone.

It is recommended to site three exploratory wells, aiming at the up flow zones along faults 1 and 2 in Figure 78.

## REFERENCES

- Abbate, E., Passerini, D., and Zan, L., 1995: Strike-slip faults in a rift area: A transect in the Afar Triangle, East Africa. *Tectonophysics* 241, 67-97.
- Aquater, 1979: *Prefeasibility study, phase I – Geothermal resources exploration project – Tendaho area*. EIGS and Ministry of Foreign Affairs of Italy, San Lorenzo in Campo, report IDROGE A04221.
- Aquater, 1980: *Geothermal resource exploration project Tendaho area, feasibility study - Phase II*. EIGS and Ministry of Foreign Affairs of Italy, San Lorenzo in Campo, report.
- Aquater, 1996: *Tendaho geothermal project, final report*. MME, EIGS, Government of Italy, Ministry of Foreign Affairs, San Lorenzo in Campo, report.
- Archie, G.E., 1942: The electrical resistivity log as an aid in determining some reservoir characteristics. *Tran. AIME*, 146, 54-67.
- Armadillo E., Rizzello, D., and Stimac J., 2014: *Geophysical summary of the Tendaho area*. Report for United Nations Environmental Program and the Geological Survey of Ethiopia.
- Árnason, K., 1989: *Central-loop transient electromagnetic sounding over a horizontally layered earth*. Orkustofnun, Reykjavík, report OS-89032/JHD-06, 129 pp.
- Árnason, K., 2006a: *TemX. A graphically interactive program for processing central-loop TEM data, a short manual*. ÍSOR – Iceland GeoSurvey, Reykjavík, 10 pp.
- Árnason, K., 2006b: *TEMTD: A program for 1D inversion of central-loop TEM and MT data, a short manual*. ÍSOR – Iceland GeoSurvey, Reykjavík, 16 pp.
- Árnason, K., 2008: *The magneto-telluric static shift problem*. ÍSOR – Iceland Geo-Survey, report, ISOR-08088, 17 pp.
- Árnason, K., 2015: The static shift problem in MT soundings. *Proceedings of the World Geothermal Congress 2015, Melbourne, Australia*, 19-25.
- Árnason, K., Eysteinnsson, H., and Hersir, G.P., 2010: Joint 1D inversion of TEM and MT data and 3D inversion of MT data in the Hengill area, SW Iceland. *Geothermics*, 39, 13-34.
- Árnason, K., Flóvenz, Ó.G., Georgsson, L., and Hersir, G.P., 1987: Resistivity structure of high temperature geothermal system in Iceland. *Proceedings of International Union of Geodesy and Geophysics (IUGG) XIX General Assembly, Vancouver, Canada, Abstract V-2*, 477.
- Árnason, K., Karlsdóttir, R., Eysteinnsson, H., Flóvenz, Ó.G., and Gudlaugsson, S.Th., 2000: The resistivity structure of high-temperature geothermal systems in Iceland. *Proceedings of the World Geothermal Congress 2000, Kyushu-Tohoku, Japan*, 923-928.
- Battistelli, A., Amdeberhan, Y., Calore, C., Ferragina, C. and Wale, A., 2002: Reservoir engineering assessment of Dubti geothermal field, northern Tendaho Rift, Ethiopia. *Geothermics*, 31, 381-406.
- Bekele, B., 2012: *Review and reinterpretation of geophysical data of Tendaho geothermal field*. GSE, Addis Ababa, unpublished report, 96 pp.
- Belachew, M., Ebinger, C., and Cote, D., 2013: Source mechanisms of dike-induced earthquakes in the Dabbahu-Manda Hararo rift segment in Afar, Ethiopia: implications for faulting above dikes. *Geophys. J. Int.*, 192, 907-917.

- Berdichevsky, M.N., and Dmitriev, V.I., 1976: Basic principle of interpretation of magnetotelluric curves. In: Adam, A., (ed), *Geoelectric and geothermal studies*. Akademini Kiado, 165-221.
- Berdichevsky, M.N., and Dmitriev, V.I., 2002: *Magnetotellurics in the context of the theory of ill-posed problems*. Society of Exploration of Geophysicists, USA, 215 pp.
- Berckhemer, H., and Baier, B., 1975: Deep seismic sounding in Afar region and on the highland of Ethiopia. *Proceedings of the International Symposium on the Afar Region and Related Rift Problems*. Schweizerbart, I, Stuttgart, 89-107.
- Berkthold, A., 1975: Magneto-telluric measurements in the Afar area. Afar Depression of Ethiopia. *Proceeding of the International Symposium on the Afar Region and Related Rift Problems*, Schweizerbart, I, Stuttgart, 262-275.
- Beyene A.M., and Abdelsalam, M.G., 2005: Tectonics of the Afar Depression. A review and synthesis. *J. African Earth Sciences*, 41-1/2, 41-59.
- Cagniard, L., 1953: Basic theory of the magneto-telluric methods of geophysics prospecting, *Geophysics*, 18, 605-645.
- Cattin, R., Doubre, C., and de Chabalier, J.B., 2005: Numerical modelling of Quaternary deformation and post-rifting displacement in the Asal-Ghoubbert rift (Djibouti, Africa). *Earth Planet. Sci Lett.*, 239, 352-367.
- Christensen, A., Auken, E., and Sorensen, K., 2006: The Transient electromagnetic method. *Ground Water Geophysics*, 71, 179-225.
- Clarke, J., Gamble, T.D., Goubau, W.M., Koch, R.H., and Miracky, R.F., 1983: Remote reference magnetotellurics: Equipment and procedures. *Geophys. Prosp.*, 31, 149-170.
- Constable, C.S., Parker, R.L., Constable, C.G., 1987: Occam inversion: A practical algorithm for generating smooth models from electromagnetic sounding data. *Geophysics*, 52, 289-300.
- Craig, H., 1977: *Isotopic geochemistry and hydrology of geothermal waters in Ethiopian Rift Valley*. Scripps Institution of Oceanography, Isotopic Laboratory, report 77-14, 147 pp.
- Dakhnov, V.N., 1962: Geophysical well logging. *Q. Colorado Sch. Mines*, 57-2, 445 pp.
- DeGroot-Heldlin, C., and Constable, S., 1990: Occam's inversion to generate smooth, two-dimensional models from magnetotelluric data. *Geophysics*, 55, 1613-1624.
- Eagles, G., Gloaguen, R., and Ebinger, C., 2002: Kinematics of the Danakil microplate, *Earth Planet. Sci. Lett.*, 203, 607-620.
- Endeshaw, A., 1988: Current status (1987) of geothermal exploration in Ethiopia. *Geothermics* 17, 477-488.
- ELC, 2015a: *Consultancy services for geothermal surface exploration in Tendaho Alalobeda, Ethiopia*. ELC, geological report.
- ELC, 2015b: *Consultancy services for geothermal surface exploration in Tendaho Alalobeda, Ethiopia*. ELS, geochemical report.
- ELC, 2015c: *Consultancy services for geothermal surface exploration in Tendaho Alalobeda, Ethiopia*. ELS, gravimetric report.

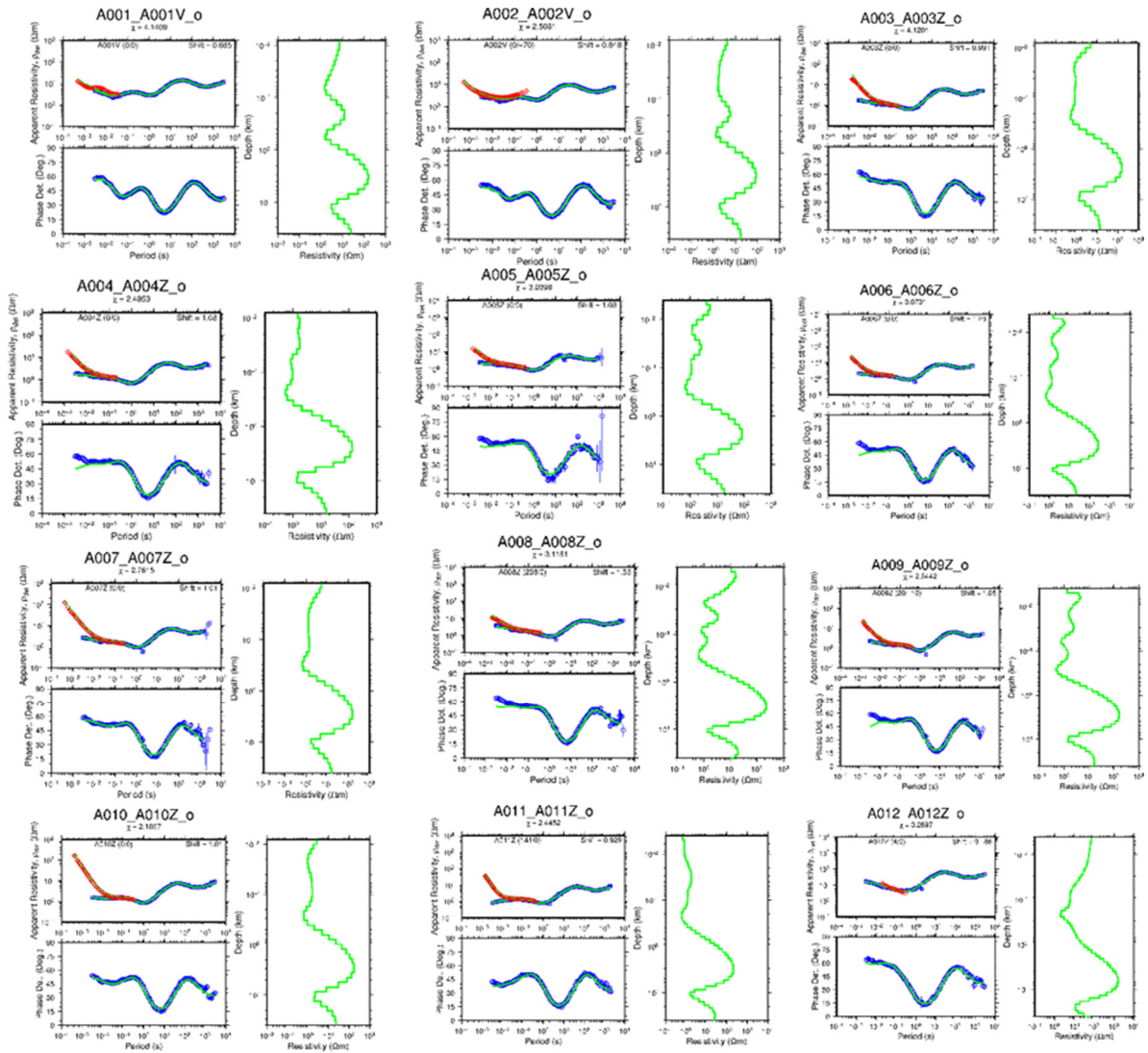
- Eysteinnsson, H., 1998: TEMRESD, TEMMAP and TEMCROSS plotting programs. ÍSOR – Iceland GeoSurvey, unpublished programs and manuals.
- Flóvenz, Ó.G., Georgsson, L.S., and Árnason, K., 1985: Resistivity structure of the upper crust in Iceland, *J. Geophys Res.*, 90-B12, 10,136-10,150.
- Flóvenz, Ó.G., Hersir, G.P., Sæmundsson, K., Ármannsson, H., and Fridriksson, Th., 2012: Geothermal energy exploration techniques. In: Sayigh, A. (ed.), *Comprehensive Renewable Energy*, 7. Elsevier, Oxford, UK, 51-95.
- Fournier, R.O., 1973: Silica in thermal waters. Laboratory and field investigations. *Proceedings of the International Symposium on Hydrogeochemistry and Biochemistry, Tokyo, 1, Clark Co., Washington D.C.*, 122-139.
- Gamble, T.D., Goubau, W.M., Clarke, J., 1979: Magnetotellurics with a remote magnetic reference. *Geophysics*, 44, 53-68.
- Giggenbach, W.F., 1988: Geothermal solute equilibria. Derivation of Na-K-Mg-Cl geothermometers. *Geochem. Cosmochim. Acta*, 52, 2749-2765.
- Giggenbach, W.F., Sheppard, D.S., Robinson B.W., Stewart M.K., and Lyon G.L., 1994: Geochemical structure and position of the Waiotapu geothermal field, New Zealand. *Geothermics*, 23, 599-644.
- Gonfiantini, R., Borsi, S., and Ferrara, G., 1973: Isotopic composition of waters from the Danakil Depression, Ethiopia. *Earth and Planetary Science Letter*, 18, 13-21.
- Goubau, W.M., Gamble, T.D., and Clarke, J., 1979: Magnetotelluric data analysis: removal of bias. *Geophysics*, 43, 1157-1169.
- Hersir, G.P., and Árnason, K., 2009: Resistivity of rocks. *Paper presented at the Short Course on Surface Exploration for Geothermal Resources, organized by UNU-GTP and LaGeo, Santa Tecla, El Salvador*, 8 pp.
- Hersir, G.P., and Björnsson, A., 1991: *Geophysical exploration for geothermal resources. Principles and applications*. UNU-GTP, Iceland, report 15, 94 pp.
- Jestin, F., Huchon, P., and Gaulier, J.M., 1994: The Somalia plate and the East African Rift System: present-day kinematics, *Geophys. J. Int.*, 116, 637-654.
- JICA, 2015: The project for formulating master plan on development of geothermal energy in Ethiopia. JICA and GSE, internal report.
- Jiracek, G.R., 1990: Near-surface and topographic distortion in electromagnetic induction. *Survey in Geophysics*, 11, 163-203.
- Jones, A.G., 2002: Magnetotelluric data processing and analysis. *MT short course, SEG*.
- Kato, Y., and Kikuchi, T., 1950: On the phase difference of earth current induced by the changes of the earth's magnetic field, part 1. *Sci. Rep. Tohoku Uni.*, 5<sup>th</sup> Ser., 2, 139-141.
- Kearey, P., and Brooks, M., 1994: *An introduction to geophysical exploration* (2<sup>nd</sup> ed.). Blackwell Scientific Publ., London, 236 pp.
- Kebede, S., 2009: Status of geothermal exploration and development in Ethiopia. *Proceedings of Short Course IV on Exploration for Geothermal Resources, organized by UNU-GTP, KenGen and GDC, Lake Naivasha, Kenya*, 35 pp.

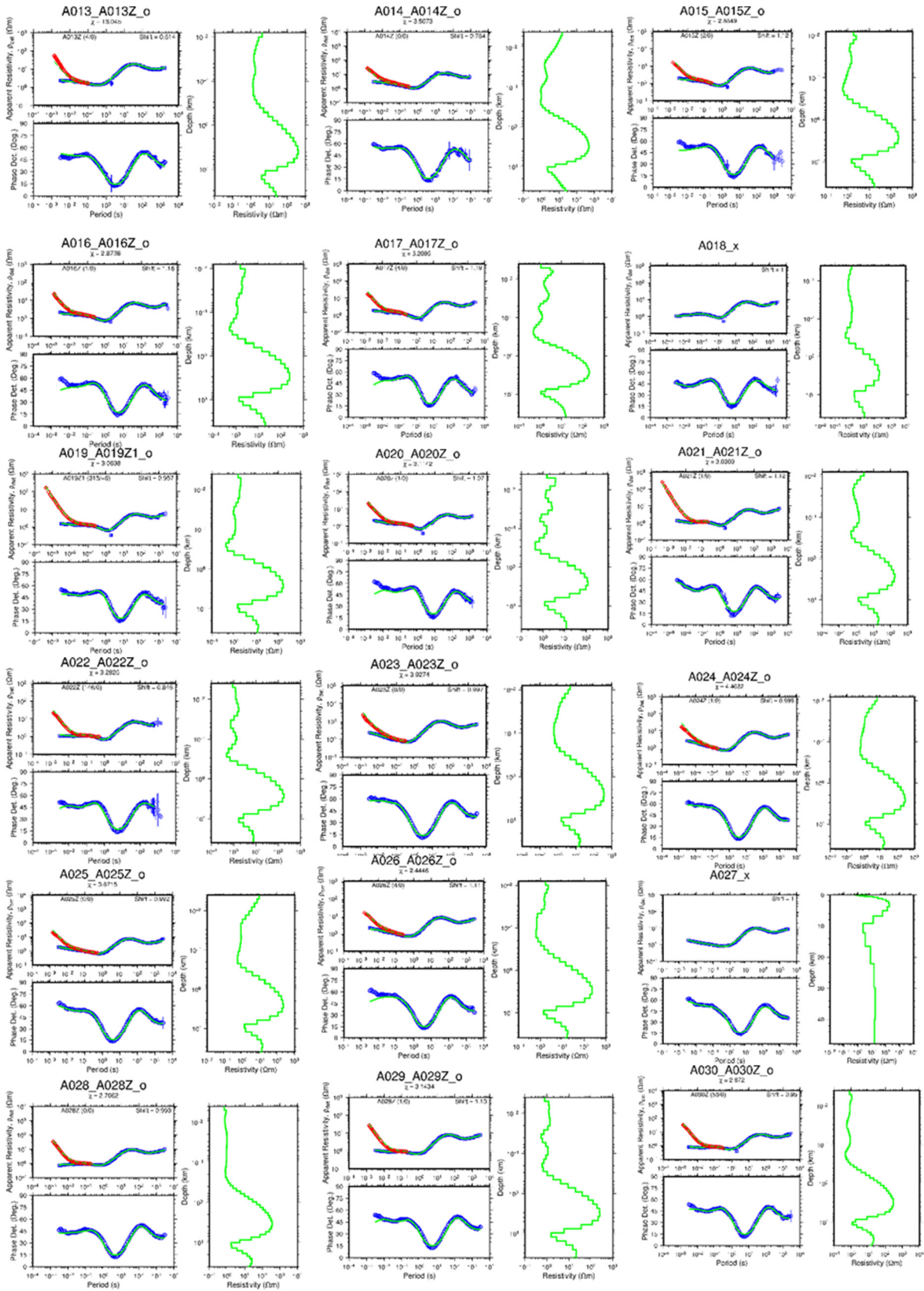
- Kebede, S., 2013: Geothermal exploration and development in Ethiopia: Status and Future plan. *Proceedings of Short Course VIII on Exploration for Geothermal Resources, organized by UNU-GTP, KenGen and GDC, Lake Naivasha, Kenya*, 35 pp.
- Keller, G.V. and Frischknecht, F.C., 1966: *Electrical methods of geophysical prospecting*. Pergamon, NY, 519 pp.
- Levenberg, K., 1944: A method for the solution of certain non-linear problems in least squares. *The Quarterly of Applied Mathematics*, 2, 164-168.
- Lévy, L., Gibert, B., Sigmundsson, F., Flóvenz, Ó.G., Hersir, G.P., Briole, P., and Pezard, P., 2018: The role of smectites in the electrical conductivity of active hydrothermal systems: electrical properties of core samples from Krafla volcano, Iceland. *Geophysical J. International*, 215-3, 1558–1582.
- Lichoro, C.M., 2013: *Multi-dimensional interpretation of electromagnetic data from Silali geothermal field in Kenya: Comparison of 1-D, 2-D and 3-D MT inversion*. University of Iceland, Faculty of Earth Sciences, MSc thesis, UNU-GTP. Iceland, report 4, 10+135 pp.
- Lkhagvasuren, S., 2016: Resistivity surveying in geothermal exploration with an application to the Eyjafjörður low-temperature area, N-Iceland. Report 25 in: *Geothermal training in Iceland*. UNU-GTP, Iceland, 469-494.
- Mamo, T., and Bekele, B., 2014: Surface geological mapping at Tendaho geothermal field, Ethiopia. *Proceedings of the ARGeo-C5 Conference, Nairobi, Kenya*, 12 pp.
- Marquardt, D., 1963: An algorithm for least-squares estimation of nonlinear parameters. *SIAM Journal on Applied Mathematics*, 11, 431-441.
- Megersa, G., and Getaneh, E., 2006: *Geological, surface hydrothermal alteration and geothermal mapping of Dubti-Semera area, Tendaho geothermal field*. GSE, Addis Ababa, unpubl. report, 66 pp.
- Pádua, M.B, Padilha, A.L. and Vitorello, Í., 2002: Disturbances on magnetotelluric data due to DC electrified railway: a case study from Southeastern Brazil. *Earth, Planets and Space*, 54 591-596.
- Parkinson, W., 1959: Directions of rapid geomagnetic variations. *Geophysics. J. R. Astr. Soc.*, 2, 1-14.
- Phoenix Geophysics, 2009: *V5 system 2000 MTU/MTU-A user's guide*. Phoenix Geophysics Ltd., Toronto, Canada. 178 pp.
- Quist, A.S., and Marshall, W.L., 1968: Electrical conductance of aqueous sodium chloride solutions from 0 to 800°C and at pressures to 4000 bars. *J. Phys. Chem.*, 72, 684-703.
- Reddy, I.K., Rankin, D., Phillips, R.J. 1977: Three-dimensional modelling in magnetotelluric and magnetic vibrational sounding. *Geophys. J.R. Astr. Soc.*, 51, 313-325.
- Redfield, T.F., Wheeler, W.H., and Often, M., 2003: A kinematic model for the development of the Afar depression and its paleogeographic implications. *Earth Planet. Sci Lett.*, 216, 383-398.
- Simpson, F., and Bahr, K., 2005: *Practical magnetotellurics*. Cambridge University Press, Cambridge, UK, 270 pp.
- Sims, W.E., Bostic, F.X., and Smith, H.W., 1971: The Estimation of Magnetotelluric Impedance Tensor Elements from Measured Data. *Geophysics*, 36 (5): 798-967.
- Siripunvaraporn, W., and Egbert, G., 2000: An efficient data-subspace inversion method for 2-D magnetotelluric data. *Geophysics*, 65, 791-803.

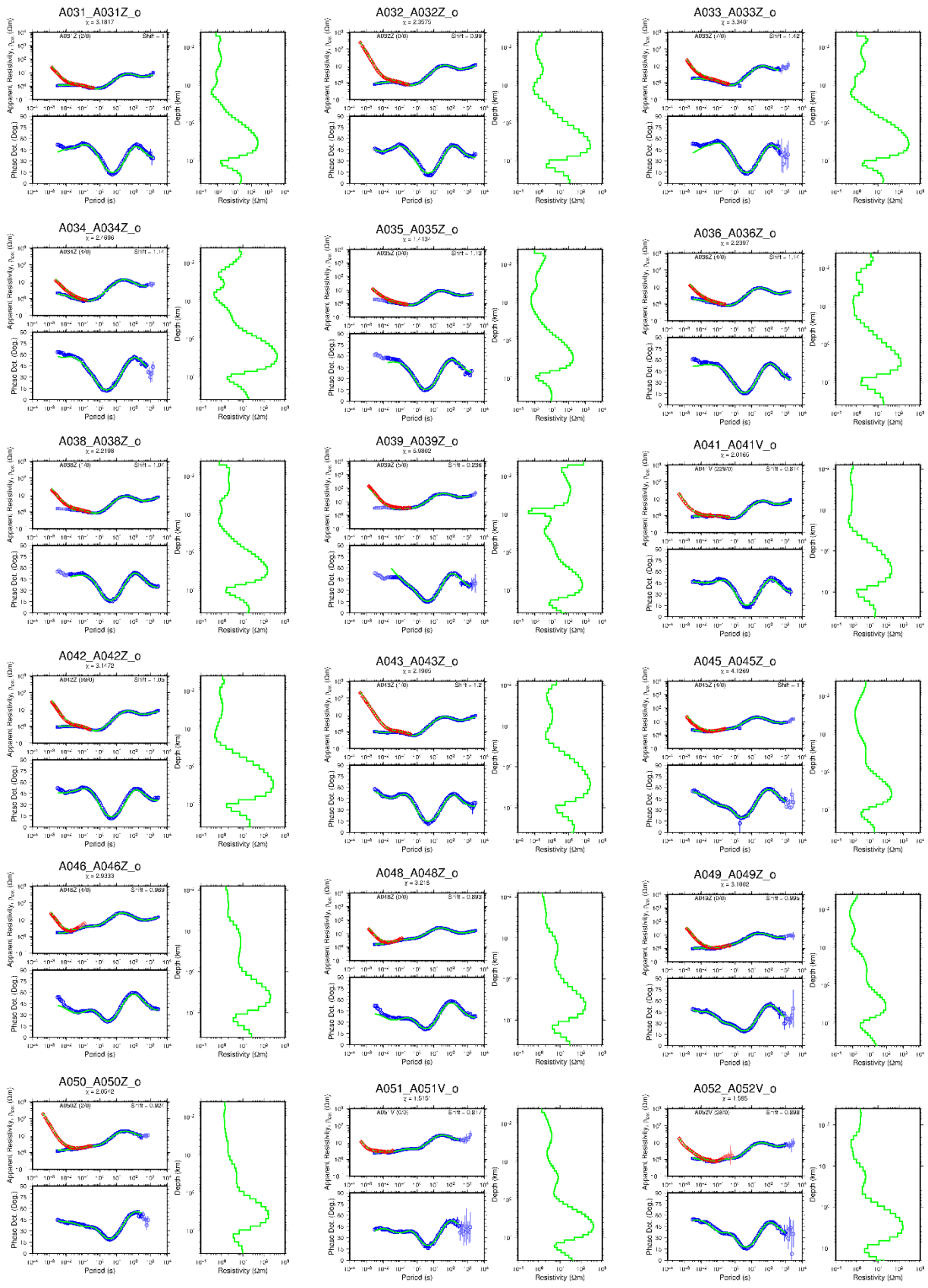
- Siripunvaraporn, W., and Egbert, G., 2009: WSINV3DMT: vertical magnetic field transfer function inversion and parallel implementation. *Phy. Earth Planet. Int.* **173**, 317-329.
- Siripunvaraporn, W., Egbert, G., Lenbury, Y. and Uyeshima, M., 2005: Three dimensional magnetotelluric: data space method. *Physics of the Earth and Planetary Interiors*, **150**, 3-14.
- Stein, R. S., Briole, P., Ruegg, J.C., Tapponnier, P., and Gasse, F., 1991: Contemporary Holocene and Quaternary deformation of the Asal Rift, Djibuti: Implications for the mechanics of slow spreading ridges. *J. Geophys. Res.*, **96**, 21, 789-21, 806.
- Sternberg, K.B., Wasburne, J.C., and Pellerin, L., 1988: Correction for the static shift in magnetotellurics using transient electromagnetic soundings. *Geophysics*, **53-11**, 1459-1468.
- Stimac, J., 2015: Intrusion related geothermal systems. In: *Encyclopedia of Volcanoes* (2<sup>nd</sup> ed.), 799-822.
- Stimac, J., Armadillo, E., Rizzello, D., and Mandeno, E. 2014: *Geothermal resource assessment of the Tendaho area*. Completed for UNEP and the Geological Survey of Ethiopia, internal report, 83 pp.
- Swift, C.M., 1967: *A magnetotelluric investigation of an electrical conductivity anomaly in the southwestern United States*. *Geology and geophysics*. Massachusetts Institute of Technology, Ph.D. thesis, Cambridge, MA.
- Teclu, A., and Mekonen, M., 2013: *Preliminary radon soil geochemical survey at Alalobeda geothermal prospect (Tendaho geothermal field)*. GSE, GREAD, Addis Ababa, internal report, 55 pp
- Teklemariam, M., and Beyene, K., 2005: Geothermal exploration and development in Ethiopia. *Proceedings of the World Geothermal Congress, Antalya, Turkey*, 24-29.
- Teklesenbet B., A., 2012: *Multidimensional inversion of MT data from Alid geothermal area, Eritrea; comparison with geological structures and identification of a geothermal reservoir*. University of Iceland, MSc thesis, UNU-GTP, report 1, 10+92 pp
- Tikhonov, A.N., 1950: On determination of electric characteristics of deep layers of the Earth crust (in Russian). *Dokl. Acad. Nauk SSSR* **151**, 295–297
- UNDP, 1973: *Geology, geochemistry and hydrology of hot springs of the East African Rift System within Ethiopia*. UNDP, December report DD/SF/ON/11, NY.
- Ussher, G., Harvey, C., Johnstone, R., and Anderson, E., 2000: Understanding the resistivities observed in geothermal systems. *Proceedings of the World Geothermal Congress 2000, Kyushu-Tohoku, Japan*, 1915-1920.
- Volland, H., 1982: *Handbook of atmospheric* (vol.1). CRC Press, Boca Raton, FL.
- Vozoff, K., 1990: Magnetotelluric principle and practice. *Geophysics*, **99**, 441-471.
- Wiese, H., 1962: Geomagnetic depth probing. Part II: The direction of strike of the underground structures of the electrical resistance, derived from geomagnetic variations (in German). *Geofis. Pura et Appl.*, **52**, 83–103.
- Wolfenden, F.M., Williams, M.A.J., and Aumento, F., 2004: Tensional fissures and crustal extension rates in the northern part of the Main Ethiopian Rift. *J. Afr. Earth Sci.*, **38**, 183-197.

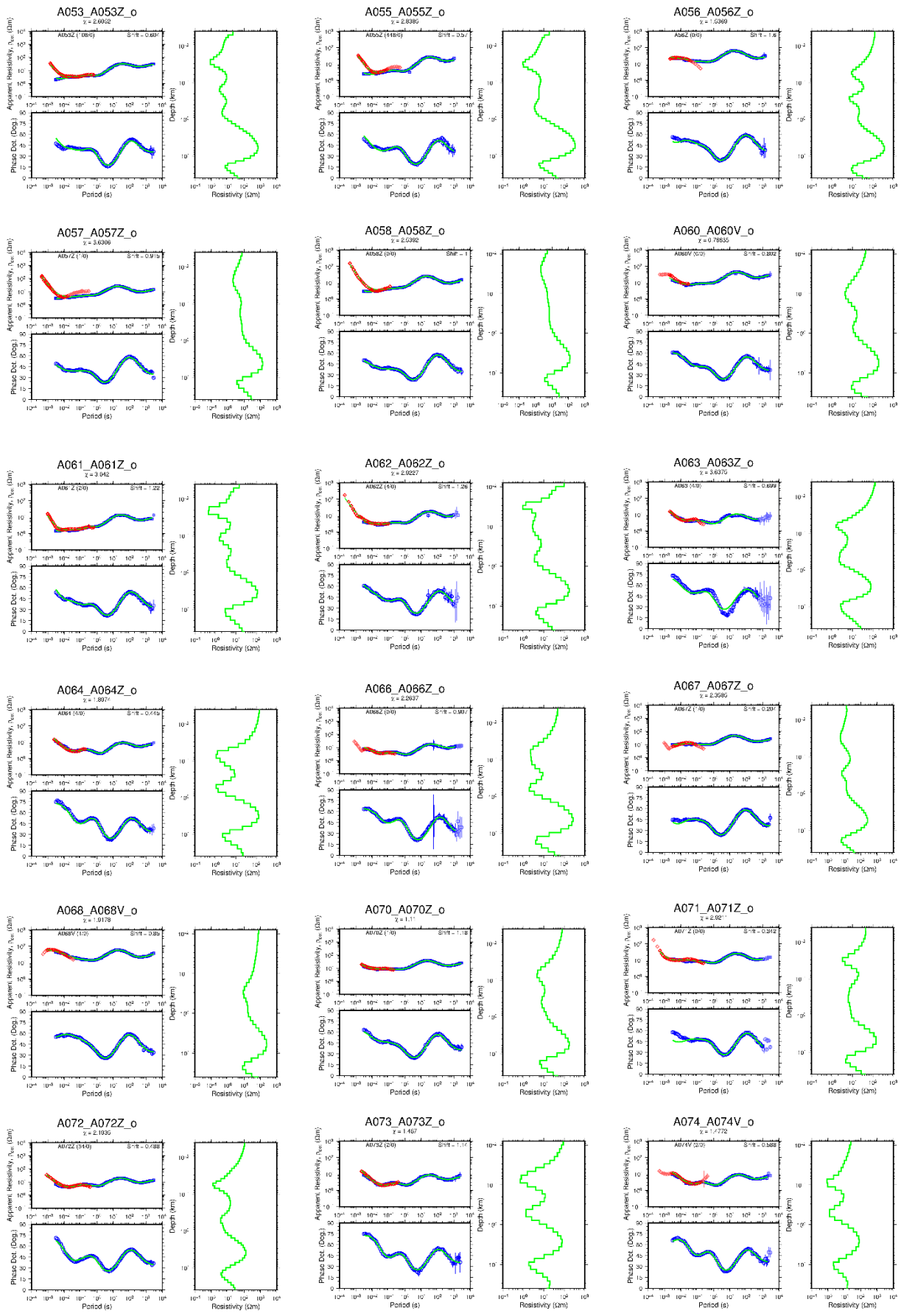
## APPENDIX I: 1D joint inversion of MT and TEM data

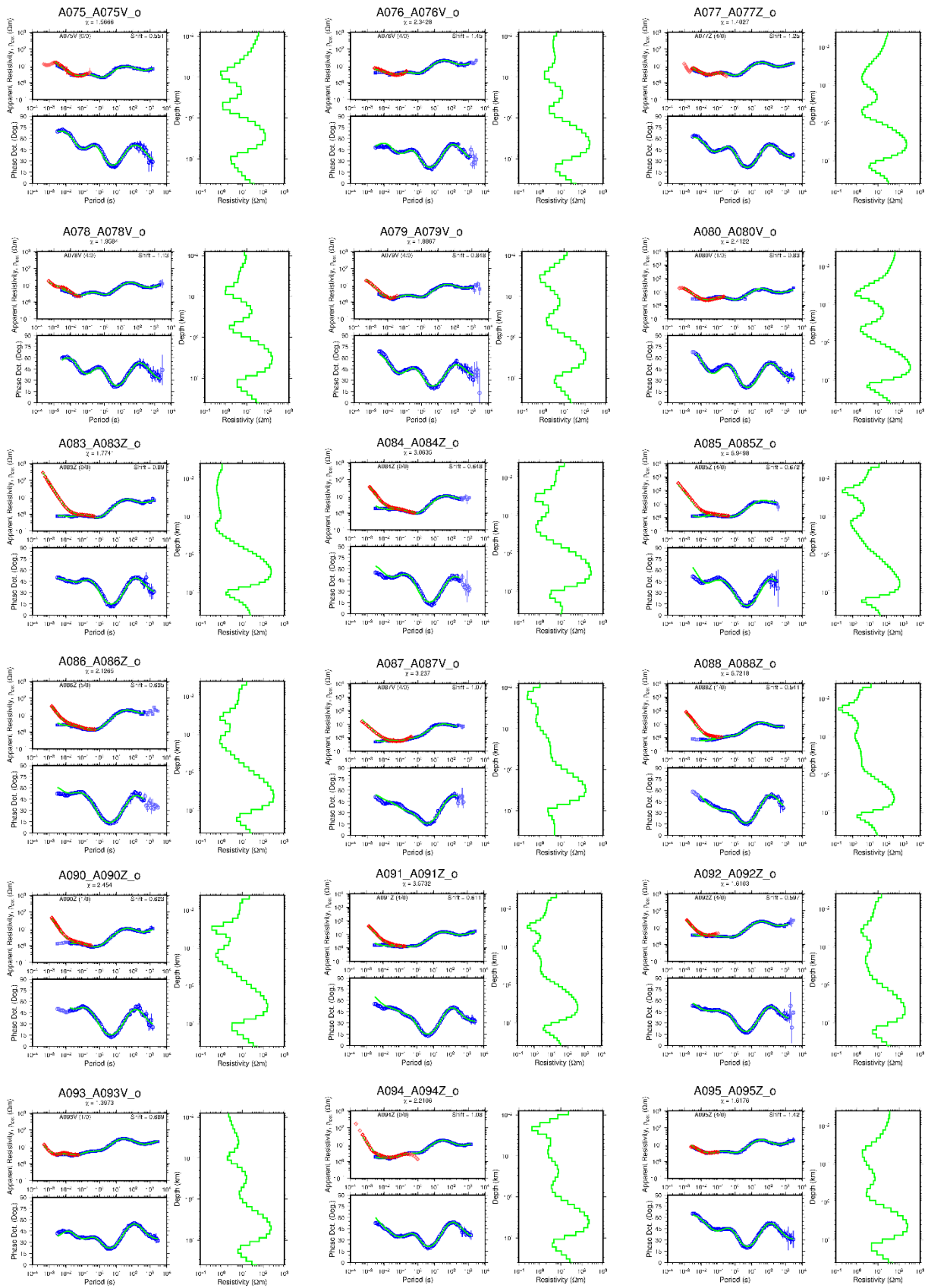
Results from the 1D joint inversion of MT and TEM data are shown here. Red diamonds represent TEM apparent resistivity transformed to a pseudo-MT curve; blue squares are measured apparent resistivity; blue circles are apparent resistivity and phase derived from the determinant of the MT impedance tensor, light blue data not used for the inversion, vertical blue lines error bars. Green lines to the right represent results of the 1D resistivity inversion model and to the left panel its synthetic MT apparent resistivity and phase response. The number on top of each figure corresponds to the name of the MT and TEM station; number below the MT station: chi square ( $\chi$ ) – a measure of the fit between the measured data and the model data. The number in parentheses (x/z) represents the distance between the two stations and their elevation difference, respectively. The resistivity model is plotted in a logarithmic scale (log10) both for the resistivity and the phase.

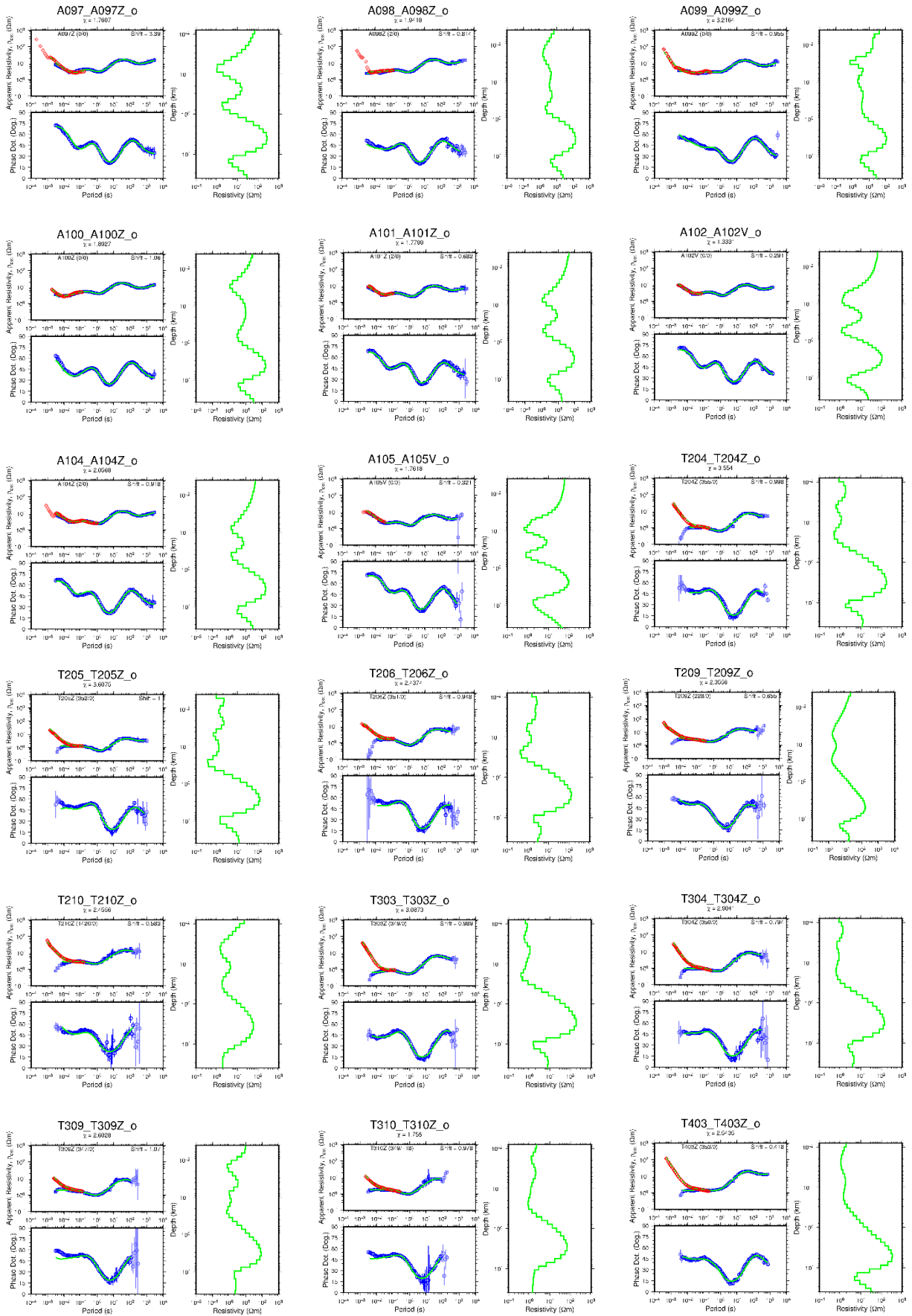


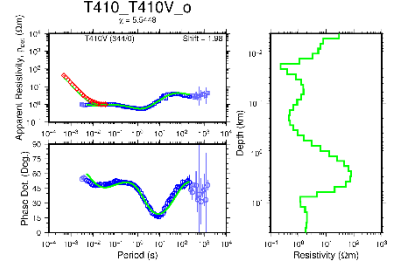
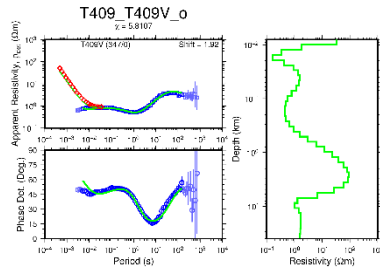
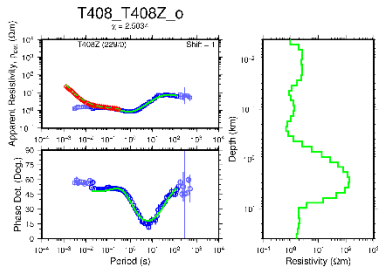
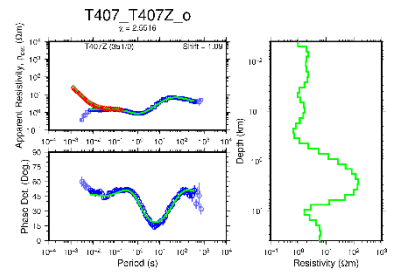
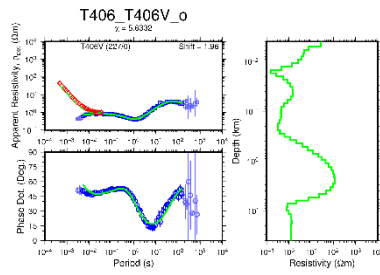
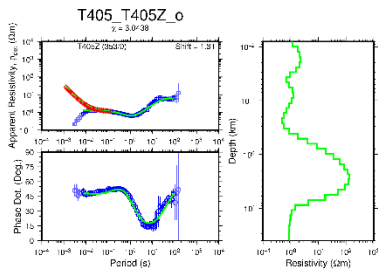












**APPENDIX II: Resistivity cross-sections based on 1D joint inversion;  
presented for two different depth ranges**

Location of the cross-sections is shown in Figure 40 in the main text.

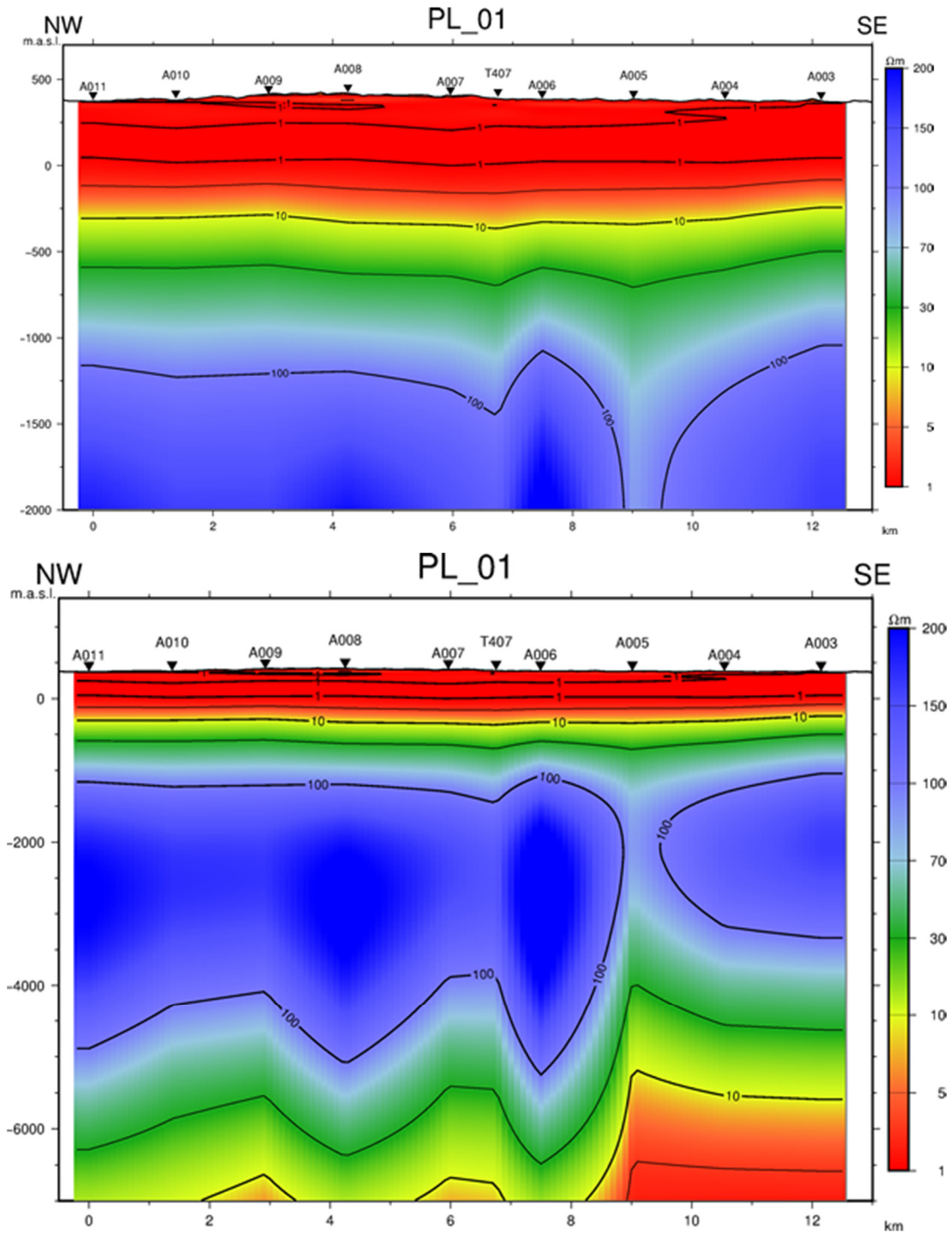


FIGURE 1: Cross-section PL-01

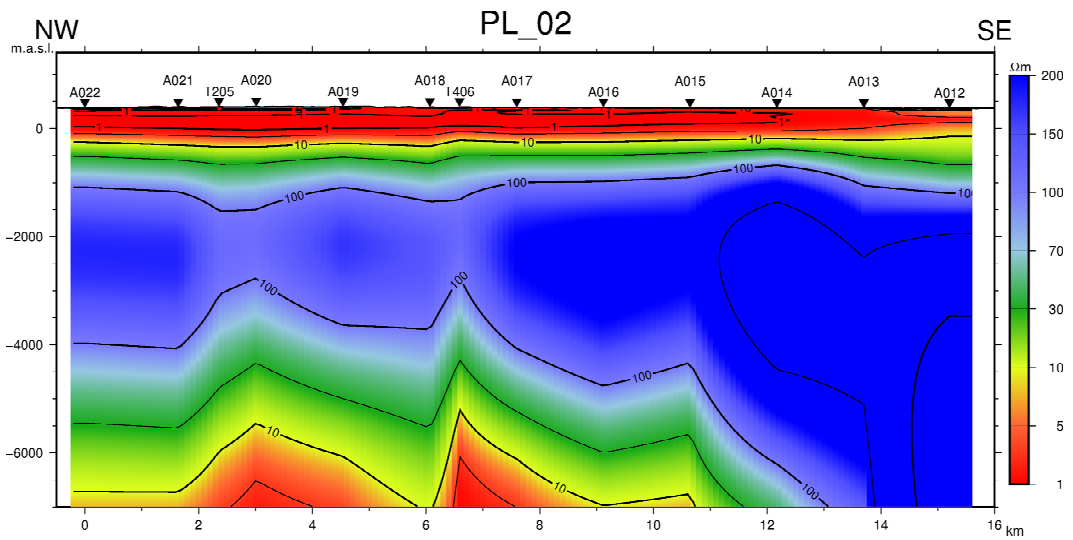
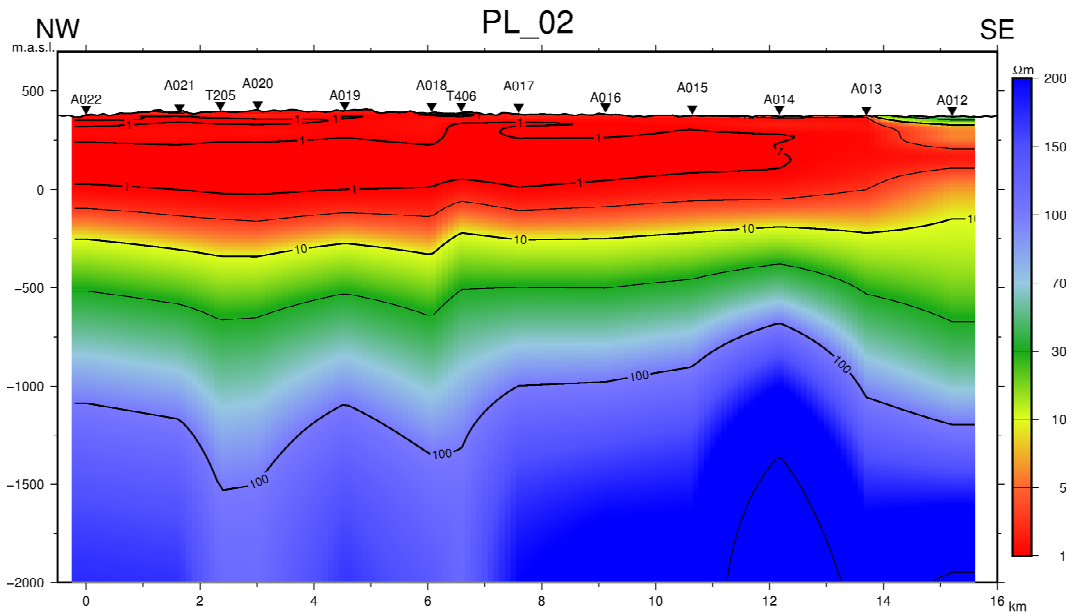
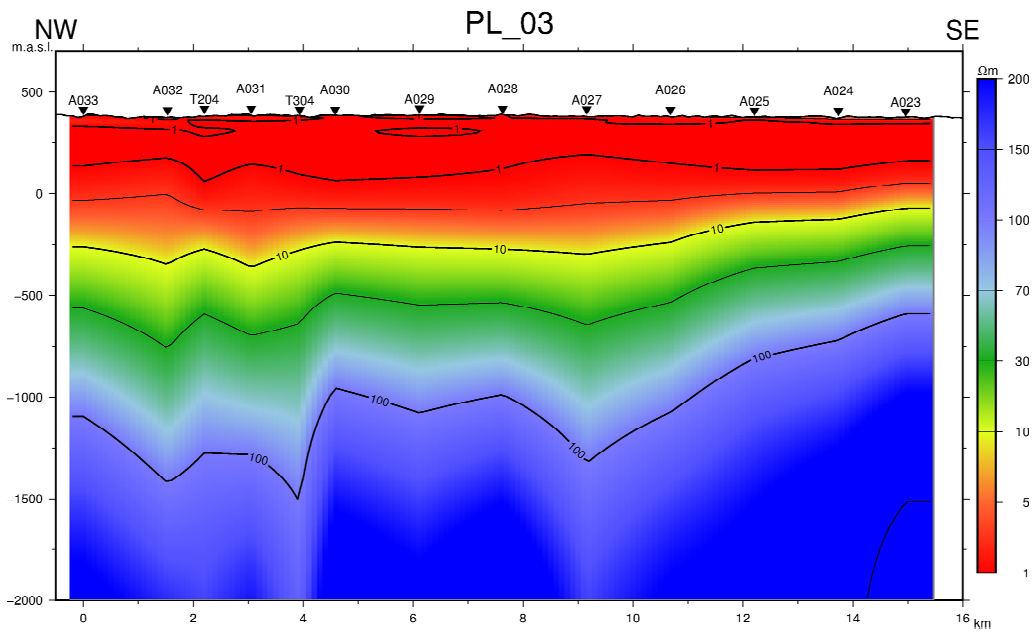


FIGURE 2: Cross-section PL-02



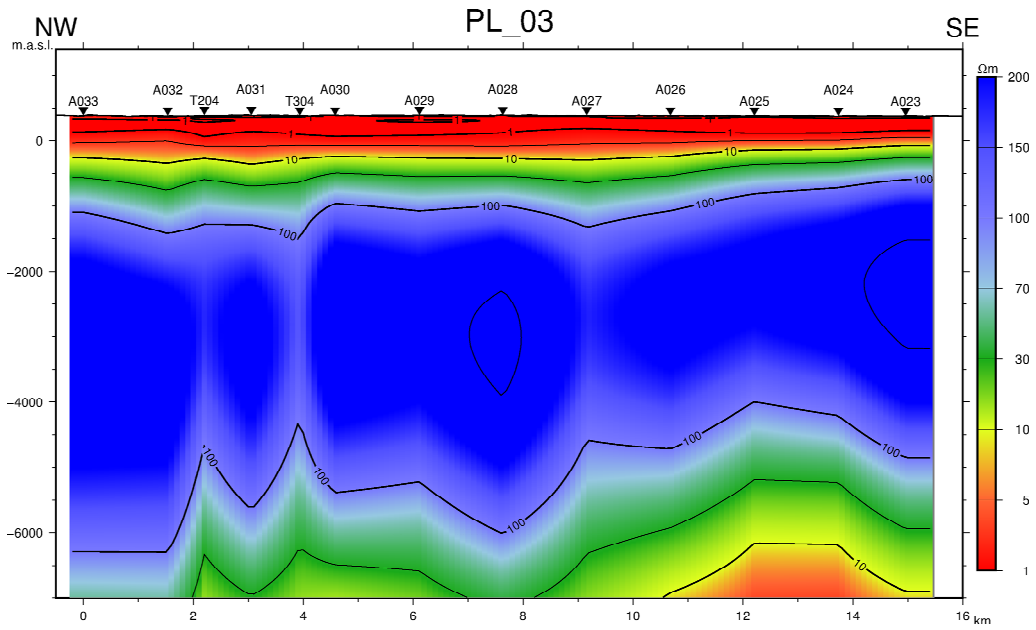


FIGURE 3: Cross-section PL-03

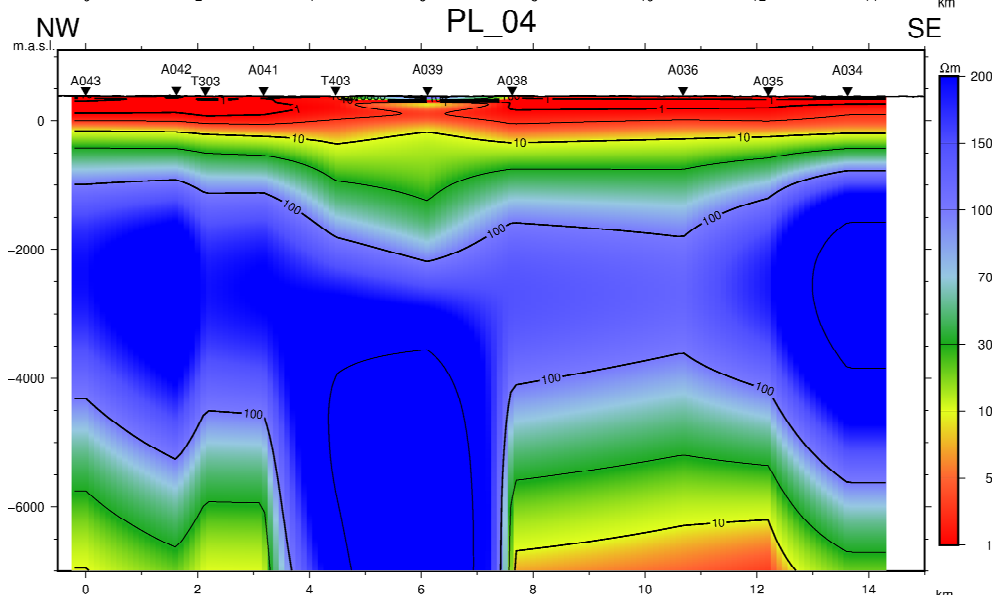
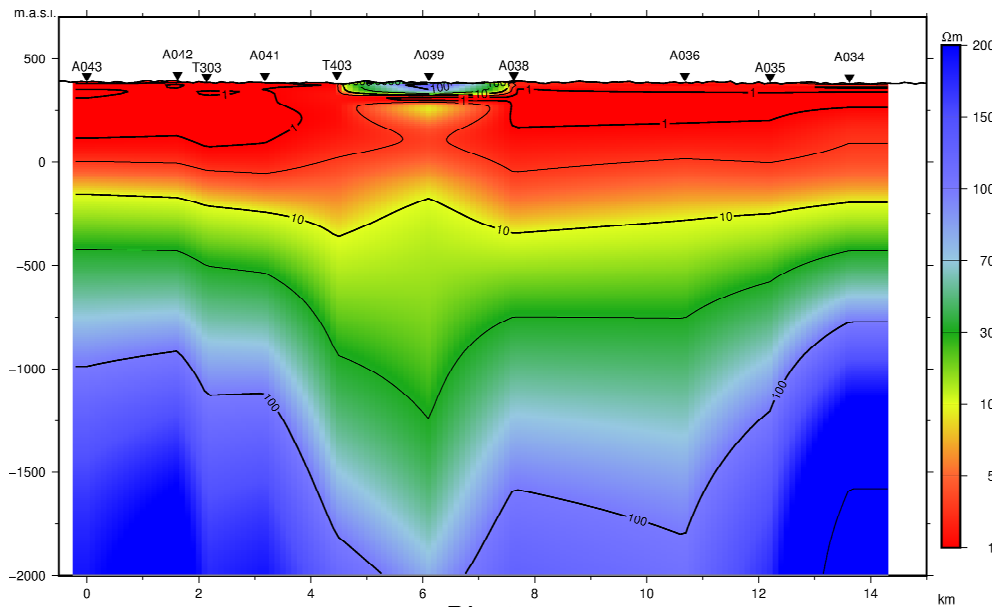


FIGURE 4: Cross-section PL-04

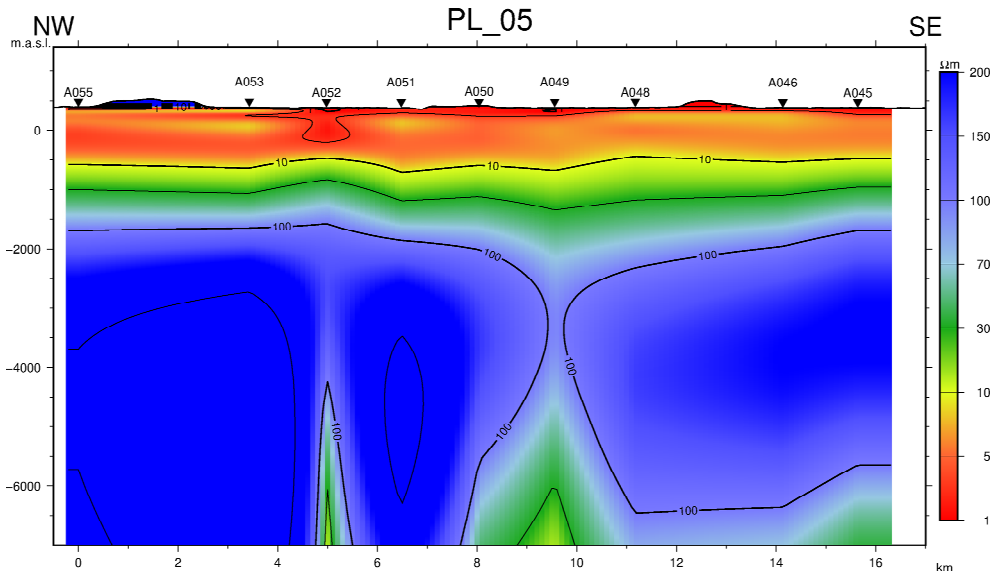
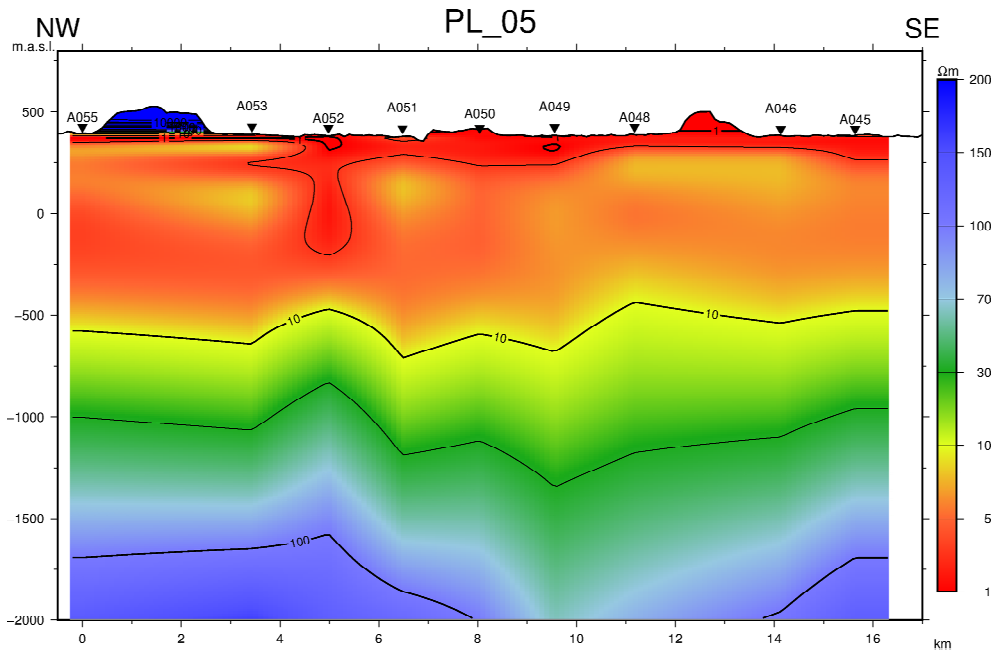
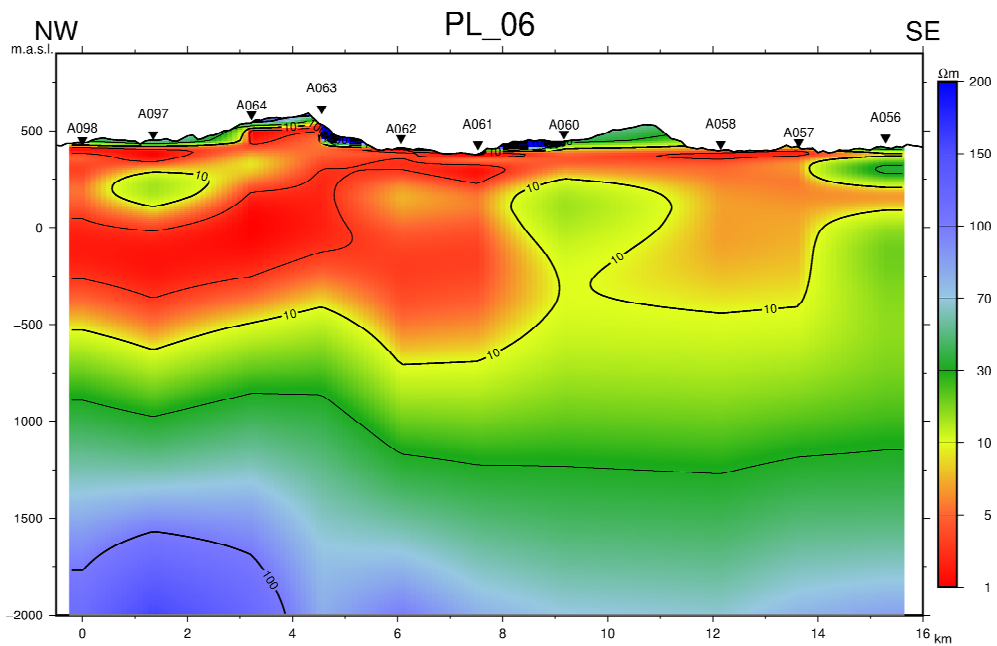


FIGURE 5: Cross-section PL-05



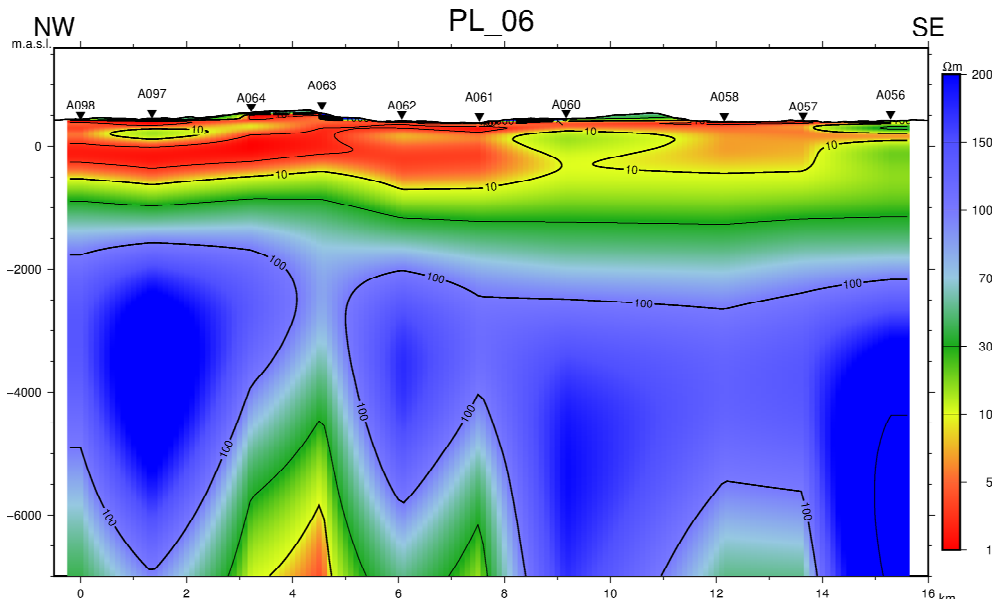


FIGURE 6: Cross-section PL-06

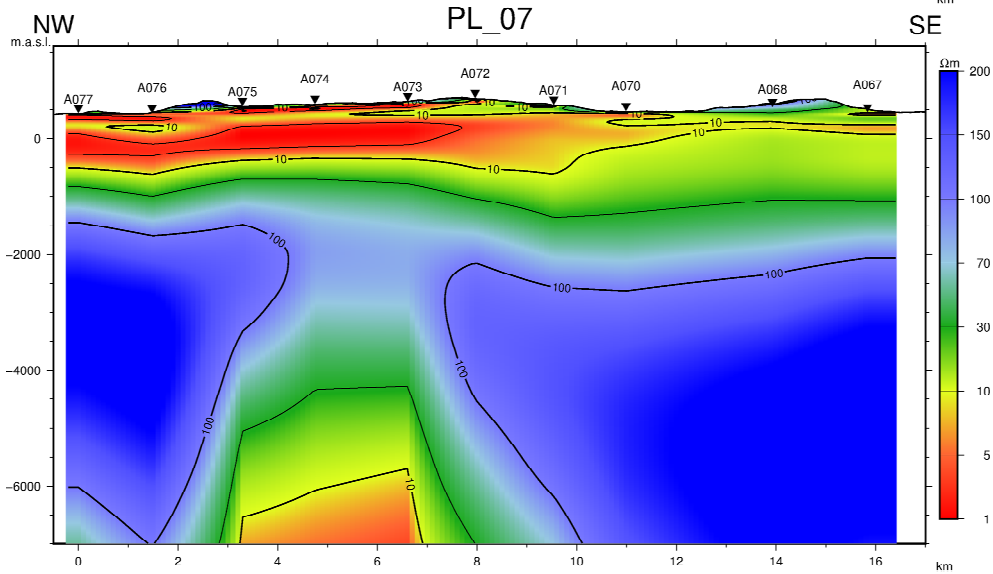
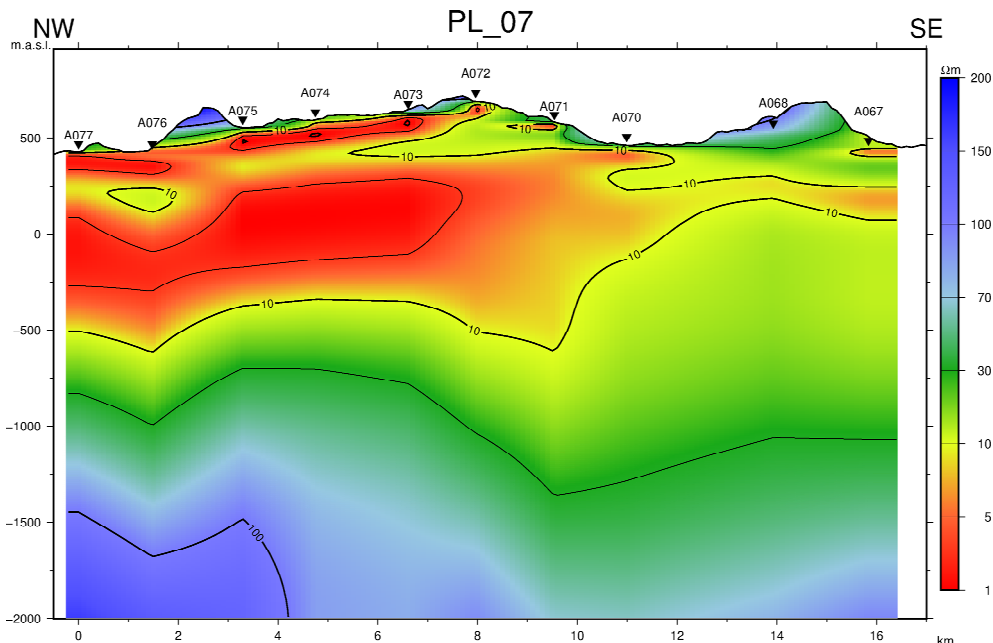


FIGURE 7: Cross-section PL-07

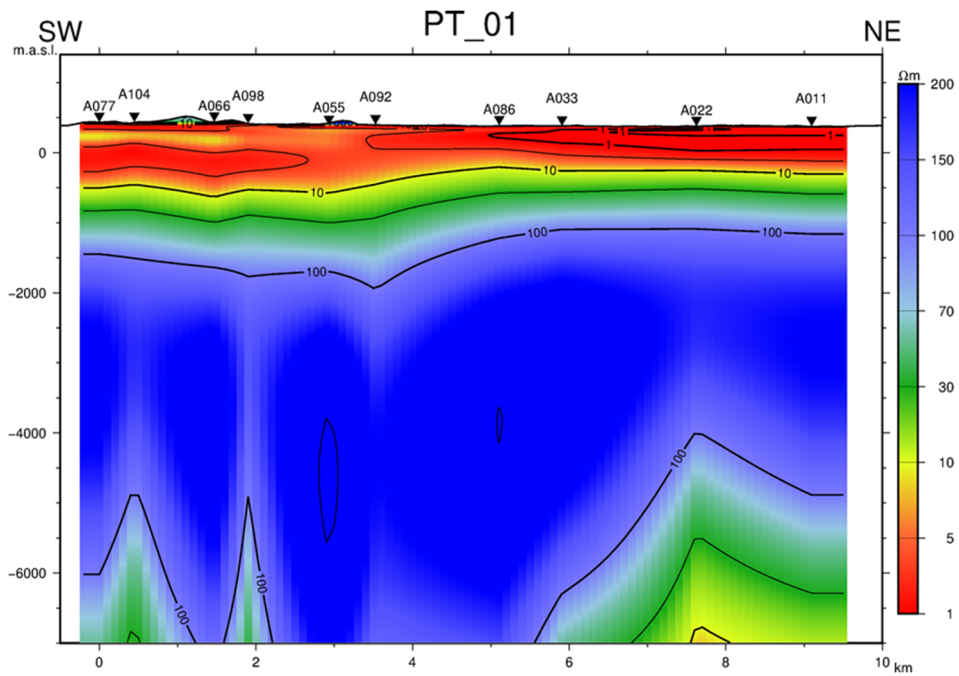
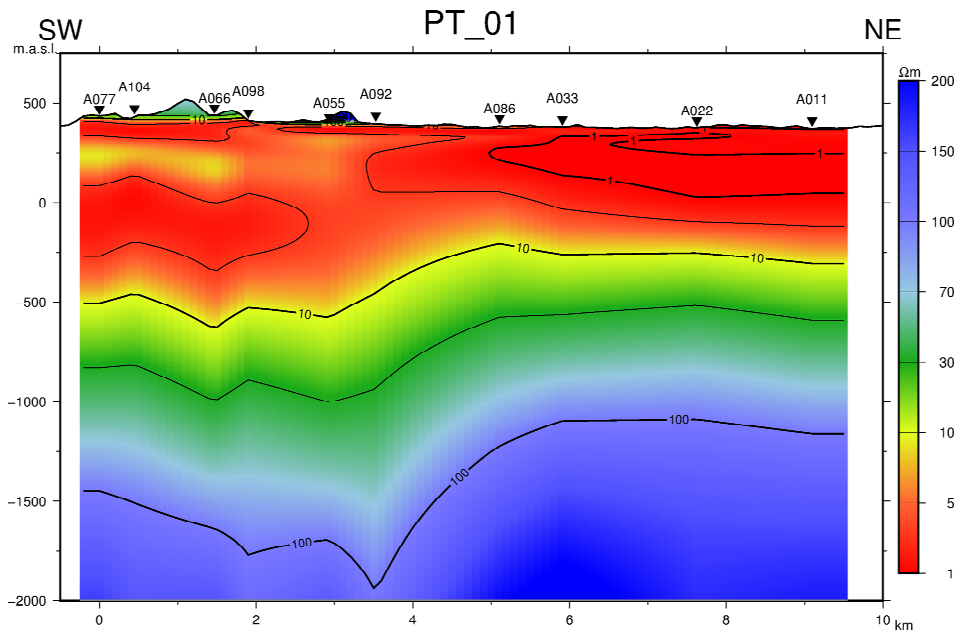
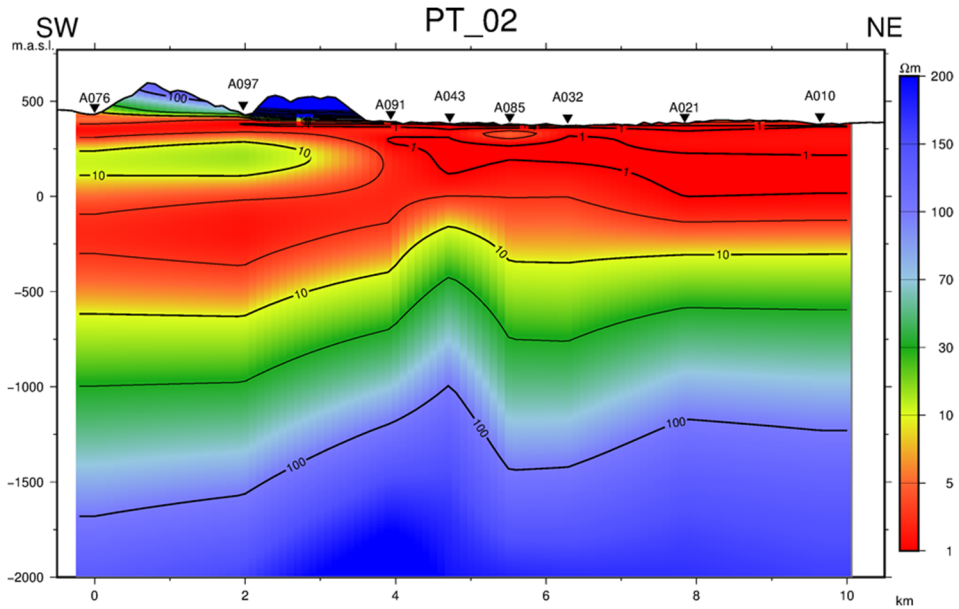


FIGURE 8: Cross-section PT-01



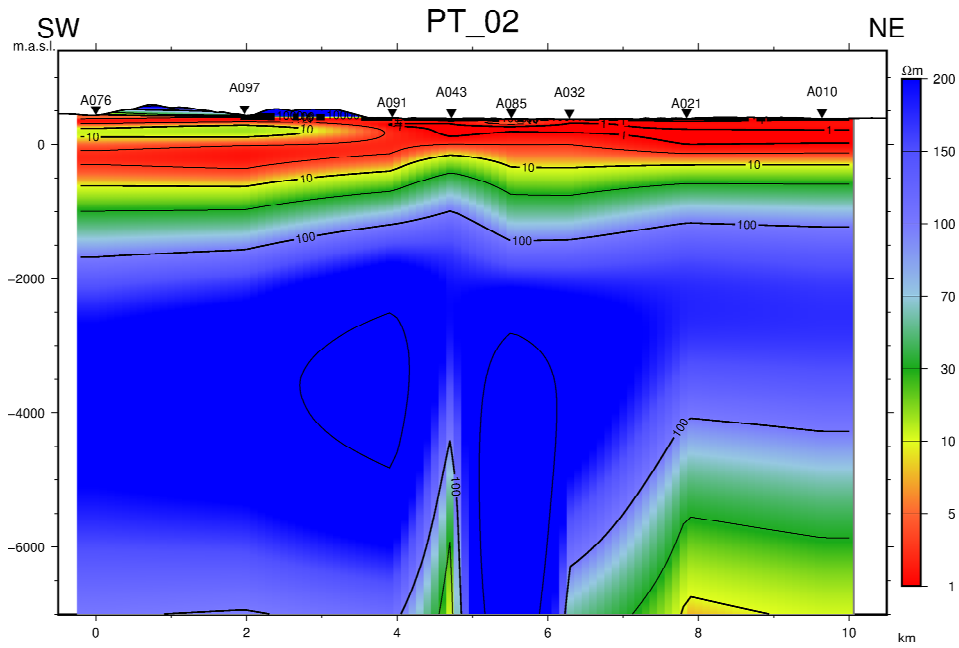


FIGURE 9: Cross-section PT-02

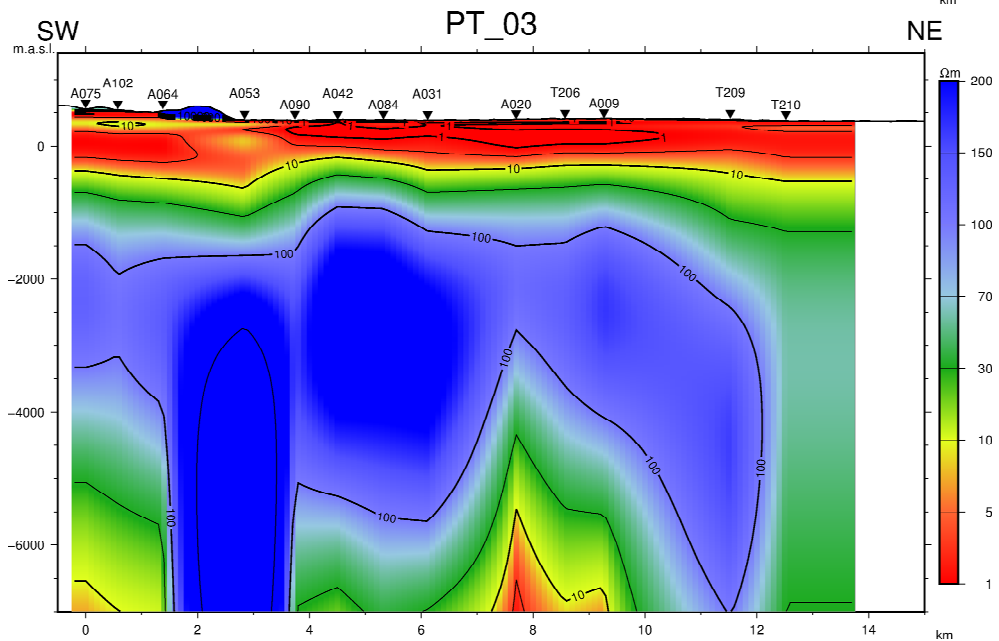
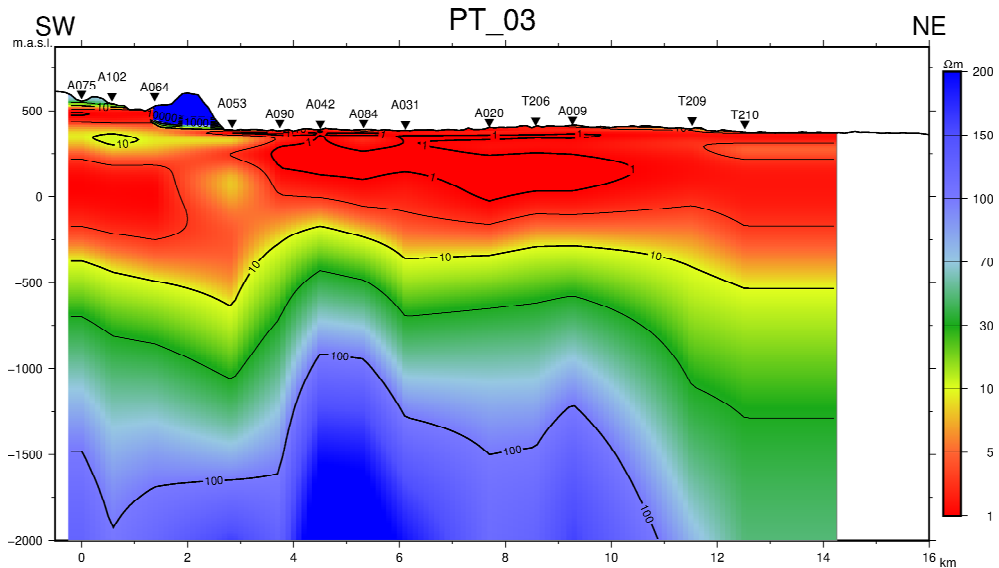


FIGURE 10: Cross-section PT-03

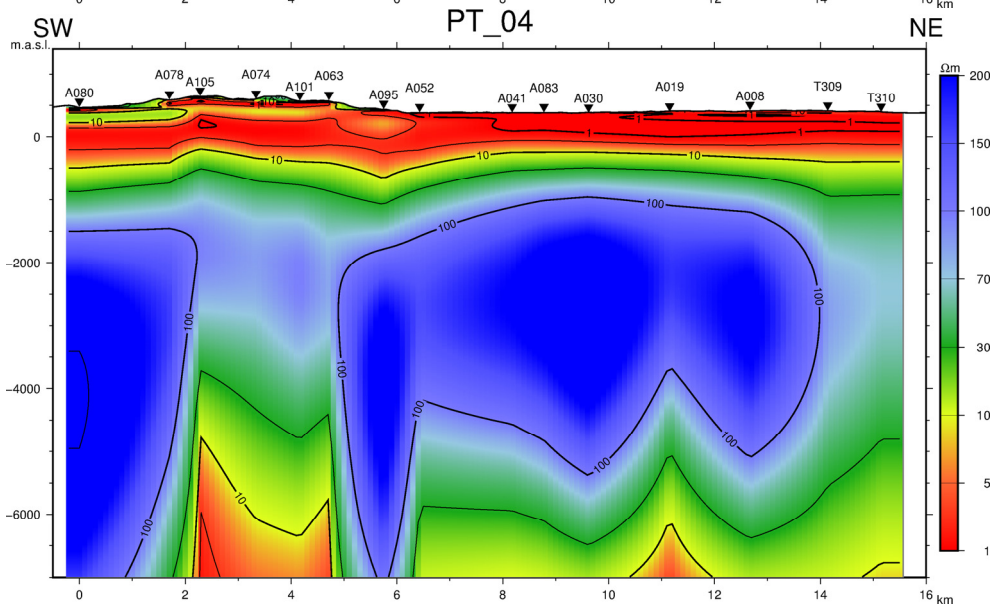
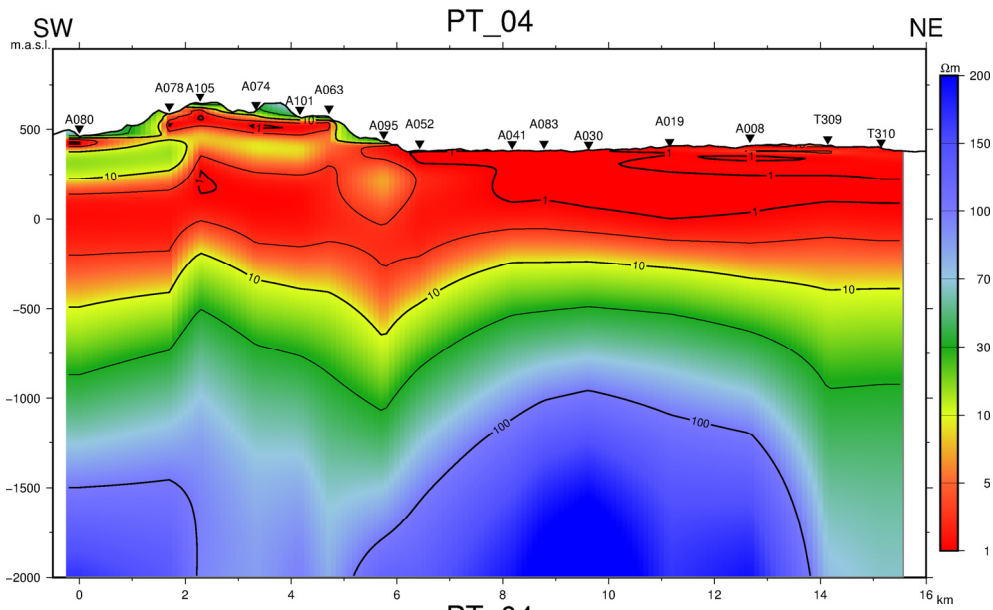
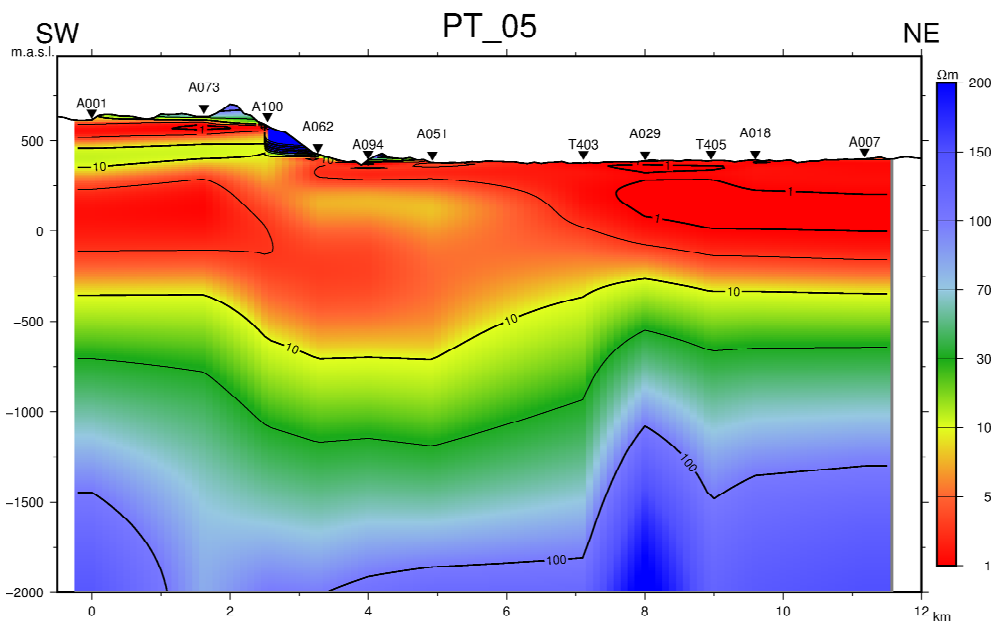


FIGURE 11: Cross-section PT-04



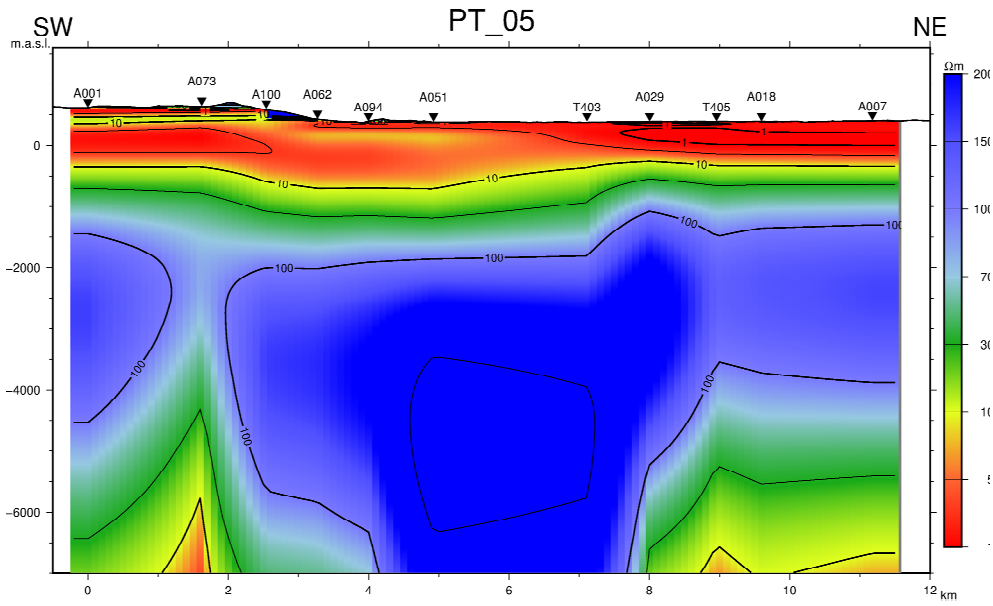


FIGURE 12: Cross-section PT-05

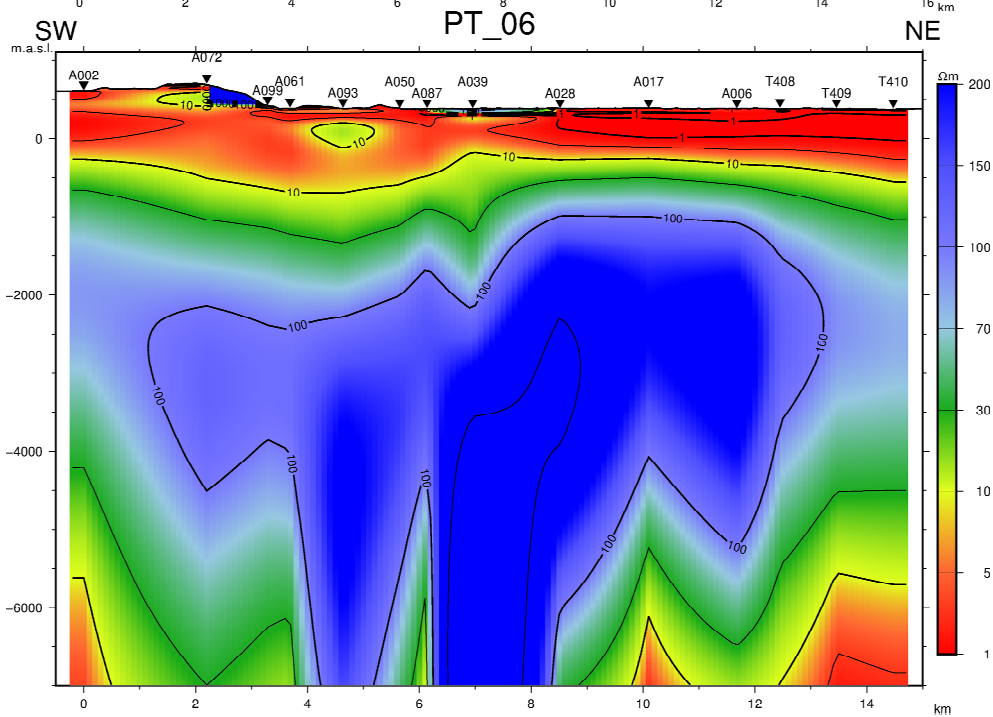
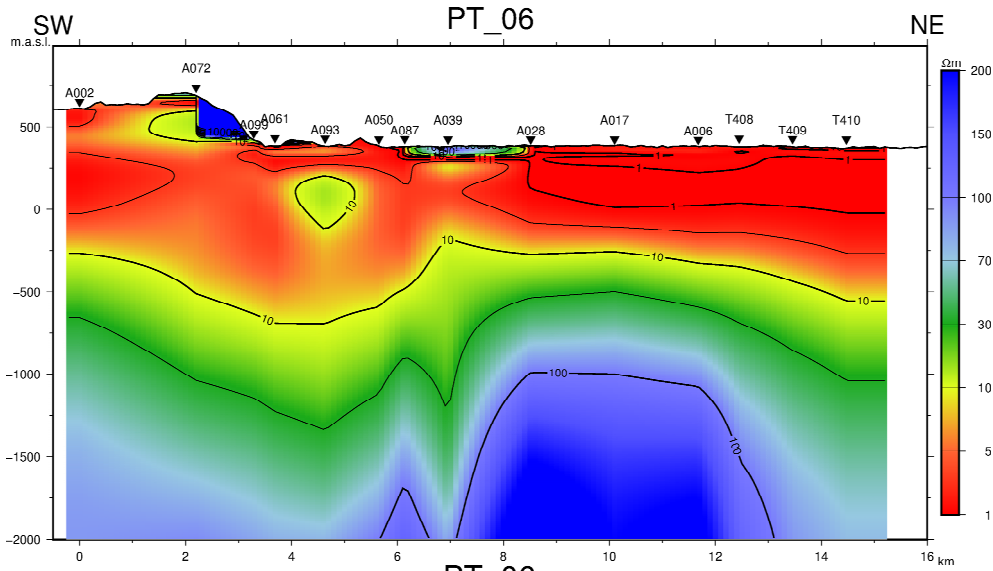


FIGURE 13: Cross-section PT-06



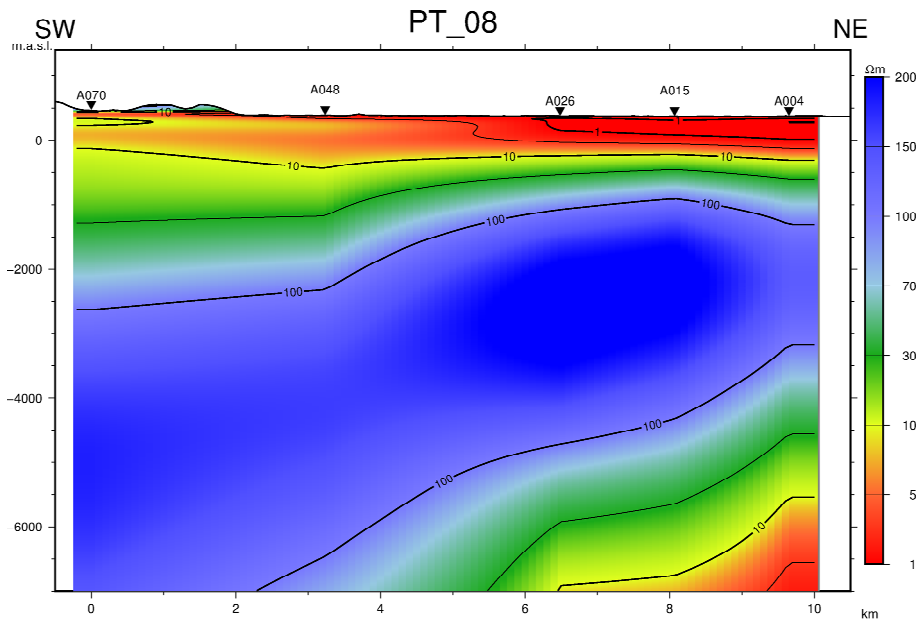


FIGURE 15: Cross-section PT-08

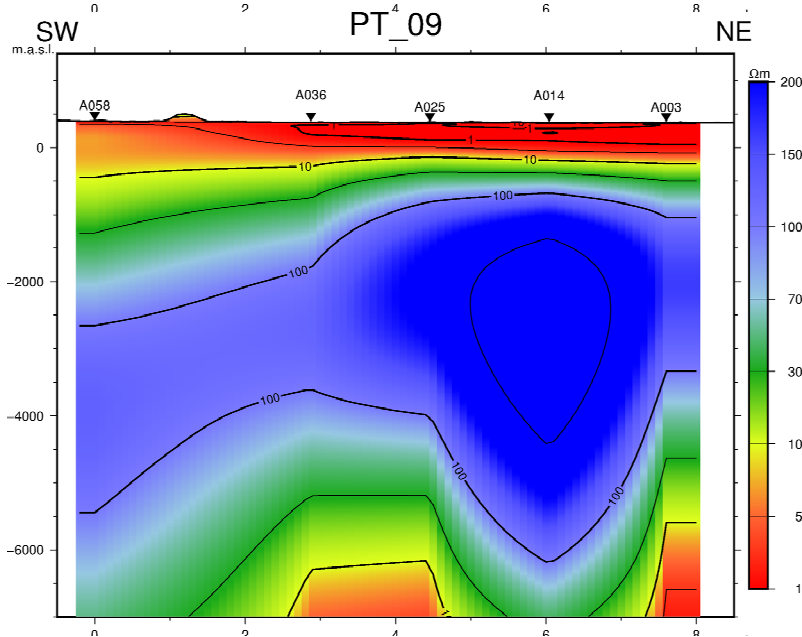
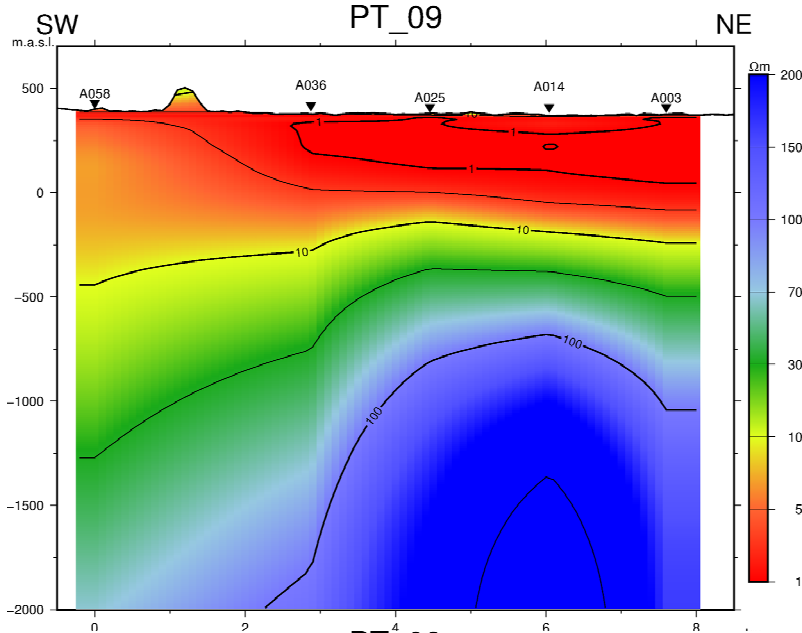


FIGURE 16: Cross-section PT-09

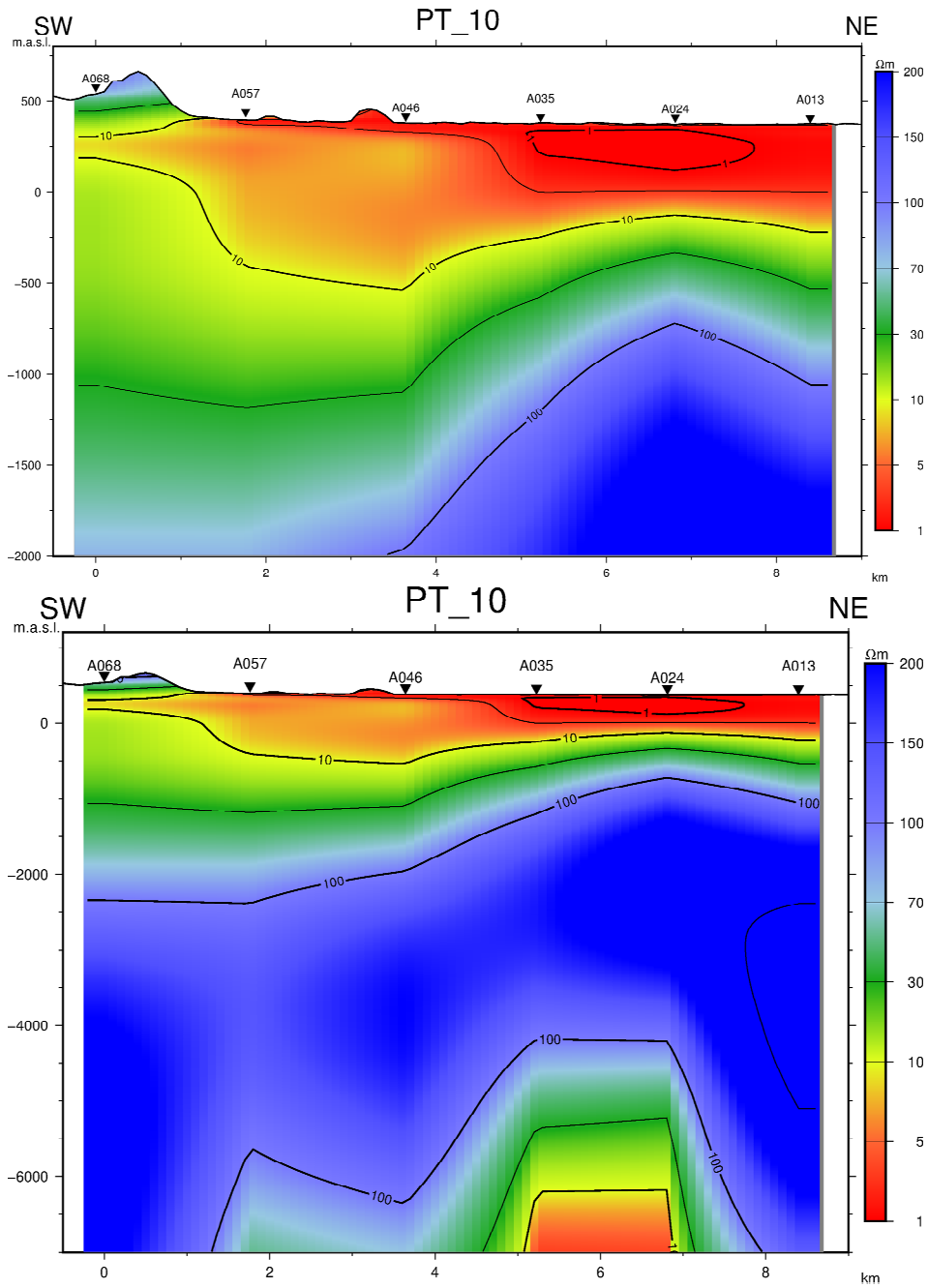


FIGURE 17: Cross-section PT-10

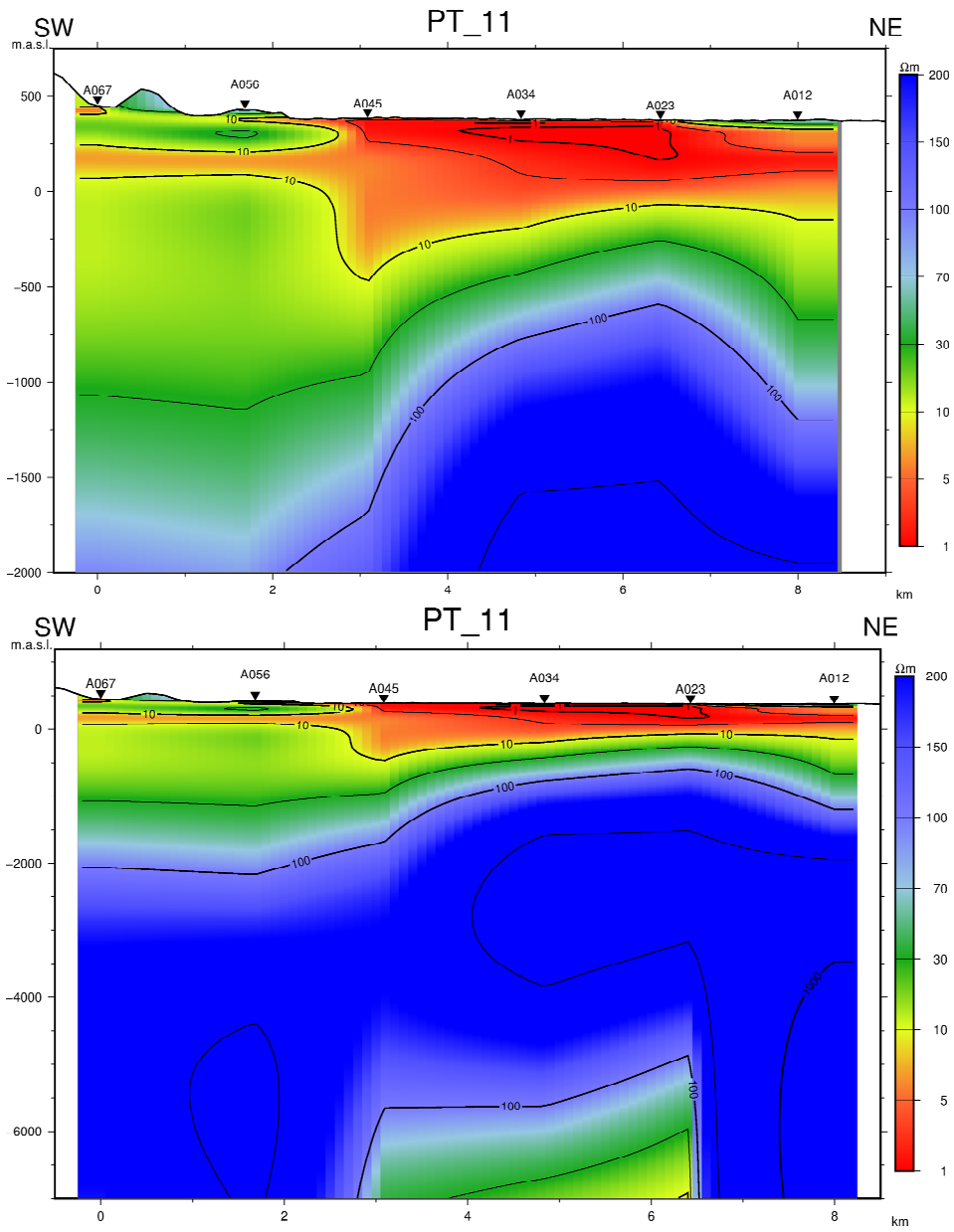
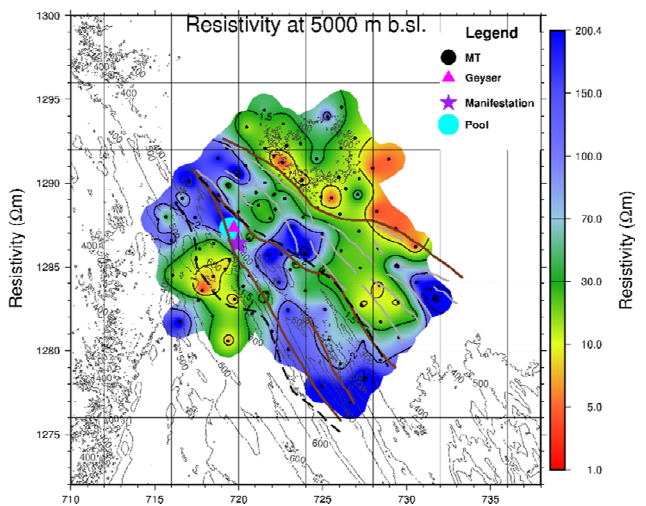
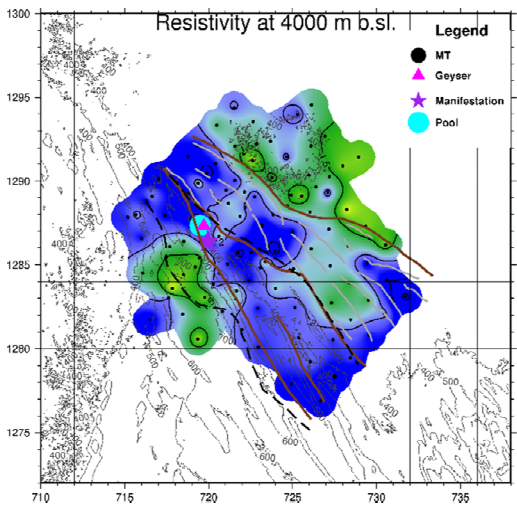
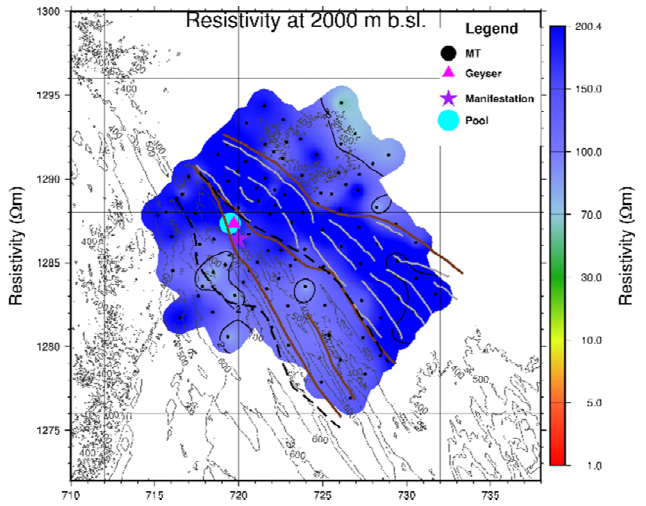
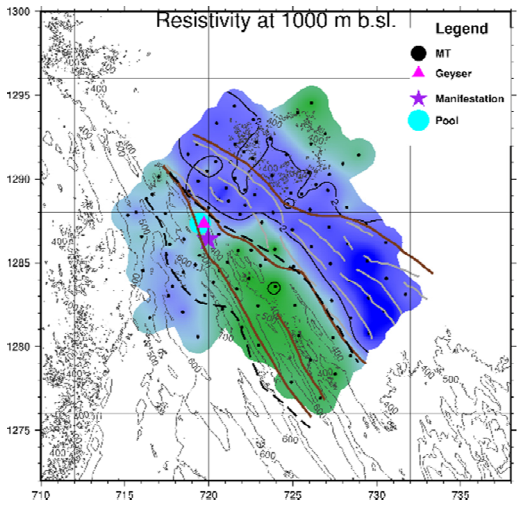
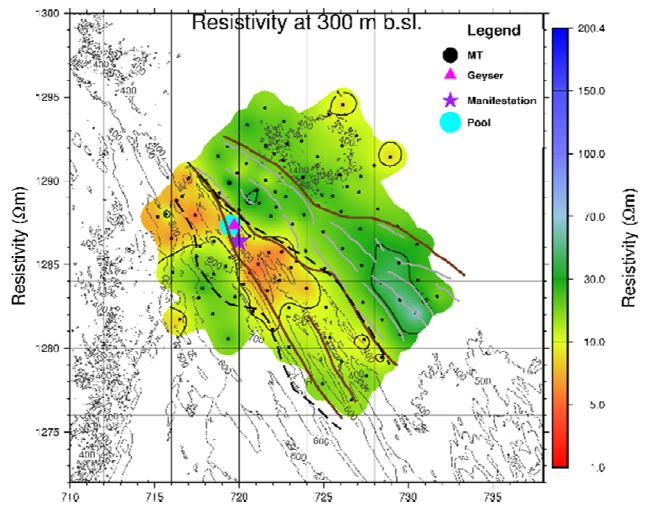
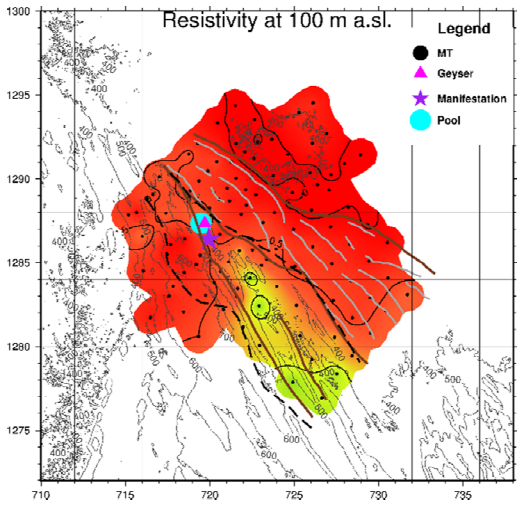
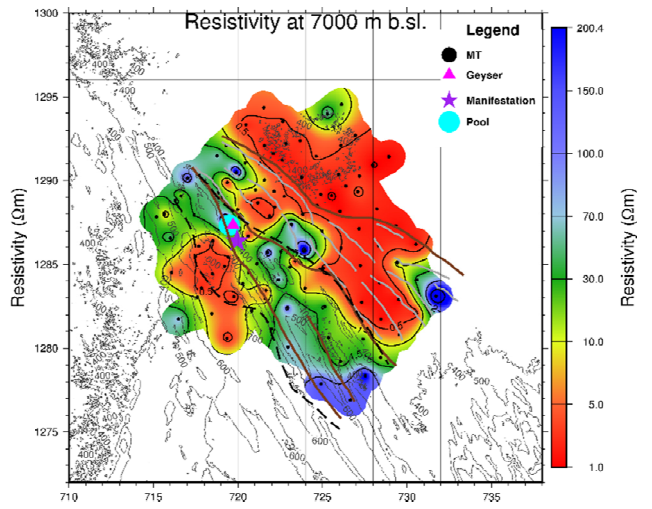
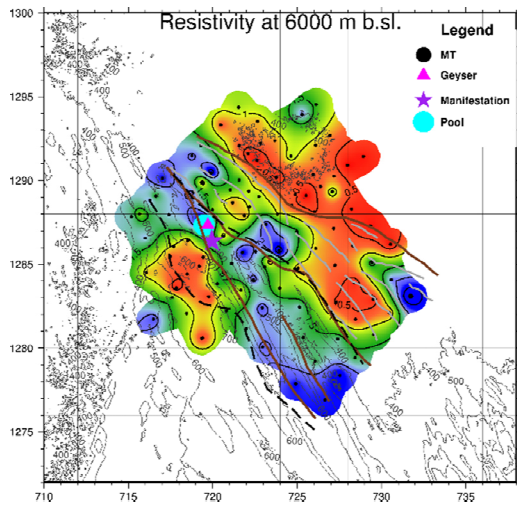


FIGURE 18: Cross-section PT-11

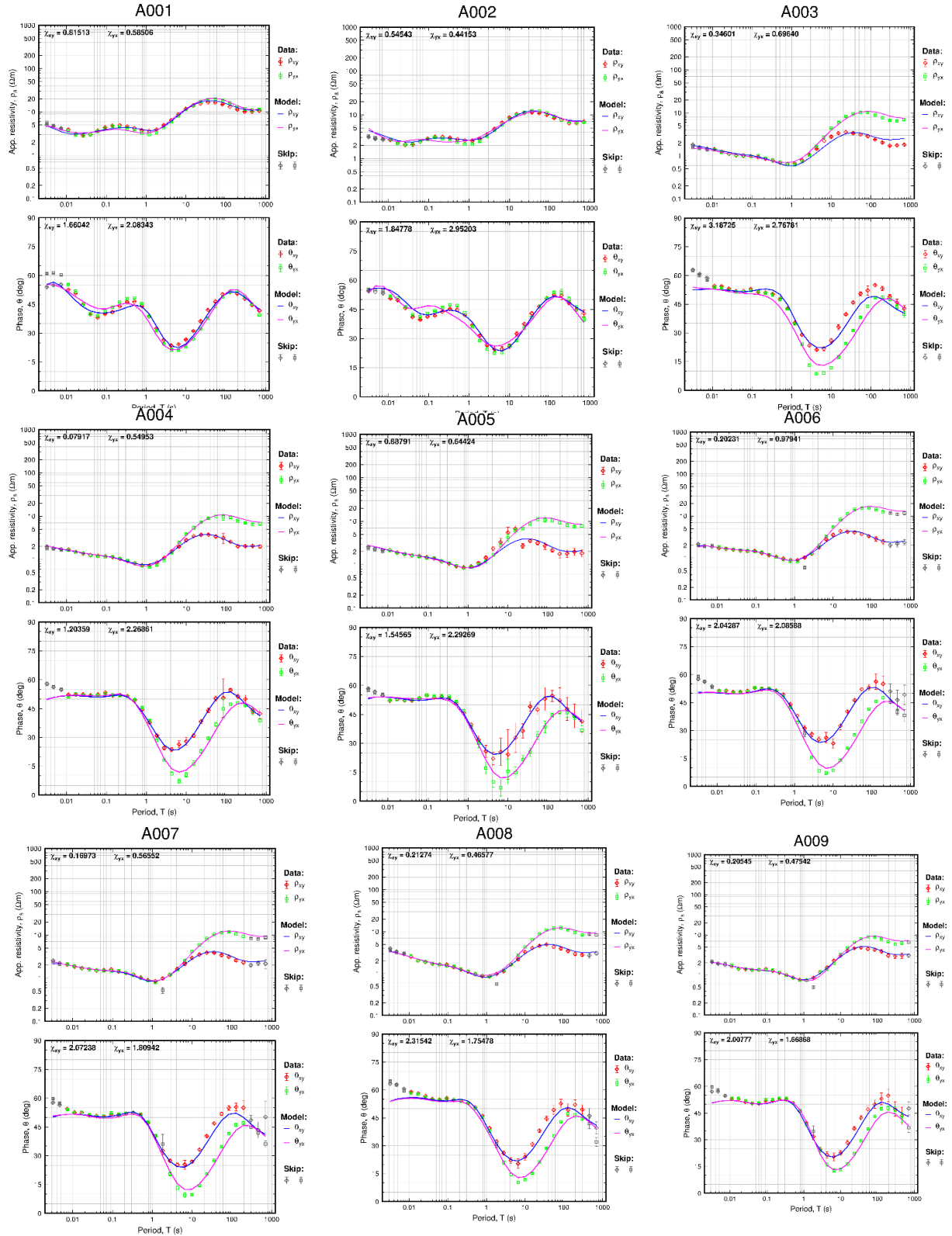
### APPENDIX III: Resistivity depth slices / maps based on 1D joint inversion

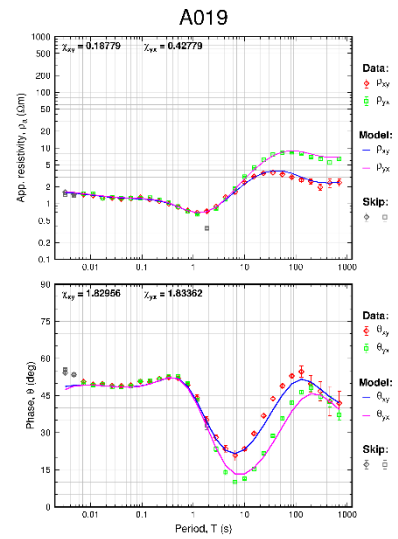
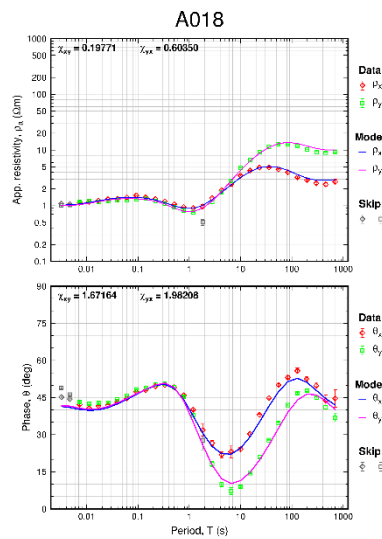
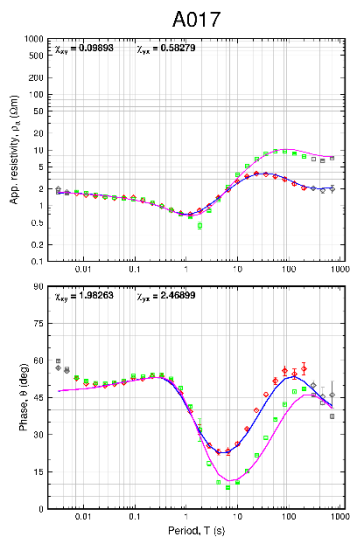
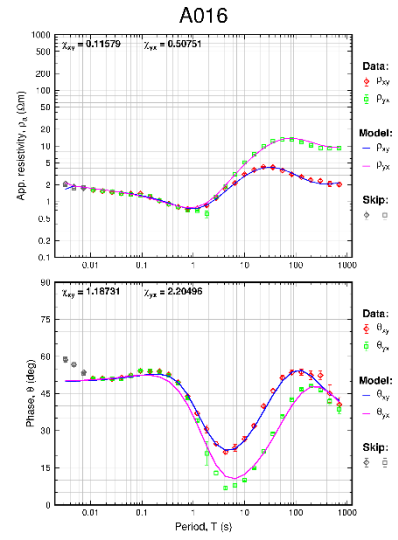
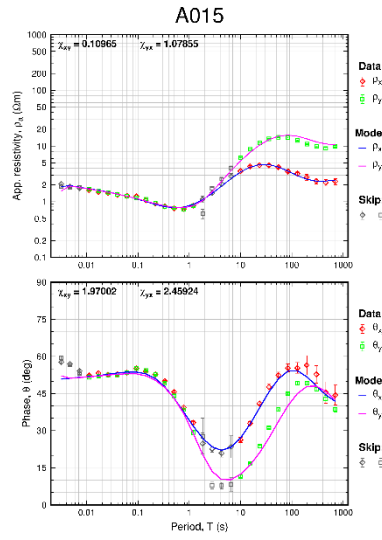
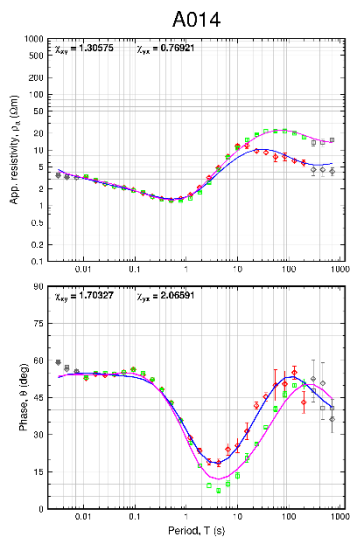
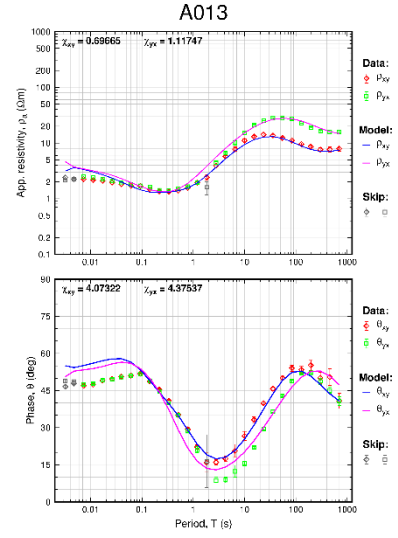
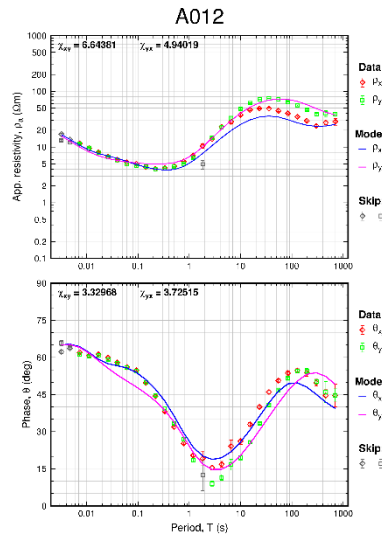
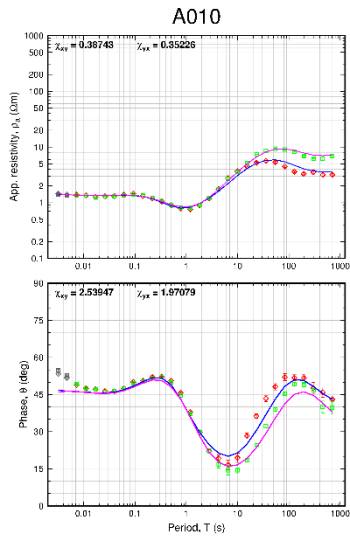


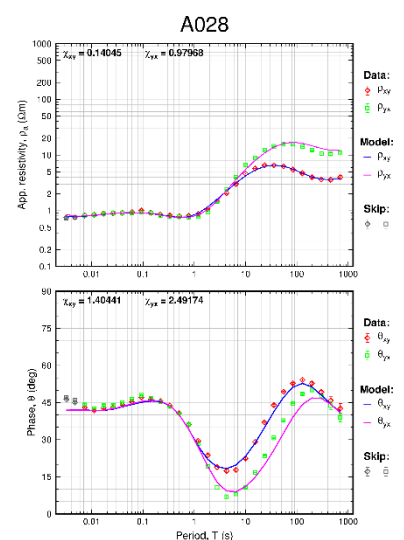
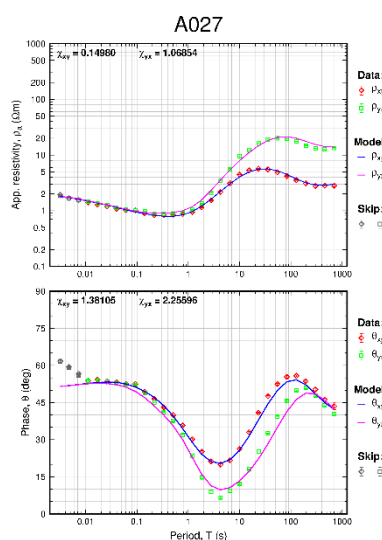
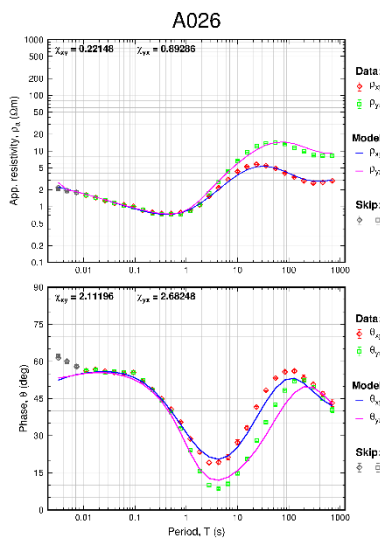
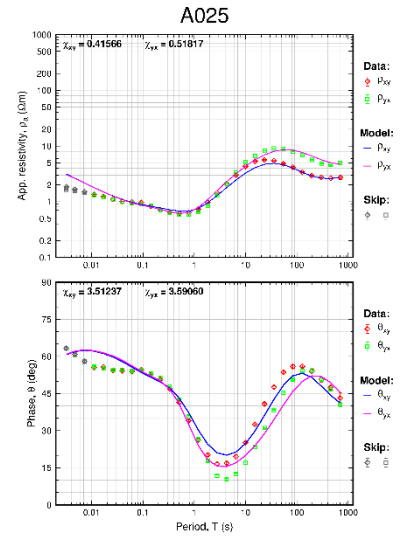
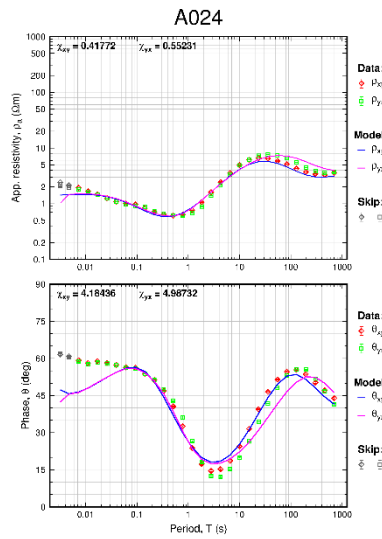
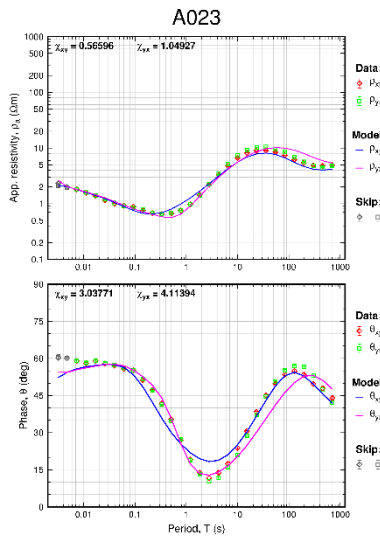
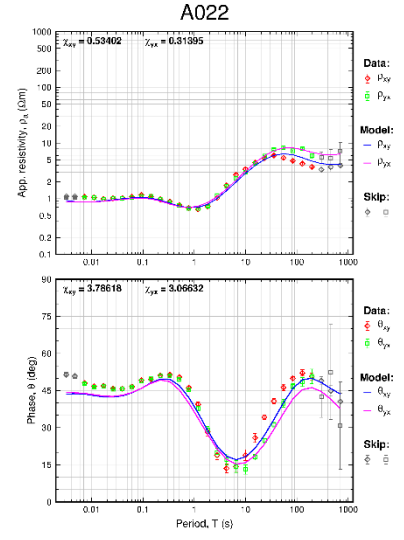
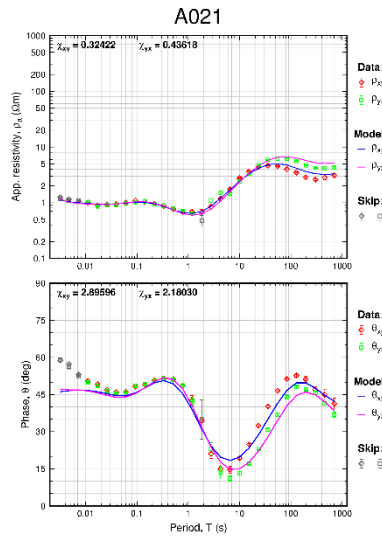
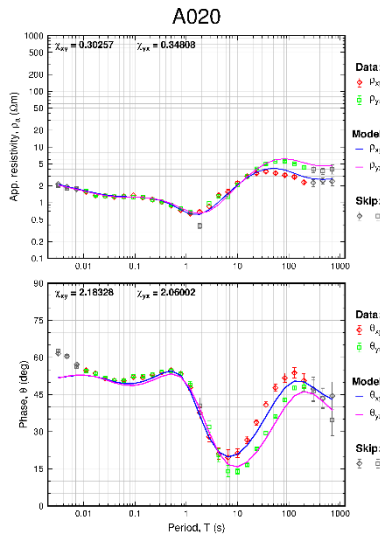


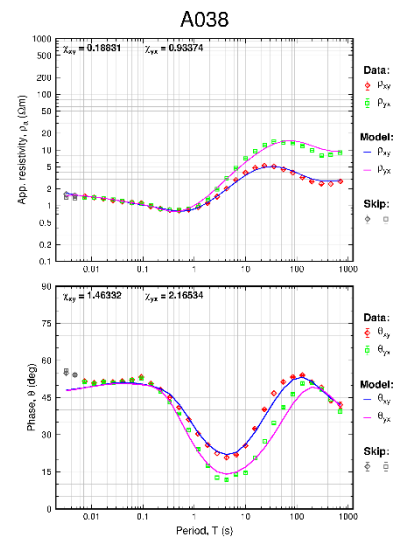
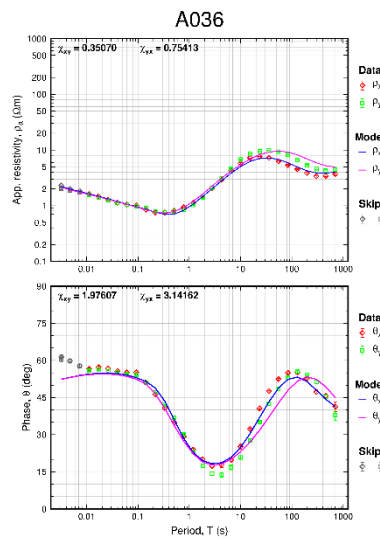
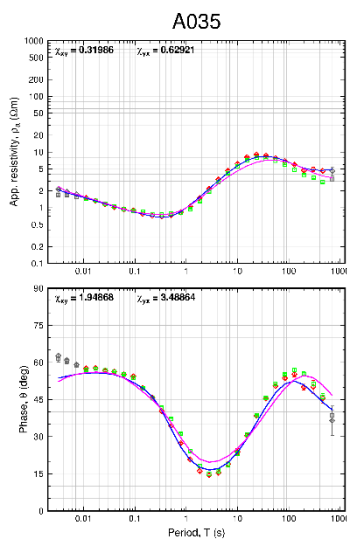
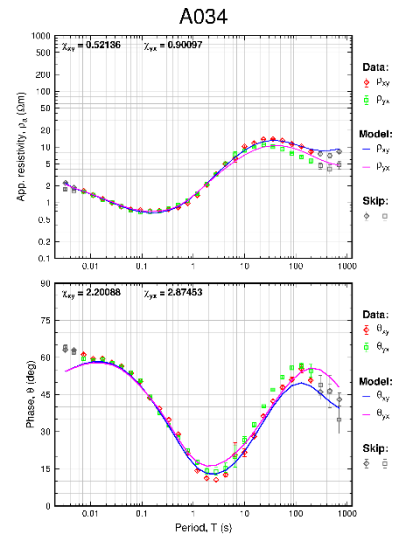
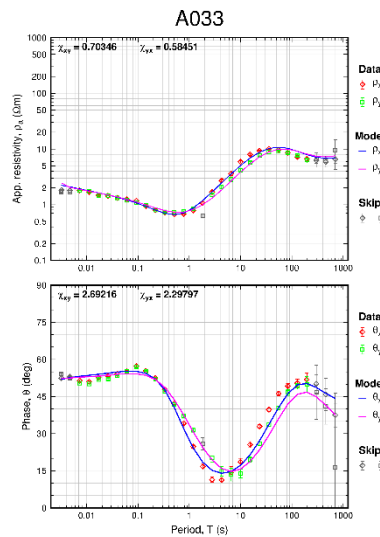
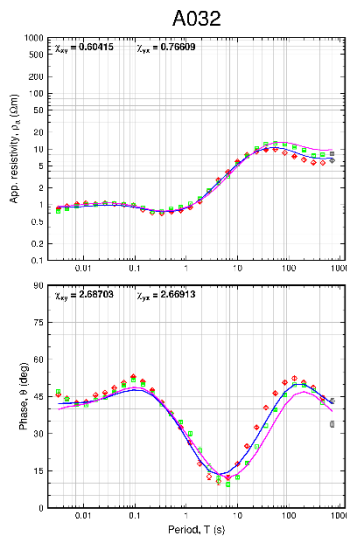
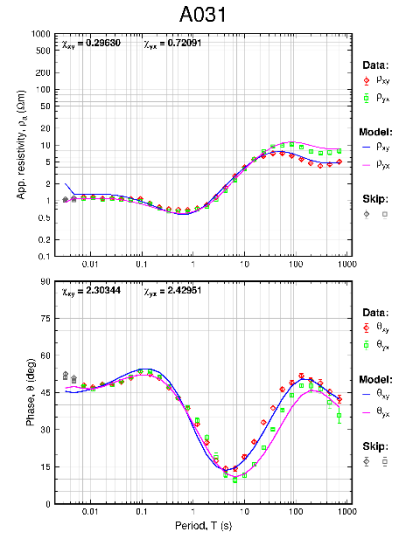
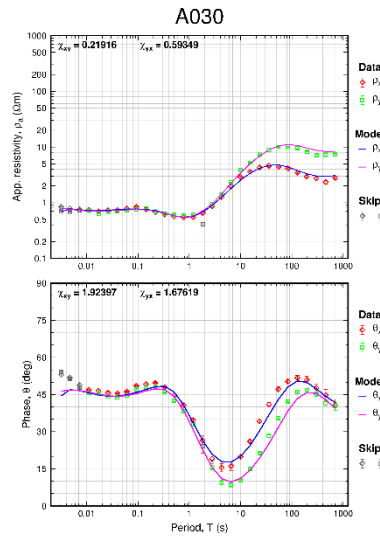
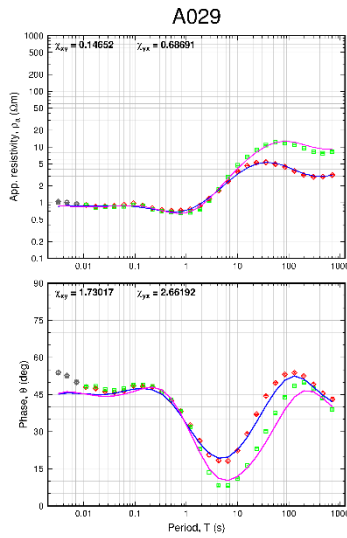
## APPENDIX IV: 3D inversion data fit

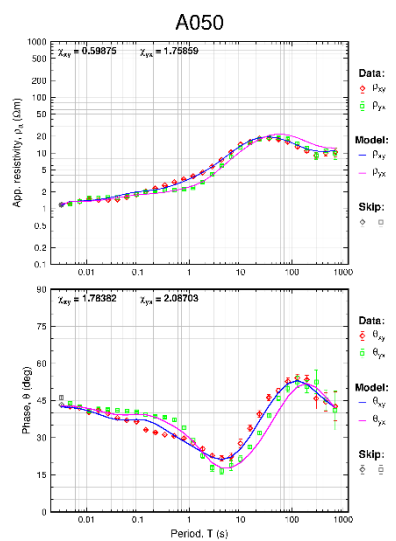
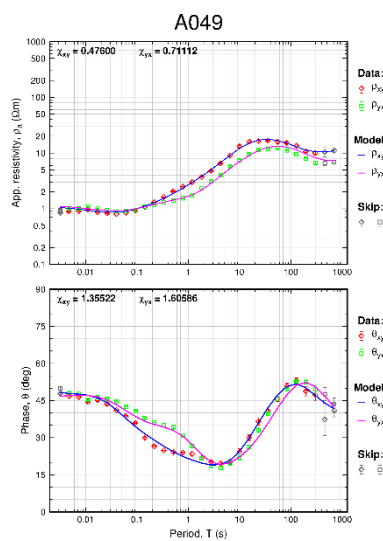
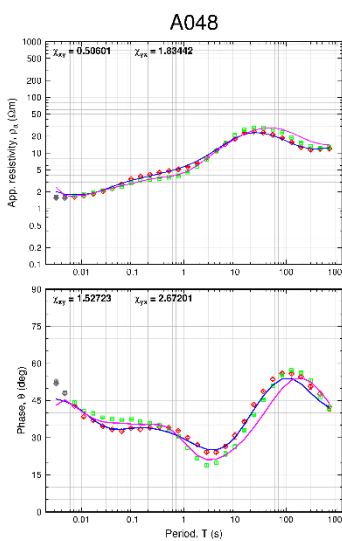
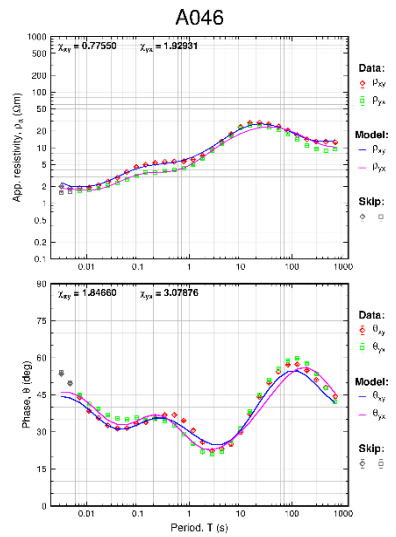
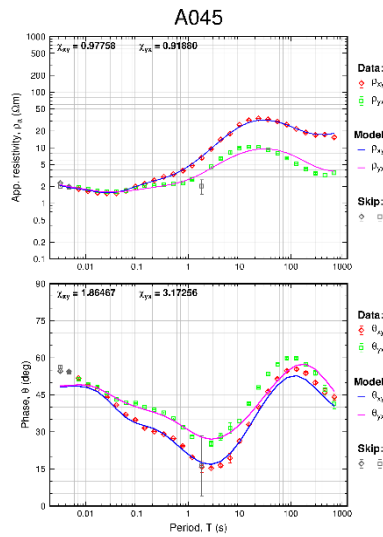
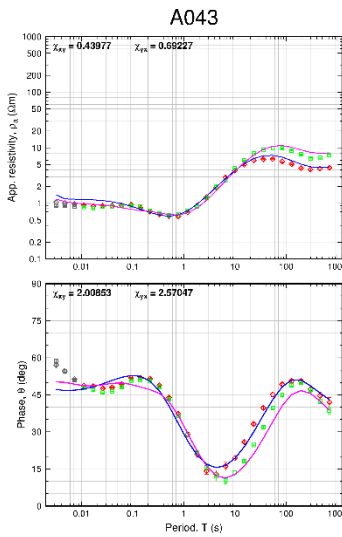
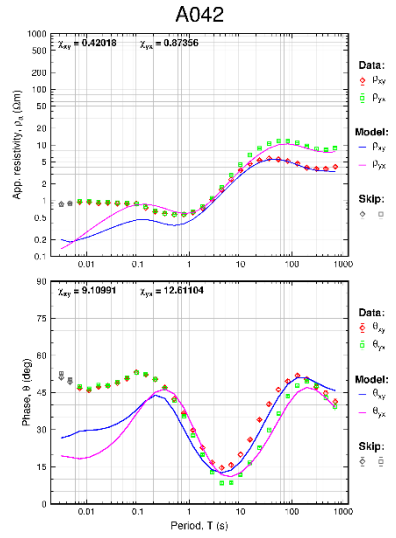
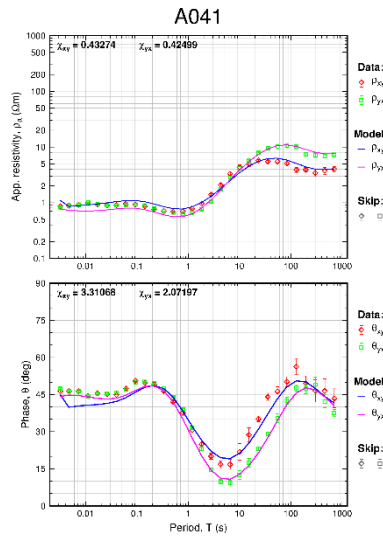
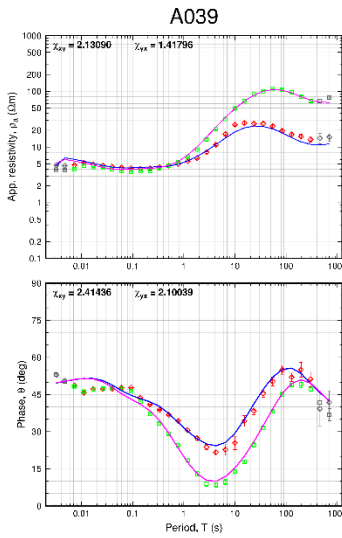
Data fit for the resampled static shift corrected MT data for all the inverted soundings presented as apparent resistivity and phase and the calculated response of the final model using as a starting model, a model compiled from joint 1D inversion of individual TEM/MT sounding pairs (J1D). The data misfit is defined as the RMS (Root-Mean-Square) of the difference between the measured and calculated values of the off diagonal impedance tensor elements (real and imaginary part). The RMS misfit for the final model based on the 10  $\Omega\text{m}$  homogenous half-space initial model was 1.2.

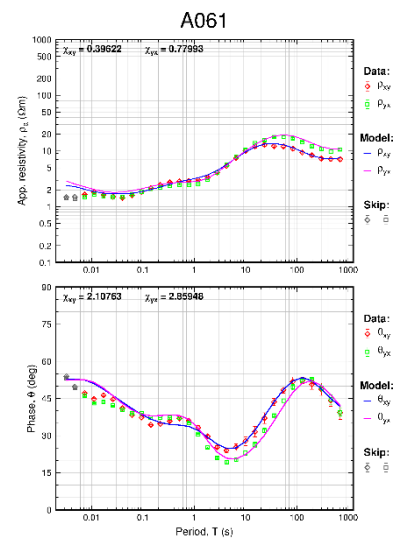
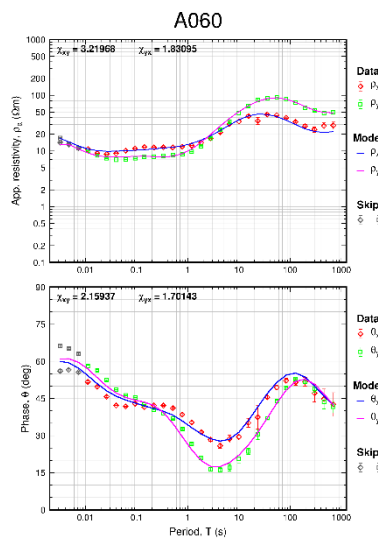
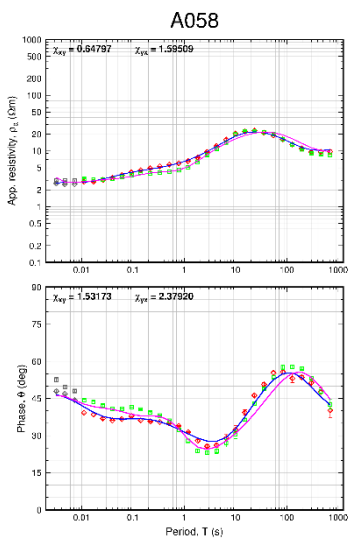
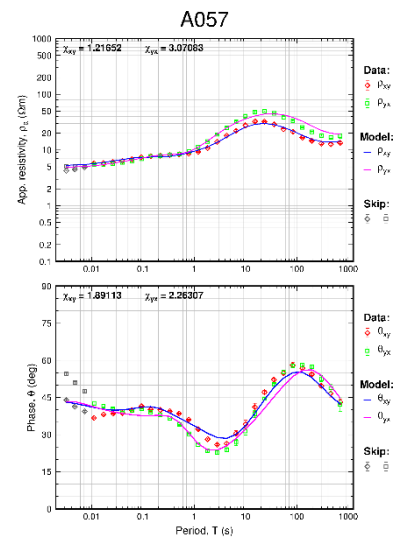
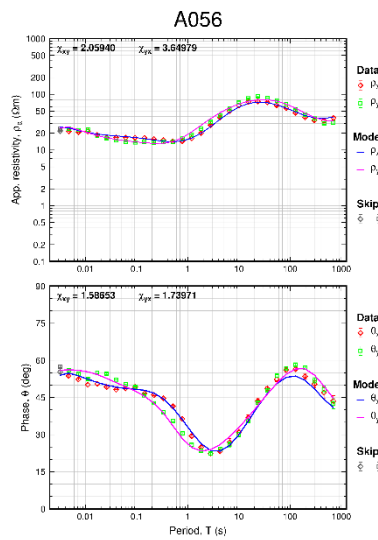
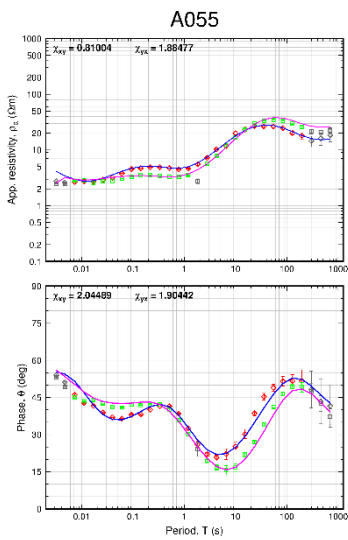
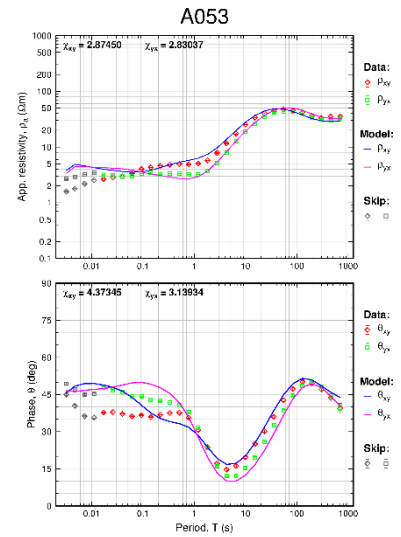
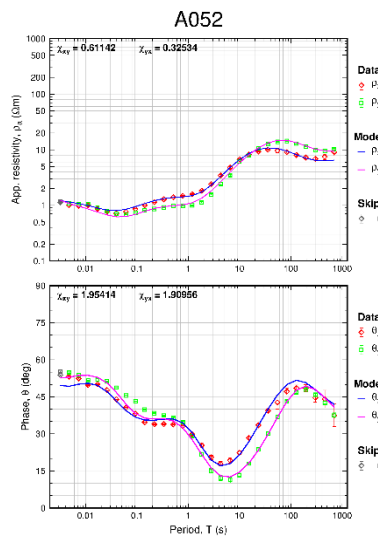
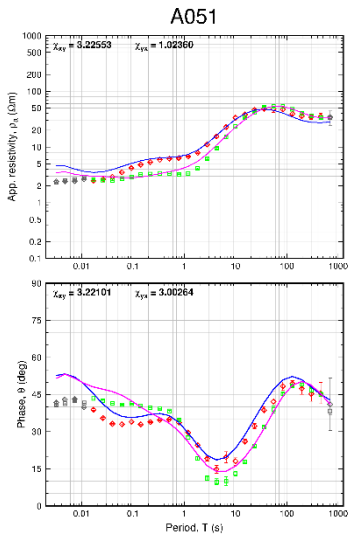


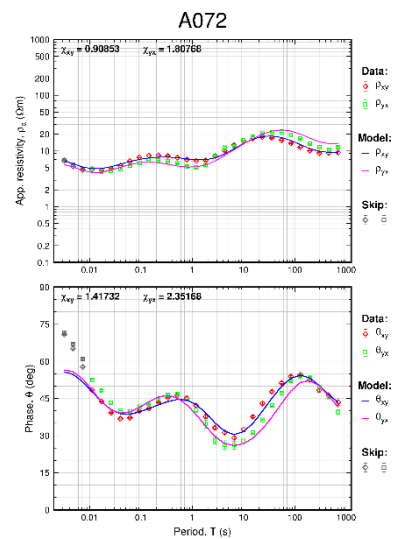
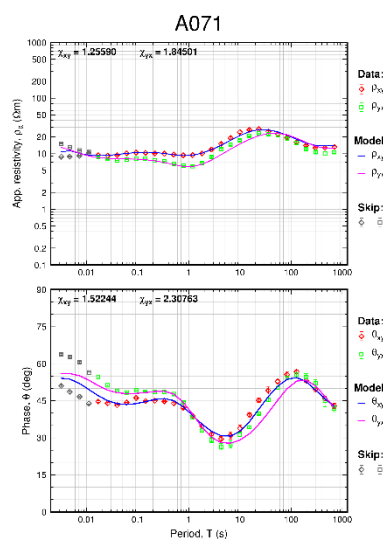
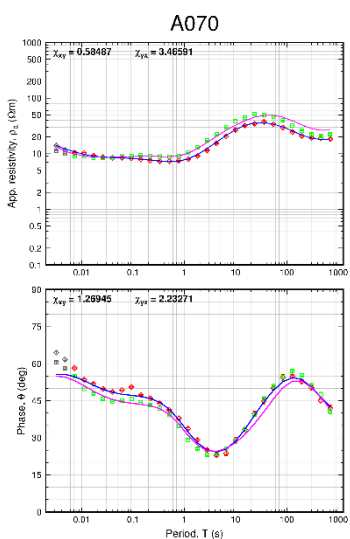
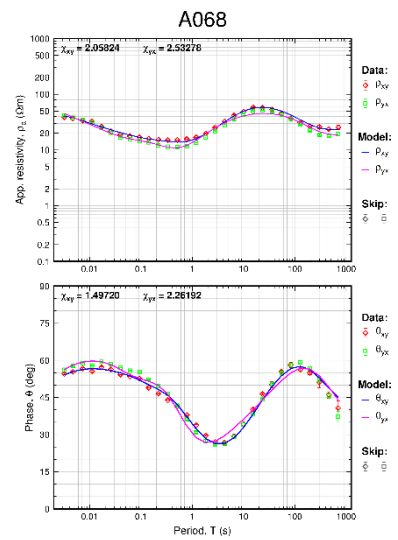
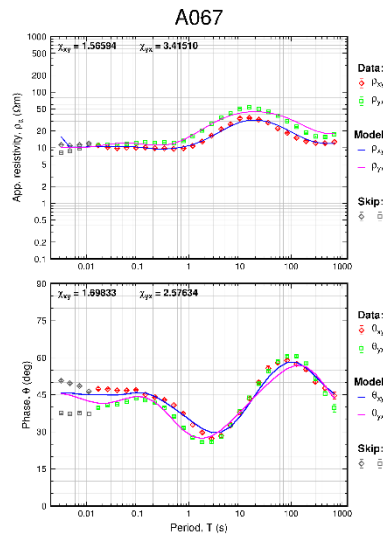
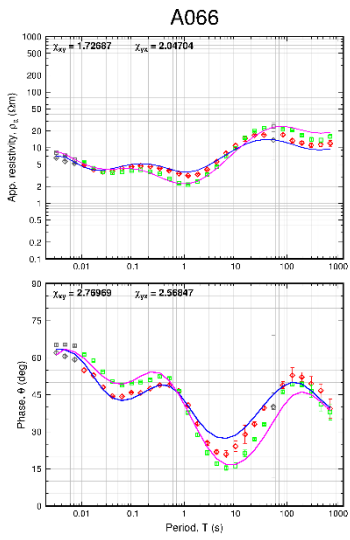
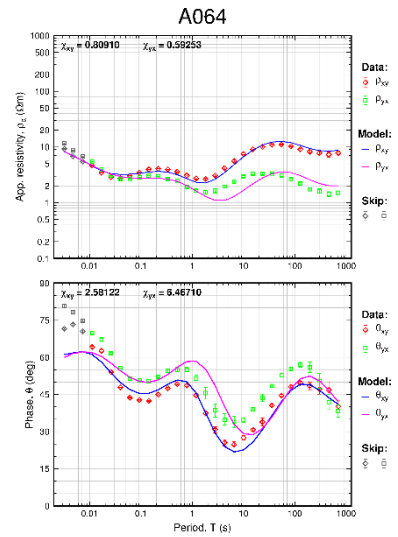
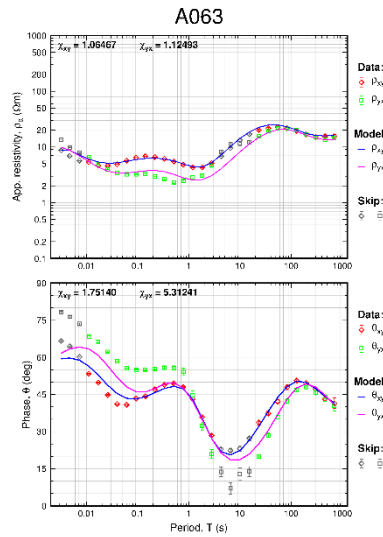
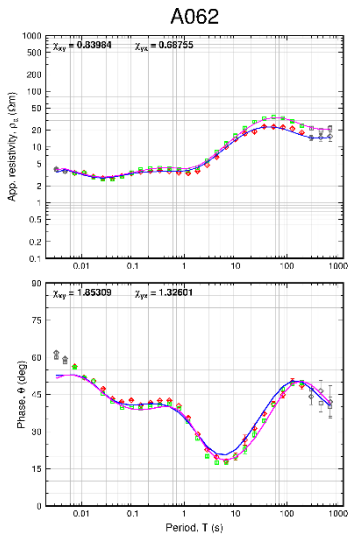


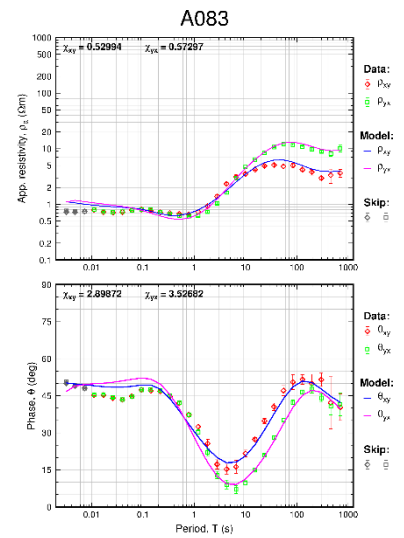
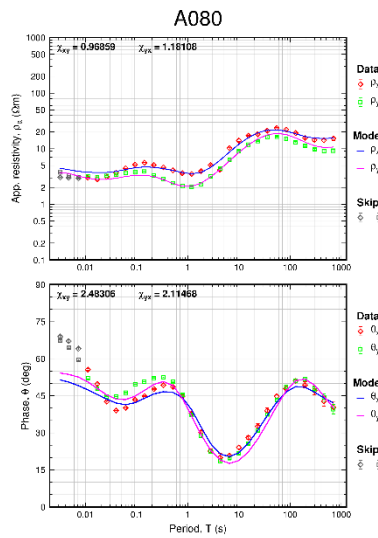
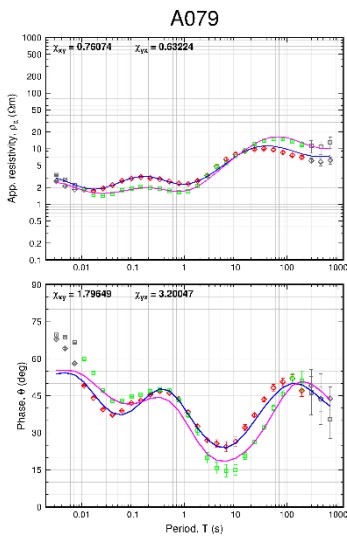
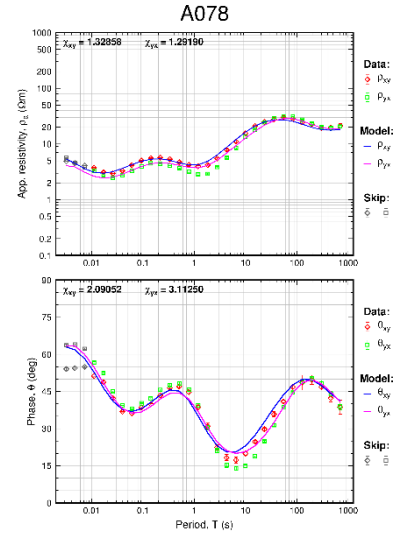
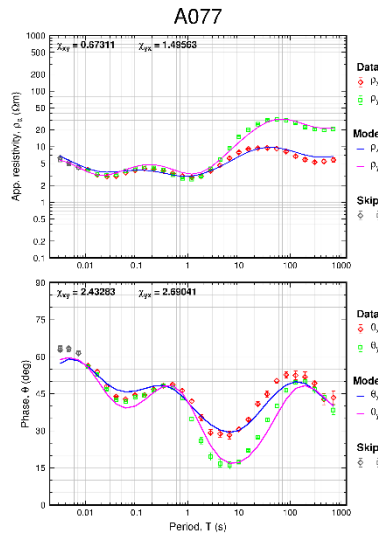
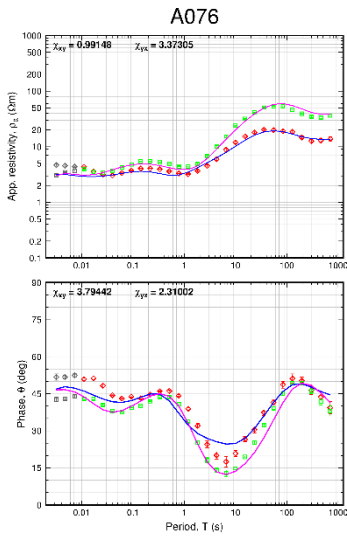
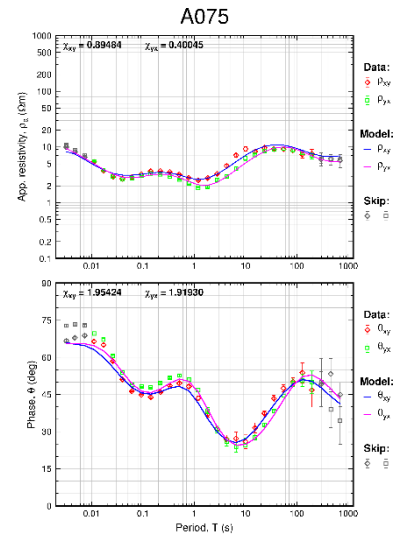
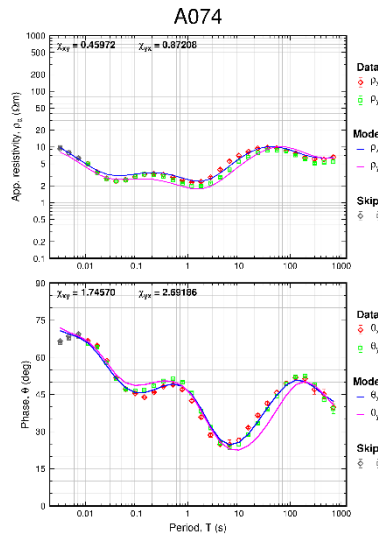
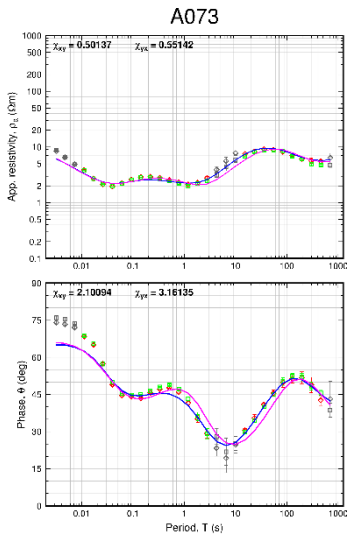


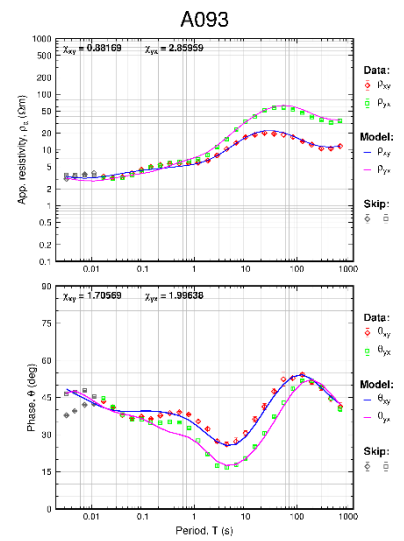
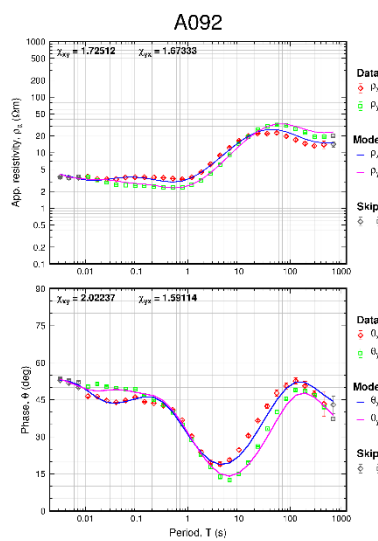
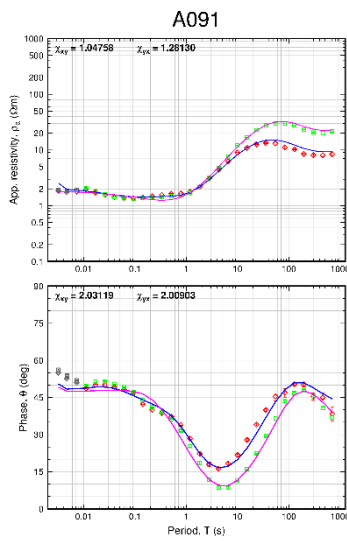
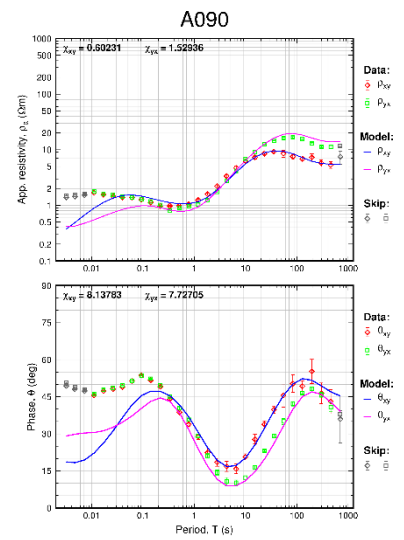
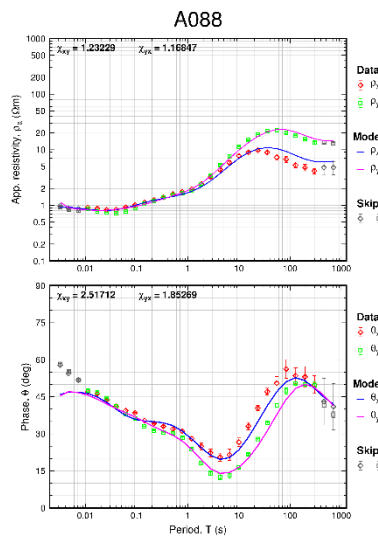
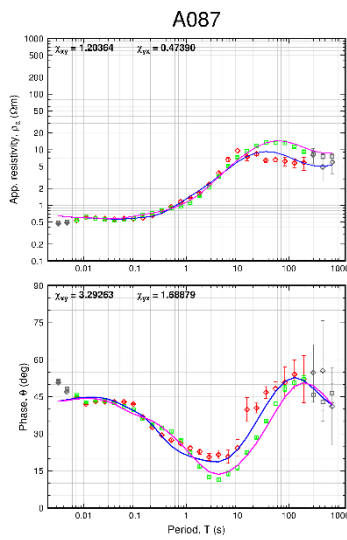
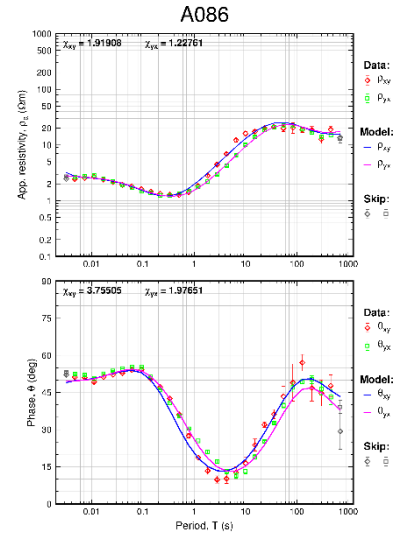
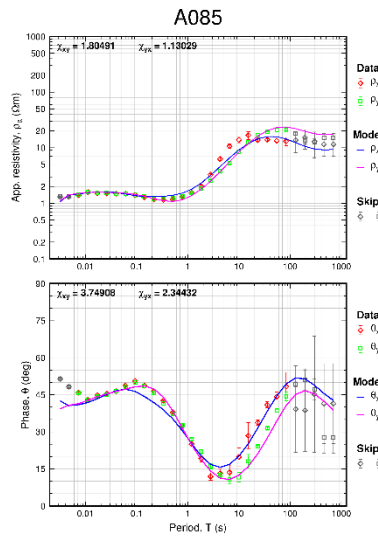
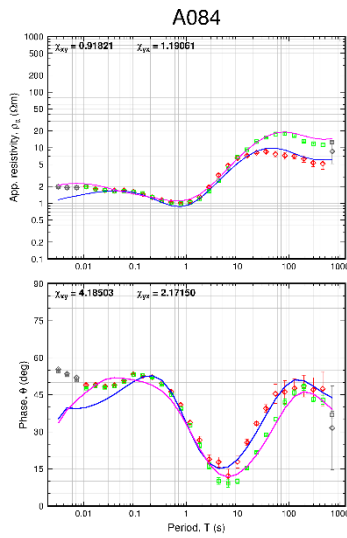


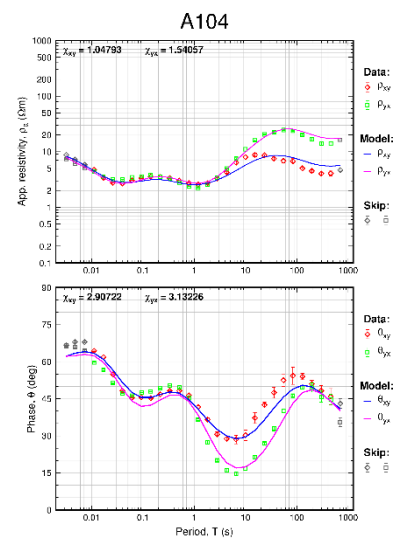
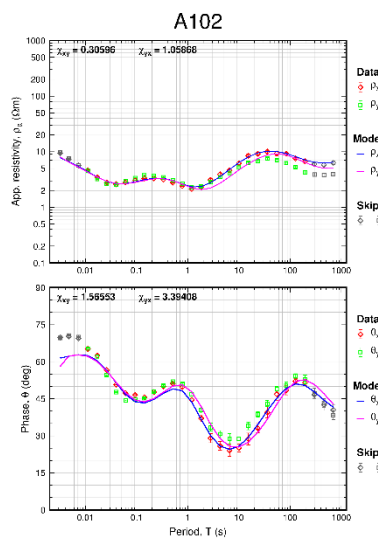
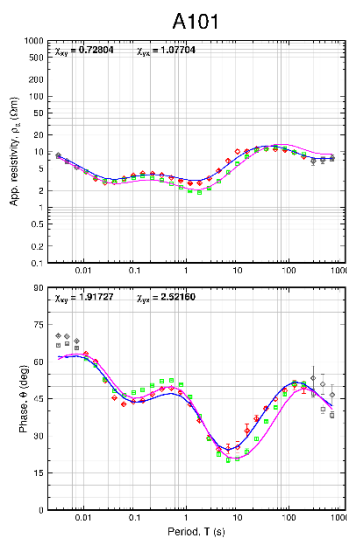
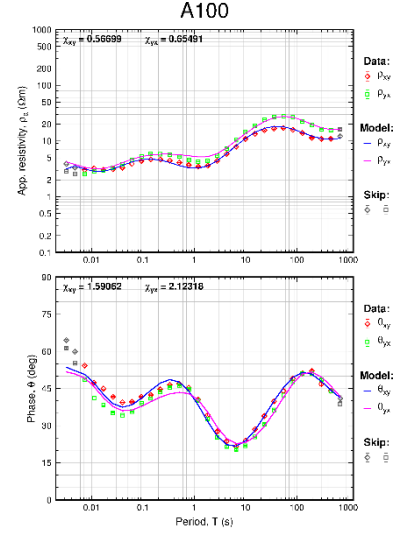
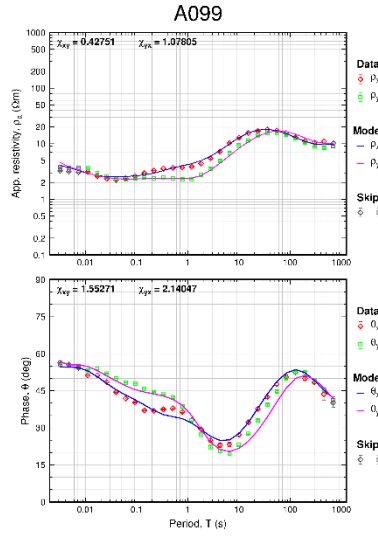
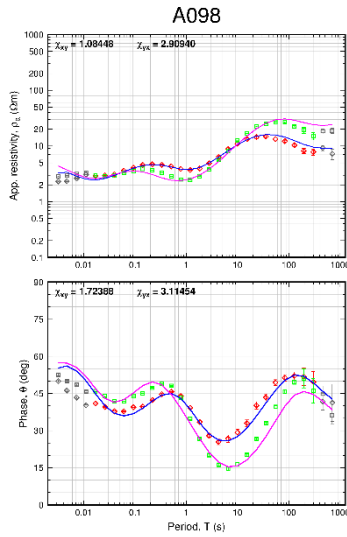
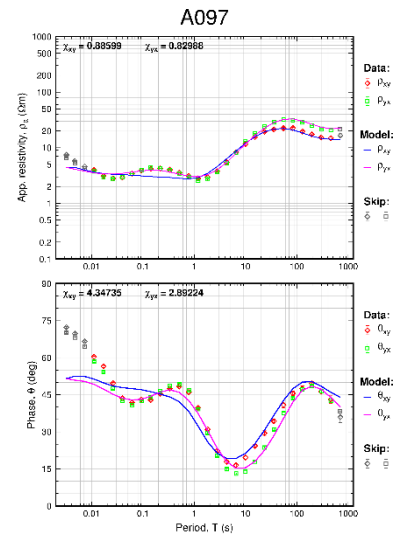
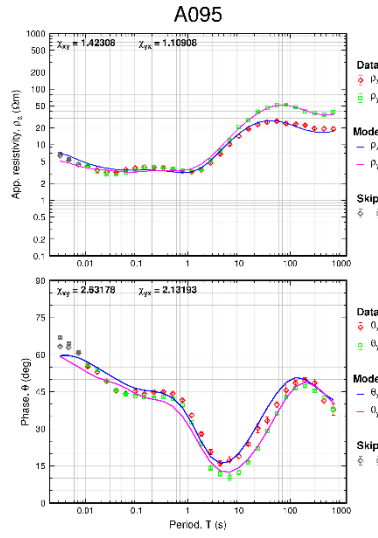
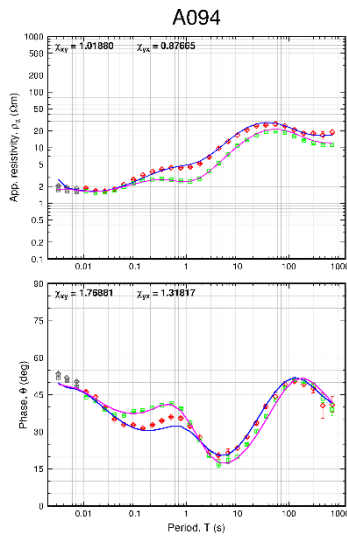


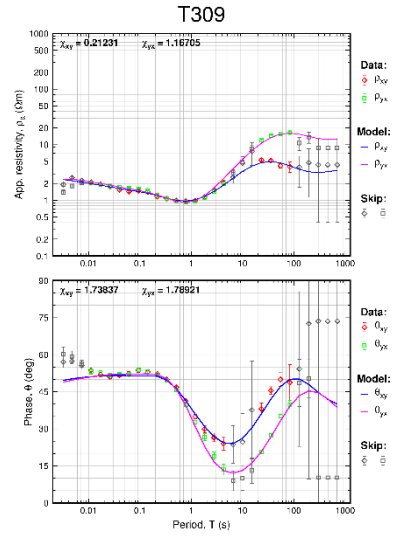
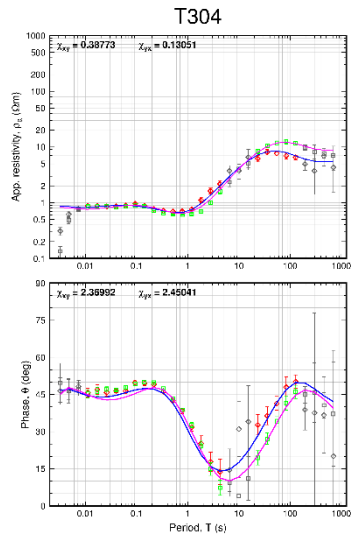
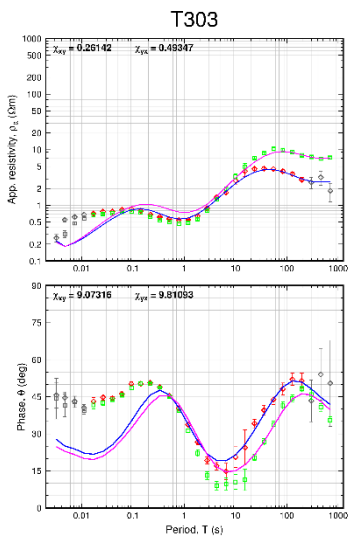
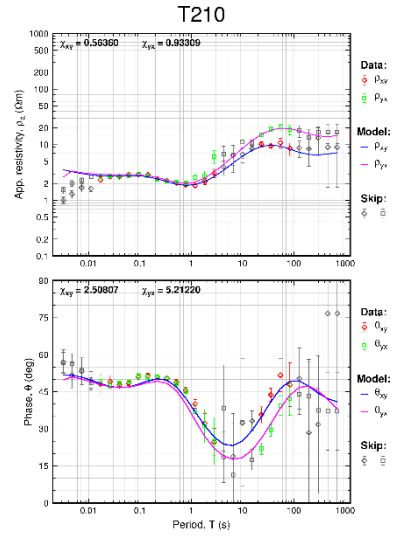
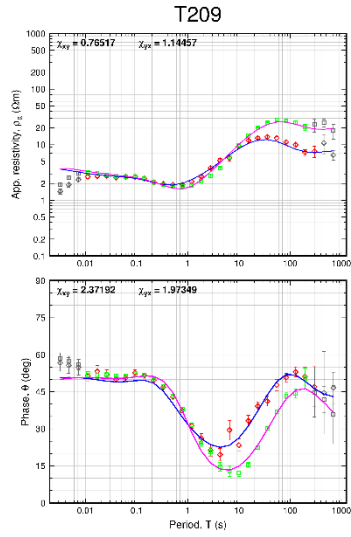
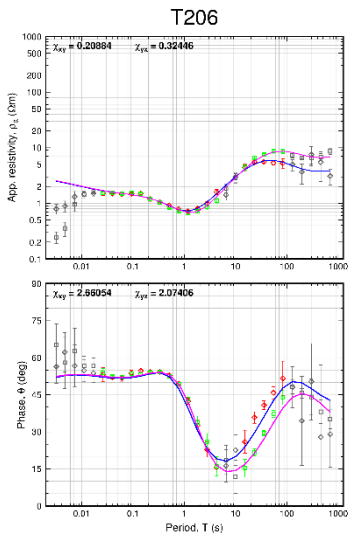
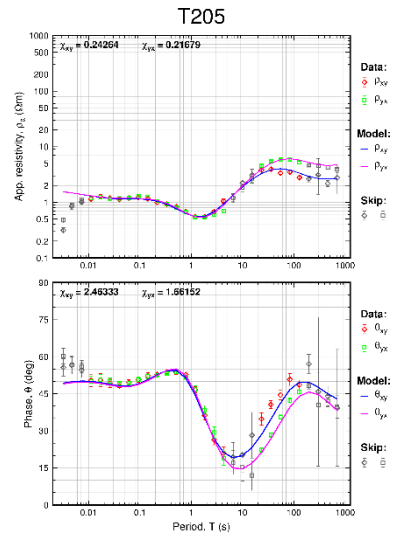
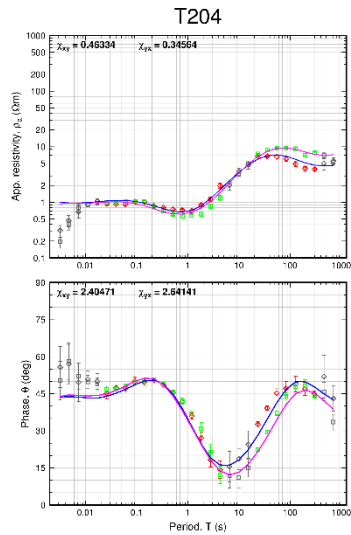
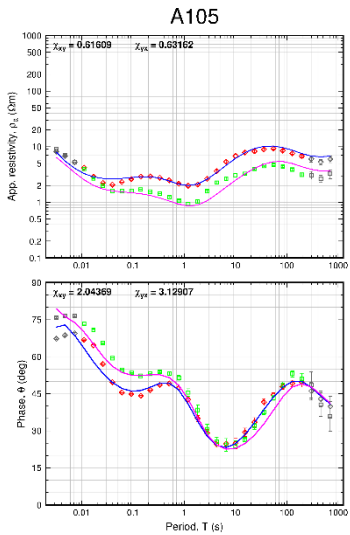


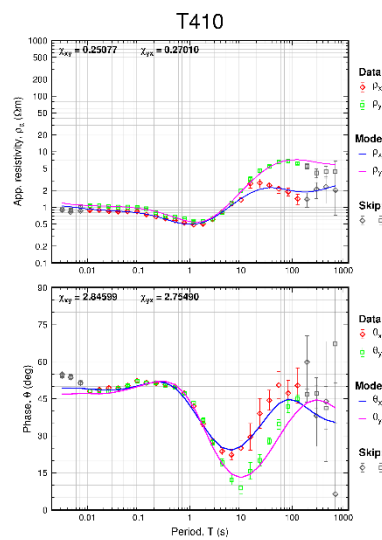
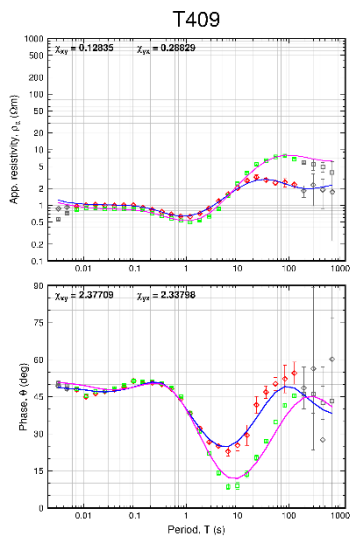
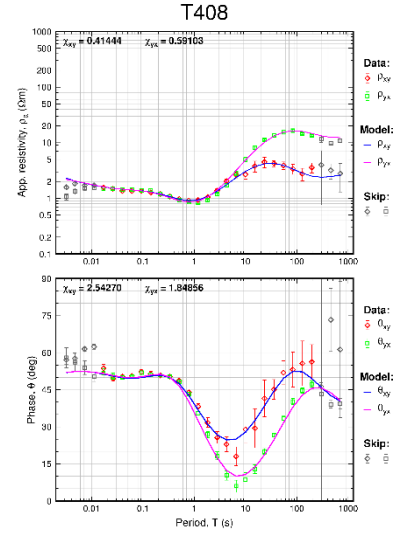
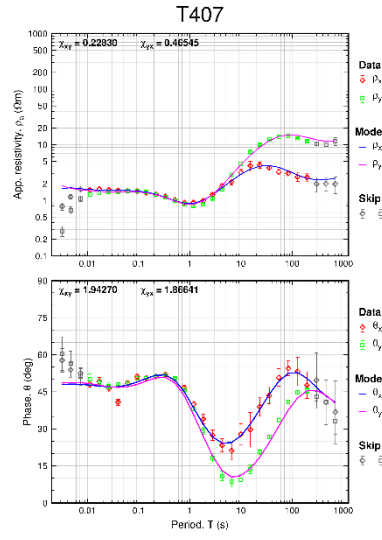
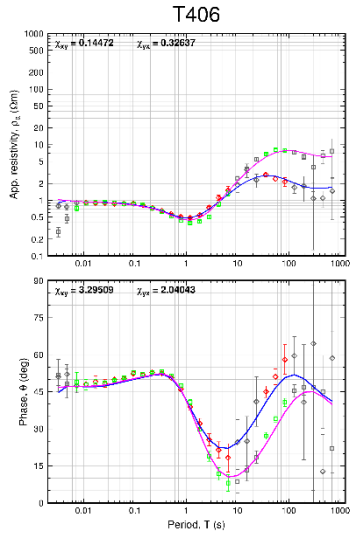
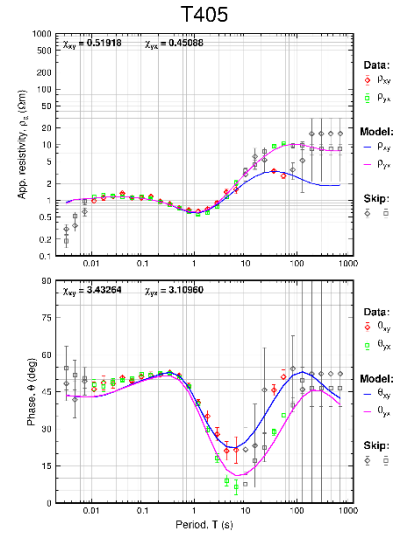
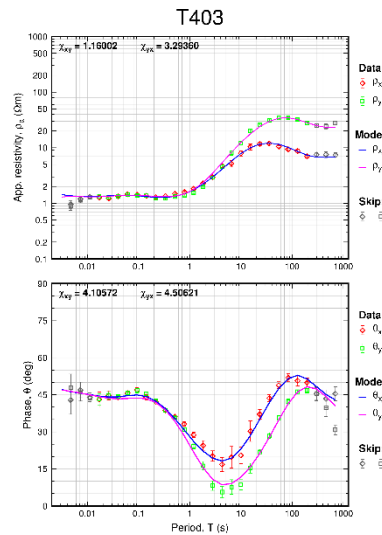
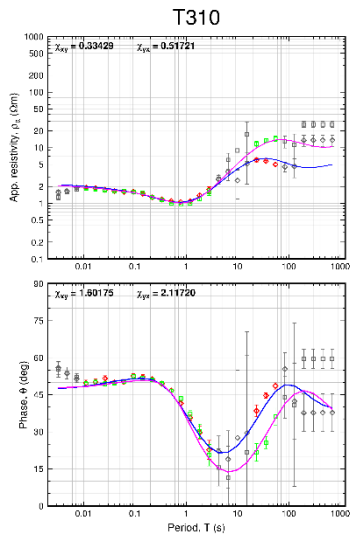






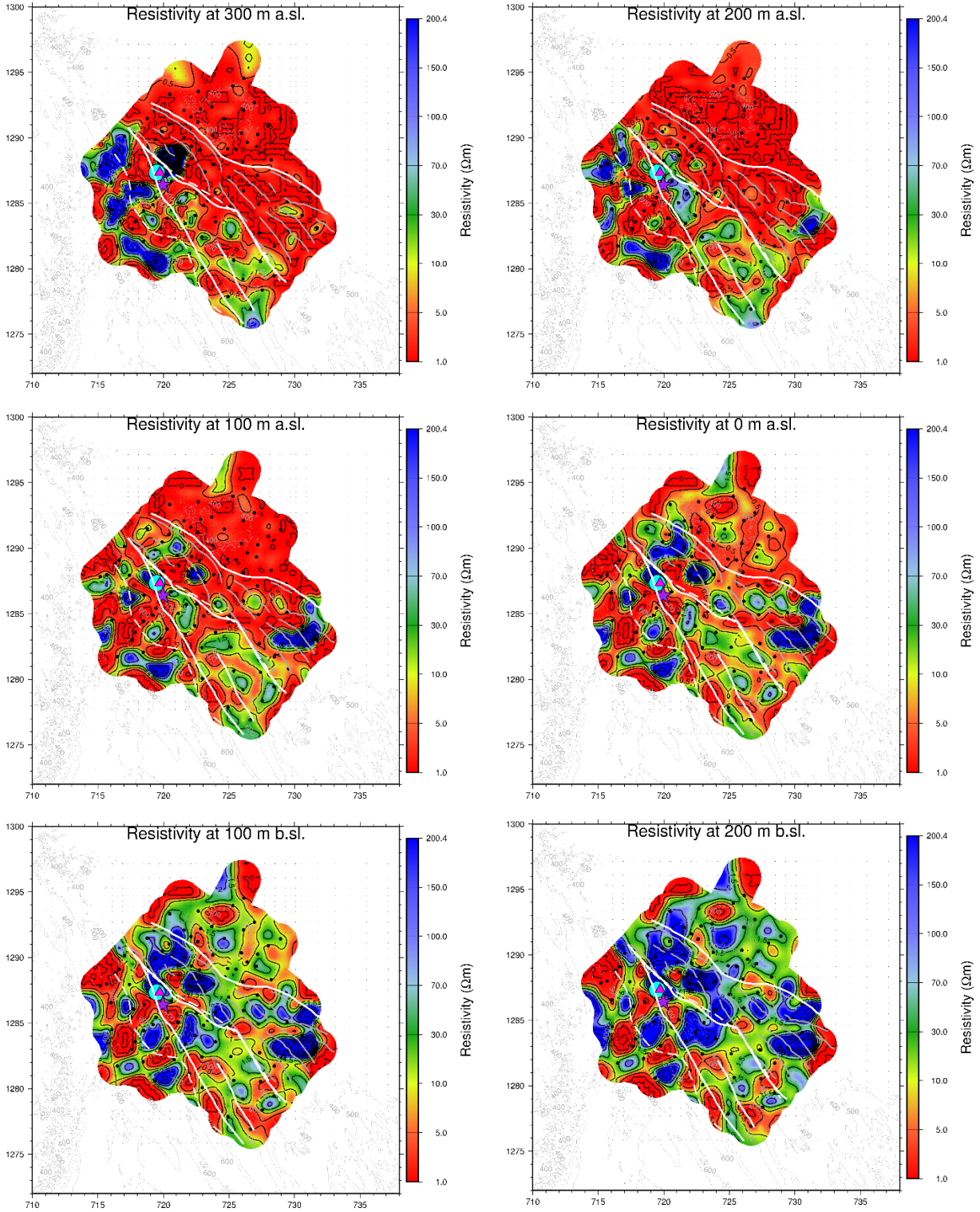


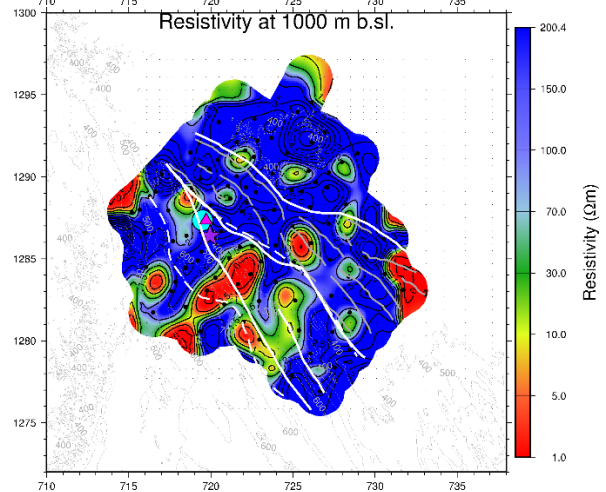
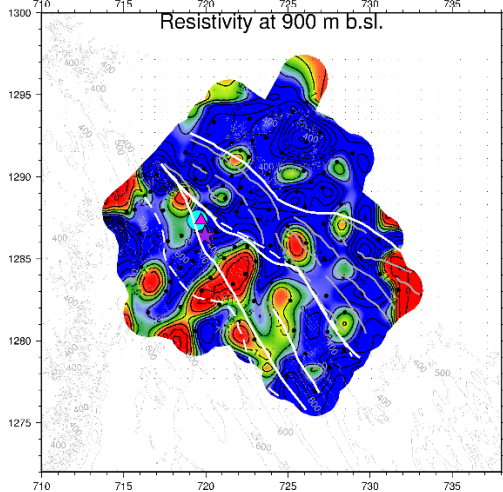
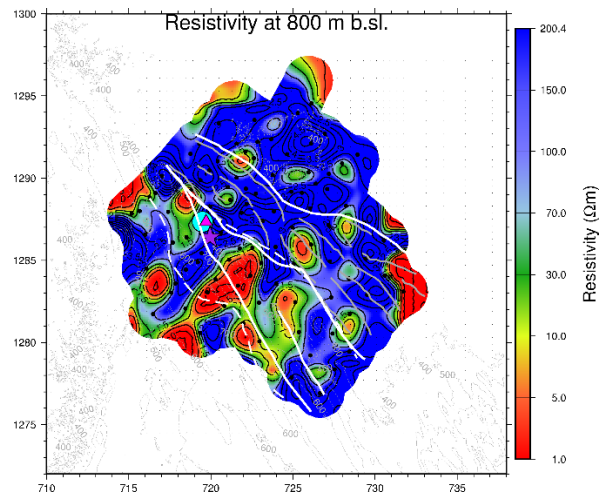
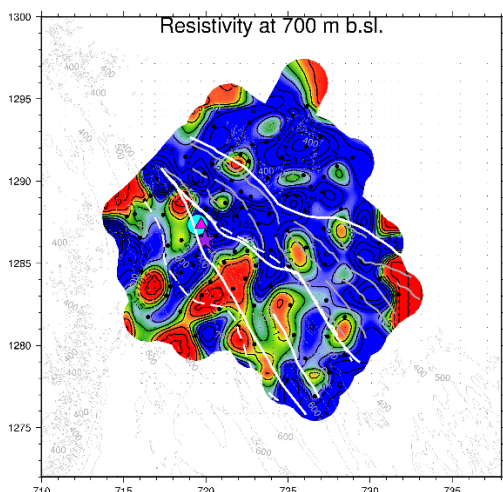
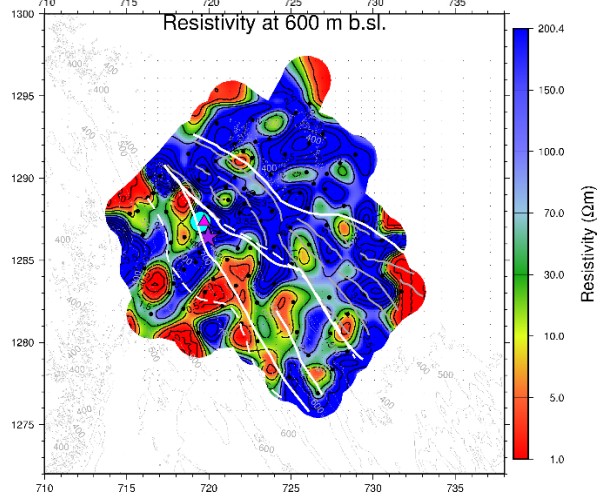
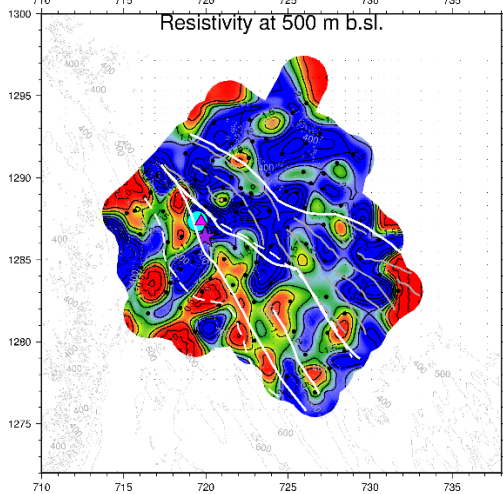
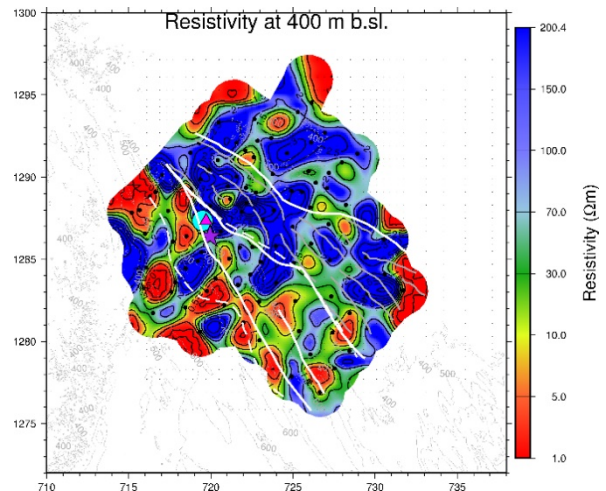
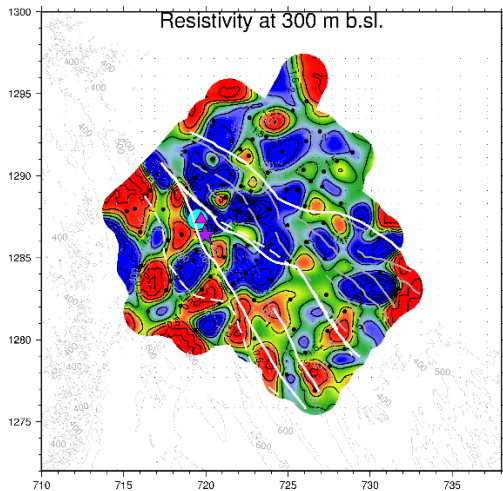


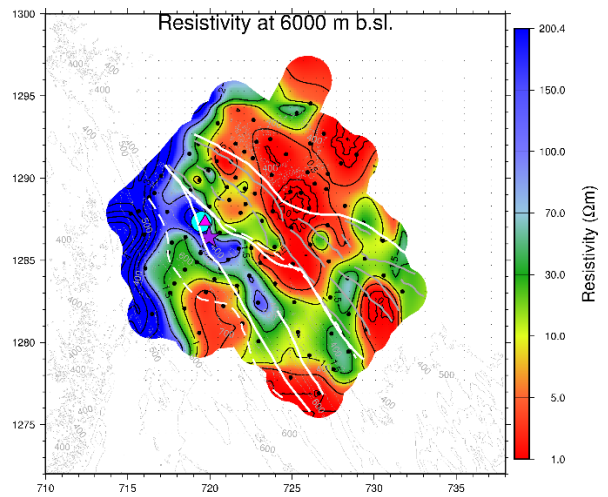
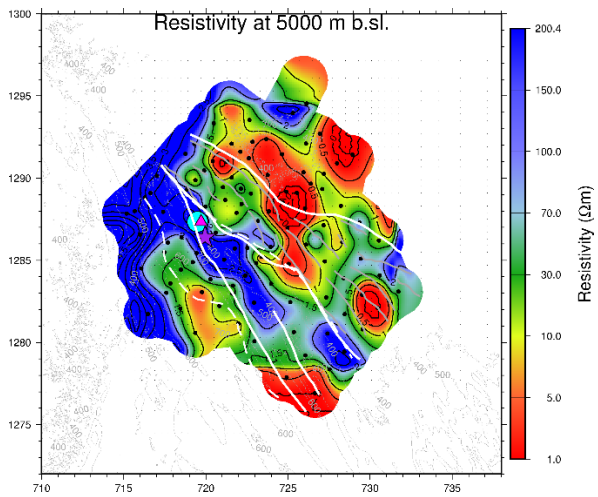
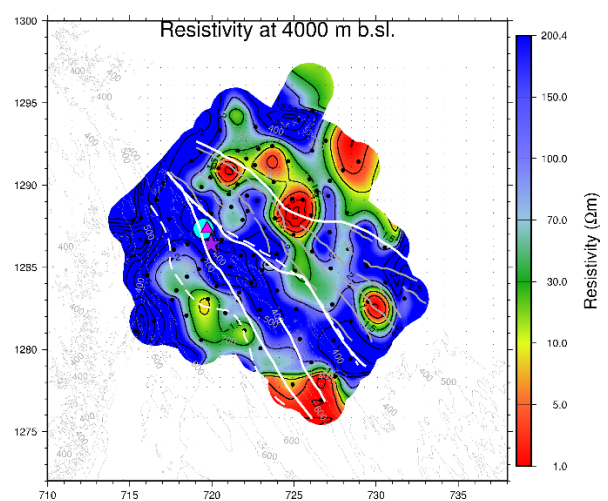
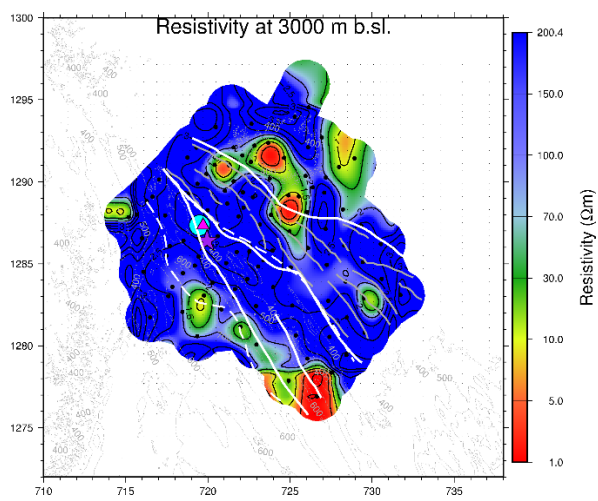
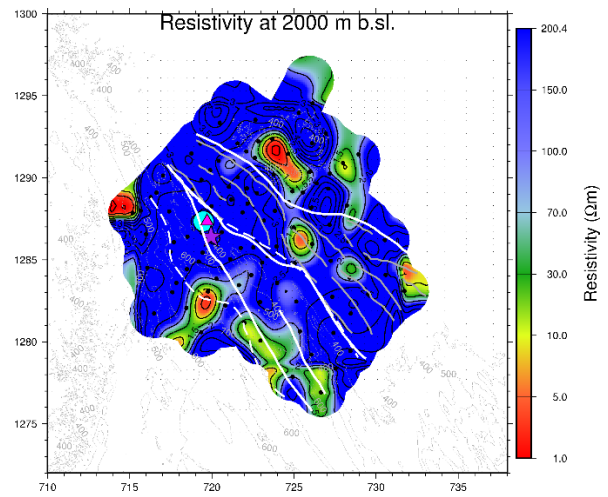
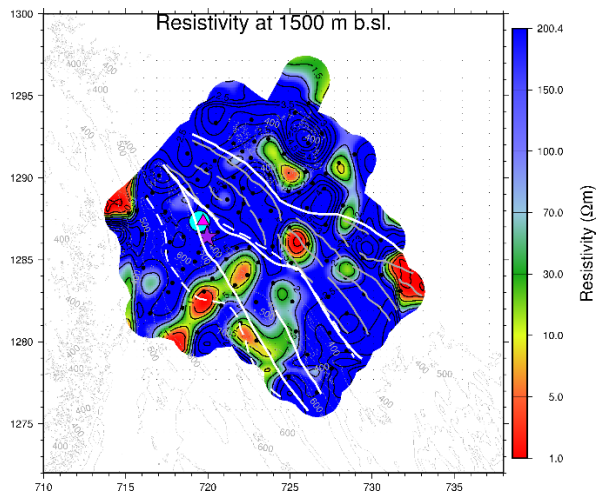


## APPENDIX V: 3D resistivity depth slices

Depth-slices based on the resistivity model from 3D inversion of the static shift corrected MT data using as a starting model, a model compiled from joint 1D inversion of individual TEM/MT sounding pairs (J1D). The model has been smoothed and elevation corrected. For Figure legend see Figure 57.







**APPENDIX VI: Resistivity cross-sections based on the 3D inversion  
presented for two different depth ranges**

Elevation corrected N-S and E-W lying cross-sections, through the denser part of the model grid, using as a starting model, a model compiled from joint 1D inversion of individual TEM/MT sounding pairs (J1D). The locations of the cross-sections are given in the right corner of each Figure.

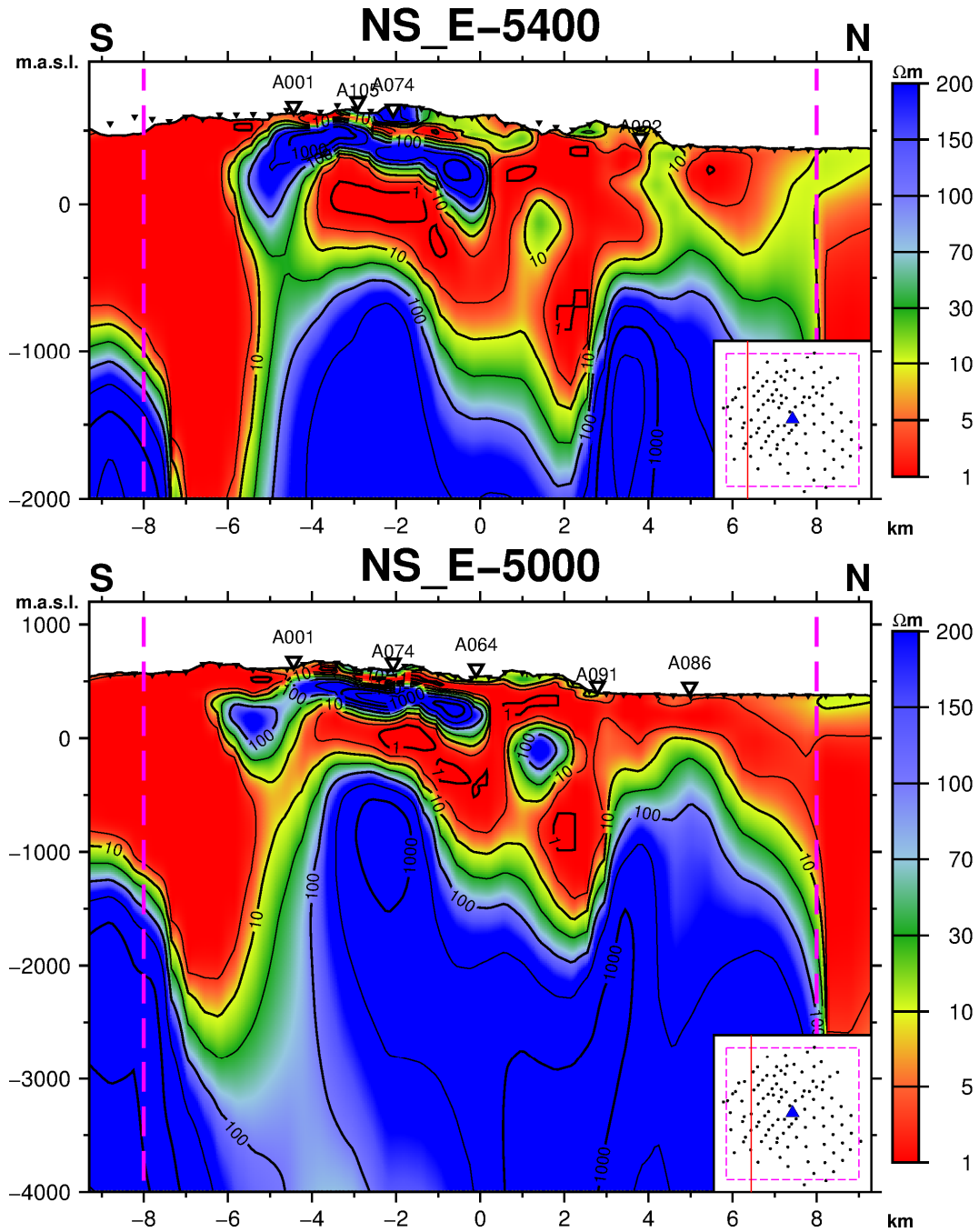


FIGURE 1: Cross-sections N-S, E -5400 and E -5000

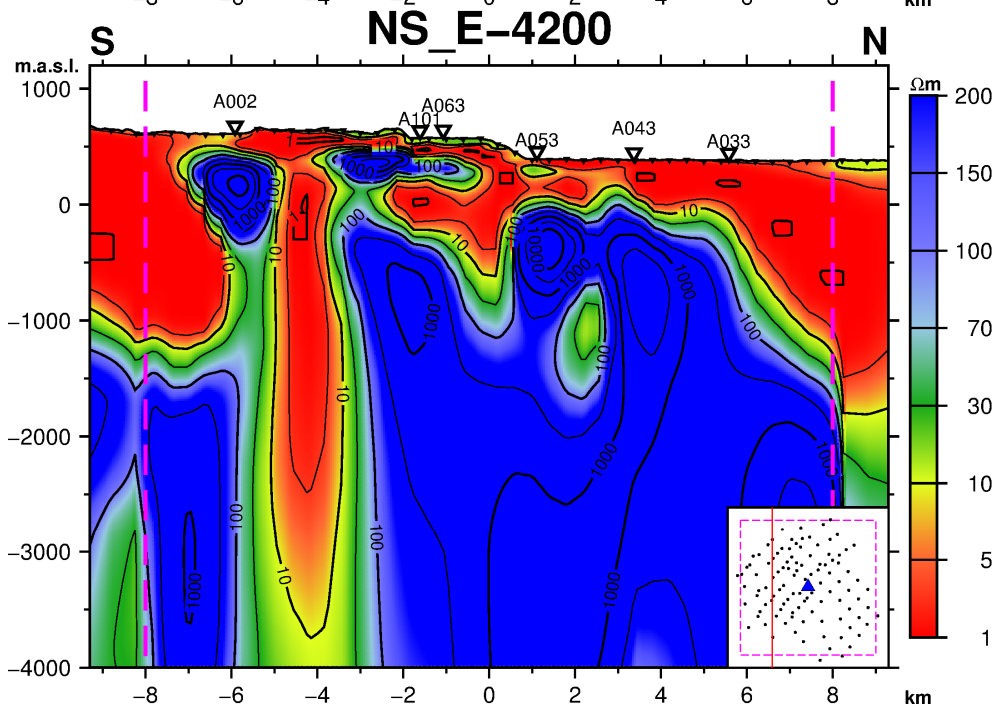
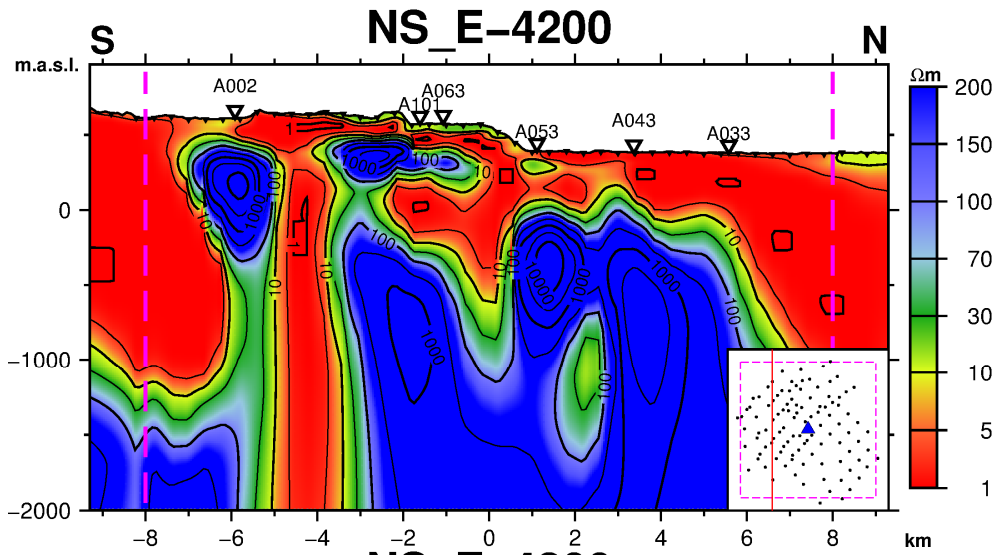
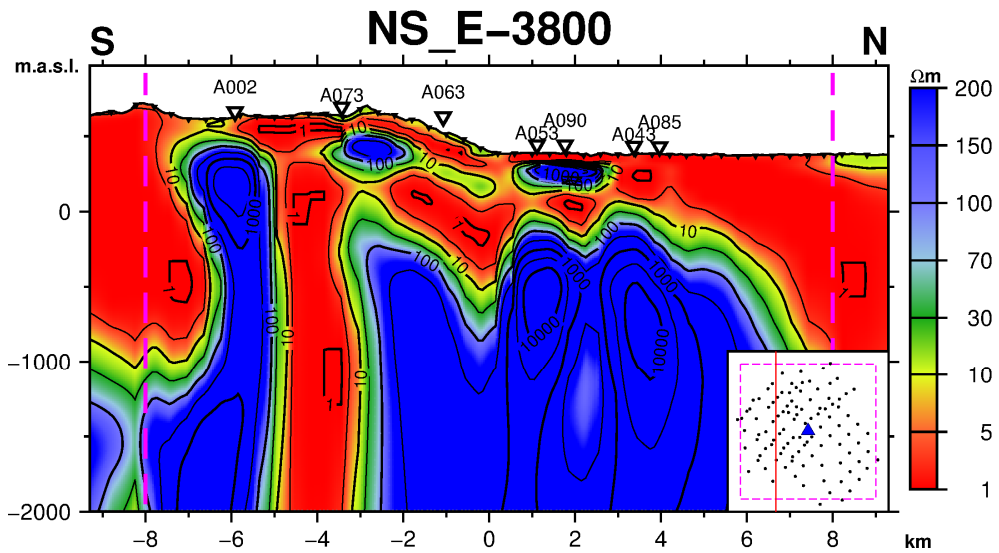


FIGURE 2: Cross-section N-S, E -4200



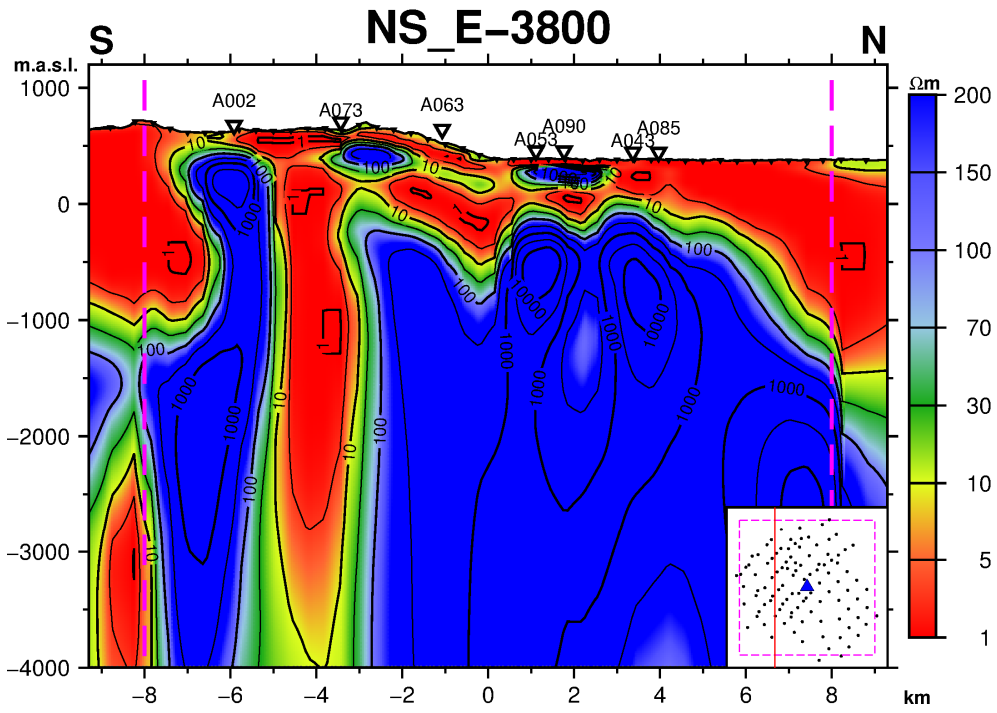


FIGURE 3: Cross-section N-S, E -3800

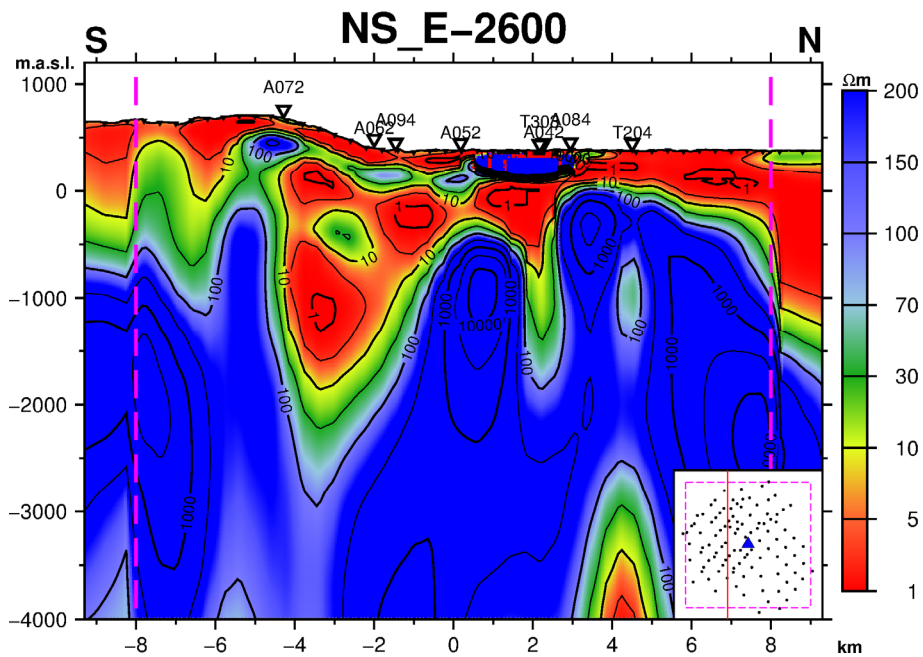
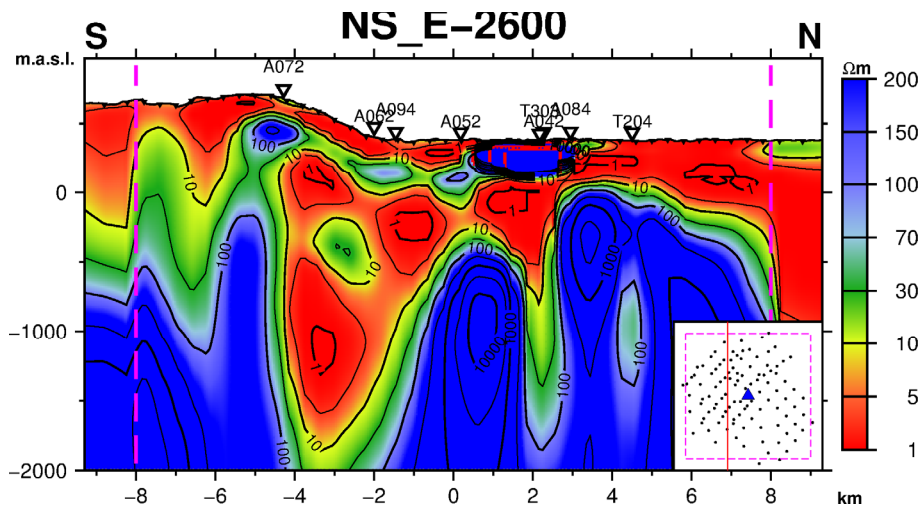


FIGURE 4: Cross-section N-S, E -2600

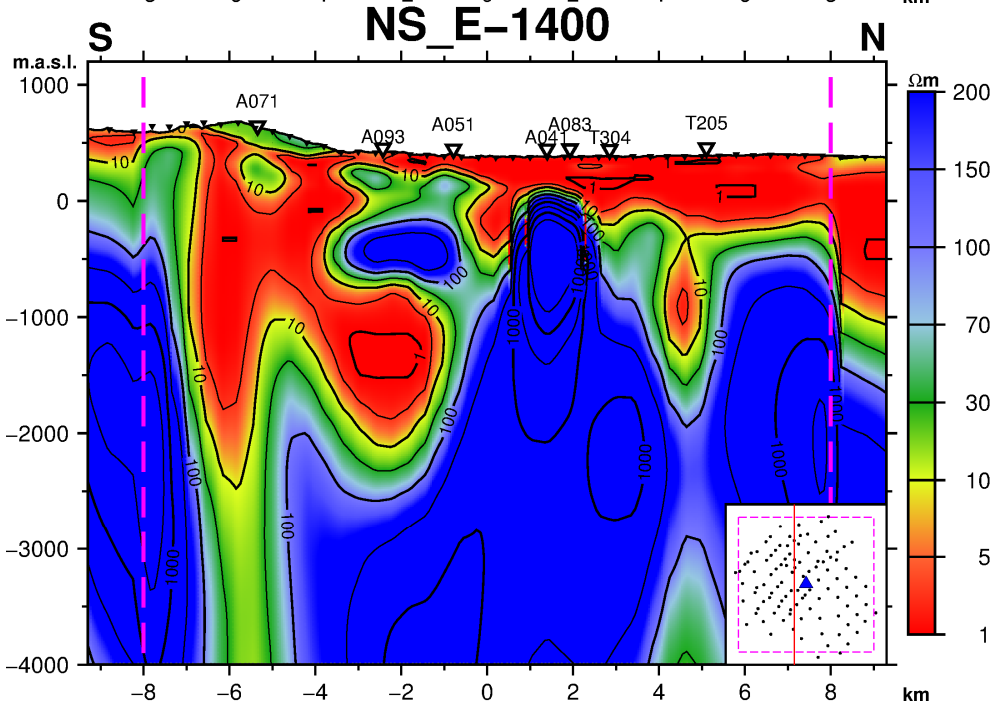
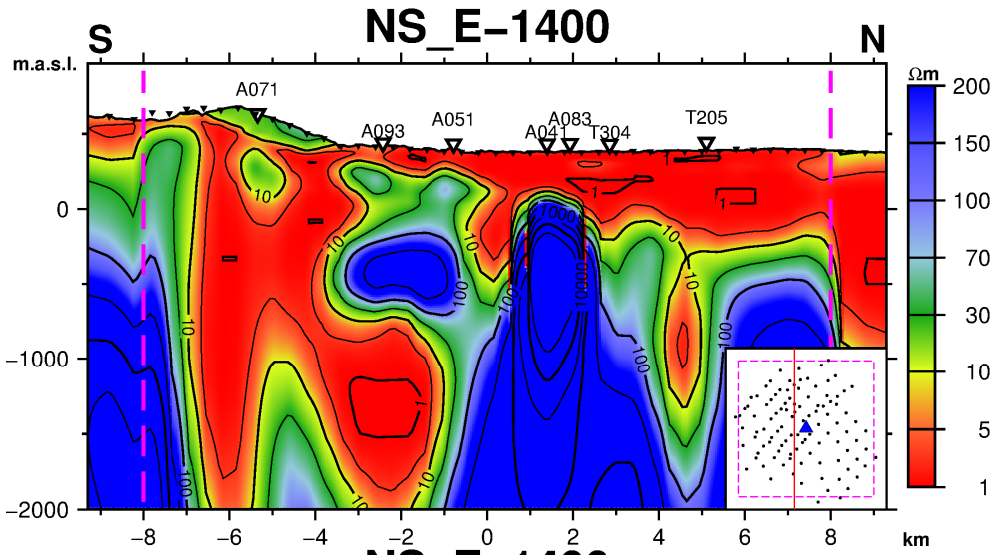
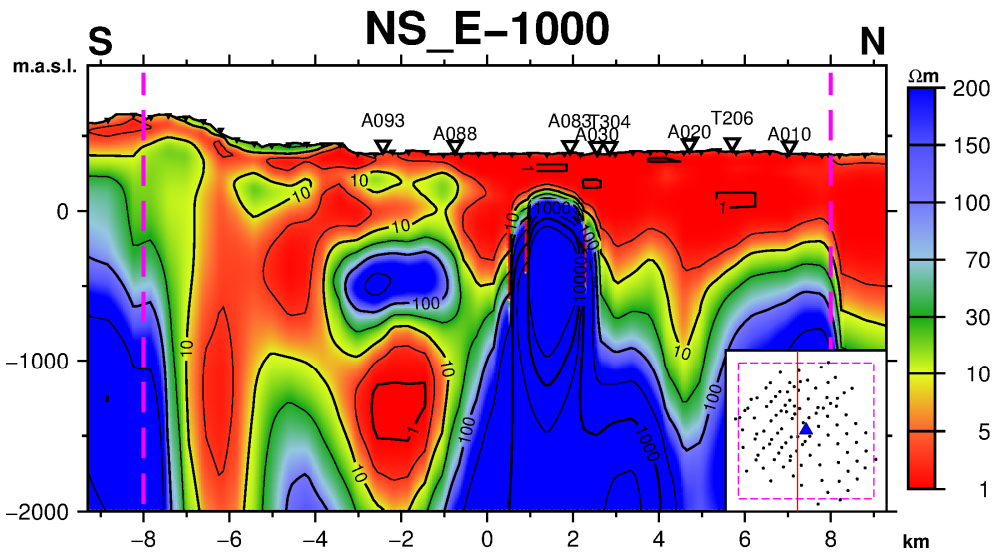


FIGURE 5: Cross-section N-S, E -1400



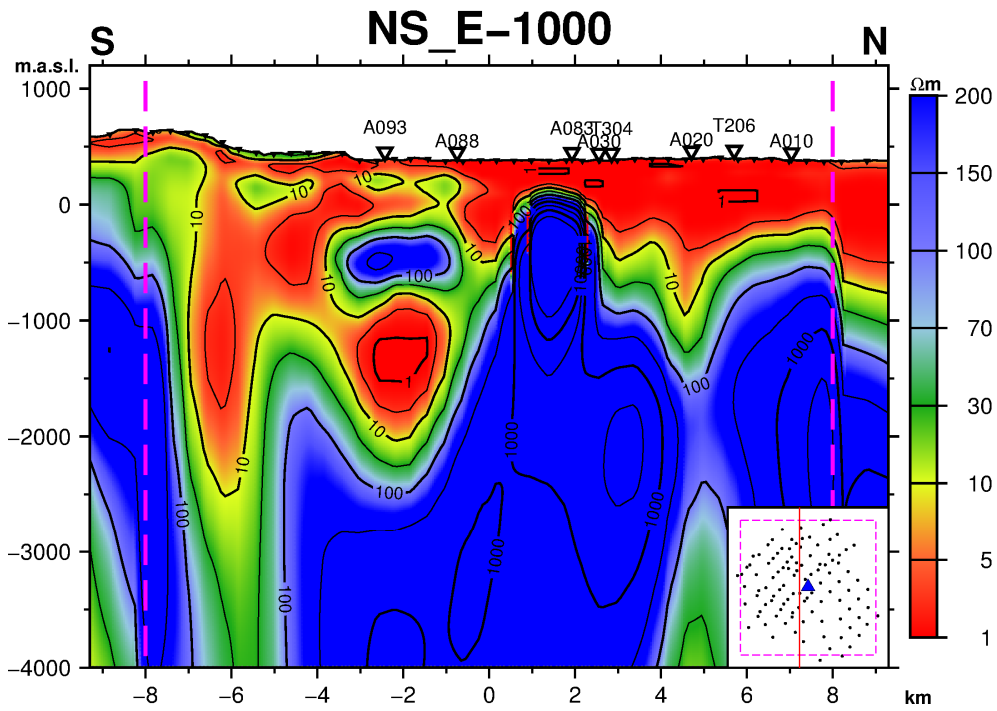


FIGURE 6: Cross-section N-S, E -1000

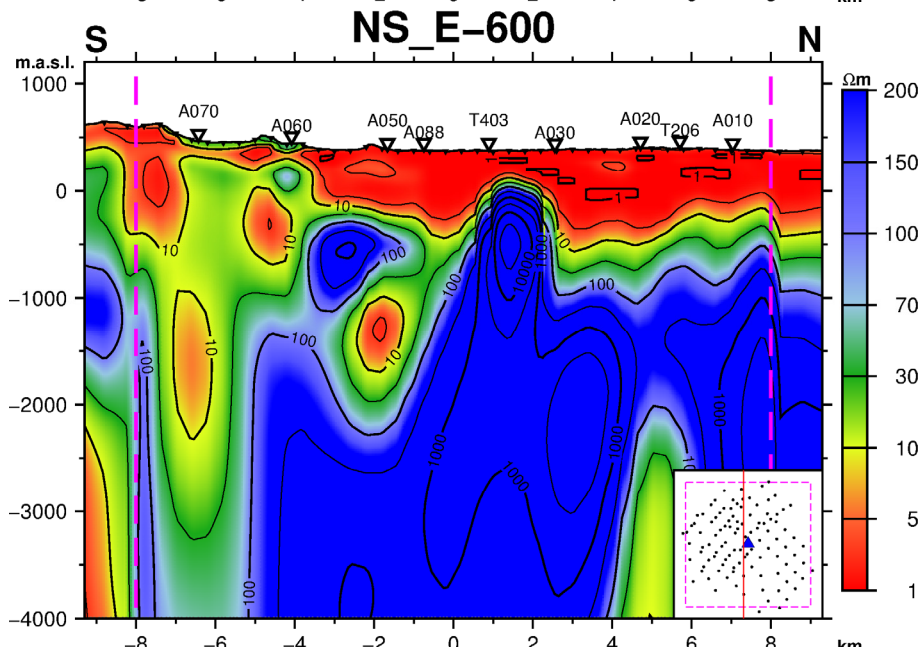
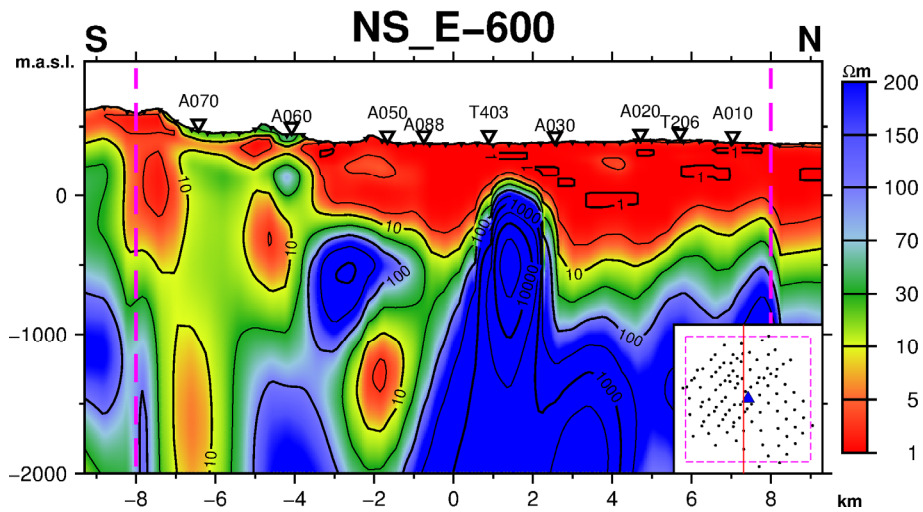


FIGURE 7: Cross-section N-S, E -600

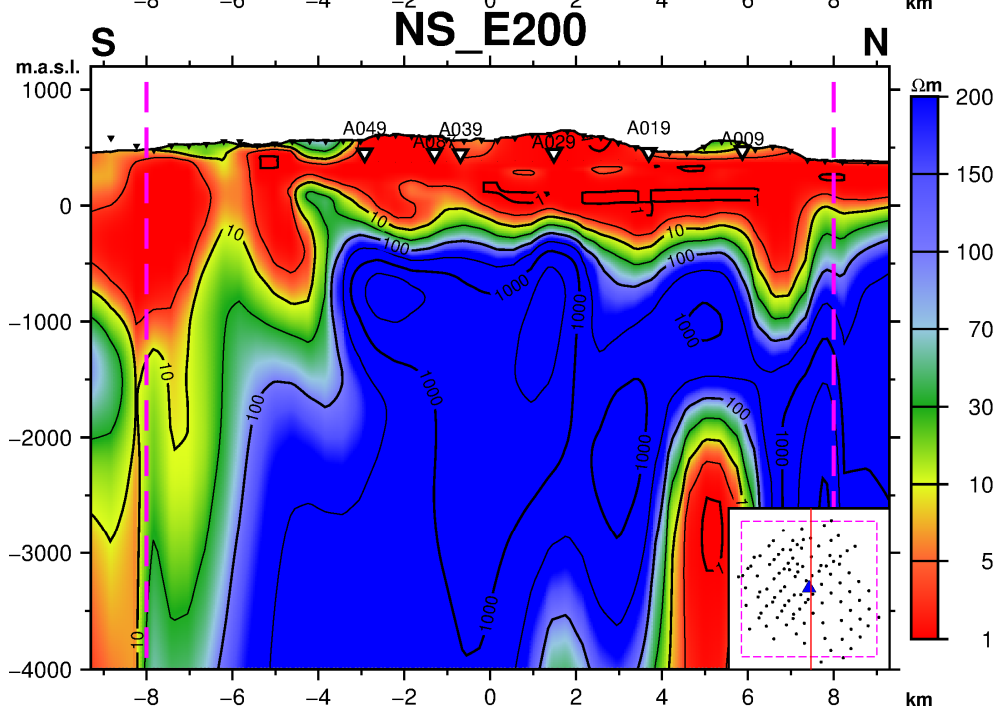
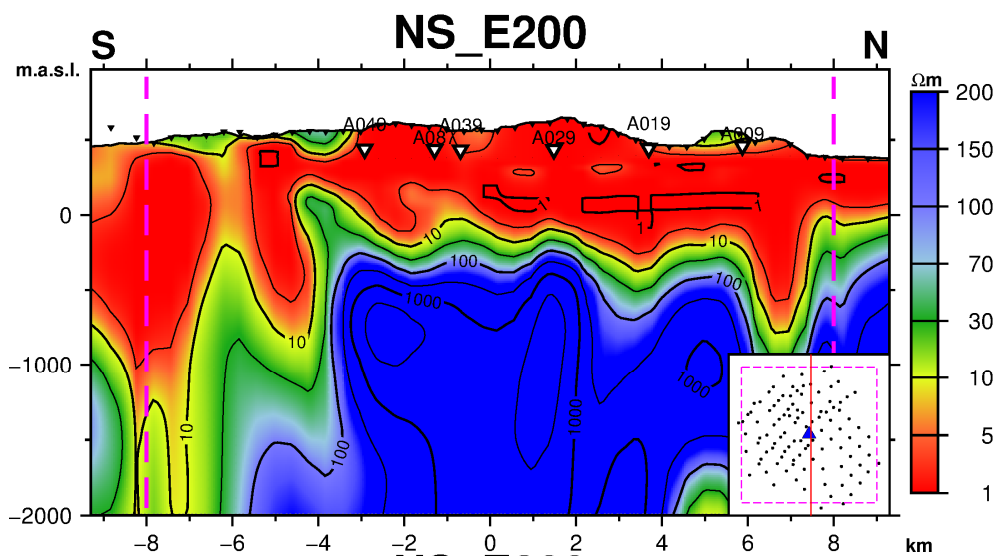
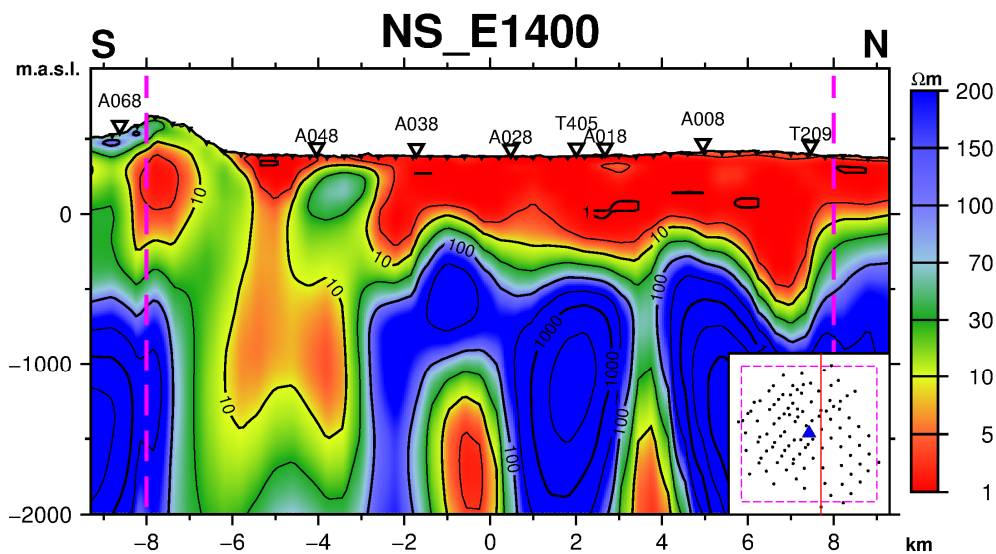


FIGURE 8: Cross-section N-S, E 200



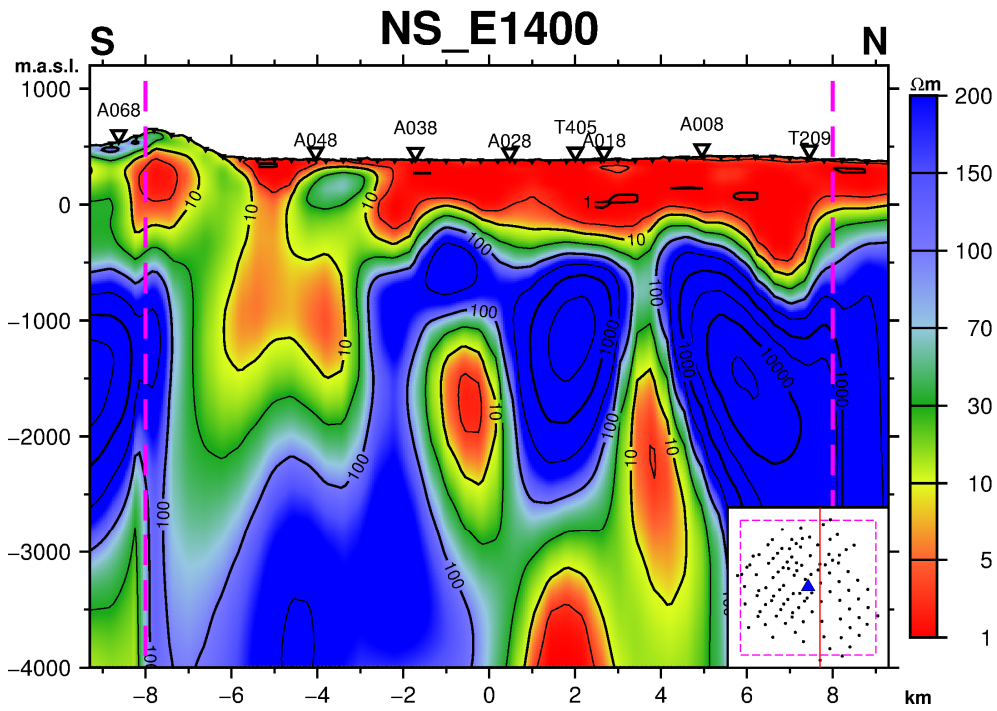


FIGURE 9: Cross-section N-S, E 1400

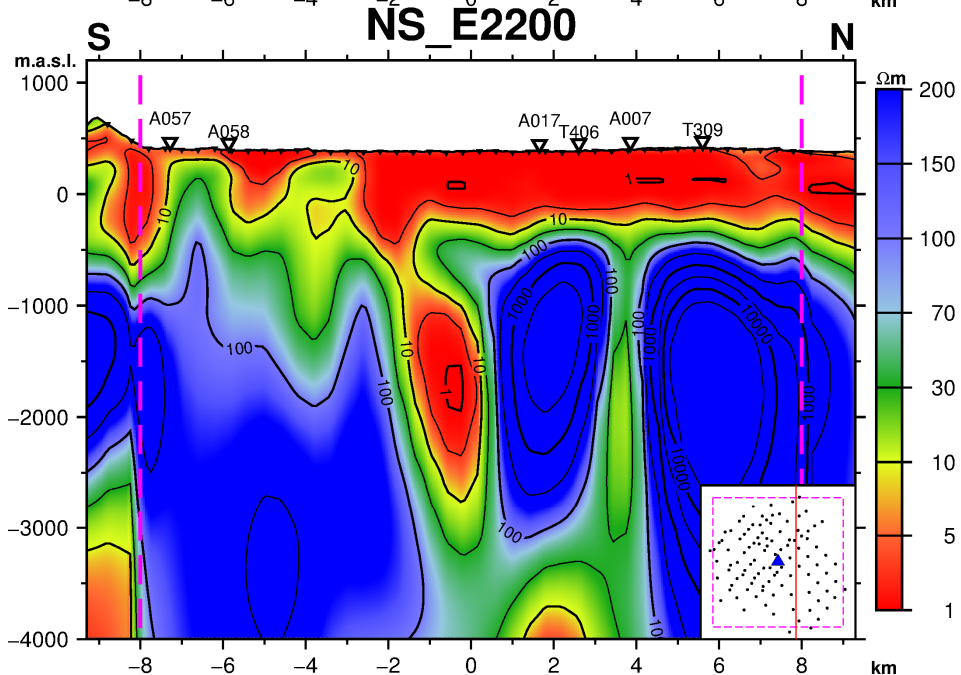
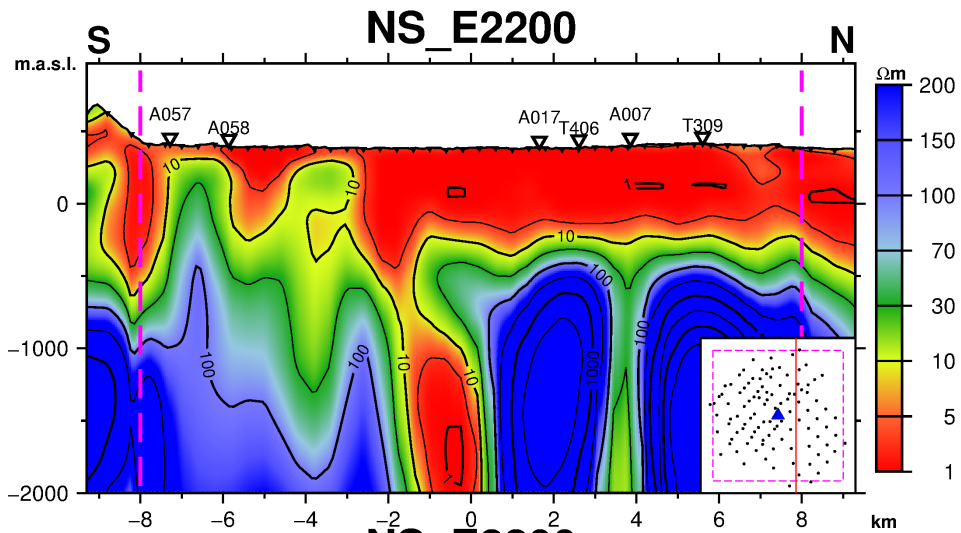


FIGURE 10: Cross-section N-S, E 2200

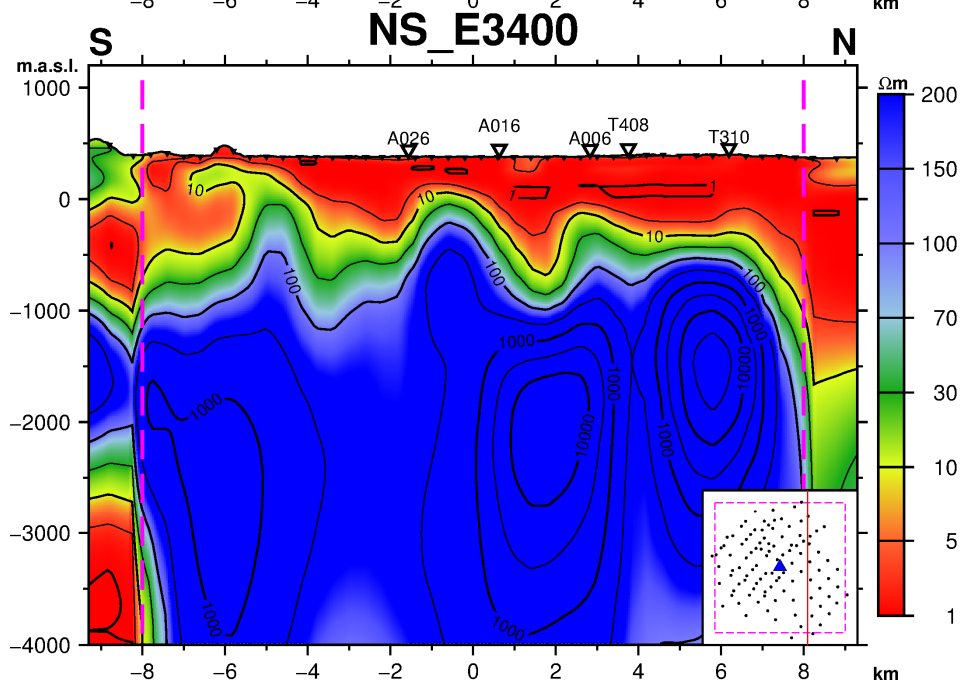
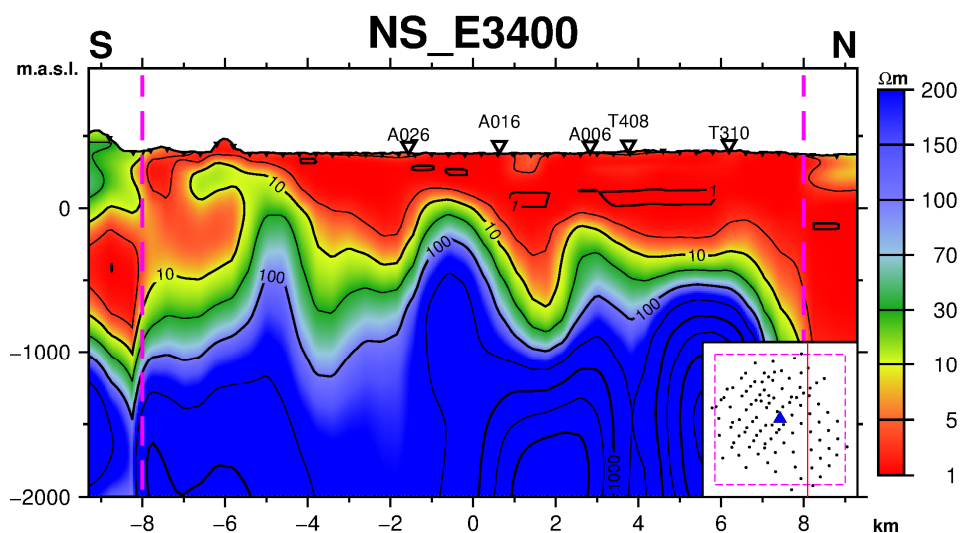
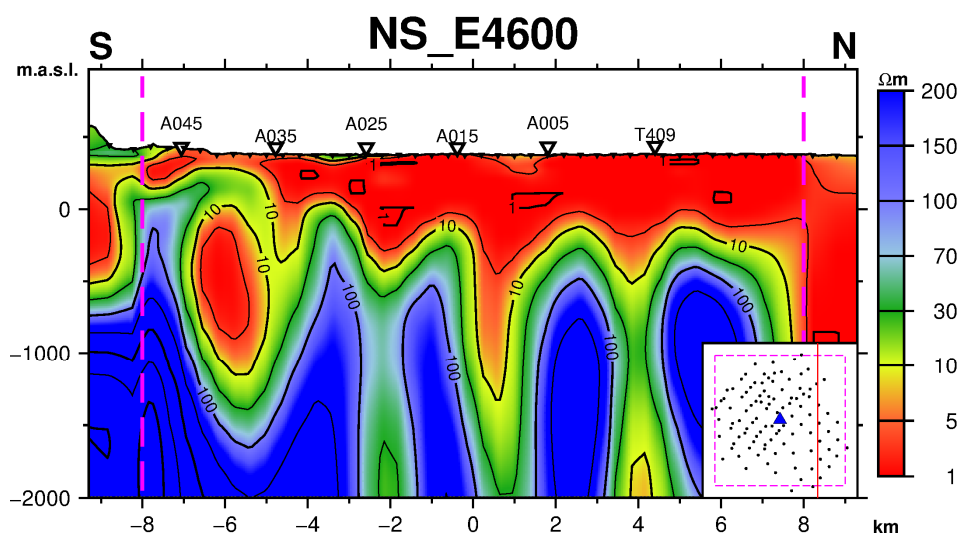


FIGURE 11: Cross-section N-S, E 3400



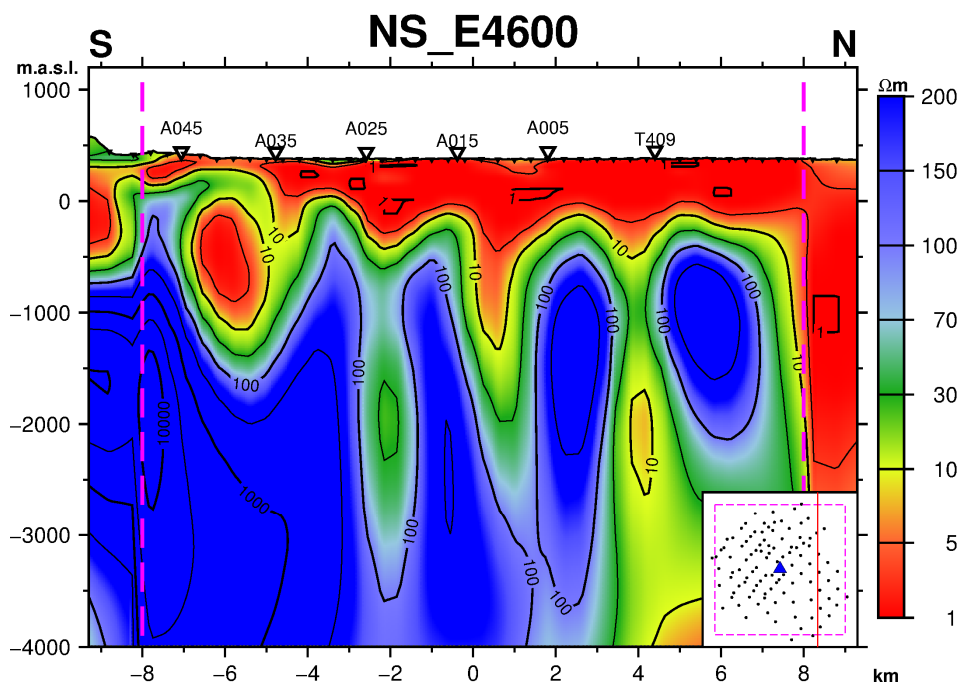


FIGURE 12: Cross-section N-S, E 4600

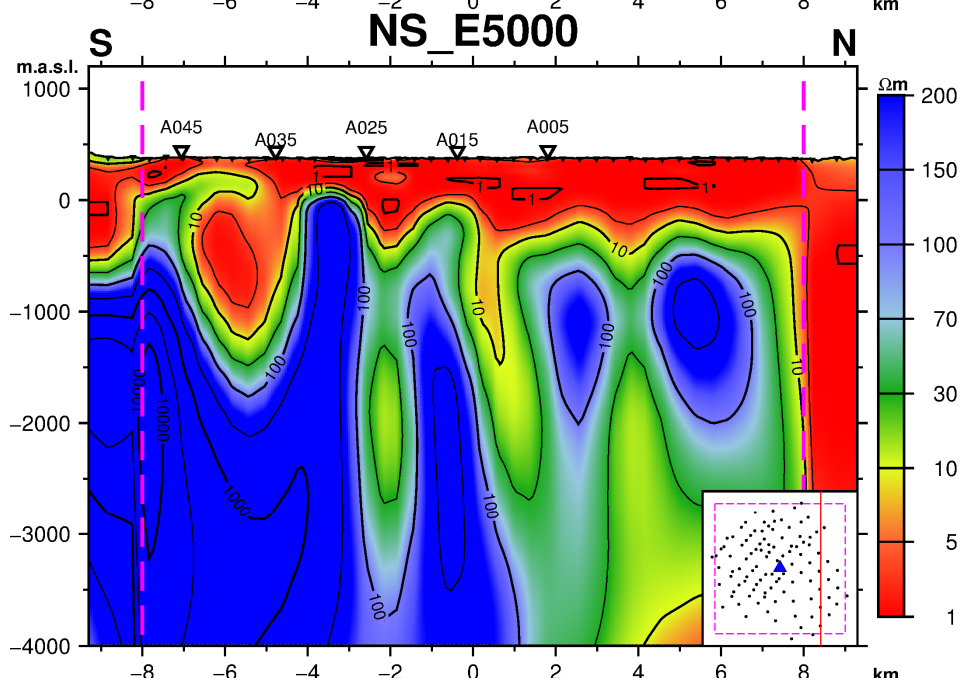
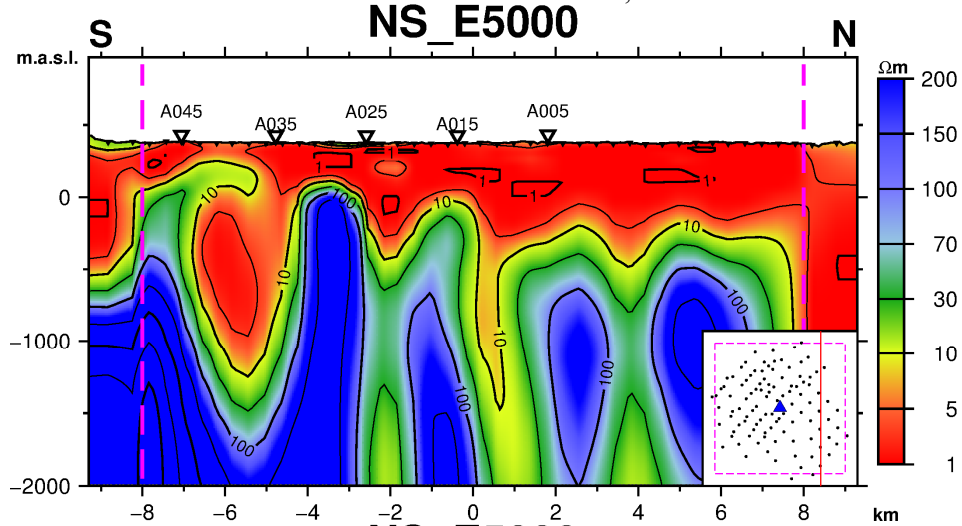


FIGURE 13: Cross-section N-S, E 5000

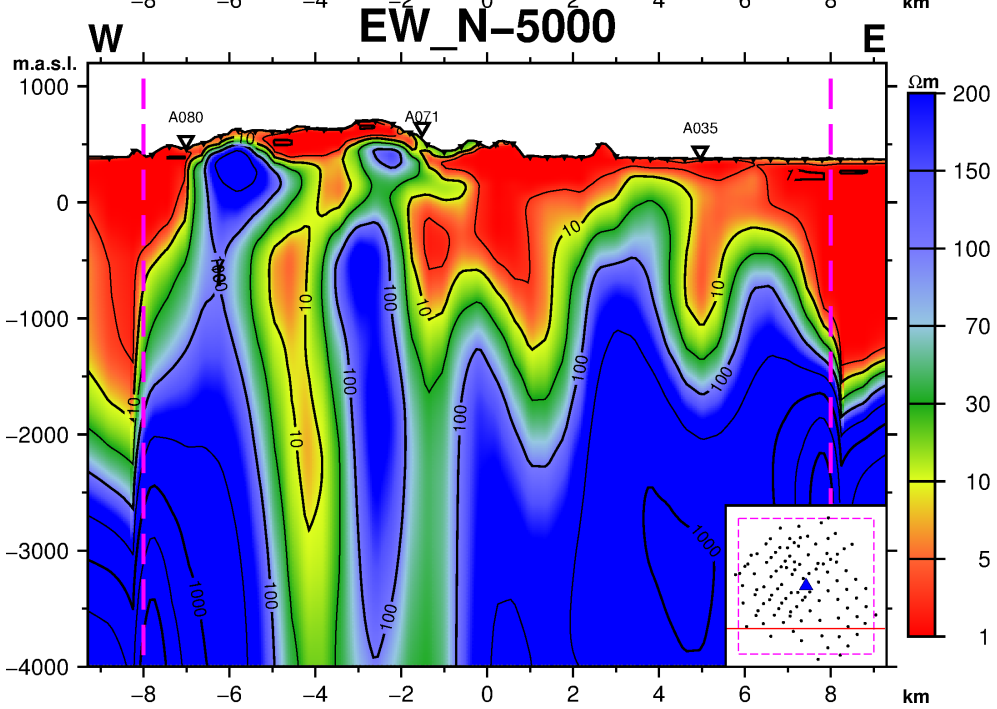
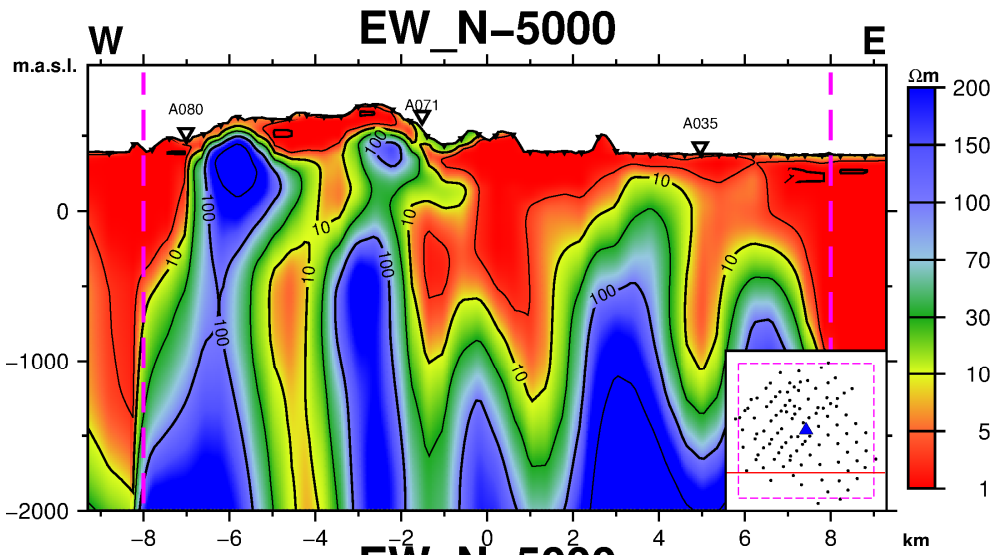
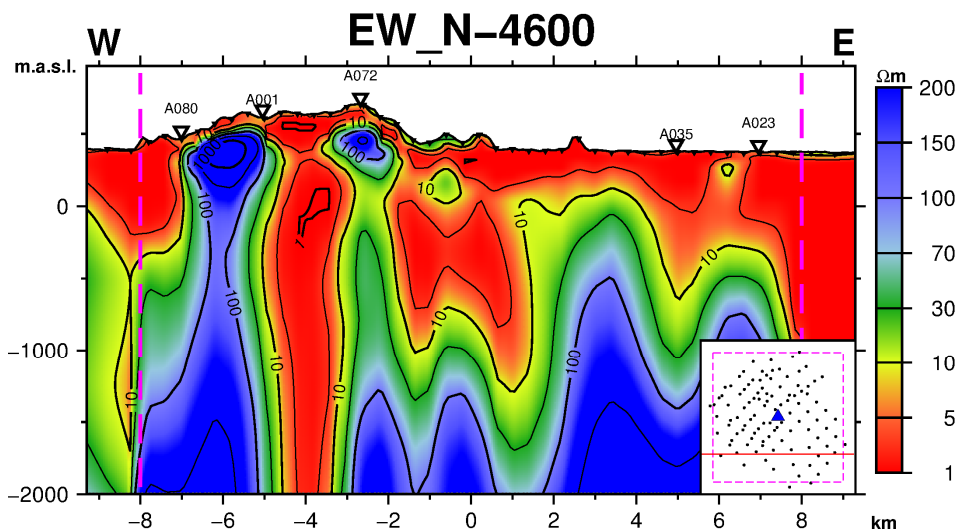


FIGURE 14: Cross-section E-W, N -5000



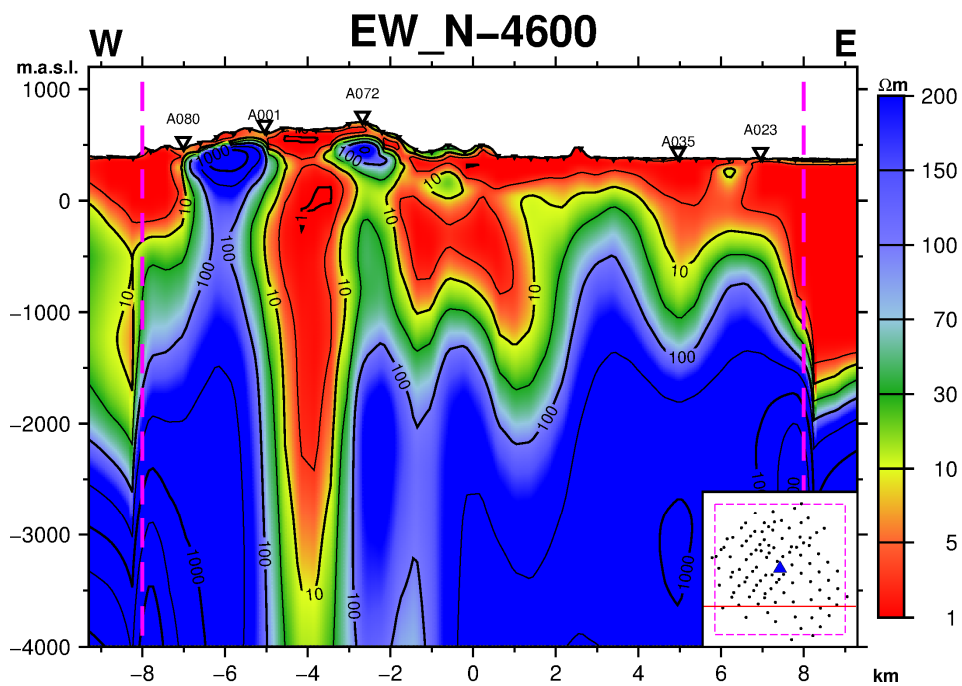


FIGURE 15: Cross-section E-W, N -4600

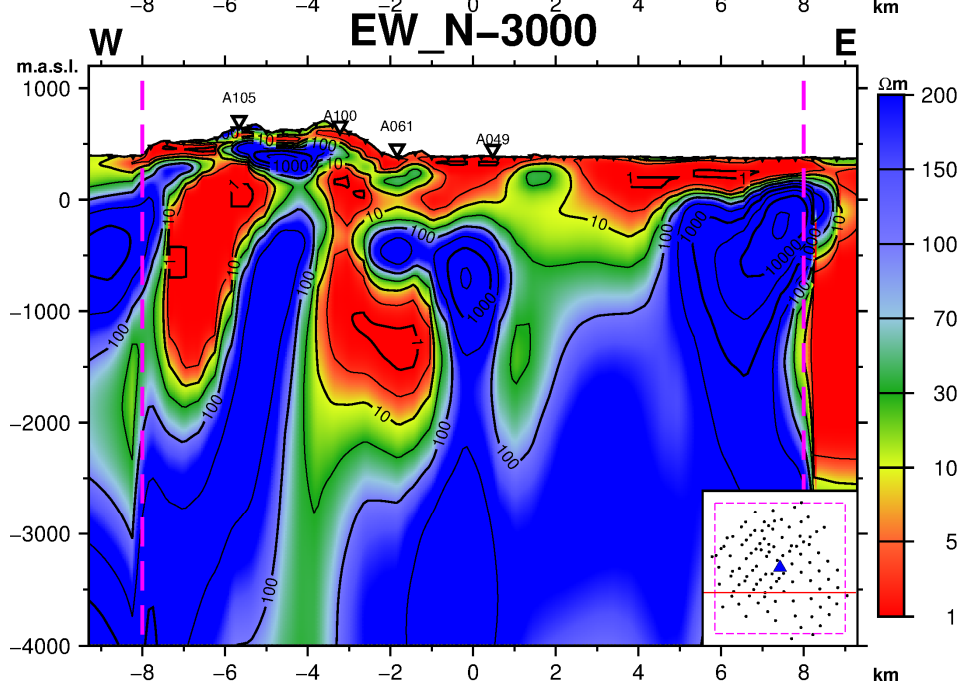
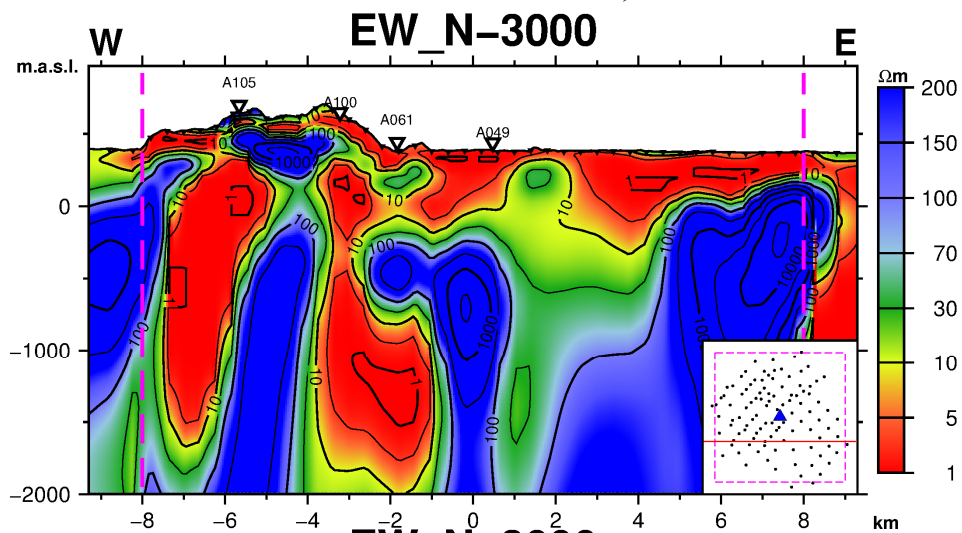


FIGURE 16: Cross-section E-W, N -3000

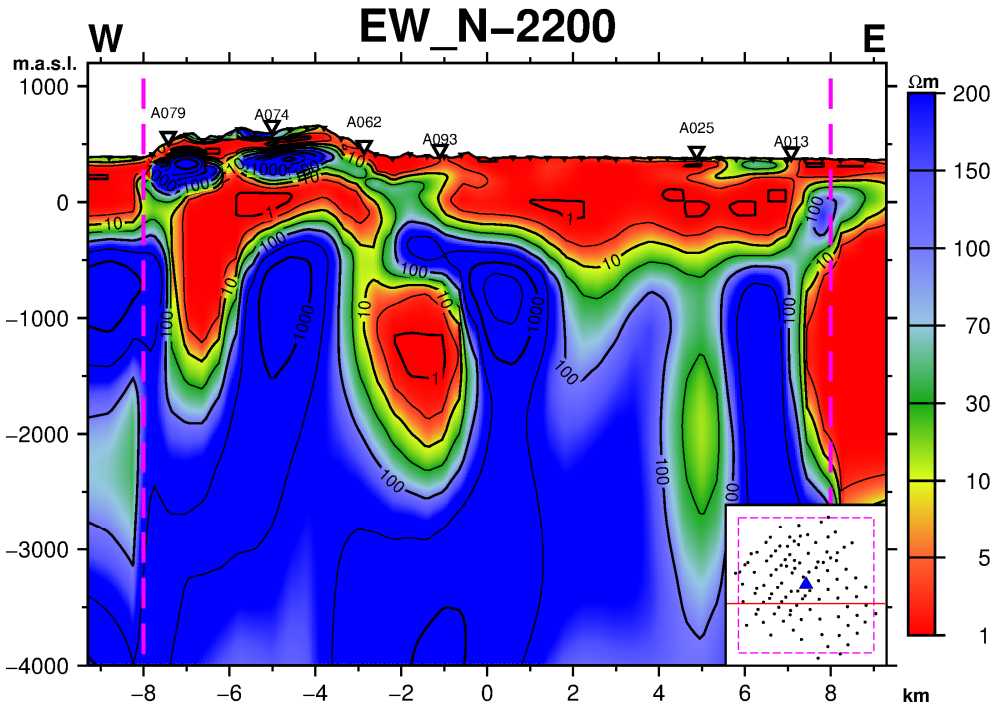
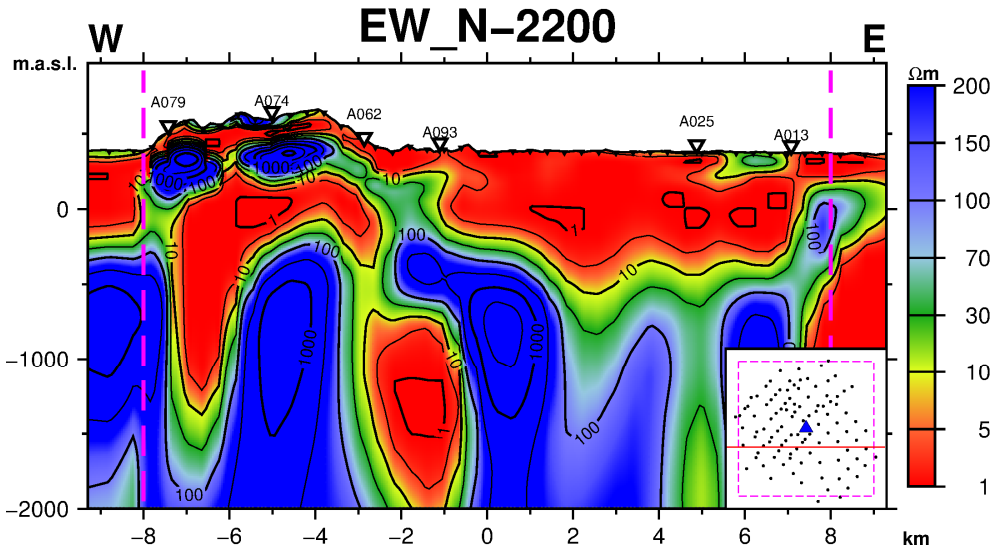
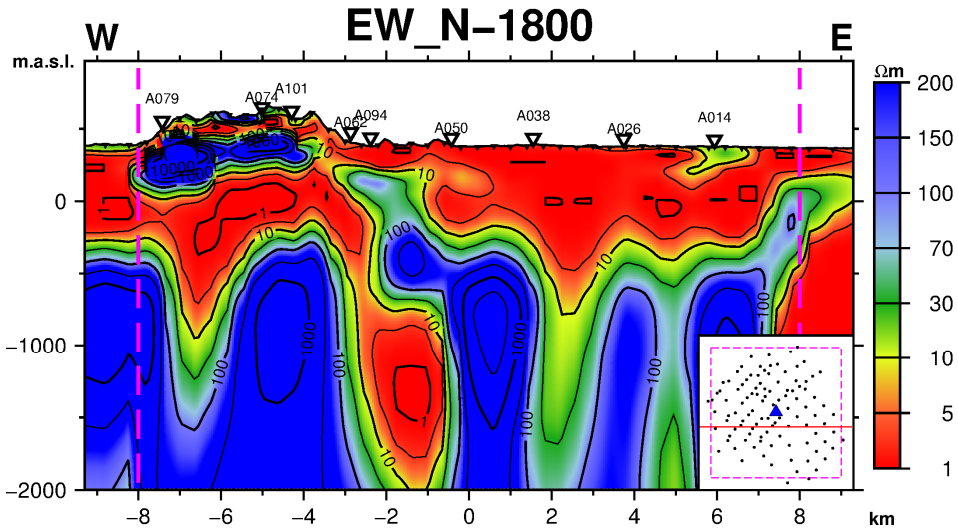


FIGURE 17: Cross-section E-W, N -2200



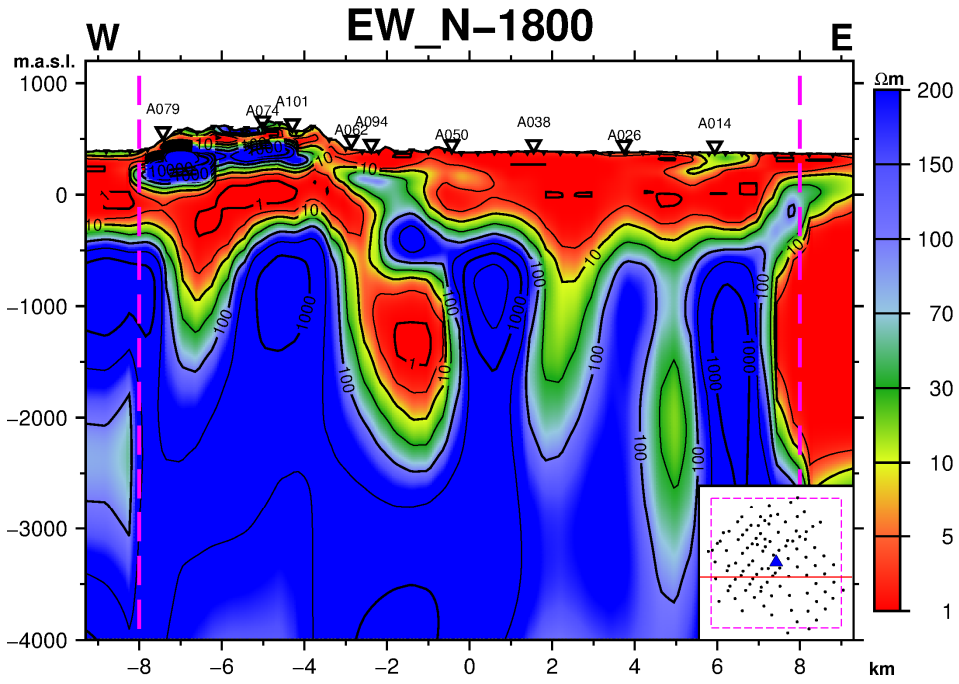


FIGURE 18: Cross-section E-W, N -1800

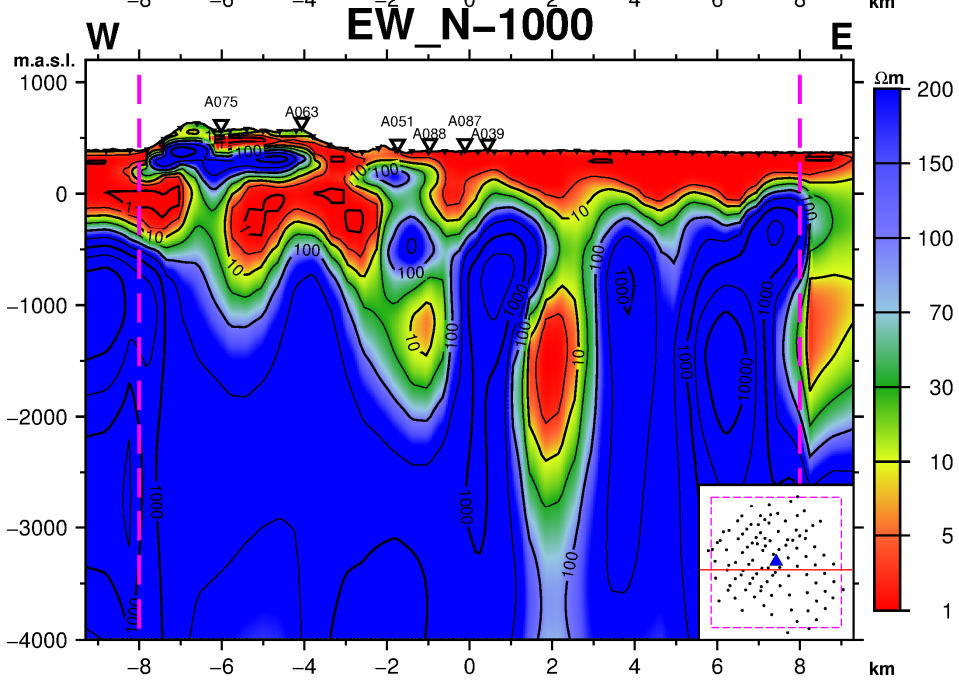
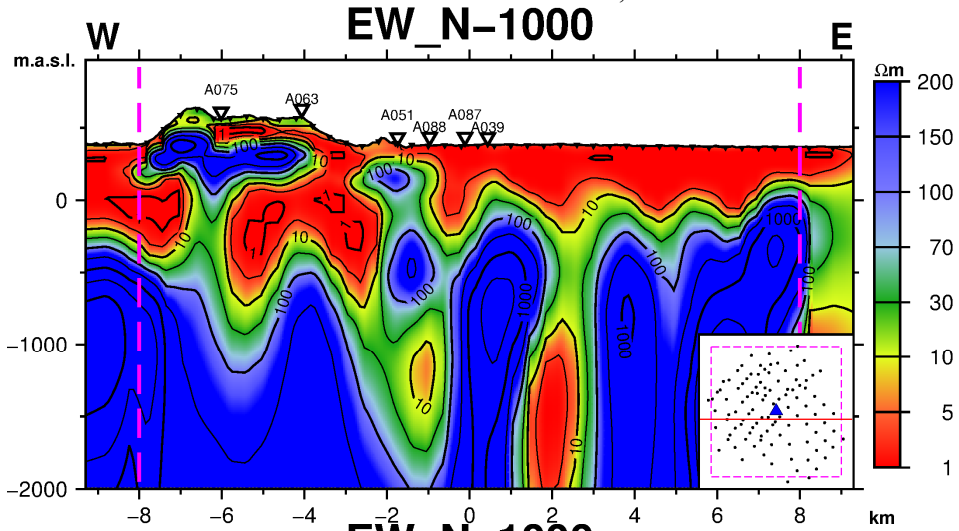


FIGURE 19: Cross-section E-W, N -1000

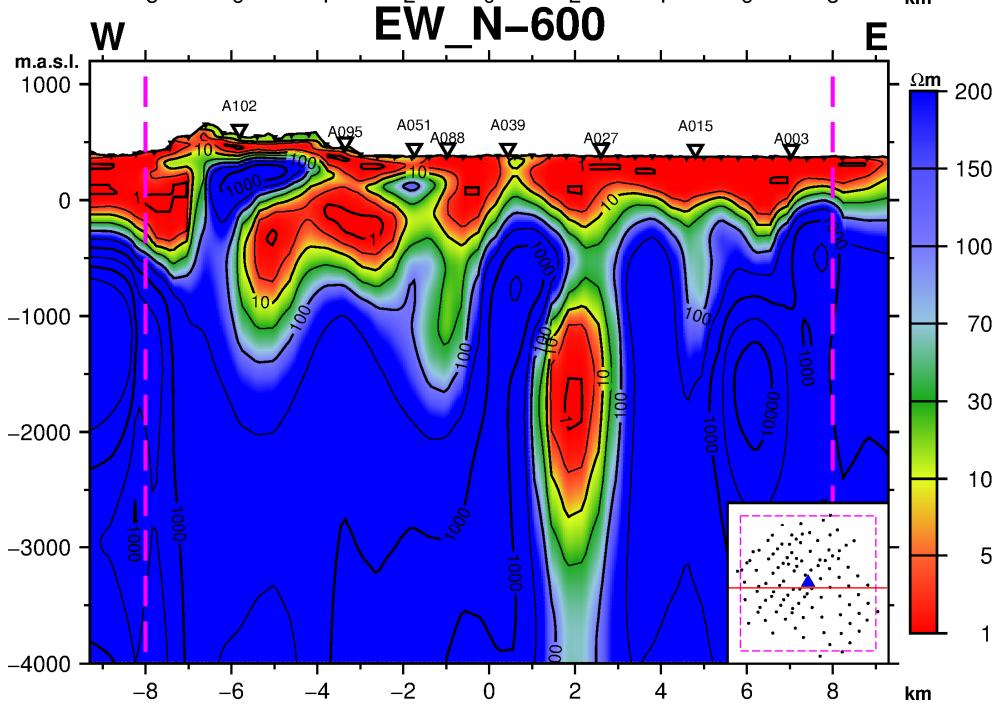
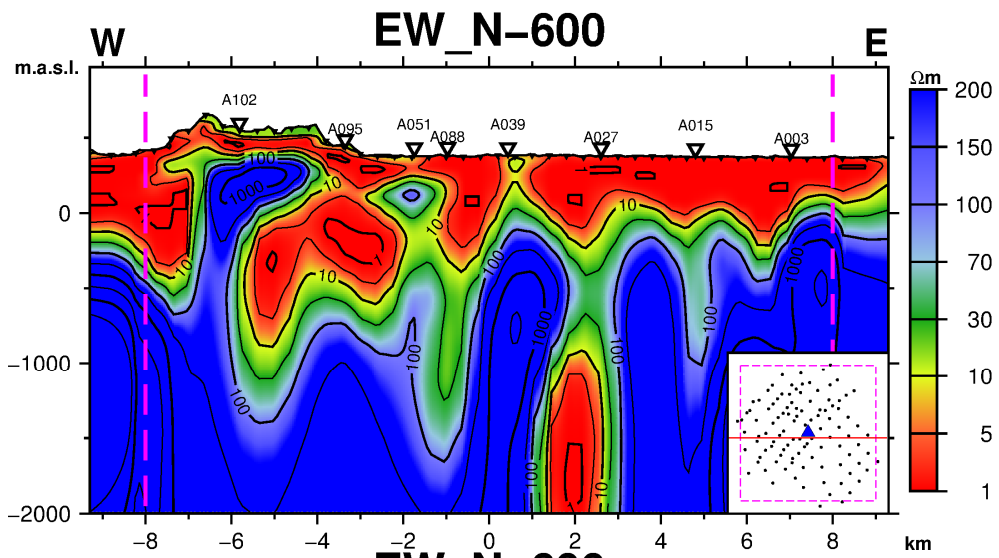
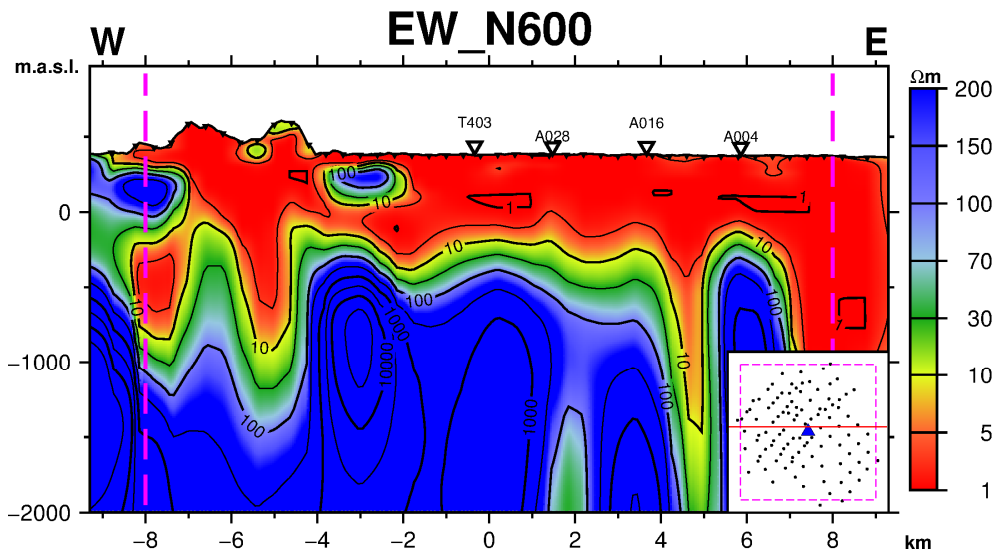


FIGURE 20: Cross-section E-W, N -600



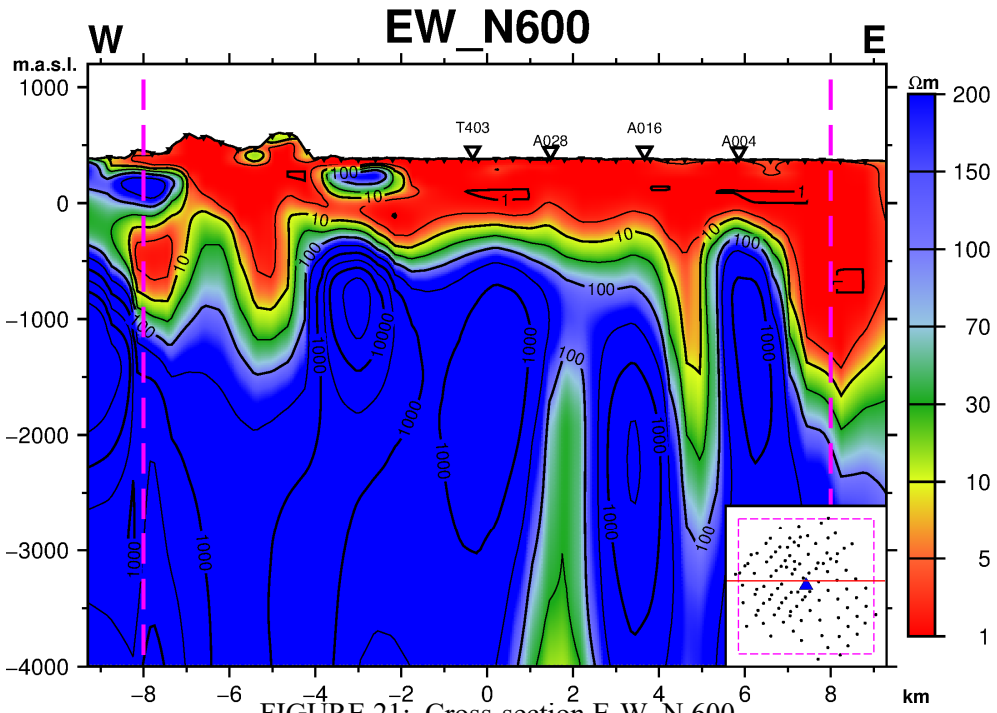


FIGURE 21: Cross-section E-W, N 600

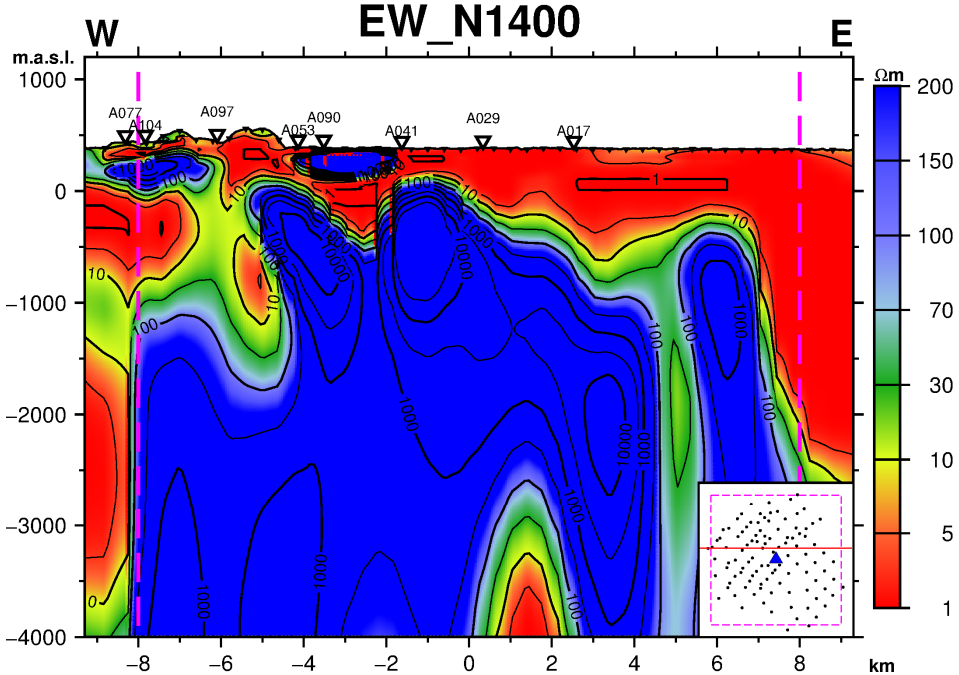
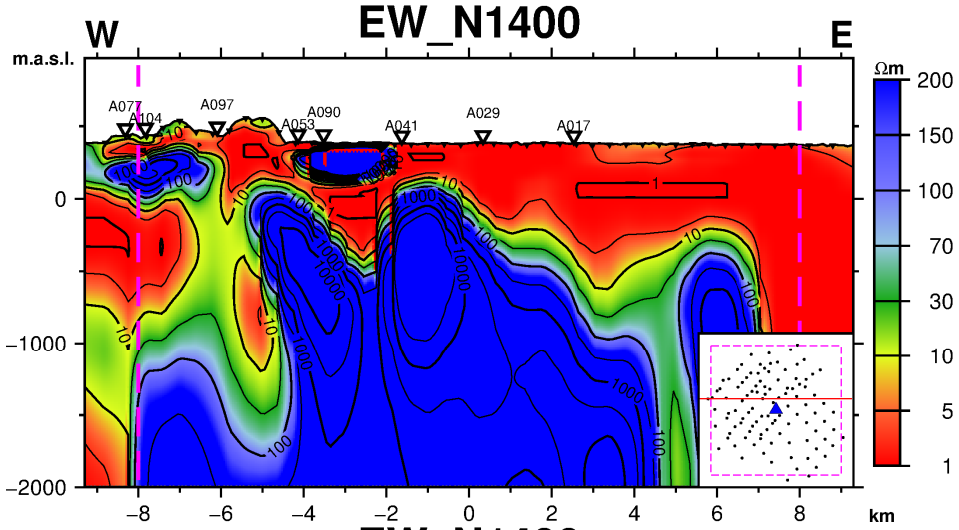


FIGURE 22: Cross-section E-W, N 1400

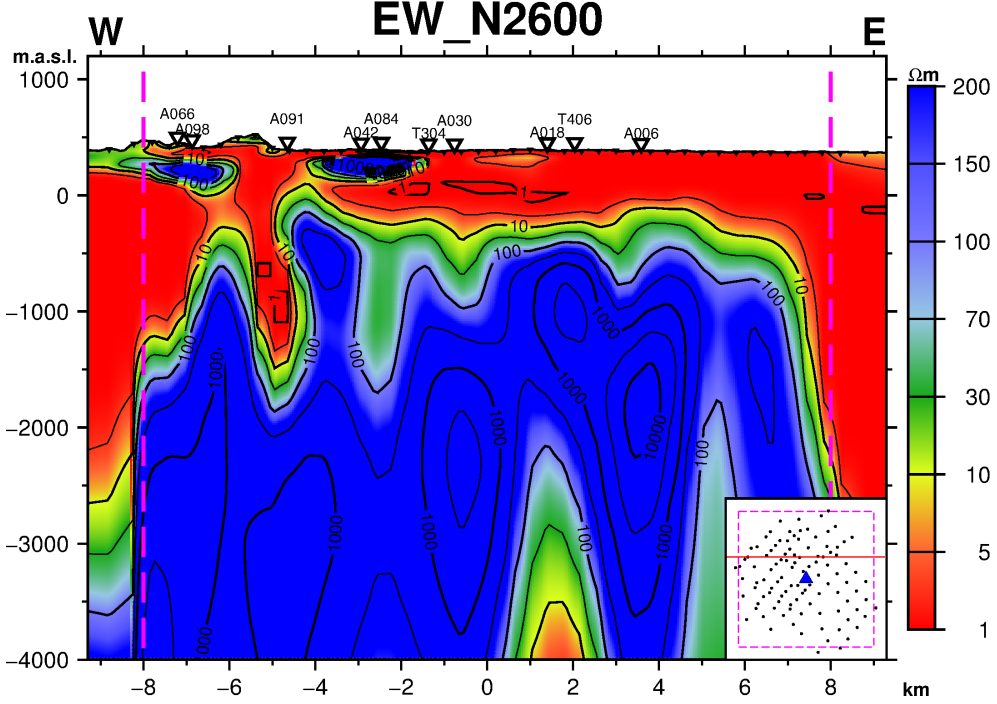
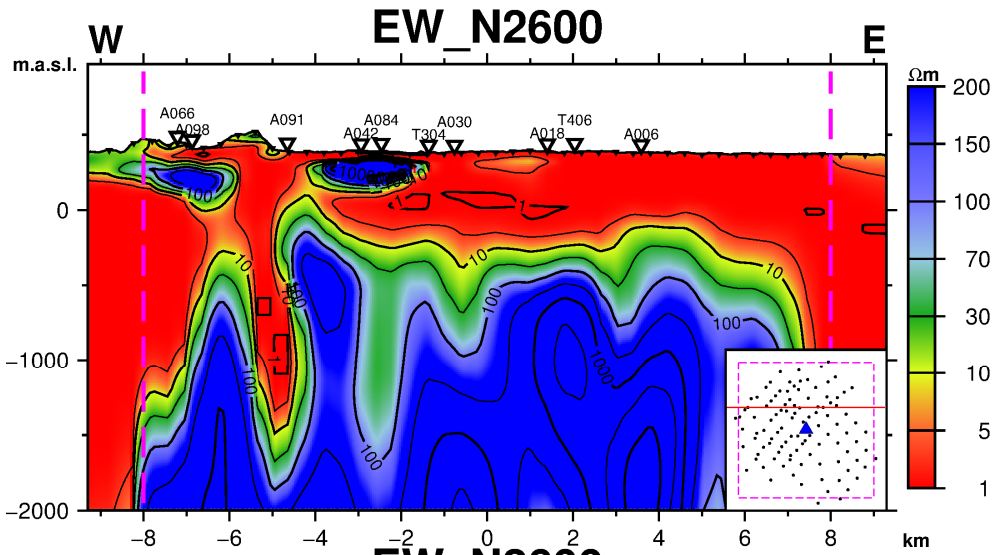
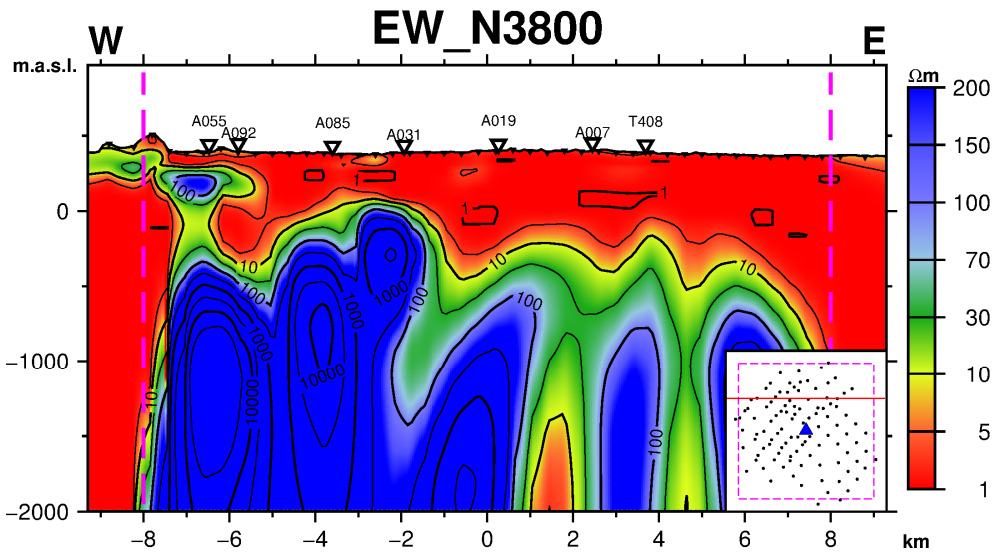


FIGURE 23: Cross-section E-W, N 2600



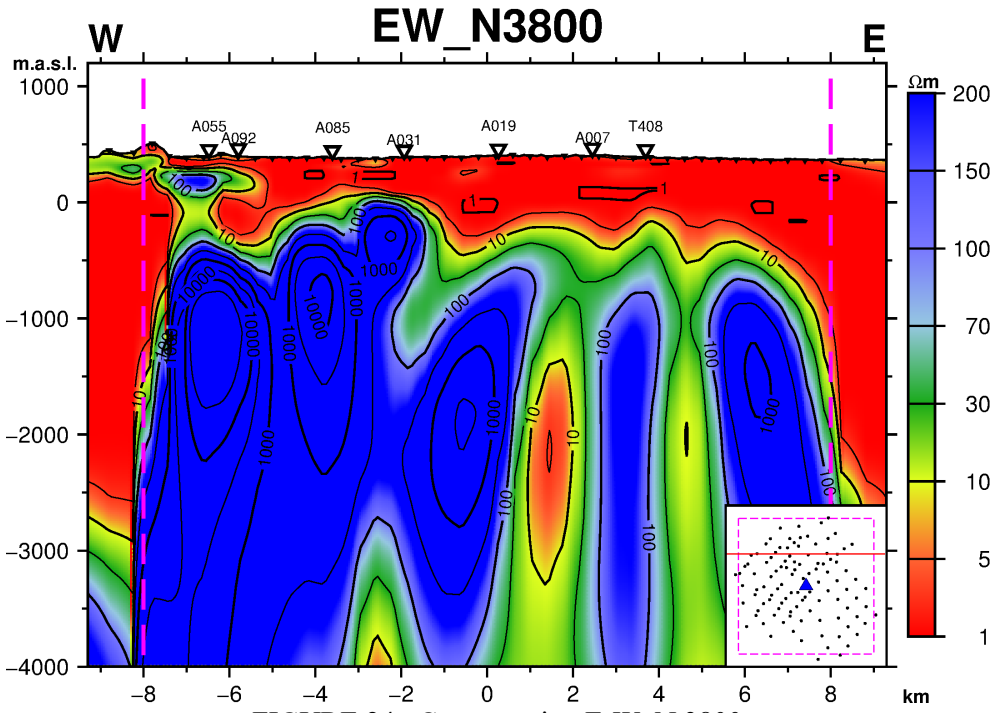


FIGURE 24: Cross-section E-W, N 3800

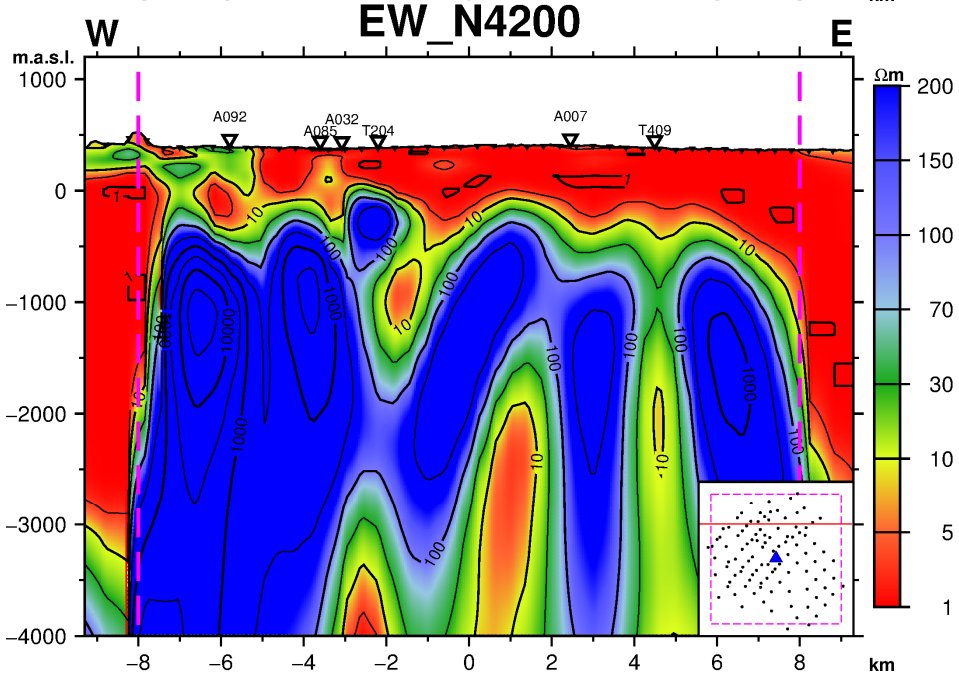
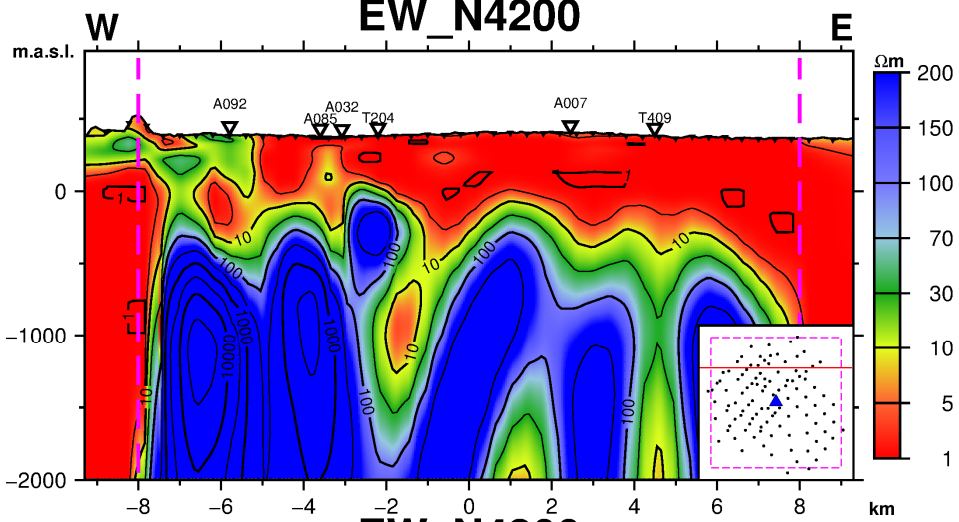


FIGURE 25: Cross-section E-W, N 4200

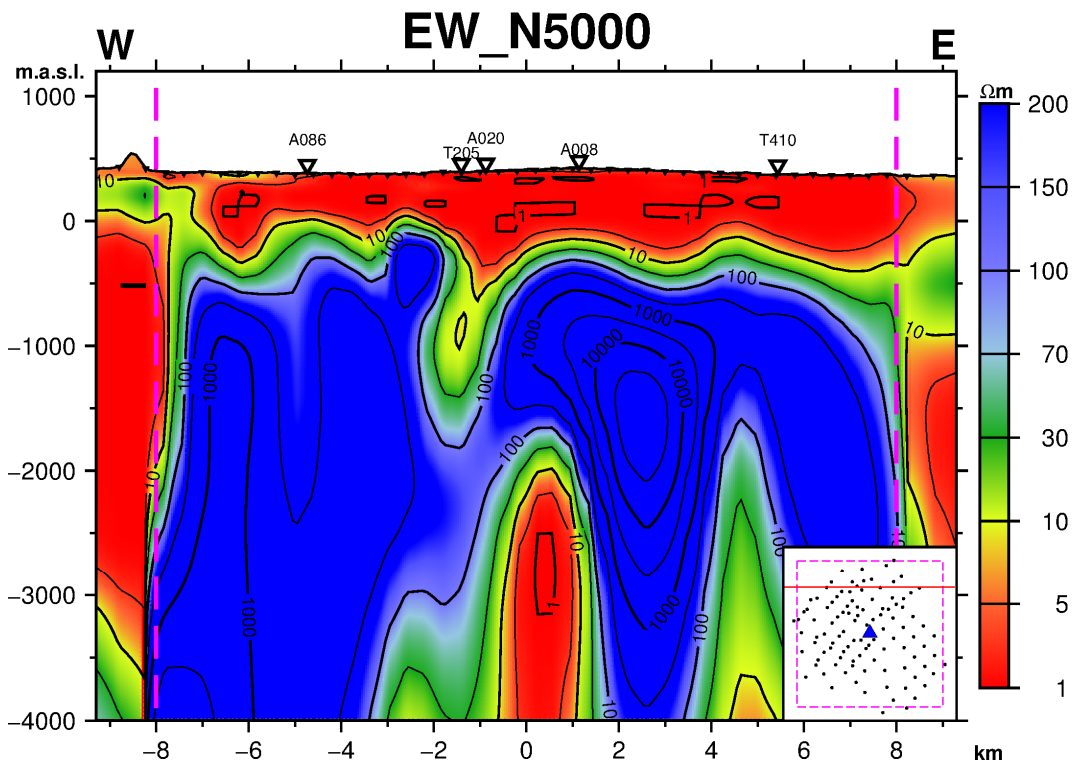
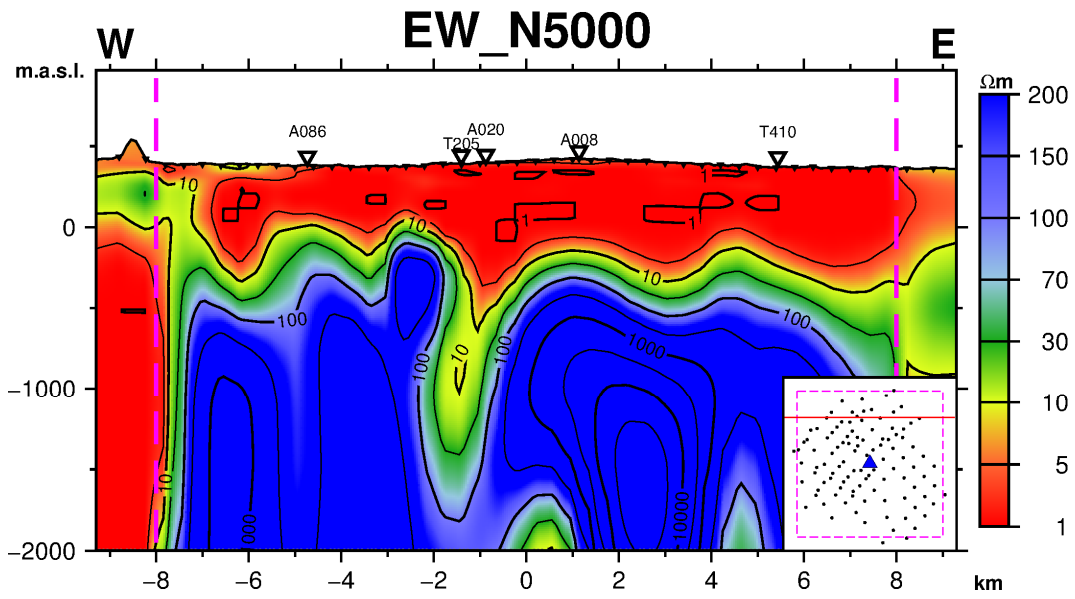


FIGURE 26: Cross-section E-W, N 5000

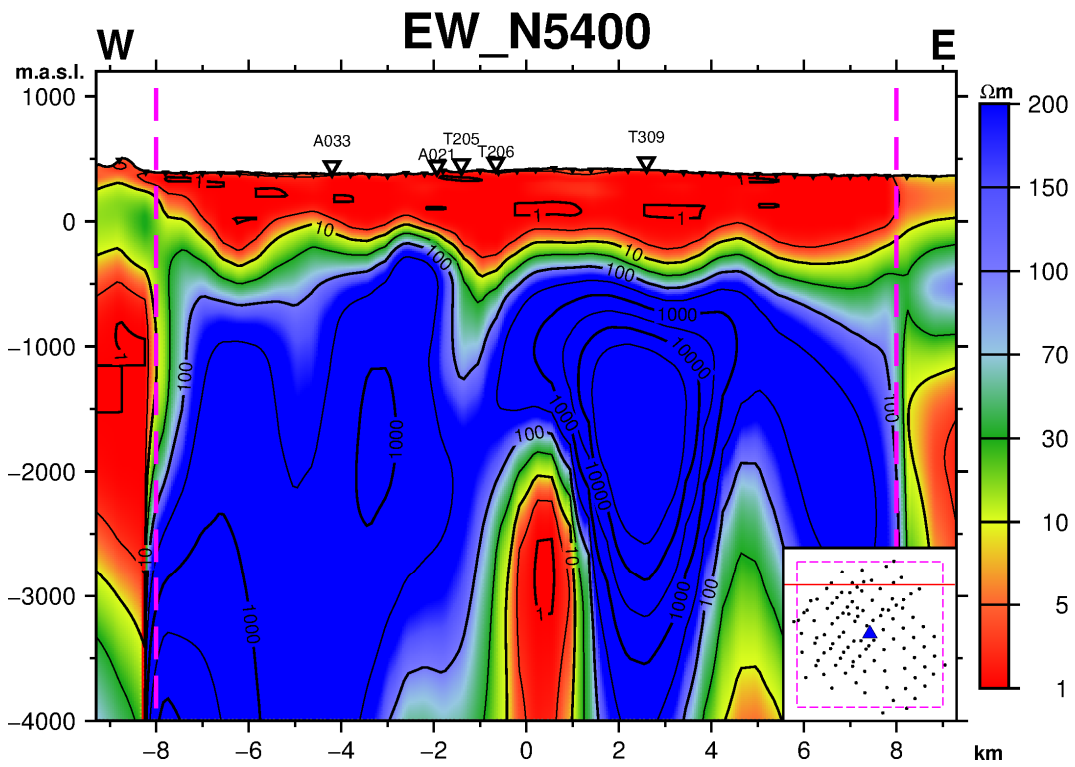
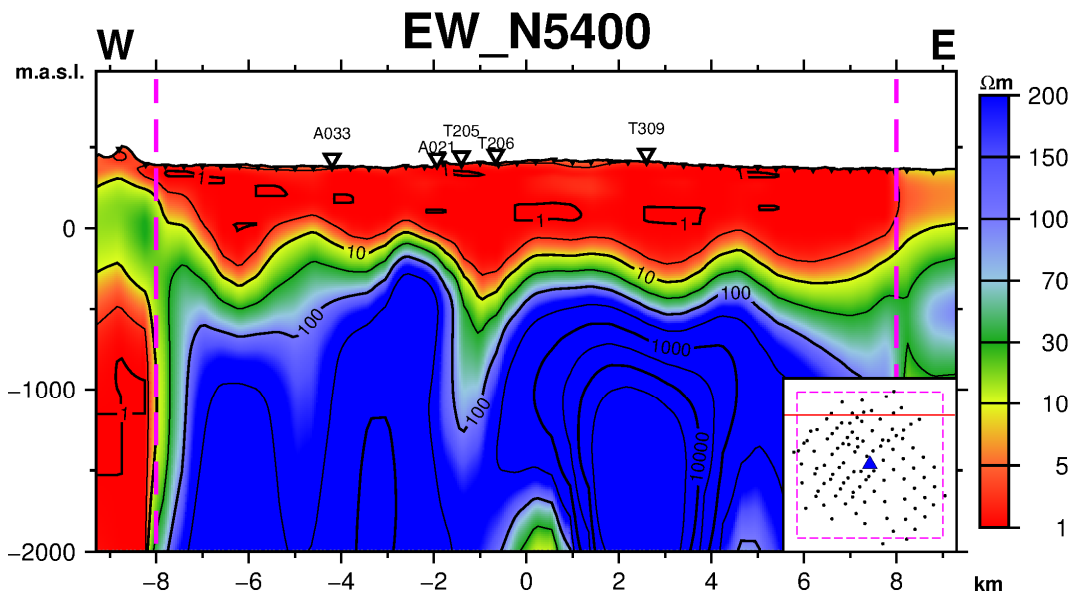


FIGURE 27: Cross-section E-W, N 5400